Diss. ETH No. 29698

MECHANO-REGULATED INTERACTIONS BETWEEN TISSUE TRANSGLUTAMINASE 2 AND FIBRILLAR FIBRONECTIN: ELUCIDATING THE BINDING INTERFACE AND THE MECHANISM

A thesis submitted to attain the degree of

DOCTOR OF SCIENCES

(Dr. sc. ETH Zurich)

presented by

KATERYNA SELCUK

(MSc ETH Biology)

born on 20.08.1986

accepted on the recommendation of

Prof. Dr. Viola Vogel, examiner

Dr. Alexander Leitner, co-examiner

Prof. Dr. Elisabetta Verderio Edwards, co-examiner

2023

The universe is under no obligation to make sense to you.

— Neil deGrasse Tyson

Table of Contents

Abstract……..iv

Zusammenfassung vi

List of figures ix

List of tables xi

List of abbreviations.....xii

1 Scope of the thesis 1

1.1 Motivation and significance. 2
1.2 Objectives. 4

2 Biological background 7

2.1 Transglutaminase 2 (TG2) – a multifunctional protein comprising many talents. 8
2.2 Structural organization of transglutaminase 2 and its conformational states: a case why a two-state model is not sufficient. 10
2.3 Why TG2 conformation matters: conformation-selective protein-protein interactions of TG2 with its intracellular and extracellular binding partners. 14
2.4 Adhesive functions and adhesive signaling of the transglutaminase 2 bound to fibronectin. 16
2.5 Adhesion-dependent pathophysiological mechanisms mediated by transglutaminase 2 in complex with fibronectin. 18
2.6 Fibronectin - a key component of the ECM, its conformations and fibrillogenesis. 19
2.7 Fibronectin as a mechanochemical switch. 22
2.8 Transglutaminase 2 and fibronectin interaction: what is known. 23
2.9 Final remarks. 24

3 Technical background and methodology.....26

3.1 Fibronectin-fiber (FN fiber) stretch assay. 27
3.2 Förster (Fluorescence) resonance energy transfer (FRET): general concepts. 28
3.3 FN-FRET – a nanoscale tensional probe to assess FN conformations and FN fiber strain. 32
3.4 Final remarks. 33

4 TG2-FN interactions are tuned by the mechanical strain of FN fibers.....34

4.1 Motivation. 35
4.2 Mechanical stretching of FN fibers reduces their affinity for TG2 bound to GDP.. 35

4.3 Spatial proximity between TG2's N-terminal domain and the C-terminal β-barrels is required for its mechano-regulated binding to FN. ... 42
4.4 Catalytic activity of TG2 has no effect on the loss of mechano-regulated binding to fibrillar FN. ... 48

5 Providing mechanistic and structural insights into the synergistic role of TG2's C-terminal β-barrel domains in the mechano-regulated binding ... 50

5.1 Motivation. ... 51
5.2 TG2's affinity to surface-adsorbed FN depends on its conformation and the presence of the C-terminal β-barrel domains. ... 51
5.3 C-terminal β-barrels of $TG2_{GDP}$ interact with the regions outside of the canonical gelatin-binding domain (GBD) of FN in solution. ... 54

6 TG2-FN complex: XL-MS guided integrative structural modeling and validation ... 61

6.1 Motivation. ... 62
6.2 Crosslink-guided structural modelling of TG2 and FN. ... 62
6.3 Crosslink-guided HADDOCK docking of TG2 with FNI_{7-9} revealed a parallel alignment of FN's type I modules with TG2's C-terminal β-barrels. ... 65
6.4 Collagen-mimicking peptide R1R2 and $TG2_{GDP}$ compete for binding to FN fibers. ... 67

7 Significance and conclusions ... 70

7.1 Implications and outlook. ... 71
7.2 Study limitations and future directions. ... 77

8 Supplementary Information ... 79

8.1 Supplementary Note 1: Structure prediction and structure refinement. ... 86
8.2 Supplementary Note 2: Analysis of accessible interaction space. ... 99
8.3 Supplementary Note 3: Protein-protein docking. ... 106

9 Materials and methods ... 115

9.1 Reagents ... 116
9.2 FN isolation from human blood plasma ... 116
9.3 Fluorescence labelling of FN and transglutaminases ... 116
9.4 FN labelling with donors and acceptors for FRET ... 117
9.5 FN fiber stretch assay ... 117
9.6 Induction of conformational changes of TG2 in the presence of its allosteric effectors ... 118
9.7 A dose-response competition assay with the R1R2 peptide ... 118
9.8 Calcium dose-response experiment ... 118
9.9 FRET confocal microscopy of FN fibers with bound TG2-647 ... 119
9.10 Ratiometric FRET image analysis and a correlation of TG2-647 binding with FN-FRET ratios ... 119

9.11 Statistical analysis for FN fiber stretch assays 120
9.12 Microplate FN-TG2 binding assay 120
9.13 Chemical crosslinking 121
9.14 Sample processing and mass spectrometric analysis 121
9.15 Identification of crosslinked peptides 122
9.16 Integrative structural modeling and docking 123
9.17 Data availability statement 123

10 Appendices 124

10.1 Protocols 124
10.1.1 Fluorescent bioconjugation of proteins (TG2 or FN) with amine-reactive dyes 124
10.1.2 Fibronectin-fiber stretch assay 127
10.2 ImageJ macro for quick batch conversion of images saved in a proprietary format to TIFF format 130
10.3 Condensed script which computes TG2-AF647 intensity and normalizes it pixel-by-pixel to FN-AF488 intensity 131

References 135

Acknowledgements 153

Abstract

Transglutaminase 2 (TG2) is a multifunctional protein that plays a vital role in stabilizing extracellular matrix (ECM) proteins through enzymatic crosslinking mostly during tissue growth, repair, as well as under various pathological conditions including inflammation, fibrosis, and cancer. Apart from its well-established enzymatic crosslinking activity, TG2 also binds non-covalently to numerous ECM proteins, both intracellularly and within the ECM, sometimes serving as a protein scaffold. One of the most well-known and well-characterized binding partners of TG2 in the ECM is fibronectin (FN), which also plays a critical role in tissue repair, tissue growth and in various pathological conditions where it is overexpressed. Cells exert cytoskeletal traction forces though integrin-mediated focal adhesions to stretch and partially unfold soluble FN and assemble it into insoluble fibrillar networks in the ECM.

TG2 acts as an adhesion co-receptor for FN, enhancing its interaction with integrins and forming TG2-FN-integrin ternary complexes on cell surfaces. This enhances cell adhesion, migration, proliferation, and cell survival. Thanks to this scaffolding function, TG2 helps to stabilize integrin-ECM adhesions, thereby enhancing cell attachment to the ECM and positively influencing cell survival and preventing anoikis. Both TG2 and FN are overexpressed in multiple cancers and is associated with poor patient prognosis. Given the anti-apoptotic and pro-survival role of the TG2-FN-integrin complex, efforts are underway to develop therapeutic inhibitors of TG2-FN interaction. Consequently, improving our understanding of the binding interface of the TG2-FN complex, as well as gaining mechanistic insights into the interaction can drive the development of novel therapeutics that block adhesion of tumor cells to the ECM.

Despite the recognized significance of TG2-FN interactions, the precise mechanisms governing these interactions and their response to mechanical forces within the fibrillar ECM networks remain elusive. Many FN domains have been shown to function as mechanochemical switches: when FN fibers are mechanically stretched or relaxed, this can alter structure-function relationships by either exposing otherwise cryptic binding epitopes or by destroying the available binding sites, consequently affecting the protein's biochemical functions, and downstream signaling cascades. Intriguingly, the gelatin binding domain (GBD) of FN, located within the $FNI_6FNII_{1\text{-}2}FNI_{7\text{-}9}$ region, which also overlaps with the primary binding site of TG2 on FN, acts as such mechanochemical switch in the interactions of FN with collagen I. The interaction between TG2 and fibrillar FN remains poorly understood, primarily because most studies have focused on utilizing soluble or surface-adsorbed FN or FN fragments, which differ in their conformations from multimeric insoluble FN fibers.

To address this issue, we employed a well-established *in vitro* FN fiber stretch assay in combination with a Förster resonance energy transfer (FRET) nanoscale sensor that probes the mechanical strain of FN. This approach is more physiologically relevant because it allows for the manual deposition of FN fibers that display the range of conformations present in the ECM fibrillar networks deposited by living cells. Additionally, it offers control by allowing the adjustment of the FN fiber strain externally. As the FRET-sensor provides optical read-outs of the FN fiber strain, ligand binding can be correlated with the mechanical strain of FN fibers, thereby helping us decipher the elusive structure-function relationships.

Using this approach, we discovered that the binding of a potent ECM crosslinking enzyme to ECM fibers is mechano-regulated. TG2's binding to FN is tuned by the mechanical tension of FN fibers, with TG2 predominantly co-localizing with low-tension FN fibers, while FN fiber stretching reduces their affinity for TG2. We provide mechanistic and structural insights into this mechano-regulated binding by demonstrating that it relies on the proximity between the N-terminal β-sandwich and C-terminal β-barrels of TG2. In contrast, when TG2 is in an "open-state", in which C-terminal domains move away from N-terminal, TG2 bound to FN fibers equally, regardless of FN fiber strain.

To gain deeper insights into the novel binding mechanism, we employed crosslinking mass spectrometry (XL-MS) to map the binding interface of the TG2-FN complex. XL-MS revealed indeed a novel TG2-FN synergy site within TG2's C-terminal β-barrels that interacts with FN regions outside of the previously known canonical gelatin binding domain, specifically FNI_2 and $FNIII_{14-15}$. To complement our experimental findings, we utilized *in silico* integrative structural modeling, leveraging experimental crosslinks obtained from XL-MS as distance restraints to guide the molecular modeling and protein-protein docking of the TG2-FN complexes. One of the docking poses revealed a parallel alignment of FNI_{7-9} modules with the C-terminal β-barrels of TG2, further supporting the hypothesis of the synergy site within TG'2 C-terminal β-barrels.

To further validate our model and incorporate other principal ECM interactors into our FN fiber pulling assays, we conducted binding studies where TG2 was competing with the collagen-mimicking R1R2 peptide for their common binding site on FN. This was done because the binding sites of TG2, R1R2 and collagen I have been mapped to the same region of FN, which is FnI_{8-9}. This competition binding assay revealed that TG2 binding to relaxed FN fibers decreased with increasing R1R2 peptide concentrations, and that the addition of the R1R2 peptide completely abrogated TG2 mechano-regulated binding and its mechanical FN fiber strain-sensing.

In summary, our experimental and computational findings shed light on a previously unknown role of the two C-terminal β-barrel domains of TG2. We propose that they serve as a "synergy binding site" for FN and are essential for mechano-regulated TG2 binding to FN. Contrary to previous assumptions, we demonstrated here that TG2's conformational states affect its interactions with FN, as mechano-regulated binding is only possible when the N-terminal and C-terminal domains of TG2 are in spatial proximity. We propose that TG2 could serve as a FN fiber strain sensor modulating cell-ECM interactions, such as cell adhesion, spreading and migration, as well as cell phenotype decision making, depending on the tensional state of ECM fibers, thereby modulating a tissue response in homeostasis, wound healing and if excessive, in pathological transformations. And reciprocally, that FN fibers could serve as a reversible ECM storage space for TG2. These properties of the TG2-FN bond would thereby modulate tissue responses in cancer, wound healing, and homeostasis. Proteomics data are available via ProteomeXchange with identifier PXD043976 and integrative modelling structures are available via PDB-Dev.

Zusammenfassung

Gewebetransglutaminase 2 (TG2) ist ein multifunktionales Protein, das eine wichtige Rolle bei der Stabilisierung von Proteinen der extrazellulären Matrix (ECM) durch enzymatische Vernetzung während des Wachstums, der Reparatur und der Entzündung von Gewebe spielt. Abgesehen von seiner bekannten enzymatischen Vernetzungsaktivität bindet TG2 auch nicht-kovalent an zahlreiche ECM-Proteine, sowohl intrazellulär als auch innerhalb der ECM, und dient manchmal als Proteingerüst. Einer der bekanntesten und am besten charakterisierten Bindungspartner von TG2 in der ECM ist das Fibronektin (FN), das auch eine entscheidende Rolle bei der Gewebereparatur und dem Gewebewachstum spielt und bei verschiedenen pathologischen Zuständen überexprimiert wird. Zellen üben über Integrin-vermittelte fokale Adhäsionen Zugkräfte auf das Zytoskelett aus, um lösliches FN zu entfalten und in der ECM zu unlöslichen fibrillären Netzwerken zusammenzufügen.

TG2 fungiert als Adhäsions-Korezeptor für FN, indem es dessen Interaktion mit Integrinen verstärkt und ternäre TG2-FN-Integrin-Komplexe auf der Zelloberfläche bildet. Dies fördert die Zelladhäsion, Migration, Proliferation und das Überleben der Zellen. Dank dieser Gerüstfunktion fördert TG2 die Interaktion zwischen FN und Integrinen, was letztlich die Zellanhaftung an die ECM erhöht und das Zellüberleben positiv beeinflusst und Anoikis verhindert. Der TG2-Fn-Komplex ist bei zahlreichen Krebsarten überexprimiert und wird mit einer schlechten Patientenprognose in Verbindung gebracht. Angesichts der anti-apoptotischen und überlebensfördernden Rolle des TG2-FN-Komplexes wird derzeit an der Entwicklung therapeutischer Inhibitoren der TG2-FN-Interaktion gearbeitet. Ein besseres Verständnis der Bindungsschnittstelle des TG2-FN-Komplexes sowie mechanistische Erkenntnisse über die Interaktion können daher die Entwicklung neuer Therapeutika vorantreiben, die die Adhäsion von Tumorzellen an die ECM blockieren.

Trotz der anerkannten Bedeutung der TG2-FN-Wechselwirkungen sind die genauen Mechanismen, die diese Wechselwirkungen und ihre Reaktion auf mechanische Kräfte innerhalb der fibrillären Netzwerke der ECM steuern, nach wie vor nicht bekannt. Es hat sich gezeigt, dass viele FN-Domänen als mechanochemische Schalter fungieren: Wenn FN-Fasern mechanisch gedehnt oder gelockert werden, verändert dies die Struktur-Funktions-Beziehung, indem die kryptischen Bindungsepitope freigelegt oder die verfügbaren Bindungsstellen zerstört werden, was wiederum die biochemischen Funktionen des Proteins und die nachgeschalteten Signalkaskaden beeinflusst. Interessanterweise fungiert die Gelatinebindungsdomäne (GBD) von FN, die sich in der FNI6FNII1-2FNI7-9-Region befindet, die sich auch mit der primären Bindungsstelle von TG2 auf FN überschneidet, als ein solcher mechanochemischer Schalter in den Wechselwirkungen von FN mit Kollagen I. Die Wechselwirkung zwischen TG2 und fibrillärem FN ist nach wie vor nur unzureichend verstanden, vor allem weil sich die meisten Studien auf die Verwendung von löslichem oder an der Oberfläche adsorbiertem FN oder FN-Fragmenten konzentriert haben, die sich in ihrer Konformation von unlöslichen FN-Fasern unterscheiden.

Um dieses Problem zu lösen, haben wir einen gut etablierten In-vitro-Test zur Dehnung von FN-Fasern in Kombination mit dem Förster-Resonanz-Energie-Transfer (FRET)-Sensor im Nanomaßstab für mechanische Dehnungen verwendet. Dieser Ansatz ist physiologisch

relevanter, da er die manuelle Ablagerung von FN-Fasern ermöglicht, die alle Konformationen aufweisen, die in den von lebenden Zellen abgelagerten ECM-Fibrillennetzen vorkommen. Darüber hinaus bietet er die Möglichkeit, die Dehnung der FN-Fasern von außen zu steuern. Darüber hinaus liefert der FRET-Sensor optische Informationen über die Konformation der FN-Fasern. Auf diese Weise können wir die Bindung von Liganden mit der mechanischen Belastung der FN-Fasern korrelieren, was uns hilft, die schwer fassbaren Struktur-Funktions-Beziehungen zu entschlüsseln.

Mithilfe dieses Ansatzes entdeckten wir, dass die Bindung eines Vernetzungsenzyms an ECM-Fasern mechanisch reguliert ist. Die Bindung von TG2 an FN wird durch die mechanische Spannung der FN-Fasern gesteuert, wobei TG2 überwiegend mit FN-Fasern mit geringer Spannung kolokalisiert, während die Dehnung der FN-Fasern ihre Affinität für TG2 verringert. Wir bieten mechanistische und strukturelle Einblicke in diese mechanisch regulierte Bindung, indem wir zeigen, dass sie auf der Nähe zwischen dem N-terminalen β-Sandwich und den C-terminalen β-Fässern von TG2 beruht. Wenn sich TG2 in einer "offenen" Konformation befindet, bindet es gleichermaßen an FN-Fasern, unabhängig von der FN-Faserbelastung.

Um tiefere Einblicke in den neuartigen Bindungsmechanismus zu erhalten, haben wir die Crosslinking-Massenspektrometrie (XL-MS) eingesetzt, um die Bindungsschnittstelle des TG2-FN-Komplexes zu kartieren. XL-MS zeigte in der Tat eine neuartige TG2-FN-Synergiestelle innerhalb der C-terminalen β-Fässer von TG2, die mit FN-Regionen außerhalb der bisher bekannten kanonischen Gelatine-Bindungsdomäne interagiert, insbesondere FNI2 und FNIII14-15. Um unsere experimentellen Befunde zu ergänzen, nutzten wir die integrative Strukturmodellierung in silico, wobei wir experimentelle Querverbindungen aus XL-MS als Distanzbeschränkungen nutzten, um die molekulare Modellierung und das Protein-Protein-Docking der TG2-FN-Komplexe zu steuern. Eine der Docking-Posen zeigte eine parallele Ausrichtung der FNI7-9-Module mit den C-terminalen β-Fässern von TG2, was die Hypothese der Synergiestelle innerhalb der C-terminalen β-Fässer von TG2 weiter unterstützt.

Um unser Modell weiter zu validieren und andere wichtige ECM-Interaktoren in unsere FN-Faserziehversuche einzubeziehen, führten wir Bindungsstudien durch, bei denen TG2 mit dem Kollagen nachahmenden R1R2-Peptid um ihre gemeinsame Bindungsstelle auf FN konkurrierte. Dies wurde durchgeführt, weil die Bindungsstellen von TG2, R1R2 und Kollagen I in derselben Region von FN, nämlich FnI8-9, kartiert wurden. Dieser Wettbewerbstest zeigte, dass die Bindung von TG2 an entspannte FN-Fasern mit zunehmender R1R2-Peptidkonzentration abnahm und dass die Zugabe des R1R2-Peptids die mechanisch regulierte Bindung von TG2 und seine mechanische Erkennung der FN-Faserdehnung vollständig aufhob.

Zusammenfassend lässt sich sagen, dass unsere experimentellen und rechnerischen Ergebnisse Licht auf eine bisher unbekannte Rolle der beiden C-terminalen β-Fass-Domänen von TG2 werfen. Wir schlagen vor, dass sie als "Synergie-Bindungsstelle" für FN dienen und für die mechano-regulierte TG2-Bindung an FN wesentlich sind. Im Gegensatz zu früheren Annahmen haben wir hier gezeigt, dass die Konformationszustände von TG2 seine Interaktionen mit FN beeinflussen, da eine mechano-regulierte Bindung nur möglich ist, wenn die N-terminalen und C-terminalen Domänen von TG2 in räumlicher Nähe zueinander liegen. Wir schlagen vor, dass TG2 als Sensor für die Dehnung der FN-Fasern dienen könnte, der Zell-ECM-Interaktionen wie Zelladhäsion, -ausbreitung und -migration sowie die Entscheidung über den Zellphänotyp in Abhängigkeit vom Spannungszustand der ECM-Fasern moduliert und

damit eine Gewebereaktion in der Homöostase, bei der Wundheilung und, falls übermäßig, bei pathologischen Veränderungen moduliert. Umgekehrt könnten die FN-Fasern als reversibler ECM-Speicher für TG2 dienen. Diese Eigenschaften der TG2-FN-Bindung würden somit die Gewebereaktionen bei Krebs, Wundheilung und Homöostase modulieren. Proteomics-Daten sind über ProteomeXchange mit dem Identifikator PXD043976 und integrative Modellierungsstrukturen über PDB-Dev verfügbar.

List of figures

Figure 2.1.1: Schematic view of enzymatic reactions catalyzed by TG2 transamidation activity. 9
Figure 2.2.1: Schematic illustration of TG2's domain composition, its conformational states and known binding interactions with fibronectin (FN). 14
Figure 2.4.1: Schematic depiction of TG2's interactions with other components of adhesive signaling complexes on the cell surface. 17
Figure 2.6.1: Schematic overview of FN domain arrangement and major ECM interaction sites 21
Figure 2.8.1: Schematic illustration of the known interaction sites on TG2 and FN. 24
Figure 3.1.1: Schematic illustration of the FN fiber stretch assay. 28
Figure 3.2.1: Schematic illustration of the main concepts underlying Förster Resonance Energy Transfer. 31
Figure 4.2.1: FN-FRET denaturation with guanidine hydrochloride in solution. 37
Figure 4.2.2: TG2 preferentially co-localizes with FN fibers under low strain, as revealed by the FN fiber stretch assay. 38
Figure 4.2.3: FN fiber stretch assay performed with WT gpTG2 in the presence of 1 mM GDP+ 1 mM EDTA on FN fibers deposited as intersections. 41
Figure 4.3.1: FN fiber stretch assay performed with WT gpTG2 in the presence of increasing Ca2+ concentrations on horizontally deposited FN fibers under low strain (20%). 44
Figure 4.3.2: FN fiber stretch assay data showing the dependence of mechano-regulated TG2-FN binding on TG2's conformational states and its C-terminal β-barrels. 45
Figure 4.3.3: FN fiber stretch assay with WT hrTG2 and short hrTG2(1-465aa). 46
Figure 4.3.4: FN fiber stretch assay with WT gpTG2. 47
Figure 4.4.1: FN fiber stretch assay performed with hrTG2's inactive Cys277Ser mutant. 48
Figure 5.2.1: Microplate protein-binding assay data with TG2 binding to surface-adsorbed full-length FN, or to FN's 45 kDa gelatin binding domain (GBD) fragment. 53
Figure 5.3.1: Crosslinks identified with the XL-MS of the $TG2_{GDP}$ and FN complex reveal that TG2's C-terminal β-barrel domains interact with regions outside of the canonical FN's GBD. 56
Figure 5.3.2: XL-MS of TG2 and 45 kDa-FN and TG2 and FN complexes using trypsin as a protease. 58
Figure 5.3.3: XL-MS of TG2 and 45 kDa-FN and TG2 and FN complexes using chymotrypsin as a protease. 60
Figure 6.2.1: Schematic overview of the integrative structural modelling workflow of TG2 complexed to FN, which is presented in detail in Supplementary Note 1-3. 64
Figure 6.3.1: Protein-protein docking with HADDOCK of TG2 complexed with selected FN fragments guided with experimental crosslinks as distance restraints. 66

Figure 6.4.1: FN fiber stretch assay reveals a dose-dependent competition between the collagen-mimicking peptide R1R2 and WT gpTG2$_{GDP}$ for binding to FN fibers under high, as well as low strain..... 68
Figure 6.4.2: Competition FN fiber stretch assay between the collagen-mimicking peptide R1R2 (Streptococcus equi) and WT gpTG2 in the presence of 1mM GDP and 1mM EDTA. 69
Figure 7.1.1: Sketch illustrating the proposed model of TG2's mechano-regulated binding to FN fibers..... 76
Figure 7.2.1: FN-FRET and TG2-647 image acquisition and correction parameters. 80
Figure 7.2.2: TG2-647 binding to FN-FRET fibers deposited orthogonally to each other in the presence of 1mM GDP and 1mM EDTA, imaging, and image analysis illustration. 82
Figure 7.2.3: TG2-647 binding to FN-FRET fibers unidirectionally deposited in the presence of 1 mM GDP and 1 mM EDTA, imaging, and image analysis illustration. 84
Figure 8.3.1: DisVis analysis of the accessible interaction space between TG2 and GBD. 108
Figure 8.3.2: DisVis analysis of the accessible interaction space between TG2 and FN fragments. 110
Figure 8.3.3: Predicted model of TG2 and GBD complex obtained using crosslink-guided docking with HADDOCK. 111
Figure 8.3.4: Predicted model of TG2 and FNI2-3 complex obtained using crosslink-guided docking with HADDOCK. 112
Figure 8.3.5: Predicted model of TG2 in complex with FNIII14-15 as obtained using crosslink-guided docking with HADDOCK. 113
Figure 8.3.6: Predicted model of TG2 and FNI7-9 complex obtained using crosslink-guided docking with HADDOCK. 114
Figure 10.1.1: A schematic view of the FN fiber-stretch assay and the experimental setup. 128

List of tables

Table 8.1-1: Crosslinked residues within FNI2-3: 87
Table 8.1-2: Crosslinked residues within GBD (FNI_6-$FNII_{1-2}FNI_{7-9}$): 89
Table 8.1-3: Crosslinked residues within $FNIII_{14-15}$: 93
Table 8.1-4: Crosslinked residues within TG2. 97
Table 8.2-1: Crosslinked residues between TG2 and FNI_{2-3}. 100
Table 8.2-2: Accessible complexes consistent with at least N restraints..... 101
Table 8.2-3: Z-score for each restraint 101
Table 8.2-4: Crosslinked residues between TG2 and GBD. 102
Table 8.2-5: Accessible complexes consistent with at least N restraints..... 102
Table 8.2-6: Z-score for each restraint. 103
Table 8.2-7: Crosslinked residues between TG2 and FNI_{7-9}. 104
Table 8.2-8: Crosslinked residues between TG2 and $FNIII_{14-15}$. 104
Table 8.2-9: Accessible complexes consistent with at least N restraints..... 105
Table 8.2-10: Z-score for each restraint. 105
Table 10.1-1: FN fiber pulling, and uniaxial stretch device set up – short summary..... 128

List of abbreviations

45-kDa FN	45-kDa fibronectin fragment, gelatin-binding domain
AF	Alexa Fluor
CB-CB	β-carbon--β-carbon distance
DMTMM	4-(4,6-dimethoxy-1,3,5-triazin-2-yl)-4-methylmorpholinium
DSS	Disuccinimidyl suberate
ECM	Extracellular matrix
ED	Euclidean distance
EDTA	Ethylenediaminetetraacetic acid
FRET	Förster Resonance Energy Transfer
FN	Fibronectin
FN-AF488	Fibronectin labelled with Alexa Fluor 488
FN fiber	Fibronectin fiber
FN-FRET	Fibronectin labeled for Förster Resonance Energy Transfer
GBD	Gelatin-binding domain (of fibronectin)
GDP	Guanosine diphosphate
GSSG	Oxidized glutathione
GTP	Guanosine triphosphate
gpTG2	Guinea pig transglutaminase 2
HADDOCK	High Ambiguity Driven protein-protein DOCKing
H-bond	Hydrogen bond
hrTG2	Human recombinant transglutaminase 2
I-TASSER	Iterative Threading ASSEmbly Refinement
LC-MS/MS	Liquid chromatography with tandem mass spectrometry
oxTG2	Oxidized TG2
PDB	Protein Data Bank
PDH	Pimelic dihydrazide
QMEAN	Qualitative Model Energy Analysis

RGD	Arginylglycylaspartic acid (arginine-glycine-aspartate)
RT	Room temperature
R1R2	Collagen-mimicking peptide, FN-binding protein of the pathogen *Streptococcus equi*.
SAXS	Small angle X-ray/neutron scattering
SEC	Size-exclusion chromatography
Short TG2	Mutant transglutaminase 2 variant with deleted C-terminal β-barrels 1 and 2
TG2	Transglutaminase 2
TG2-AF647	Transglutaminase 2 labelled with Alexa Fluor 647
$TG2_{Ca2+}$	Transglutaminase 2 bound to calcium: catalytically active open conformation
$TG2_{EDTA}$	Transglutaminase 2 in solution with ethylenediaminetetraacetic acid (EDTA)
$TG2_{GDP}$	Transglutaminase 2 bound to guanosine diphosphate (GDP): catalytically inactive closed conformation
$TG2_{Z006}$	Transglutaminase 2 bound to the Z006 inhibitor: catalytically inactive open linear conformation
WT	Wild type
WT gpTG2	Wild type guinea pig TG2
XL-MS	Crosslinking mass spectrometry
Z006	Z-DON-Val-Pro-Leu-OMe, “Z-DON” inhibitor of TG2 catalytic activity

1 Scope of the thesis

1.1 Motivation and significance.

The growing field of mechanobiology has revealed that not only the biochemical, but also the physical properties of the extracellular matrix (ECM) have a major impact on cell decision making in development, hemostasis and wound healing[1–4], and when altered can drive pathological transformations, including progressive cancer and fibrotic pathologies[5]. Enzymatic crosslinking of ECM fibers is necessary for the mechanical stabilization during tissue growth and repair, but also plays a major role as the driver of fibrotic diseases and malignancy[6–8]. Transglutaminase 2 (TG2), also referred to as tissue transglutaminase, is mostly retained within the cell under homeostatic conditions, but upon tissue injury or inflammation, its expression and subsequent export to the cell surface and the extracellular environment are strongly upregulated[9–12]. Once secreted, TG2 alters the physico-chemical properties of the extracellular environment by enzymatically crosslinking various ECM proteins, making the ECM stiffer and more resistant to proteolytic degradation. In turn, this triggers various downstream effects which change cell behavior and promote cell adhesion, migration and fibroblast proliferation[11,13]. While these processes are essential to stabilize the provisional ECM during wound healing, they need to be tightly regulated, and aberrant TG2 activity leads to pathological fibrosis[6,14,15]. Indeed, it was shown in healthy tissues that most externalized TG2 is catalytically inactive and only transiently activated by stress signals[16,17]. However, the crosslinking activity is only one component of the large functional arsenal of TG2. Numerous studies have shown that it also acts as a non-enzymatic scaffold protein that interacts with many ECM components and cell-surface receptors to support cell adhesion, migration, proliferation and survival, such as fibronectin, collagen, vitronectin, integrins, syndecan-4, several growth factor receptors and others[18,19].

Fibronectin (FN) is one of the best characterized binding partners of TG2 in the ECM, which is overexpressed during development, tissue growth and repair as well as under various pathological conditions. FN polymerizes to form fibrous matrices that promote cell adhesion, migration, and proliferation. Usually, cells adhere to FN through transmembrane receptors called integrins through the Arg-Gly-Asp (RGD) integrin binding site on $FNIII_{10}$, and additionally the synergy site on $FNIII_9$, which is selectively recognized by integrin $\alpha5\beta1$. However, RGD-dependent cell adhesion and the associated outside-in integrin signaling may be disrupted during extensive tissue damage, ECM degradation and remodeling. Blocking of the cell adhesion with synthetic RGD-peptides causes reduction in FN-integrin interaction and in the absence of TG2 leads to detachment-induced apoptosis (anoikis) in many cell types[14,19,20]. However, when TG2 is expressed on the cell surface, it can rescue cells from anoikis when RGD-dependent adhesion is blocked, thereby promoting cell survival[14,20–22]. This rescue does not depend on the enzymatic activity of TG2, but requires FN-binding together with the assistance of Syndecan-4's heparan sulfate chains and/or non-canonical binding to β1-integrins[14,20,23]. Furthermore, TG2-FN interaction enhances deposition of FN fibers with assistance from Syndecan-4 and β1-integrins, when RGD-dependent adhesion is attenuated, thus helping to quickly restore the extracellular environment after injury[22,24]. Finally, it also binds to the Stachel, which is the extracellular domain of adhesive GPCRs[25].

Given the pro-survival adhesive properties of the TG2-FN complex, it is not surprising that high expression levels of TG2 favor metastasis formation in multiple cancers[8,26–31].

Consequently, TG2 upregulation in these tumors is strongly associated with poor patient outcome[32]. This makes the TG2-FN complex a compelling drug target[7,13]. Currently, efforts are underway to develop small molecule inhibitors that disrupt the TG2-FN interface[33–36]. Thus, a deeper mechanistic and structural understanding of the TG2-FN interaction sites would not only shed light on its role in wound healing and cancer, but it would also assist the rational design of drugs.

TG2 consists of four domains: an N-terminal β-sandwich, a catalytic core, and two C-terminal β-barrels (**Figure 2.2.1 A-C**). While previous structural studies have characterized TG2 in two conformational states ("open" and "closed") using crystallography[37,38], evidence suggests that these two states do not adequately capture the protein's conformational plasticity. When TG2 is bound to GDP, GTP or other purine nucleotides, it adopts an enzymatically inactive “closed” conformation. In this state, the C-terminal β-barrel domains tightly fold over the catalytic domain, obstructing access to the active site (PDB:1KV3)[38] (**Figure 2.2.1 A**). However, when the active site is covalently bound to an irreversible inhibitor Z-DON, TG2 undergoes a large conformational change (PDB:2Q3Z)[37]. The β-barrel domains are prevented from interacting with the catalytic core, resulting in an “open”, extended conformation (**Figure 2.2.1 B**). Although the PDB:2Q3Z conformation is often associated with the catalytically active TG2, due to the readily accessible active site, there are doubts regarding its true representation of the active form[39]. Firstly, PDB:2Q3Z contains a Cys370-Cys371 disulfide bridge near the active site, which if formed inhibits TG2 catalytic activity too[40,41]. Secondly, the formation of this disulfide bridge induces local changes in the peptide backbone conformation, disrupting the calcium binding sites[41]. Consequently, the PDB:2Q3Z structure, bound to Z-DON inhibitor, does not include any calcium ions, despite their known requirement for its crosslinking function[37]. Finally, no crystal structure of catalytically active TG2 bound to calcium ions has been solved to date. Therefore, it is unlikely that the extended conformation observed in the Z-DON inhibitor-bound TG2 structure accurately represents the calcium-bound catalytically active protein. Indeed, small angle X-ray/neutron scattering (SAXS/SANS), hydrogen-deuterium exchange (HDX) and biosensor measurements suggest that the calcium bound TG2 assumes an “open” conformation distinct from the two known structures[41–43]. The reversible formation of the Cys370-Cys371 disulfide bond acts as a redox switch, inactivating TG2 in the oxidative environment of ECM and desensitizing it to the presence of effectors[40]. In fact, experimental evidence indicates that the Z-DON inhibitor-bound structure resembles the oxidized TG2, i.e. TG2 in the extended effector-free state[41,43]. Thus, TG2 can adopt more than the two crystallographically captured conformations and exists in at least three different states: nucleotide binding favors the “closed” conformation[38], while high calcium concentrations predominantly induce the “open”, but yet not identified conformation[41,43]. Importantly, only this open state is catalytically active. In the absence of calcium, or GDP/GTP and under oxidative conditions, TG2 assumes a catalytically inactive, yet “open” effector-free state[41] (**Figure 2.2.1 D**).

While significant progress has been made towards mapping the interactions between TG2 and FN more precisely, previous studies that sought to investigate TG2-FN interactions were either performed with soluble dimeric FN or with shorter FN fragments[21,44–49]. Thus, nothing is known about how FN fibrillogenesis might affect its interactions with TG2. Soluble FN, as well as many of its fragments adopts a quaternary structure, which is distinct from the

insoluble fibrillar form in the ECM[50–52]. Although the exact structure of the fibrillar FN remains unknown, mutagenesis and then a super-resolution microscopy study has shown that that FN fibrillogenesis requires the N-terminal FnI_{1-5} domains[53] and that FN polymerizes in a antiparallel fashion with an N-terminal overlap of almost 40 nm[54]. Cell-mediated stretching of FN fibers during FN fibrillogenesis can either create additional interaction sites for its binding partners, or structurally perturb others[55]. Many FN domains were shown to act as mechanochemical switches: when FN fibers are mechanically stretched or relaxed, this can either destroy or open up binding epitopes, thereby altering the protein's biochemical functions and changing downstream outside-in cell signaling[55–63]. Intriguingly, we have previously demonstrated that the gelatin binding domain (GBD) of FN, located on the $FNI_6FNII_{1-2}FNI_{7-9}$ region, which also overlaps with the main binding site of TG2 on FN (**Figure 2.8.1**), acts as such mechanochemical switch in FN interactions with collagen I[61]. Thus, we asked here whether changes in the tensional state of FN fibers and their force-induced mechanical stretching and partial unfolding might also have an impact, or possibly regulate the binding of TG2 to FN.

1.2 Objectives.

The thesis work is organized into three specific aims, each of which is summarized below:

1. *Explore whether the mechanical strain experienced by FN fibers can modulate interactions with TG2 (Chapter 4).*

In this chapter, we investigated whether mechanical strain affects the interaction between FN fibers and TG2. TG2 is known to bind to FN in the extracellular matrix and co-localize with FN-matrix forming ternary adhesive complexes including β-integrins. When the work on this thesis had begun, nothing was known whether the mechanical strain in FN fibers can influence the interactions of FN with TG2. To address this, we utilized a well-established *in vitro* FN fiber stretch assay coupled with Förster resonance energy transfer FN-probes, which act as a sensor of mechanical strain experienced by the fiber. Our findings reveal that TG2's interactions with FN fibers are tuned by the mechanical strain of FN fibers, with TG2 preferentially co-localizing with FN fibers experiencing low strain (relaxed condition). Furthermore, we established that TG2's mechano-regulated binding to FN depends on the spatial proximity of TG'2 C-terminal β-barrels with N-terminal β-sandwich. This discovery suggests that the FN-binding epitope on TG2 is contingent on the conformational states of TG2.

The work presented in this chapter (Chapter 4) has been published in Matrix Biology.

Kateryna Selcuk, Alexander Leitner, Lukas Braun, Fanny Le Blanc, Paulina Pacak, Simon Pot, Viola Vogel, **Transglutaminase 2 has higher affinity for relaxed than for stretched fibronectin fibers**, Matrix Biology, Volume 125, 2024, Pages 113-132, ISSN 0945-053X, https://doi.org/10.1016/j.matbio.2023.12.006

2. *Gain structural insights into the novel mechanism of the mechano-regulated binding between TG2 and FN (Chapter 5).*

Building on the mechano-regulated binding observed in Chapter 4, we hypothesized the presence of an unrecognized synergy binding site on TG2's C-terminal β-barrels. Therefore, we sought to investigate this further in Chapter 5. This chapter aims to explore the novel role of TG2's C-terminal β-barrel domains in mechano-regulated binding with FN. Our results demonstrate that TG2 exhibits differential binding to surface-adsorbed FN, with binding affinity dependent on TG2's conformation. Specifically, TG2 in the "closed-state" binds to surface-adsorbed FN with higher affinity. Additionally, the presence of C-terminal β-barrel domains is crucial, as TG2 lacking these domains does not exhibit the differential binding to surface-adsorbed FN. Moreover, through crosslinking mass spectrometry, we confirmed that TG2's C-terminal β-barrel domains interact with regions outside of FN's canonical gelatin-binding domain, specifically FNI2 and FNIII14-15. These findings reinforce the role of C-terminal β-barrel domains in mediating mechano-regulated binding to FN.

The work presented in this chapter (Chapter 5) has been published in Matrix Biology.

Kateryna Selcuk, Alexander Leitner, Lukas Braun, Fanny Le Blanc, Paulina Pacak, Simon Pot, Viola Vogel, **Transglutaminase 2 has higher affinity for relaxed than for stretched fibronectin fibers**, Matrix Biology, Volume 125, 2024, Pages 113-132, ISSN 0945-053X, https://doi.org/10.1016/j.matbio.2023.12.006

3. *Generate in silico models of TG2-FN protein-protein complexes by exploiting experimental XL-MS data as distance restraints using bioinformatics approaches (Chapter 6).*

It has been long established that TG2 interacts with FN by binding to the gelatin-binding domain (GBD) of FN with its N-terminal β-sandwich. However, it was not known that TG2's C-terminal β-barrels can interact with FN too. After finding above that through interaction of TG2's C-terminal β-barrels with FN regions outside of the canonical GBD, in Chapter 6, we perform integrative structural modeling of the TG2-FN complexes by utilizing experimental crosslinks as distance restraints, which we obtained from TG2-FN complexes in solution. Through crosslink-guided protein-protein docking with DisVis/HADDOCK, we predict models of TG2-FNI_{7-9}, TG2-FNI_{2-3}, and TG2-$FNIII_{14-15}$ protein complexes. Notably, the high-scoring docking pose of the TG2-FNI_{7-9} complex supports the parallel alignment of FNI_{8-9} modules with TG2's C-terminal β-barrel domains, offering atomic-scale structural evidence for the role of C-terminal domains as a synergy binding site. Furthermore, it is known that both TG2 and collagen I bind to FNI_{7-9}, however, it has not been investigated experimentally whether they can compete for the binding to FN fibers under various strain conditions. We thus investigated whether TG2 and collagen I might compete for binding to FN fibers under varying strain conditions. Our experiments revealed that TG2 binding to FN fibers decreases in a dose-dependent manner in the presence of the collagen-mimicking peptide R1R2, both under high and low fiber strain conditions.

The work presented in this chapter (Chapter 6) has been published in Matrix Biology.

Kateryna Selcuk, Alexander Leitner, Lukas Braun, Fanny Le Blanc, Paulina Pacak, Simon Pot, Viola Vogel, **Transglutaminase 2 has higher affinity for relaxed than for stretched fibronectin fibers**, Matrix Biology, Volume 125, 2024, Pages 113-132, ISSN 0945-053X, https://doi.org/10.1016/j.matbio.2023.12.006

2 Biological background

2.1 Transglutaminase 2 (TG2) – a multifunctional protein comprising many talents.

Transglutaminase 2 (TG2) is a 75kDa protein that belongs to the transglutaminase family, which comprises eight other catalytically active members (TG1-7, Factor XIIIa) and one catalytically inactive member erythrocyte protein 4.2. Discovered in 1957, TG2 has been extensively studied, due to its ubiquitous presence in nearly all tissues, including in extracellular spaces, the plasma membrane, cytosol, and certain organelles such as the nucleus and mitochondria[64]. The other members of the transglutaminase family include keratinocyte transglutaminase (TG1), epidermal transglutaminase (TG3), prostate transglutaminase (TG4), TG5 (expressed mainly by foreskin keratinocytes), TG6 and TG7 (expressed in testes, lungs and brain), and Factor XIIIa, an important component of the blood coagulation cascade[15].

The first discovered and best-known function of TG2 is its transamidation (or covalent crosslinking) activity, demonstrated by Heinrich Waelsch in 1957[65]. This activity is strictly calcium-dependent and is performed by the catalytic triad composed of cysteine 277 (C277), histidine 335 (H335) and aspartate 358 (D358), which are the critical residues for TG2 transamidation. The reaction proceeds in two steps: the formation of a thioester intermediate through the nucleophilic attack by cysteine on the acyl donor (γ-carboxamide group of glutamine), resulting in the release of ammonia as byproduct. In the second step, the ε-amino group of lysine, acting as the acyl acceptor, attacks on the thioester bond, leading to the formation of a covalent inter-molecular ε-(γ-glutamyl)lysine isopeptide bond[66]. It is important to note that transamidation does not always result in the crosslinking of two proteins; it can also involve the addition of a small biological amine, serving as a form of post-translational modification of the substrate protein[18]. In the absence of primary amine and the presence of water, a water molecule can act as an acyl acceptor, causing the de-amidation (hydrolysis) of the glutamine residue and its conversion to glutamic acid residue by TG2 (**Figure 2.1.1**).

Due to its transamidation activity, TG2 can introduce significant modifications to proteins and the extracellular matrix (ECM), altering their properties and functions, thereby leading to various biological consequences, such as changes in cell behavior and disruption of homeostasis. TG2 crosslinks numerous major matrix proteins within the ECM, including fibronectin, laminin, collagen, fibrinogen, vitronectin, osteonectin (also called SPARC), osteopontin, among others[66]. Transamidation of these ECM proteins by TG2 results in their stabilization, increased stiffness of the ECM, and enhanced resistance to degradation by matrix metalloproteinases. These characteristics resemble those observed in fibrotic ECM, where excessive TG2 has been established to play a pathological pro-fibrotic role in multiple organs[6,67].

However, crosslinking is just one of many functions performed by TG2, leading to its description as a "Molecular Swiss Army Knife"[18]. This versatile protein exhibits an extraordinary range of enzymatic and non-enzymatic functions. For instance, TG2 has been shown to act as a GTPase and a G-protein coupled receptor[68], to possess kinase phosphorylating activity[69], and to exhibit protein disulphide isomerase activity[70].

Given the multifunctionality of TG2, it is not surprising that it has been implicated in various pathophysiological mechanisms over the years, including neurodegenerative diseases (such as Alzheimer's, Parkinson's, and Huntington's disease), autoimmune diseases (such as Celiac disease), highly aggressive cancers (such as glioblastoma, ovarian and breast cancers), and fibrosis, among others.

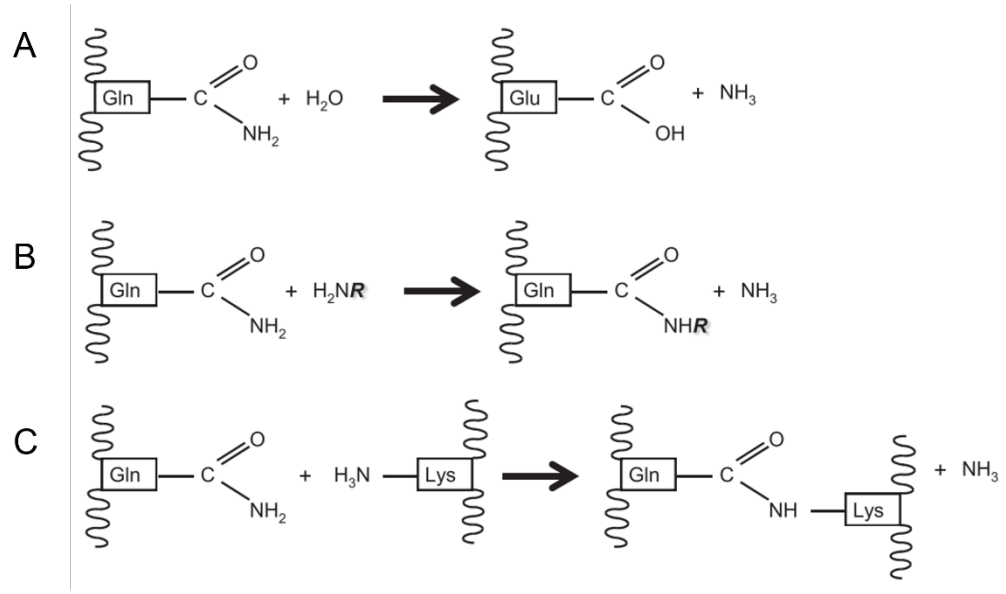

Figure 2.1.1: Schematic view of enzymatic reactions catalyzed by TG2 transamidation activity. (A) TG2 catalyzes deamidation of glutamine and converts it to a glutamate. In this case TG2 uses water molecules as an acyl-acceptor to deamidate glutamine. (B) TG2 can catalyze post-translational modifications of proteins when a primary amine (small biological amine) acts as an acyl-acceptor. (C) TG2 can crosslink two proteins by forming a covalent isopeptide bond between glutamine and lysine. In this case, ε-group of lysine acts as the acyl-acceptor. Adapted from S. Gundemir et al[18].

In the gluten-sensitive enteropathy, specifically celiac disease, TG2 plays a dual role as both the target of autoantibodies as well as the enzyme responsible for deamidating gluten peptides. Gluten peptides, which are derived from wheat, rye, or barley, contain numerous glutamine residues that are targeted by TG2 in the small intestine. TG2 catalyzes the deamidation of these peptides, converting them into negatively charged glutamic acid residues. This TG2-mediated gluten deamidation plays a central role in the pathogenesis of celiac disease, as the deamidated peptides have increased binding affinity to immune cells, leading to an immune reaction and the production of autoantibodies. Furthermore, TG2 itself becomes a target of autoantibodies[71,72]. In the context of neurodegenerative diseases, TG2 has been found to crosslink amyloid-β peptide and tau protein, suggesting its involvement in the aggregation of amyloid-β and tau in affected individuals[73,74]. Additionally, nuclear TG2 crosslinking activity has been implicated in the promotion of huntingtin aggregate formation in the frontal cortex of patients with Huntington's diesease[75]. In fibrosis, apart from its role in

ECM stabilization through crosslinking, TG2 plays a significant role in the activation of the profibrotic cytokine TGF-β, one of the most potent profibrotic stimuli[6].

Over the past decade, TG2 has been implicated in multiple cancers, with upregulation of TG2 being associated with poor clinical outcomes. The involvement of TG2 in cancer is multifaceted and encompasses both its enzymatic and non-enzymatic functions, as well as it depends on the intracellular or extracellular localization of TG2. The transamidase and GTPase functions of TG2 have been linked to the promotion of oncogenic phenotypes[31]. However, in recent years, the importance of non-enzymatic functions of TG2 in activating oncogenic pathways through its interactions with integrins and the ECM protein fibronectin (FN) has emerged. These non-enzymatic protein-protein interactions mediated by TG2 have been shown to stabilize "outside-in" signaling, involving FAK, Akt, β-catenin, Src, and the epidermal growth factor receptor (EGFR). These interactions have been clearly implicated in cancer progression and metastasis[76,77].

Although, the presence of TG2 on the cell surface and within the ECM has been acknowledged for a considerable time period, the prevailing notion was that its primary role in the extracellular space was to enhance ECM stability by facilitating the formation of isopeptide bonds among the ECM proteins. While this function remains crucial, recent discoveries have unveiled a more intricate contribution of the non-enzymatic roles of TG2. Over the span of a few years, a notable paradigm shift has occurred in the field, sparked by the realization that TG2 serves as cell surface adhesion protein, exerting profound influence on the regulation of critical cellular processes such as cell adhesion, migration, survival and proliferation[18,19,78]. This revelation has underscored the complexity of TG2's functionality, surpassing initial assumptions, and shedding light on additional mechanisms, beyond its transamidation activity, through which TG2 is implicated in numerous pathophysiological mechanisms. The elucidation of non-enzymatic protein-protein interactions mediated by TG2 in pathological processes opens new avenues for the design of novel therapeutic drugs.

In this thesis, we will specifically focus on the non-enzymatic interactions of TG2 with FN, both on the cell surface and within the ECM. These interactions will be examined in greater detail in the subsequent sections of this thesis, aiming to enhance our understanding of their implications in relevant biological processes.

2.2 Structural organization of transglutaminase 2 and its conformational states: a case why a two-state model is not sufficient.

TG2 acts on 165 different substrates as currently described in the “TRANSDAB” wiki database (http://genomics.dote.hu/mediawiki/index.php/Main_Page). The covalent modification of these substrate proteins by TG2 significantly influences their functions. Hence, it is not unexpected that multiple regulatory mechanisms tightly govern the activity of TG2. Presently, researchers have elucidated at least three distinct regulatory mechanisms that influence TG2 activity: allosteric regulation through either calcium, or guanosine nucleotides GTP/GDP, or through a redox mechanism. Each of these regulatory mechanisms induces a distinct and considerable conformational change in TG2, with the prevalence of one over the

others being dependent on the redox environment and concentrations of allosteric effectors, which differ from intracellular to extracellular localization of TG2[79].

The multifunctional nature of TG2 can be attributed to the structural arrangement of its four domains and the large conformational variations it undergoes, giving it functional versatility. TG2 consists of an N-terminal β-sandwich (1–140 aa), the catalytic core (141–460 aa) and two C-terminal β-barrel domains (461–586 and 587–687 aa)[38] (**Figure 2.2.1 A-C**). Among these domains, the C-terminal β-barrel domains of TG2 can reposition relative to the other two domains, enabling significant conformational changes[37,80].

Early studies established guanine nucleotides GDP/GTP and Ca^{2+} as the principal reciprocal allosteric regulators of TG2 GTPase and transamidase activities[81]. An excess of Ca^{2+} as typically found extracellularly enhances TG2's transamidation activity, while inhibiting its GTPase activity. Conversely, elevated GDP/GTP concentrations as found intracellularly promote TG2's GTPase activity while impeding its transamidation activity[82]. Prior to the resolution of any high-resolution crystal structure of TG2, investigations into TG2's conformation through circular dichroism and intrinsic tryptophan fluorescence revealed that TG2 bound to GDP/GTP adopted a different conformation compared to its conformation when bound to calcium[83]. This insight shed light on how GDP/GTP and Ca^{2+} could exert opposing effects on TG2 transamidation activity. Subsequently, when high-resolution crystal structures of TG2 bound to GTP and irreversible peptide-mimetic inhibitor Z-DON were eventually resolved, they unveiled two distinct conformational states of TG2. The initial resolved crystal structure depicted GTP-bound TG2 (PDB:1KV3) and revealed a closed conformation, where the C-terminal β-barrels of TG2 were closely wrapped around the catalytic core[38] (**Figure 2.2.1 A**). This structure elucidated the mechanism underlying the inhibition of TG2 transamidase activity by guanine nucleotides. Specifically, in the GTP-bound form, access to the active site Cys277 was obstructed by two loops of the first β-barrel, with active site Cys277 forming a hydrogen bond with the conserved Tyr516 on the first β-barrel[38].

A few years after the resolution of the GTP-bound TG2 structure, a crystal structure of TG2 bound to an irreversible peptide-mimetic inhibitor Z-DON was determined (PDB:2Q3Z)[37]. This structure presented a notably different conformation in which the β-barrels moved away from the catalytic core, causing all four domains to align almost linearly[37] (**Figure 2.2.1 B**). Given that in this "open-state" structure, the β-barrels did not obstruct access to the active site Cys277, it became prevalent in the literature to associate this structure with the Ca^{2+}-bound catalytically active TG2[79]. However, evidence has accumulated suggesting that PDB:2Q3Z might not represent the natural Ca^{2+}-bound TG2 configuration. Firstly, the Z-DON inhibitor-bound TG2 structure did not contain any bound Ca^{2+} ions when it crystallized[37]. Calcium is essential for TG2 catalytic activity, and TG2 can bind up to six Ca^{2+} ions within the catalytic core (**Figure 2.2.1 C**), which induces changes that expose the active site[84]. Secondly, the Z-DON bound TG2 structure was characterized by the formation of intramolecular Cys370-Cys371 disulfide bonds, which are recognized as a redox switch that regulates TG2 catalytic activity in the extracellular environment, ultimately inactivating the enzyme[40]. Indeed, TG2 possesses a redox-sensitive cysteine triad, comprised of Cys230, Cys370, and Cys371, which constitute the regulatory mechanism involved in the oxidative inactivation of TG2. In this mechanism, Cys230 serves as a redox sensor, promoting the formation of the Cys370-Cys371 disulfide bond[40,85]. This disulfide bond formation induces significant local conformational

changes, and given that Cys230 is in close proximity to one of the Ca^{2+} binding sites, the formation of the disulfide bond likely disrupts and prevents further Ca^{2+} binding[37]. For oxidized TG2 to regain catalytic activity, reduction of the disulfide bonds is necessary, a process likely regulated by Thioredoxin under physiological conditions[17,85]. Consequently, the PDB:2Q3Z crystal structure is likely inert and may not necessarily represent the true equivalent of the Ca^{2+}-bound enzymatically competent TG2.

Hydrogen-deuterium exchange (HDX-MS) studies have provided invaluable insights into the equilibrium dynamics of TG2's conformational states in the presence or absence of its effectors[41]. HDX-MS analyses revealed that effector-free TG2 (in the absence of its GTP/GDP and Ca^{2+} effectors) exists in an equilibrium of two states: the "open" and "closed" states. The increase in GTP levels shifts this equilibrium toward the "closed" conformation, while treatment with the Z-DON inhibitor shifts it toward the "open" conformation. Importantly, the effector-free "open" conformation aligns with the deuterium uptake of the Z-DON bound TG2 in the absence of Ca^{2+}, as both conformations are characterized by the presence of disulfide bonds on Cys370-Cys371[41].

Lastly, it is noteworthy that the crystal structure of Ca^{2+}-bound TG2 has not yet been determined. Curiously, the crystal structure of Ca^{2+}-bound TG3 (epidermal transglutaminase) is available and closely resembles the crystal structure of GTP-bound TG3 and GTP-bound TG2, rather than the “open-state” TG2 bound with the Z-DON inhibitor[86]. Both small-angle x-ray scattering studies and switchSENSE biosensor analyses of Ca^{2+}-bound TG2 have demonstrated that TG2 adopts an open conformation in the presence of calcium, which significantly differs from the conformation of Z-DON bound TG2[42,43].

In light of the aforementioned discussions, the two-state model falls short of fully describing the intricate conformational landscape of TG2. Accumulated evidence suggests that this versatile protein can exist in at least three distinct conformational states (**Figure 2.2.1 D**). Upon an increase in GTP/GDP levels, TG2 adopts a "closed" conformation, as observed in the PDB:1KV3 structure. In the absence of effectors and under oxidizing conditions in the extracellular matrix, TG2 assumes an effector-free "open" conformation, characterized by the formation of Cys370-Cys371 disulfide bonds. Under reducing conditions and elevated Ca^{2+} concentrations, TG2 adopts an as-yet-undetermined "open" conformation that differs from the effector-free "open" state. Crucially, only the Ca^{2+}-bound "open" conformation of TG2 displays enzymatic activity.

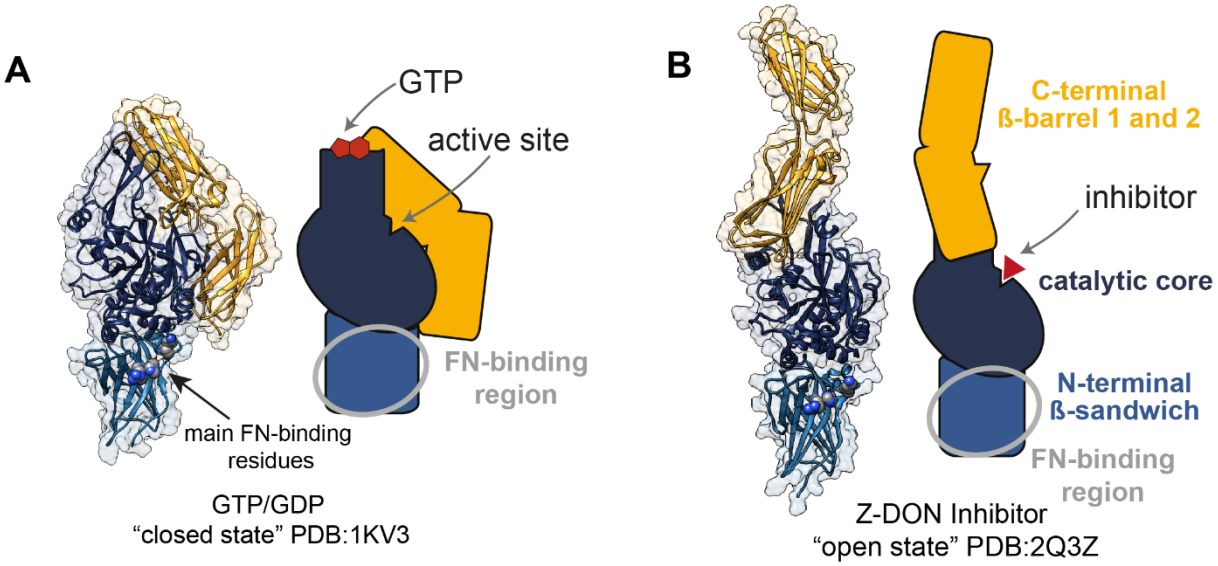
A
GTP
active site
FN-binding region
main FN-binding residues
GTP/GDP
"closed state" PDB:1KV3
B
C-terminal ß-barrel 1 and 2
inhibitor
catalytic core
N-terminal ß-sandwich
FN-binding region
Z-DON Inhibitor
"open state" PDB:2Q3Z

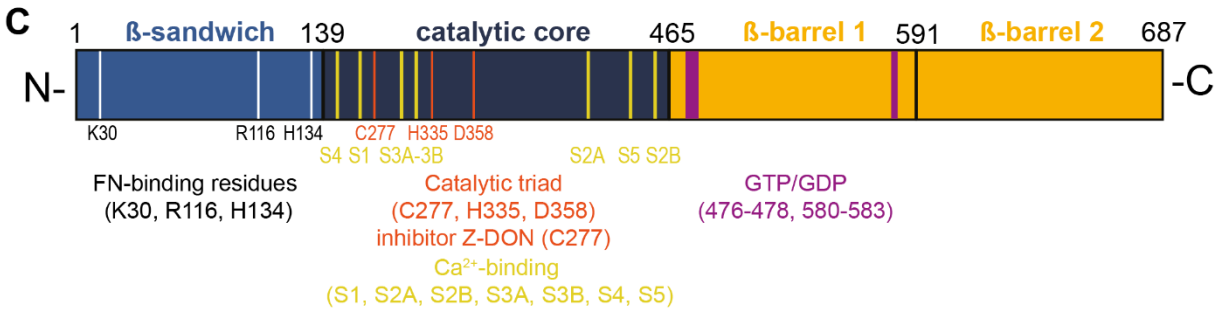
C
1 ß-sandwich 139 catalytic core 465 ß-barrel 1 591 ß-barrel 2 687
N-
-C
K30
R116 H134
C277 H335 D358
S4 S1 S3A-3B
S2A S5 S2B
FN-binding residues (K30, R116, H134)
Catalytic triad (C277, H335, D358)
inhibitor Z-DON (C277)
Ca2+-binding (S1, S2A, S2B, S3A, S3B, S4, S5)
GTP/GDP (476-478, 580-583)

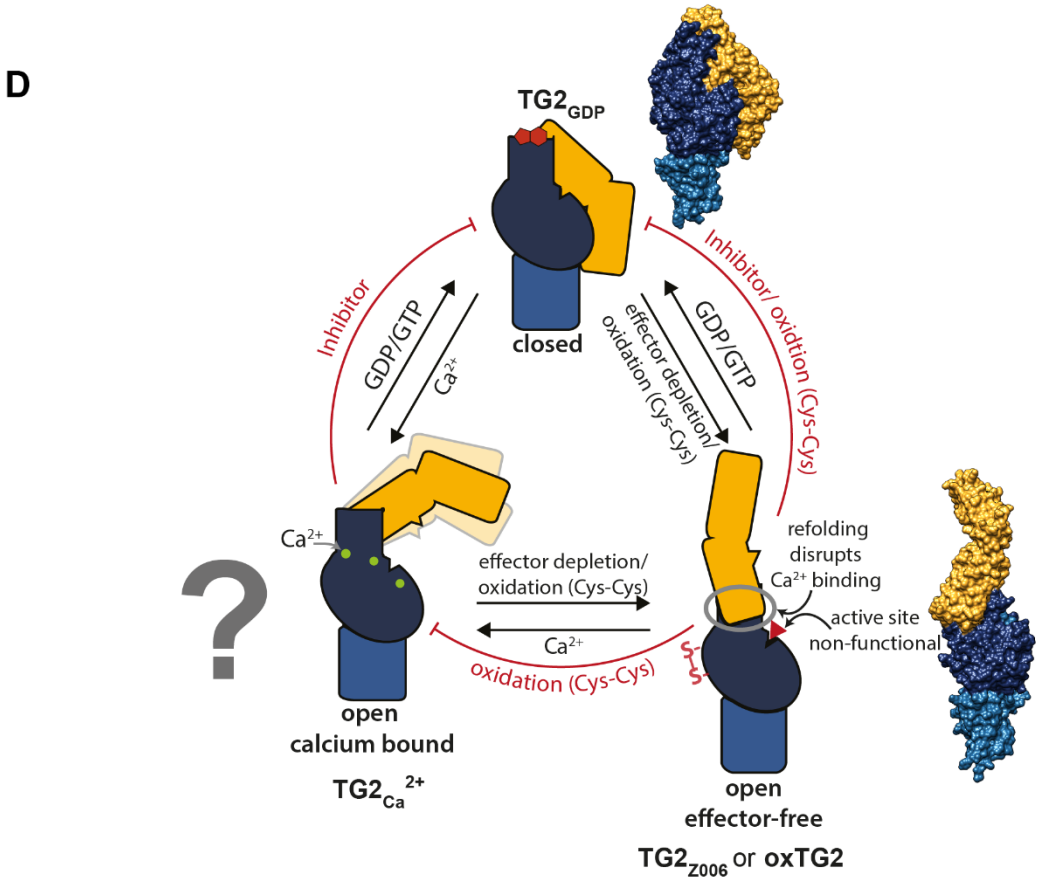
D
TG2GDP
closed
Inhibitor
GDP/GTP
Ca2+
Inhibitor/ oxidtion (Cys-Cys)
effector depletion/ oxidation (Cys-Cys)
GDP/GTP
?
Ca2+
effector depletion/ oxidation (Cys-Cys)
Ca2+
oxidation (Cys-Cys)
refolding disrupts Ca2+ binding
active site non-functional
open calcium bound
TG2Ca2+
open effector-free
TG2Z006 or oxTG2

Figure 2.2.1: Schematic illustration of TG2's domain composition, its conformational states and known binding interactions with fibronectin (FN). (A) Schematic view of TG2's domain architecture based on the crystal structure of the catalytically inactive, GDP bound state (PDB:1KV3)[38]. **(B)** Schematic view of TG2's domain architecture based on the crystal structure of the catalytically inactive, Z-DON inhibitor bound TG2 (PDB:2Q3Z)[37]. The FN binding region on the N-terminal domain determined by Cardoso et al. is highlighted[46]. **(C)** Schematic illustration of the location of the known binding sites for fibronectin[46], calcium[39], GTP/GDP[87] on the linear amino acid sequence of TG2. The location of the catalytic triad is indicated as well. **(D)** TG2 can exist in an equilibrium of at least three distinct conformational states: closed - $TG2_{GDP}$, open calcium bound - $TG2_{Ca^{2+}}$ and open effector-free state. The relative population of each state depends on the concentration of its allosteric effectors – calcium (green circles) - $TG2_{Ca^{2+}}$ and GDP/GTP (red polygons) – $TG2_{GDP}$ and can be further regulated by the formation of intramolecular disulfide bridges (oxidation – oxTG2) or the binding of artificial irreversible inhibitor Z-DON (red triangle) to the active site Cys277 ($TG2_{Z006}$). Typically, GDP/GTP concentrations are high intracellularly and both calcium and oxidative conditions are high extracellularly, however, intracellular environment can be permissive for calcium induced TG2 transamidation as well[39].

2.3 Why TG2 conformation matters: conformation-selective protein-protein interactions of TG2 with its intracellular and extracellular binding partners.

Accumulating evidence suggests that TG2 interacts with certain binding partners both intracellularly and in extracellular spaces in a conformation-selective manner, independent of its crosslinking activity. This indicates that TG2 has a preferred conformational state for such interactions to occur.

Regarding such intracellular binding partners, studies have demonstrated that c-Cbl E3 Ubiquitin ligase selectively binds to TG2 in its closed state[88]. Mutant forms of TG2, specifically R580K or C277V, which are prone to assuming an open conformation[89,90], fail to bind c-Cbl. However, wild-type TG2 and the D306N/N310A TG2 mutant, which tend to assume a closed conformation[88], exhibit strong binding to c-Cbl. Such conformation-selective binding can lead to significant biological consequences. For example, ectopically expressing open conformation R580K TG2 mutants has been shown to be cytotoxic to cells. This cytotoxicity is not dependent on TG2's crosslinking ability but appears to be dependent solely on the open conformation. Inhibiting the activity of the open-state TG2 mutant R580K with irreversible inhibitors or mutating the active site Cys277 does not eliminate the cytotoxic effect[89]. Conversely, the closed-state TG2 has shown effectiveness in promoting cell survival under serum starvation conditions, whereas the open-state TG2 mutants promote cell death under normal conditions and accelerate cell death even further under serum starvation[89]. It has been demonstrated that c-Cbl E3 Ubiquitin ligase plays a role in down-regulating and degrading the EGFR (epidermal growth factor) receptor in cells. Closed-state TG2 contributes to the aggressiveness of glioblastoma brain tumors by tightly binding c-Cbl E3 Ubiquitin ligase and preventing it from targeting EGFR for lysosomal degradation[88].

As for extracellular conformation-selective binding partners of TG2, anti-TG2 antibodies derived from celiac disease patients have been shown to preferentially bind either the closed or open state of TG2, depending on the epitope[91,92]. TG2 has been implicated in the pathogenesis of celiac disease, where it deamidates gluten peptides, triggering the activation of gluten-reactive T cells and the generation of autoantibodies. In addition to gluten, TG2 itself becomes a target for autoantibody generation[93]. Researchers have identified a panel of anti-TG2 antibodies from celiac disease patients, all targeting four conformational epitopes clustered around the N-terminal domain of TG2[94]. Interestingly, these autoantibodies not only exhibit a preference for binding to a specific TG2 conformation but also appear to promote TG2 to assume a particular conformation upon binding. Hydrogen-deuterium exchange analysis conducted by Hnida and colleagues revealed that binding with certain anti-TG2 antibodies shifted the distribution of TG2 conformations towards the closed or open state[92].

Another critical extracellular binding partner for TG2 is heparan sulfate proteoglycan Syndecan-4[95]. TG2 has a strong affinity for heparan sulfate chains of Syndecan-4, which associates with TG2-FN complex and facilitates the RGD-independent cell attachment to the ECM[20]. Although the precise binding site of Syndecan-4 on TG2 remains disputed[95–97], the binding epitope on TG2 is conformational, with Syndecan-4 favoring TG2 in the closed conformation[98]. Syndecan-4 interaction with TG2 was reported to have an effect on TG2 crosslinking activity, as evidenced by Syndecan-4 stabilizing TG2 in an inactive closed conformation[96,98]. The ability of Syndecan-4 to stabilize TG2 in the closed conformation likely arises from the bi-partite epitope on TG2 comprising two clusters of amino acids, one located on the catalytic core and the other on the C-terminal β-barrel 2 of TG2, which converge into a high affinity single epitope when TG2 adopts a closed conformation[97].

Collectively, these observations suggest an intriguing prospect of protein-protein interactions orchestrating TG2 conformations, and in turn, its functions, akin to the role of allosteric effector molecules such as calcium and GDP. Hence, when investigating non-enzymatic protein-protein interactions involving TG2 and its myriad binding partners, understanding the significance of TG2 conformations is imperative.

This is particularly relevant in the light of ongoing pursuit of inhibitors of TG2 catalytic activity for therapeutic purposes[36,99]. Several such inhibitors induce significant conformational shifts in TG2. For instance, peptido-mimetic inhibitors like KCC009[100] and Z-DON[101], mimicking gliadin peptides thatTG2 deamidates in celiac disease, are commonly employed. While these specific inhibitors irreversibly bind to the active site Cys277, obstructing TG2's crosslinking activity, they inadvertently trap TG2 in the extended open conformation. This is evident from the resolved X-ray crystal structure of TG2 bound to Z-DON (PDB:2Q3Z)[37] and native PAGE of TG2 bound to KCC009[94]. Though the stabilization of TG2 in the extended open conformation by these inhibitors was not the original intent, a careful consideration should be given to the stabilization of TG2 in the extended open conformation induced by these inhibitors, as it may impact TG2 interactions with its many binding partners under physiological conditions.

2.4 Adhesive functions and adhesive signaling of the transglutaminase 2 bound to fibronectin.

TG2 is the most widely expressed member of the transglutaminase family, with virtually all cell types in the body expressing varying levels of TG2. It is found both within the cell (cytosol, nucleus, mitochondria) and outside of the cell (cell membrane and extracellular matrix)[15]. Intracellular TG2 is secreted via an unconventional mechanism involving recycling endosomes[102], leading to its deposition both on the cell-surface and ECM, creating two distinct pools of TG2 outside of the cell – cell surface TG2 and ECM TG2[19]. TG2 crosslinks various extracellular substrates, such as fibronectin, fibrin(ogen), collagen, vitronectin, and osteoponin, thereby increasing ECM stability and ECM rigidity[103]. However, recent research highlights additional crucial roles of extracellular TG2 beyond its enzymatic crosslinking activity[18].

The most prominent binding partners with which cell surface TG2 forms non-covalent protein-protein interactions are fibronectin, β-integrins, and Syndecan-4[19] (**Figure 2.4.1**). On the cell surface, TG2 forms tertiary and potentially even quaternary adhesive hetero-complexes with fibronectin, β-integrins, and Syndecan-4, which has pivotal impact on cell-ECM interactions, including cell adhesion, cell spreading, cell migration, FN-matrix assembly, and matrix remodeling[14,22,24,104,105]. TG2 associates with β1, β3 and β5 integrin subunits, with up to 40% of β1-integrins in macrophages reported to associate with TG2[19,104]. Because TG2 displays high affinity to both FN and β-integrins, it has been described as an adhesion co-receptor for FN, since TG2 acts as a scaffolding protein enhancing FN interaction with β-integrins, which in turn enhances the cell-ECM adhesive interactions[21,105]. The likely mechanism how TG2 achieves that, is by increasing integrin clustering on the cell surface, in the presence or absence of fibronectin[105,106], potentially in synergy with syndecan-4. This integrin clustering, orchestrated by TG2, enhances outside-in integrin signaling, involving FAK-Src-p190RhoGAP, increasing levels of RhoA, which subsequently stimulates its downstream target ROCK[106]. Activation of these signaling pathways, increases cell polarization, promotes formation of stress fibers and focal adhesions, all independent of TG2's crosslinking activity (**Figure 2.4.1**). Moreover, direct interaction of cell surface TG2 with FN, was reported to elevate RhoA levels and increase RhoA downstream target ROCK activation[106]. Hence, cell surface TG2's role as a scaffolding protein is crucial for amplifying integrin-mediated outside-in signaling.

TG2 also plays a major part in mediating Arg-Gly-Asp (RGD)-independent cell adhesion via quaternary adhesive complexes involving β-integrins, Syndecan-4 and FN. These complexes are thought to operate as a parallel adhesive platform during extensive tissue damage and matrix remodeling, a scenario that might disrupt normal RGD-dependent adhesion and associated integrin-mediated outside-in signaling, potentially leading to anoikis – detachment-induced apoptosis[14,20]. Thus, the TG2-FN complex supports cell attachment and spreading, even when integrin-mediated adhesion is hindered by synthetic RGD peptides, and has been demonstrated to rescue fibroblasts[14] and in osteoblasts[23] from anoikis. This RGD-independent mechanism relies on TG2-FN complex interaction with heparan sulfate chains of Syndecan-4, as disruption of these chains through heparinase treatment or Syndecan-4 knockout drastically impairs cell adhesion and spreading[14,20]. Furthermore, RGD-independent adhesion involves Syndecan-4 mediated activation of PKCα, followed by binding of activated

PKCα to β1-integrins[20] (**Figure 2.4.1**). Additionally, Syndecan-2 also participates in RGD-independent adhesion by acting as a downstream signaling molecule activating ROCK, although Syndecan-2 does not directly bind to TG2 (**Figure 2.4.1**).

In addition to its presence on the cell surface, TG2 is deposited in the ECM away from the plasma membrane, although the mechanism of this translocation and deposition is not known. In the ECM, TG2 is mostly immobilized on the FN matrix, although other interactors in the ECM have been reported, such as collagen VI, where TG2 can also be deposited and stored to a lesser degree[107,108].

Consequently, beyond its transamidation function, TG2 assumes critical roles as a nonenzymatic adapter, scaffold protein and a regulator of pro-survival signaling, and TG2-FN complex positively influences cell survival by facilitating and enhancing cell attachment to the ECM, thereby protecting cells from anoikis.

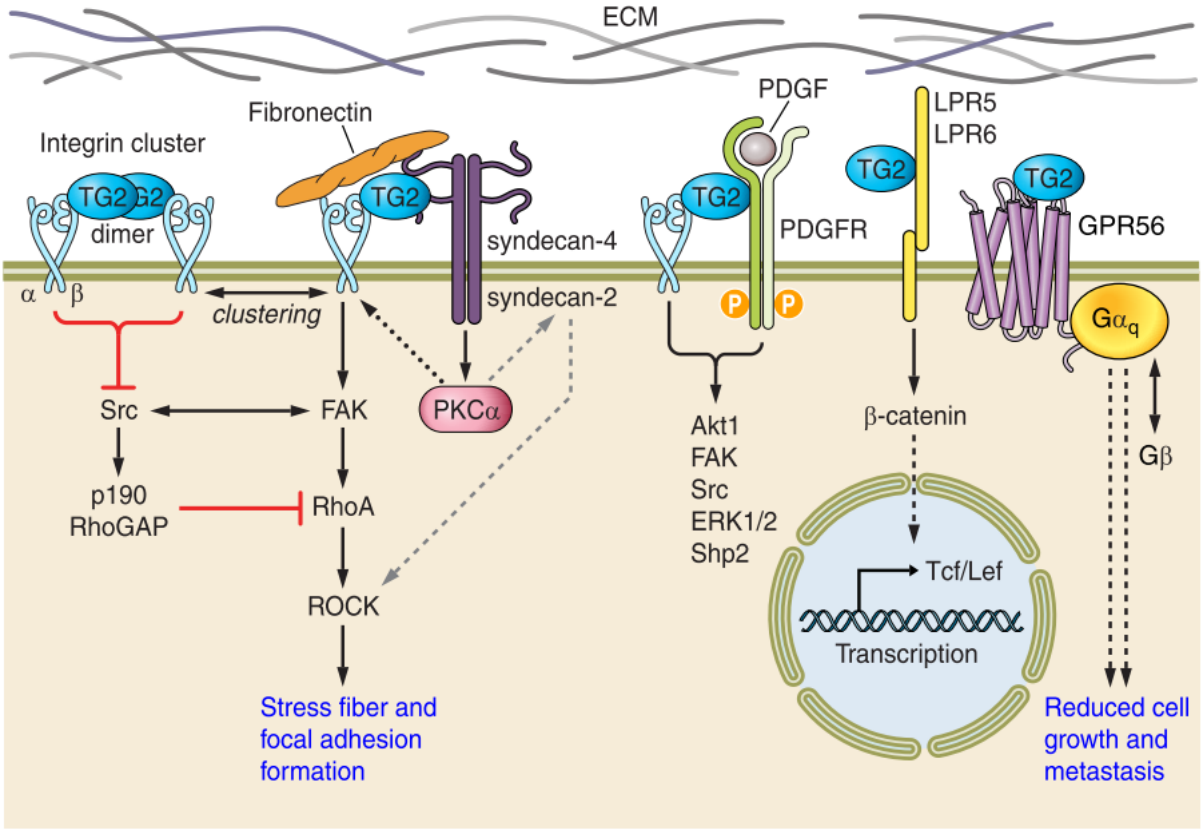

Figure 2.4.1: Schematic depiction of TG2's interactions with other components of adhesive signaling complexes on the cell surface. TG2 interacts with β-integrins, fibronectin and Syndecan-4 on the cell surface, with which it can form ternary and/or quaternary complexes mediating cell adhesion, cell migration, FN fiber deposition. Association of TG2 with β-integrins on the cell surface amplifies the outside-in signaling, resulting in increased levels of focal adhesion and stress fiber formation, as well as increased actomyosin contractility. The integrin-mediated outside-in signaling acts through FAK-Src-p190RhoGAP-RhoA-ROCK signaling pathway. Solid black lines indicate TG2-mediated activation of the outside-in signaling cascade involving the integrin transmembrane receptors. Gray dashed lines indicate the activation of

Syndecan-2 by intracellular PKCα. and the Syndecan-2-mediated activation of ROCK, which in turn induces stress fiber and focal adhesion formation. On this figure, TG2 conformational state is not considered, however, presumably, TG2 adopts a closed conformation on the cell surface and when it is in complex with Syndecan-4[97,98]. Adapted from R.L. Eckert et al[15].

2.5 Adhesion-dependent pathophysiological mechanisms mediated by transglutaminase 2 in complex with fibronectin.

TG2 has been shown to play a role in the progression of various cancer types, including ovarian cancer[109,110], breast cancer[28], glioblastoma[111] as well as pancreatic and prostate cancers[78]. Not only is TG2 involved in cancer progression, but TG2 overexpression has been also associated with poor patient prognosis in ovarian[112], pancreatic[113] and lung cancers[114]. This suggests that TG2 can function as both a tumor promoter and a factor for cancer survival[7,27]. While some of the reasons for TG2's promotion of the oncogenic phenotype can be attributed to its enzymatic crosslinking activity, a substantial portion of its tumor promoting effects result from non-covalent protein-protein interactions that TG2 mediates with its extracellular binding partners[31]. Many of these protein-protein interactions are facilitated by the TG2-FN complex, which interacts with β1-integrins.

Consequently, TG2-FN complex promotes cell survival by facilitating cell anchoring to the matrix. This mechanism operates through the activation of adhesive "outside-in" signaling (FAK-Src-p190RhoGAP-RhoA-ROCK), when TG2, FN and β1-integrins form interactions on the plasma membrane. This process ultimately enables both healthy and transformed cells to avoid anoikis, a form of apoptosis that occurs when cells detach from the extracellular matrix[18,19]. For instance, TG2 assists in the adhesion of ovarian cancer cells to the fibronectin matrix and enhances ovarian cancer cell migration; knocking down TG2 has been shown to inhibit tumor development and spreading within the peritoneal matrix[110]. TG2 achieves this by modulating the expression and distribution of β1-integrins on the cell membrane. Similarly, the TG2-FN complex has been shown to enhance FN-mediated cell attachment, survival and invasion of breast cancer cells, primarily through its close association with β1, β4 and β5 integrins[28]. Downregulating endogenous TG2 expression correspondingly reduced breast cancer cell adhesion to FN-coated surfaces. Finally, TG2 has been shown to exert an anti-apoptotic role, promoting the survival of glioblastoma cells by enhancing their attachment to fibronectin[111].

Expanding beyond cancer, adhesive interactions mediated by TG2-FN complex have also been implicated in the pathological features of multiple sclerosis (MS). TG2 enhances the adhesion and migration of astrocytes on fibronectin in the ECM, contributing to tissue remodeling and glial scarring in multiple sclerosis lesions[115,116]. Specifically, TG2 has been identified as enhancing focal adhesion formation, thereby facilitating the interaction of astrocytes with the ECM and promoting astroglial scar formation[116]. Additionally, TG2 has been reported to promote the deposition of fibril-like fibronectin in multiple sclerosis lesions, creating an environment conductive to astroglial scar formation and impeding tissue repair[117,118].

Considering the implications of TG2's noncovalent interactions with FN in these pathological conditions, targeting the TG2–fibronectin interaction holds promise for the development of novel therapeutic strategies to address these disorders. Consequently, efforts are already underway to develop small molecule inhibitors disrupting the TG2-FN binding interface[33,34,111]. Therefore, a deeper understanding of the mechanisms governing these interactions is necessary, as it could lead to innovative approaches to therapeutics aimed at disrupting cell-ECM adhesion.

2.6 Fibronectin - a key component of the ECM, its conformations and fibrillogenesis.

Fibronectin, an extracellular matrix glycoprotein, plays essential roles in wound healing and embryonic development, while also being implicated in various pathologies, such as cancer and fibrosis. Cells deposit FN into fibrillar matrices within the ECM, where it serves as a critical regulator of cell adhesion, migration, and cell survival[119].

FN exists as a large dimer composed of two subunits, each approximately 250kDa in size, connected by two disulfide bonds at their C-termini. The multifunctionality of FN is apparent in its structure –a multi-modular protein comprising of three types of repeating modules: FNI, FNII and FNIII. This structural arrangement is often likened to a “beads-on-a-string” configuration. In detail, each FN subunit contains twelve FNI modules, two FNII and 15-17 FNIII modules, with potential variations due to alternative splicing. This sums up to a total of approximately 30 modules per FN subunit[52,120] (**Figure 2.6.1 A**).

The primary reservoirs of FN are plasma FN, synthesized by hepatocytes and released into the bloodstream, and cellular FN, which cells secrete locally[52]. FN is characterized by a myriad of cryptic binding sites, including the FN-FN self-association sites - one of the earliest recognized as such. In its soluble state in plasma, FN maintains a compact globular conformation due to long-range electrostatic interactions (**Figure 2.6.1 B**).

The deposition of FN into the ECM as fibrillar structures involves cells applying contractile forces to stretch FN dimers, thereby exposing the cryptic FN-FN self-association sites[53]. Early FRET-based studies demonstrate stronger binding of soluble FN to stretched, as opposed to relaxed, FN fibers[121]. Cytoskeletal contractile forces are essential in unfolding FN dimers for their matrix deposition, as inhibition of cytoskeletal tension disrupts cell-mediated deposition of FN into matrix[122]. Notably, studies highlight the importance of FN-FN assembly sites in $FNI_{1\text{-}5}$ and $FNIII_1$ regions for FN fibrillogenesis, although other regions such as $FNIII_{10}$ and $FNIII_{12\text{-}14}$ have been reported too[123–125]. Though the bundling of FN protofibrils into thicker FN fiber cables is understood, the precise mechanisms holding these bundles together remain less clear[59,126]. This phenomenon is likely influenced by a combination of hydrogen bonds[127], intermolecular beta-strand swapping[128] and weak electrostatic interactions[120]. While FN-fibrillogenesis is not fully elucidated, a direct stochastic optical localization microscopy study suggested an anti-parallel overlap of N-termini by 30-40 nm, indicating that $FNI_{1\text{-}5}$ modules bind FNIII modules of adjacent molecules[54]. Once deposited into the matrix by cells, FN exhibits a wide range of conformations, spanning from relaxed to strained states[51,129,130].

The physiological effects of FN often necessitate its assembly into fibrils within the extracellular matrix. The binding to FN of other molecules is highly contingent on the

properties of FN fibers - the biologically functional form of FN. The biological activity of these fibers may be modulated by the conformation of FN molecules comprising the FN fiber[55,131]. For example, when cells assemble FN into matrix, FN fibrillar networks serve as the provisional matrices guiding the deposition of other matrix proteins during wound healing and matrix remodeling[119]. For instance, FN matrix is vital for collagen I deposition in the ECM; latter acts as the load-bearing structure, reducing FN matrix stretching[61]. Additionally, the FN matrix serves as a critical reservoir for growth factor storage and local bioavailability[63,131].

In addition to the significant roles FN matrix plays in cell adhesion and growth factor storage, fibronectin repetitive modules harbor a plethora of binding sites for other crucial ECM components, a selection of which are illustrated in **Figure 2.6.1 A**.

Considering that FN fibers represent the physiologically relevant and biologically active form of FN, an intriguing question emerges: How does FN fibrillogenesis influence its interaction with transglutaminase 2 (TG2), an enzyme secreted and deposited outside of the cell? This inquiry gains significance as TG2 within the ECM and on the cell surface not only interacts with soluble FN but also interfaces with the fibrillar FN matrix. Additionally, it's worth noting that TG2 is recognized for its deposition on the FN matrix within the ECM.

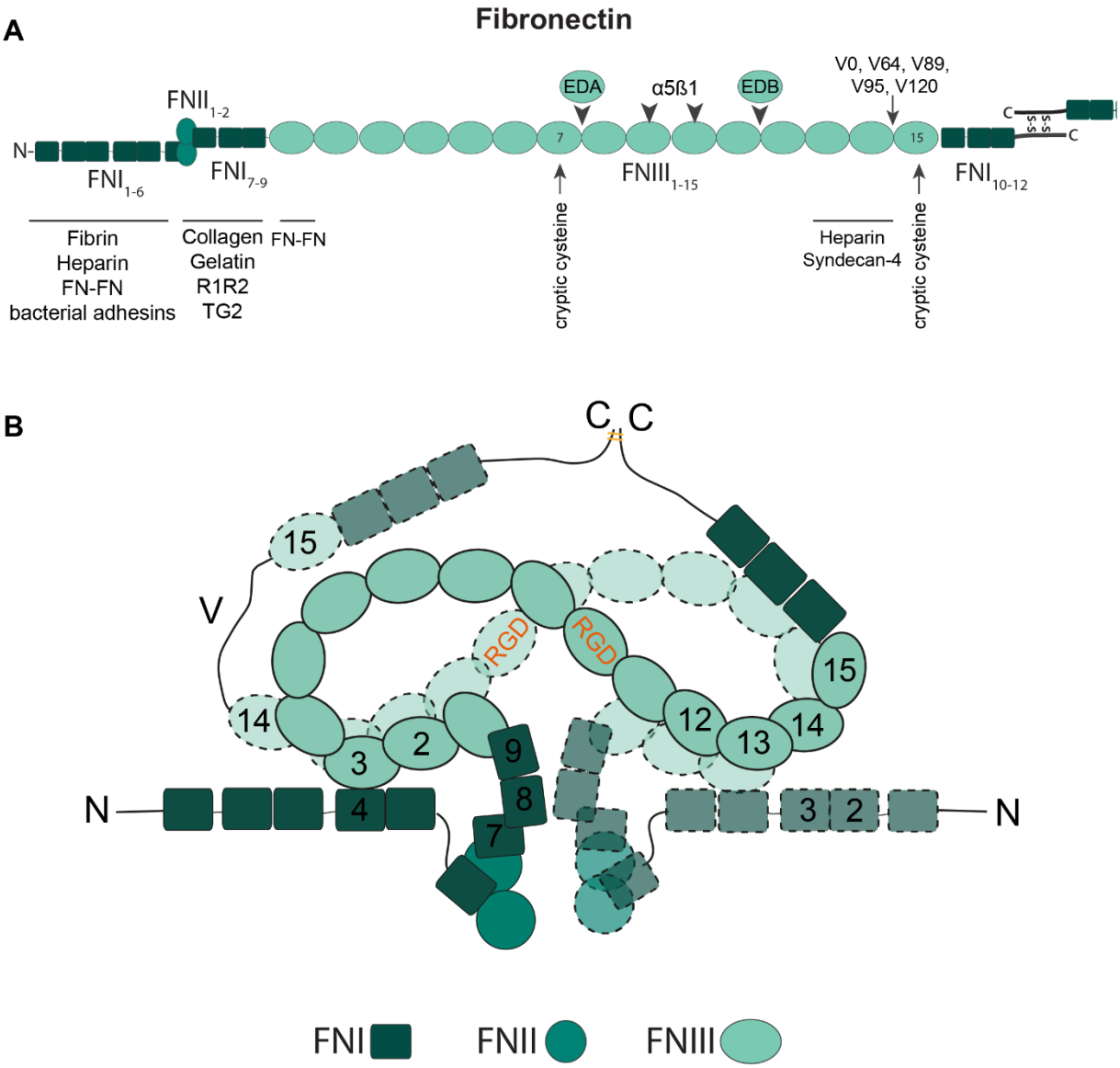

Figure 2.6.1: Schematic overview of FN domain arrangement and major ECM interaction sites(A) FN is a dimer of two subunits connected by a pair of disulfide bonds at C-termini. Only one subunit is indicated for clarity. FN subunit consists of twelve type I (FNI), two type II (FNII) and 15-17 type III (FNIII) modules, depending on alternative splicing. Extra domains EDA and EDB can be included by alternative splicing between $FNIII_7$ and $FNIII_8$ or $FNIII_{11}$ and $FNIII_{12}$ respectively. Additionally, alternative splicing may result in insertion of variable regions V0, V64, V89, V95 or V120 (labeled by the number of amino acids) between $FNIII_{14}$ and $FNIII_{15}$. Major RGD cell adhesion binding site for α5β1 integrins is located on $FNIII_{10}$ and the synergy binding site on $FNIII_9$ are indicated. The locations of some select binding partners of FN in the ECM are indicated too. **(B)** Model of the dimeric FN in globular soluble conformation as illustrated by Maurer *et al*[52]. FN dimer is stabilized in globular soluble conformation by long-range electrostatic interactions between FNI_4 and $FNIII_3$ of the same subunit and between $FNIII_{2\text{-}3}$ and $FNIII_{12\text{-}14}$. One subunit of the FN dimer is shown with solid lines and the second subunit with dashed lines. RGD motif used by many cells for cell-mediated adhesion located on $FNIII_{10}$ is indicated. **(A)**: Adapted from Kubow *et al*[61]. **(B):** Adapted from Maurer *et al*[52]

2.7 Fibronectin as a mechanochemical switch.

Formerly, it was believed that the extracellular matrix played a passive role, merely providing structural support for cell adhesion and migration. However, the emerging field of mechanobiology has illuminated that the ECM delivers both biochemical and biomechanical cues, exerting influence over crucial cell behaviors like adhesion, migration, differentiation, and survival[1,2,4,132].

Importantly, this mechanobiological interplay is reciprocal; cells not only detect and react to the mechanical properties of the extracellular matrix, but they also actively modulate ECM stiffness, ECM composition, ECM organization, and its other mechanical properties. The cellular sensing and regulation of ECM mechanics is facilitated by transmembrane receptors integrins and their associated integrin linker proteins (e.g. talin, vinculin, filamin, paxillin, and others), which connect fibrillar constituents of the ECM to the actin cytoskeleton[133–135]. Consequently, cells can sense ECM stiffness through ECM-integrin-cytoskeleton connections and adjust their behavior accordingly. For instance, ECM stiffness can exert control over cell fate on rigid versus compliant ECM; cells dependent on ECM anchorage undergo apoptosis on compliant matrices[136]. In a reciprocal manner, these same integrin-mediated adhesion links allow cells to deposit ECM, actively reorganize it, regulate its composition, and mechanical properties. Cells achieve this by crosslinking of ECM fibers and exerting force by pulling or pushing on ECM fibers via integrins using actomyosin machinery[1,137].

The emergent field of mechanobiology has introduced and established the concept of mechanochemical switches, which has been both experimentally and computationally validated. Proteins' conformations can be altered by the pulling or stretching forces produced by the actomyosin cytoskeleton. The conformational changes then switch the biochemical function of the protein, changing its binding affinity to other molecules. Essentially, this means that mechanical forces can be translated into biological signals[62]. The two main ways how cell traction forces can switch the structure-function relationship in a protein is by either disrupting the accessible binding motifs spatially stretching them, or by exposing the cryptic binding sites that would typically be buried and inaccessible[62].

A plethora of studies have pinpointed various binding sites and motifs on intracellular and extracellular proteins that function as mechanochemical switches. For example, the R3 rod domain of talin harbors a cryptic binding site for vinculin, that becomes exposed under moderate stretching force that unfolds R3 domain, allowing vinculin to bind[138]. While similar cryptic binding sites, activated by mechanical unfolding, have been identified in several other proteins[139–141], in this thesis we focus on fibrillar fibronectin. Thanks to fibronectin's multi-modular nature and its repetitive domains, it harbors not only numerous surface-exposed molecular recognition sites that can be disrupted when FN fibers are stretched, but also cryptic binding sites that are typically buried within the fully folded globular FN, and can be exposed by actomyosin contractility[142]. Indeed, fibrillar protein fibronectin was the first example for which it was shown, using the Förster Resonance Energy Transfer (FRET) tensional nanoprobes, that cell-generated forces are sufficient to stretch FN molecules, thereby exposing binding sites that facilitate fibronectin self-assembly into fibrils[122]. FN-FN binding sites that are found on the N-terminal FNI modules and on several FNIII modules act as mechanochemical switches for FN binding during FN fibrillogenesis with soluble FN binding

more strongly to stretched than to relaxed FN fibers[121]. Further FRET-based investigations have correlated partial FN unfolding upon fiber stretching with stronger or weaker binding of other FN ligands. These studies have revealed various binding sites on FN fibers that act as mechanochemical switches. For instance, monoclonal L8 antibody epitopes on FNI_9 and $FNIII_1$ are disrupted by FN fiber stretching reducing the antibody's binding affinity to stretched FN fibers[121]; stretching FN fibers exposes a cryptic binding site for cytokine IL-7, enhancing its binding affinity to stretched FN fibers[63]; multi-valent binding sites recognized by *Staphylococcus aureus* bacterial adhesins are destroyed upon FN fiber stretching which leads to a spatial mismatch[60,143].

A pivotal discovery is that the gelatin-binding domain (GBD) of FN functions as a mechano-chemical switch for collagen I binding, which preferentially co-localizes with relaxed FN fibers[61]. This is intriguing since both TG2 and collagen I share the gelatin-binding domain on FN as their binding site on FN[44,49,144]. Consequently, an intriguing question emerges: can TG2 interactions with FN also be governed by mechanical tension in FN fibers? Could GBD serve as a mechanochemical switch for TG2 and if so, what is the functional significance?

2.8 Transglutaminase 2 and fibronectin interaction: what is known.

TG2 can bind non-covalently with high affinity to both the globular soluble conformation of FN and FN deposited by cells in the fibrillar form in the ECM. Early studies employing limited proteolysis with chymotrypsin reported that the gelatin-binding domain (GBD) on FN ($FNI_6FNII_{1\text{-}2}FNI_{7\text{-}9}$) (**Figure 2.8.1 B**) is implicated in high affinity binding of TG2, independent of calcium presence or TG2 crosslinking activity[45,145]. Interestingly, ELISA competition studies have indicated that the GBD binds TG2 with the same affinity as the full-length dimeric FN[49]. Rotary shadowing electron microscopy has confirmed TG2 non-covalent interaction with the GBD and additionally suggested a possible interaction of TG2 with FNI_4 and FNI_5[145]. Soluri *et al* employing ELISA experiments highlighted that $FNI_{7\text{-}9}$ within the GBD binds TG2 to the same extent as the entire GBD, thereby narrowing the TG2-FN interaction region to $FNI_{7\text{-}9}$[44] (**Figure 2.8.1 B**). Moreover, they demonstrated that $FNI_{7\text{-}9}$ has a similar biological effect on cell adhesion, spreading and migration as the entire GBD, with no significant differences in results between cells seeded on surfaces coated with GBD or with $FNI_{7\text{-}9}$[44].

Regarding FN-binding region on TG2, it has been localized to the N-terminal β-sandwich domain. Initial studies have identified residues 2-8[47] and Asp94 and Asp97[48] as well as the β-hairpin loop formed by residues 88-106[48] as the main FN-binding residues. However, subsequent research failed to confirm these regions' interaction with FN[46,107]. The TG2-FN binding interface was later mapped using hydrogen-deuterium exchange and a combination of site-directed mutagenesis and surface plasmon resonance, revealing the crucial role of the residues K30, R116 and H134 in TG2's ability to bind FN[46]. Although these three residues are located distant, they are spatially proximate in the three-dimensional TG2 structure (**Figure 2.2.1 A-C, Figure 2.8.1 A)**. Notably, K30, R116, H134 residues were found to be evolutionary conserved across TG2 in various mammal species, whereas other members of transglutaminases family, which do not bind FN did not contain them[46]. Therefore, the

currently accepted FN-binding site on TG2 comprises K30, R116 and H134 residues, which are located on the N-terminal β-sandwich of TG2; however, the involvement of other TG2 domains in FN binding remains an open question.

Despite considerable progress in understanding TG2-FN interactions, information on how TG2 interacts with fibrillar FN is limited, as prior studies mainly utilized soluble or surface adsorbed FN or FN fragments. Given the abundance of fibrillar FN deposited by cells in the ECM, there is a need to understand the interaction between TG2 and fibrillar, which can be potentially influenced by FN fiber strain. This challenge is partly due to the lack of tools suitable for investigating binding partner interactions with fibrillar FN and correlating FN fiber strain to binding affinity of its ligands. Many assays used in the studies are limited to the use of soluble or surface-adsorbed FN.

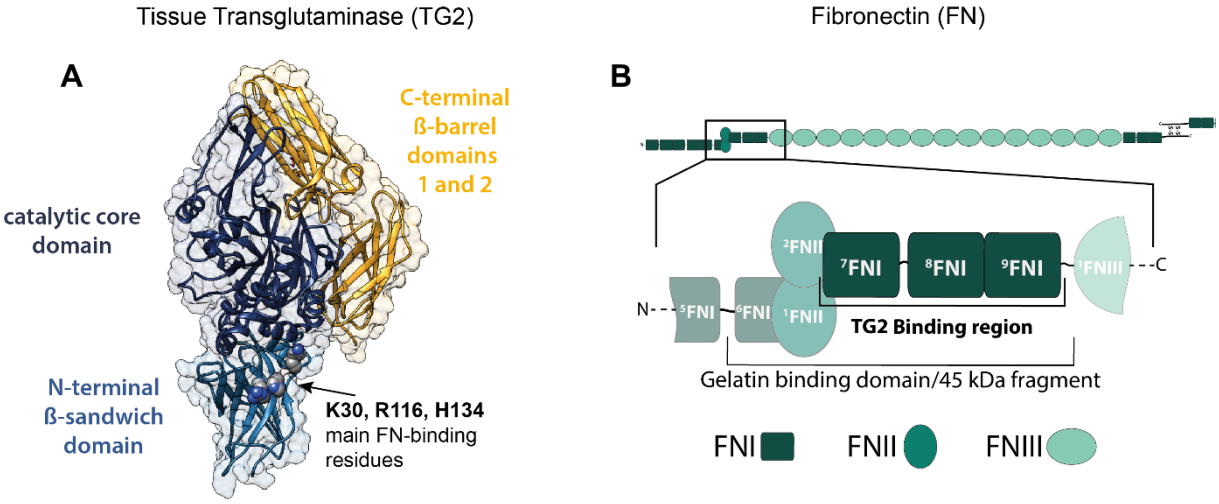

Figure 2.8.1: Schematic illustration of the known interaction sites on TG2 and FN. (A) Main FN-binding residues on the N-terminal β-sandwich of TG2 (K30, R116, H134) identified by Cardoso *et al*[46] are indicated on GDP bound crystal structure of TG2 (PDB:1KV3)[38] **(B)** Illustration of the domain architecture of FN. Only one chain of the disulfide-linked FN homodimer is fully shown (top). The TG2 binding region in the gelatin binding domain determined by Soluri et al. (FN type I modules 7-9) is highlighted in the zoom-in[44]

2.9 Final remarks.

In conclusion, the intricate interplay between TG2 and FN presents a multifaceted network of interactions that extends beyond the traditional view of enzymatic crosslinking. The versatile nature of TG2 is highlighted by its ability to exist in distinct conformational states, each with its regulatory mechanisms and functional outcomes. These conformational changes are tightly linked to the interplay between TG2 and its binding partners, both intracellular and extracellular, enabling TG2 to function as a pivotal regulator of cell-ECM interactions. Through its non-covalent associations with FN, TG2 contributes significantly to cell adhesion, migration, and survival, with implications extending to cancer progression and pathophysiological conditions. The emerging concept of mechanochemical switches introduces a new dimension to the TG2-FN interaction, where mechanical forces can modulate the binding affinity and

functional outcomes. While significant progress has been made in identifying key binding regions on both TG2 and FN, the complexity of interactions in the context of fibrillar FN necessitates further exploration. As we delve deeper into the mechanochemical aspects of TG2-FN interactions and their implications, new avenues for therapeutic interventions may arise, offering novel strategies to address conditions ranging from cancer progression to tissue remodeling. Thus, the dynamic interplay between TG2 and FN stands as a captivating topic for future research, with potential to uncover the intricate mechanisms underlying cell-ECM interactions and their role in health and disease.

3 Technical background and methodology

3.1 Fibronectin-fiber (FN fiber) stretch assay.

Under physiological conditions, actin-cytoskeletal forces exert tension on FN and unfold FN dimers by binding with integrins. However, there are certain drawbacks associated with using cell-assembled FN matrices to study structure-function relationships. The main disadvantage is that these matrices are heterogenous, consisting of highly interwoven fibers with varying thicknesses and conformations. This complexity makes it challenging to understand the structure-function relationship in relation to the mechanical strain. To address this issue, an *in vitro* FN fiber stretch assay was developed, in which FN fibers of uniform diameter can be manually deposited in an ordered pattern, and their conformation can be precisely adjusted and controlled by applying external mechanical forces [59,130].

The process involves manually extruding FN fibers from the air-water interface by gently pulling from a droplet of concentrated soluble FN using a needle. These FN fibers are then deposited onto a stretchable PDMS (Polydimethylsiloxane) membrane, which is mounted on a uniaxial stretch device. The membrane's strain can be customized, allowing for relaxation, stretching, or maintaining a native state (**Figure 3.1.1**).

There are several advantages to using the FN fiber stretch assay. First, manually pulling FN fibers results in consistent fiber thickness, which can be adjusted by varying the concentration of the FN solution. FN fibers can range from 2 to 5 µm in thickness when using FN solution concentrations between 0.2 and 2.6 mg/ml, with an average diameter of approximately 3.7 ± 1.0 µm, mirroring the thickest fibers found in the extracellular matrix deposited by fibroblasts[59]. Second, the length of the FN fibers can be tailored by adjusting the pulling motion, allowing for deposition at desired lengths and patterns on the membrane. For this study, FN fibers approximately 1 cm in length were typically deposited, either parallel to the stretch axis or in intersecting patterns. Finally, the FN fiber strain can be manually controlled and adjusted[130]. Specifically, FN fibers deposited on a relaxed membrane (-50% strain) experience strains of 20% and 219% along the stretch axis and perpendicular to it, respectively. On a stretched membrane (100% strain), FN fibers experience strains of 380% and 90% along the stretch axis and perpendicular to it, respectively. Additionally, FN fibers deposited on a native membrane experience a 140% strain due to forces in the µN range applied to the fibers[130] (**Figure 3.1.1**).

In the upcoming sections of this chapter, we will discuss the FN-FRET probe, which can be utilized to correlate the binding of various FN ligands in the ECM to FN fiber strain within the in vitro FN fiber stretch assay.

Employing the FN fiber stretch assay, we have demonstrated that collagen I predominantly co-localizes with relaxed FN fibers [61]. Bacterial adhesins exhibit preference for binding to relaxed FN fibers compared to stretched ones because stretching disrupts the multivalent binding epitopes on FN[60,143]. Conversely, the cytokine IL-7 displays a preference for binding to stretched rather than relaxed fibers[63].

In summary, the use of FRET in conjunction with manually deposited and externally stretched FN fibers provides physiologically relevant models. The FN fiber stretch assay fills a critical gap by offering a tool to investigate the physiologically relevant and active form of FN within a controlled environment.

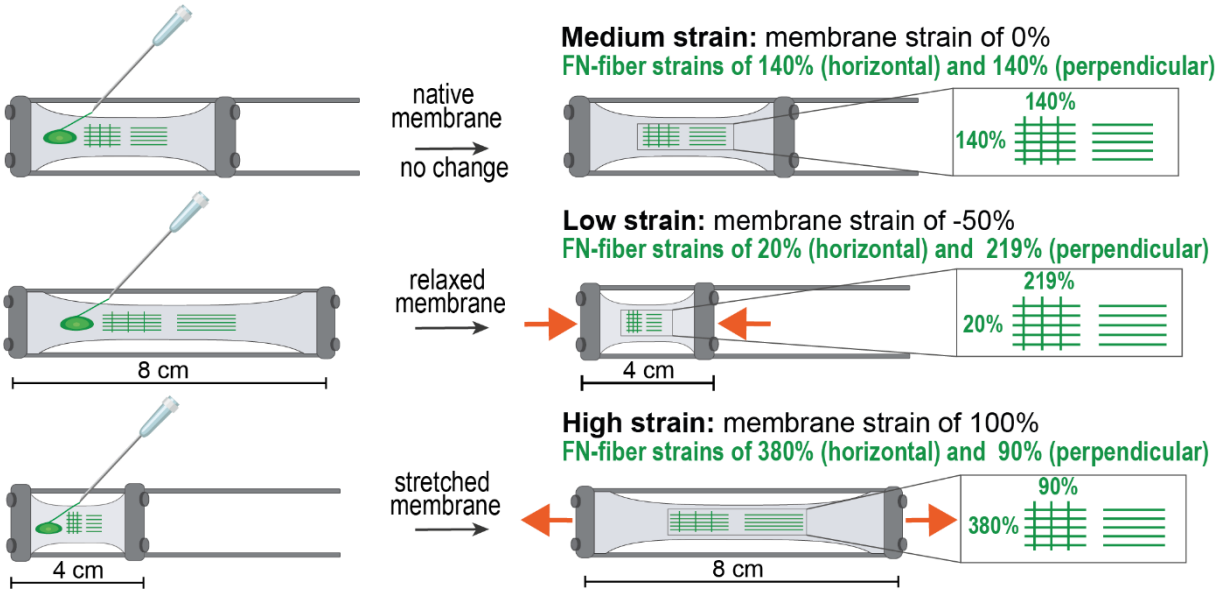

Figure 3.1.1: Schematic illustration of the FN fiber stretch assay. A schematic view of the FN fiber stretch assay and the experimental setup. FN fibers were manually pulled with a needle from a droplet of concentrated FN and deposited onto a silicone membrane mounted on the custom-made stretch device. FN fibers were pulled in two ways, either parallel to the stretch axis, or both parallel and perpendicular as intersections. Membrane was left unchanged (native), relaxed from the pre-strained position, or stretched. Previous calibration studies converted the silicone membrane strain to the corresponding FN fiber strain[130] and are indicated on the cartoon. In this study, FN fiber strains along the stretch axis of relaxed, native, and stretched membranes are referred to as low strain (20%), medium strain (140%) and high strain (380%) respectively. TG2 labeled with an Alexa Fluorophore 647 (TG2-647) was added to the deposited FN fibers and incubated in the presence of various effectors that change its conformational state.

3.2 Förster (Fluorescence) resonance energy transfer (FRET): general concepts.

Förster (Fluorescence) resonance energy transfer (FRET) is a technique used to determine molecular distances and detect molecular complexes. FRET can accurately measure molecular proximity at angstrom distances (10-100 Å) and is highly efficient if the donor and acceptor are positioned within the Förster radius, which is typically 3-6 nm. The efficiency of FRET is dependent on the inverse sixth power of intermolecular separation, making it a sensitive technique for investigating biological phenomena that produce changes in molecular proximity[146].

FRET has a historical background dating back to the early 20th century. It was first observed in 1922 by Cario and Franck when they illuminated a mixture of mercury and thallium vapors, revealing fluorescence spectra attributable solely to thallium, despite using only the wavelengths absorbed only by mercury[147]. This intriguing phenomenon laid the foundation for further exploration. The breakthrough came when Theodor Förster extended these findings, developing a more advanced theoretical framework for FRET. Förster's work highlighted two

crucial factors governing FRET: spectral overlap and intermolecular distance. He formulated the now-famous R^{-6} distance-dependence law for the rate of resonance energy transfer, which was later experimentally validated in 1965[148]. This foundational work opened the door to practical applications of FRET.

The rate of energy transfer, or efficiency, in FRET can be quantified by Förster's equation:

$$K_T = \left(1\frac{1}{\tau D}\right) \times \left(\frac{R_0}{r}\right)^6$$

where **τD** is the donor lifetime in the absence of the acceptor, **R_o** is the Förster critical distance, and **r** is the distance between donor and acceptor chromophores. When r equals R_o, it is referred to as the "Förster radius" the transfer efficiency reaches 50%, with half of the donor's excitation energy being transferred to the acceptor through resonance energy transfer at this separation radius.

FRET itself is a phenomenon wherein excess energy from an excited molecule, known as the donor, is transferred non-radiatively to an acceptor molecule in proximity. Unlike radiative energy transfer, FRET operates through long-range dipole-dipole interactions without the emission and reabsorption of photons. In such a mechanism, an excited fluorophore is treated as an oscillating dipole, capable of exchanging energy with a second dipole that oscillates with the same frequency. Thus, the concept is analogous to the behavior of coupled oscillators, such as a pair of tuning forks[149].

For FRET to occur, several conditions must be met. First, the emission and absorption spectra of the donor and acceptor molecules must overlap. Second, the donor and acceptor should be within a distance range of 1 to 10 nanometers, as FRET efficiency decreases steeply with greater separation (**Figure 3.2.1 A, B**). Additionally, the donor's fluorescence lifetime must be long enough to allow the transfer to happen[147,149]. The dipole-dipole orientation is an important factor that affects the efficiency of FRET. The strength of the interaction between the donor and acceptor dyes depends on the alignment and separation of the dipoles[149]. The orientation factor K^2 is a measure of the relative orientation of the transition dipole moments of the donor and acceptor dyes, and it can vary depending on the orientation of the dyes with respect to each other[150]. K^2 can be defined by the following equation and is illustrated in (**Figure 3.2.1 C**):

$$\mathrm{K}^2 = (\cos\Theta_T - 3\cos\Theta_D\, 3\cos\Theta_A)^2 = (\sin\Theta_D\ \sin\Theta_A\ \cos\varphi - \ 2\cos\Theta_D\cos\Theta_A)^2$$

where, **Θ_T** is he angle between the emission transition dipole of the donor and absorption transition dipole of the acceptor, **Θ_D** and **Θ_A** are angles between these dipoles and the vector that joins the donor and the acceptor transition dipole plane, **ϕ** is the angle between the acceptor and donor transition dipole planes (**Figure 3.2.1 C**). When dipoles are completely aligned, the orientation factor is said to be $K^2 = 1$, and the FRET efficiency is high. On the other hand, when there is no alignment across the x and y planes, no FRET takes place[150].

FRET finds numerous applications in biology and chemistry. It is used as a molecular ruler to probe distances up to 10 nm, allowing scientists to determine distances between biomolecules in aqueous environment with high precision when appropriately labeled with donor and acceptor fluorochromes. This technique has been instrumental in studying molecular interactions, such as those between proteins or DNA strands. Researchers can gain insights into conformational changes in macromolecules, including secondary structures. For instance, FLIM-FRET sensor was shown to be efficient in detecting changes in TG2 conformations between the “closed-state” and the “open-state” in live cells, where researches generated the triple fusion of TG2 with eYFP and mCer[80].

Moreover, FRET-assisted structural modeling benefits from the distance constraints provided by FRET efficiency. FRET efficiency can be converted into distances for comparison with structures or to use them as distance constraints in integrative FRET-assisted structural modeling. In essence, FRET serves as a versatile tool for investigating biological phenomena that influence molecular proximity[151–153].

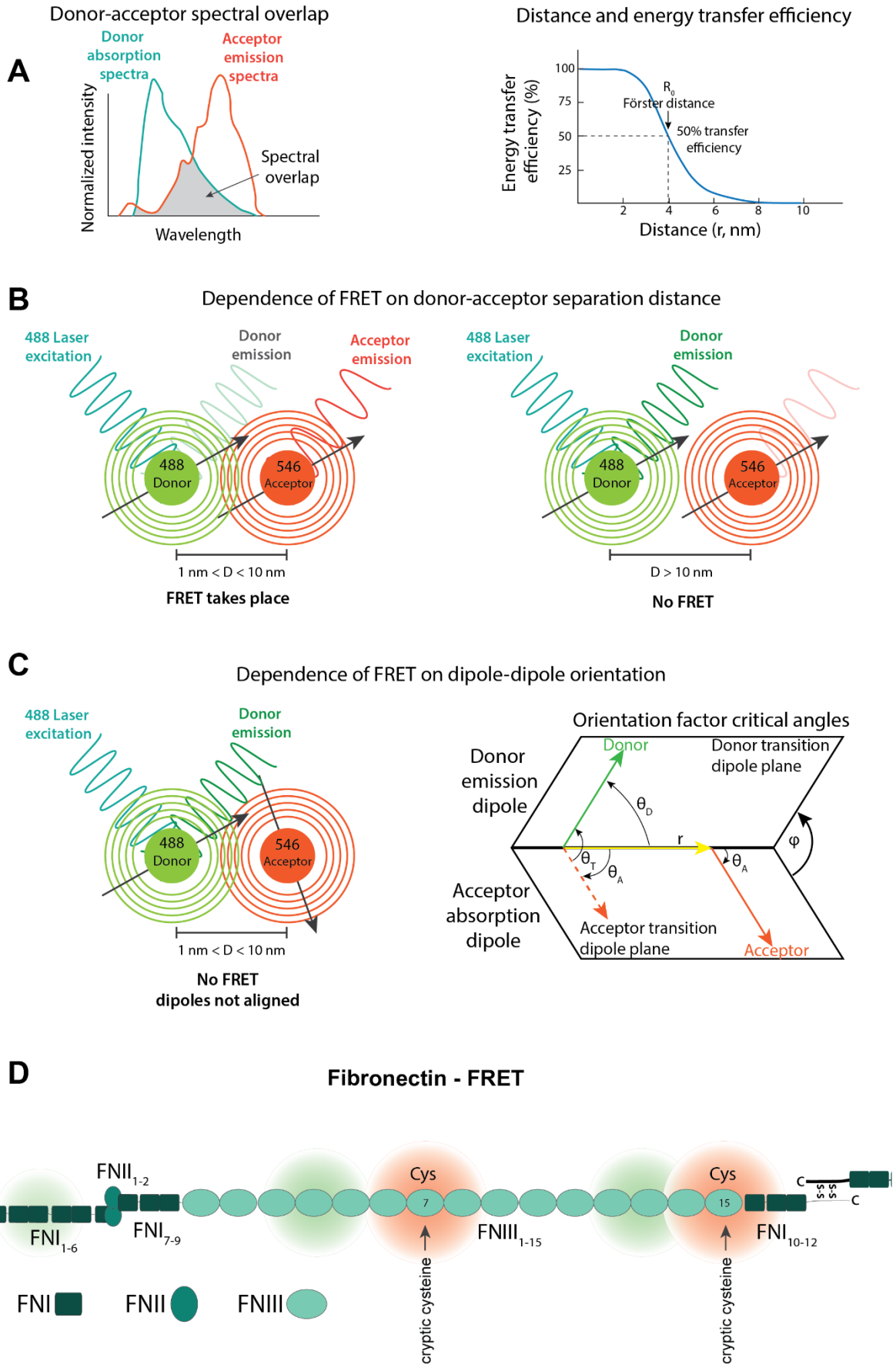

Figure 3.2.1: Schematic illustration of the main concepts underlying Förster Resonance Energy Transfer. Conditions that determine whether FRET will occur are **(A)** spectral overlap of the

donor excitation and the acceptor absorption spectra and **(B)** separation distance between donor and acceptor. The donor and acceptor should be within a distance range of 1 to 10 nanometers. **(C)** Schematic diagram showing the angles of the directions of transition dipole. **(D)** Fibronectin dimers are labeled for FRET with acceptors on the cryptic cysteines located on FNIII7 and FNIII15 and is randomly labelled with donors on primary amines. Acceptors are illustrated in orange and donors in green. Only one fibronectin subunit is shown.

3.3 FN-FRET – a nanoscale tensional probe to assess FN conformations and FN fiber strain.

We employ FRET as a tool to investigate the conformational states both of the soluble FN and the mechanical strain within FN fibers[59]. To achieve this, FN dimers are labelled at all four cryptic cysteines within $FNIII_7$ and $FNIII_{15}$. We use acceptors, specifically Alexa Fluor 546 (AF546), and randomly attach donors, Alexa Fluor 488 (AF488), to primary amines. Consequently, FRET labeling of FN is accomplished through two different chemical reactions: firstly, by conjugating the maleimide reactive group of acceptors (AF546) to thiol groups of cysteines, and secondly, by conjugating the succinimidyl ester (NHS ester) reactive group of donors (AF488) to primary amines on FN. When FN dimers are in unreduced state, contain in total four free cryptic cysteines available for the conjugation with maleimide, which are located within $FNIII_7$ and $FNIII_{15}$ modules on each monomer of the dimer (**Figure 3.2.1 D**). To make the cryptic cysteines accessible for the NHS ester reactive moiety, FN dimers are denatured in solution with guanidine hydrochloride and urea, then labelled with NHS ester AF546, after which the denaturant is removed by buffer exchange. Circular dichroism experiment have demonstrated that FN dimers can refold after denaturation and labelling with fluorophores does not interfere with refolding of FN[51].

Given our interest in detecting large conformational changes in FN dimers, and considering the large size of FN dimers, we employ multiple donor fluorophores on each FN monomer. This ensures that a randomly attached donor is within approximately 10 nm proximity of either $FNIII_7$ or $FNIII_{15}$ and the cumulative FN-FRET ratio is sensitive to the large conformational variations within the molecule. This is approach differs from the conventional use of FRET as a “spectroscopic ruler”, where a single molecule is labeled with a donor-acceptor pair, allowing for the calculation of the donor-acceptor separation distance[51,146].

The stretching of FN fiber increases the physical distance between fluorophores, resulting in a decrease in FRET. Conversely, relaxed FN-FRET fibers display higher FRET, while stretched exhibit lower FRET[51,59]. Notably, the extension of FN fibers is likely achieved by the disruption of the tertiary and then secondary structure in the FNIII modules, which, unlike FNI and FNII modules, are not stabilized by the disulfide bonds[51,154].

Using the FN-FRET nanoscale strain sensor probe, it was shown for the first time that FN fibers adopt a wide range of conformations in cell culture[129], and that actin cytoskeletal forces play a crucial role in assembling FN fibrillar networks[122].

3.4 Final remarks.

In conclusion, this chapter has explored the innovative use of Förster (Fluorescence) Resonance Energy Transfer (FRET) in conjunction with the FN fiber stretch assay to investigate the dynamic conformational states of fibronectin and the mechanical strain experienced by FN fibers. The FN-FRET nanoscale tensional probe has proven invaluable in shedding light on the diverse conformations adopted by FN fibers within cell culture and elucidating the pivotal role of actin cytoskeletal forces in FN fibrillar network assembly.

By utilizing this approach, we aim to bridge the gap in our comprehension of FN's behavior within controlled extracellular environments, thereby advancing our understanding of cell-matrix interactions and structure-function relationships tuned by the mechanical tension experienced by the fiber. These efforts hold promise for unraveling the intricacies of FN's role in mechanobiology and facilitating further discoveries in this field.

4 TG2-FN interactions are tuned by the mechanical strain of FN fibers

The work presented has been published in Matrix Biology.

Kateryna Selcuk, Alexander Leitner, Lukas Braun, Fanny Le Blanc, Paulina Pacak, Simon Pot, Viola Vogel, **Transglutaminase 2 has higher affinity for relaxed than for stretched fibronectin fibers**, Matrix Biology, Volume 125, 2024, Pages 113-132, ISSN 0945-053X, https://doi.org/10.1016/j.matbio.2023.12.006

Author contributions: KS, LB, VV conceived the study and designed the research. All FN fiber stretch experiments were performed by KS. Analysis of all confocal images and data visualization were performed by KS. LB wrote the maximum intensity projection script for Python. KS, LB, and VV wrote the manuscript.

4.1 Motivation.

The motivation driving this chapter is rooted in the intricate interplay between extracellular matrix proteins and cellular mechanotransduction. To closely mimic the high content of fibrillar FN in the extracellular environment, we employed a well-established in vitro FN fiber stretch assay along with a Förster resonance energy transfer (FRET) nanoscale FN tensional sensor. These tools have previously uncovered crucial mechano-regulated binding partners of FN, shedding light on its mechanical responsiveness. Furthermore, we are now challenged to understand the unexpected impact of TG2 conformational states on the mechano-regulated interaction with FN fibers. While previous studies suggested that TG2's binding to FN remains unaffected by TG2 effectors, which regulate TG2 conformations, our findings reveal a novel conformation-dependent mechanism that significantly alters TG2's affinity for FN fibers.

4.2 Mechanical stretching of FN fibers reduces their affinity for TG2 bound to GDP.

To mimic the high content of fibrillar FN in the extracellular environment more closely, we employed a well-established *in vitro* FN fiber stretch assay in combination with a Förster resonance energy transfer (FRET) nanoscale FN tensional sensor, which has already allowed us to identify a number of mechano-regulated binding partners of fibrillar FN[60,61,63,143]. In this assay, fibers are manually pulled with a needle tip from a droplet of FN in solution and deposited onto an elastic silicone membrane mounted on a custom-made stretch-device[59]. FN fibers were pulled and deposited either only parallel to the stretch axis, or both parallel and perpendicular to the stretch axis (**Figure 4.2.2 A**). By adjusting the strain of the silicone membrane, FN fibers can be either stretched or relaxed. In this study, FN fiber tension along the stretch axis of relaxed, native (silicone membrane strain unchanged), and stretched membranes are referred to as low strain (~20%), medium strain (~140%) and high strain (~380%) respectively, as calibrated previously[130]. Though the native membrane is not subjected to any strain, FN fibers are typically pre-strained to ~140% due to the forces required to pull them out of the droplet[130]. To provide a direct readout of the conformational distribution within FN fibers, FN dimers were labeled with multiple FRET donors (AF488) and

acceptors (AF546), and to avoid inter-molecular FRET, fibers always contained only 10% of FRET-labeled FN[51]. Due to mechanical stretching, the average distance between the donors and acceptors increases, therefore higher FN fiber tension corresponds to lower FRET-ratios, while higher FRET-ratios corresponds to more relaxed FN fibers[51,129]. We controlled the responsiveness of our FN-FRET tensional sensors after labeling by chemical denaturation with progressively increasing concentrations of guanidine hydrochloride (Gdn HCl) using well established protocols[51,63,129], and observed that as expected, FN-FRET ratio was decreasing as the denaturant caused FN to transition from compact to extended and then partially unfolded conformations in solution (**Figure 4.2.1**). Next, deposited FN fibers were incubated with Alexa-647 labeled TG2 (TG2-647), and the binding was assessed by measuring the TG2-647 fluorescence intensity, normalizing it pixel-by-pixel to the directly excited FN-FRET acceptor (TG2-647/FN-546), as described previously[63]. We color-coded pixel-by-pixel FN-FRET ratios within FN fibrils at each externally adjusted strain, to illustrate that FN displays a range of conformations, as also observed in the ECM fibrils assembled by fibroblasts[59] (**Figure 4.2.2 B**). As expected, the shift toward higher FN-FRET ratios was observed on the relaxed membrane and toward lower FN-FRET ratios on the stretched membrane. Histograms of the distribution of all FN-FRET pixels from a representative fiber, showed that higher FN-FRET ratios corresponded to low strain, and the highest TG2-647/FN-546 ratios were observed on the fiber experiencing low strain (**Figure 4.2.2 B**). To view in one image how TG2 binding affinity changes with FN fiber strain, we added human recombinant TG2 (hrTG2) to FN fibers deposited as intersections and incubated in the presence of 1 mM GDP and 1 mM EDTA. We plotted all FN-FRET pixels vs TG2-647/FN-546 pixels from the same intersection as binned scatterplots (**Figure 4.2.2 C**). When the strain of fibers parallel and perpendicular to the stretch axes was different (stretched membrane and relaxed membrane), FN-FRET vs TG2-647/FN-546 pixels segregated into two separate groups with higher TG2-647/FN-546 ratios correlating with higher FN-FRET ratios. However, when the strain along both axes was the same (native membrane), pixels remained clustered as a single group (**Figure 4.2.2 C**). This demonstrates that TG2 binding affinity to FN is dependent on FN fiber strain. We repeated this experiment using guinea pig liver TG2 (gpTG2), confirming the consistency of this result as well as its reproducibility across species (**Figure 4.2.3**).

We analyzed 15 horizontal fibers deposited parallel to the stretch axis on either native, relaxed or stretched membranes (**Figure 4.3.2 A**). When we incubated FN fibers with GDP-bound TG2 ($TG2_{GDP}$), it preferentially bound to FN fibers under low strain (~20%). $TG2_{GDP}$ binding to FN fibers under medium (~140%) or high strain (~380%) decreased significantly, compared to the low strain. In the past we have demonstrated that stretching of FN fibers may increase non-specific binding of proteins due to higher exposure of hydrophobic residues which is the consequence of stretch-induced partial protein unfolding[121]. However, we find that the binding affinity of $TG2_{GDP}$ was significantly reduced by mechanical stretching of FN fibers, which suggests that specific TG2 binding sites on FN had been being destroyed. These findings demonstrate for the first time, to the best of our knowledge, that TG2 binding to FN is regulated by the FN fiber tension and that it can be weakened when FN fibers are mechanically stretched.

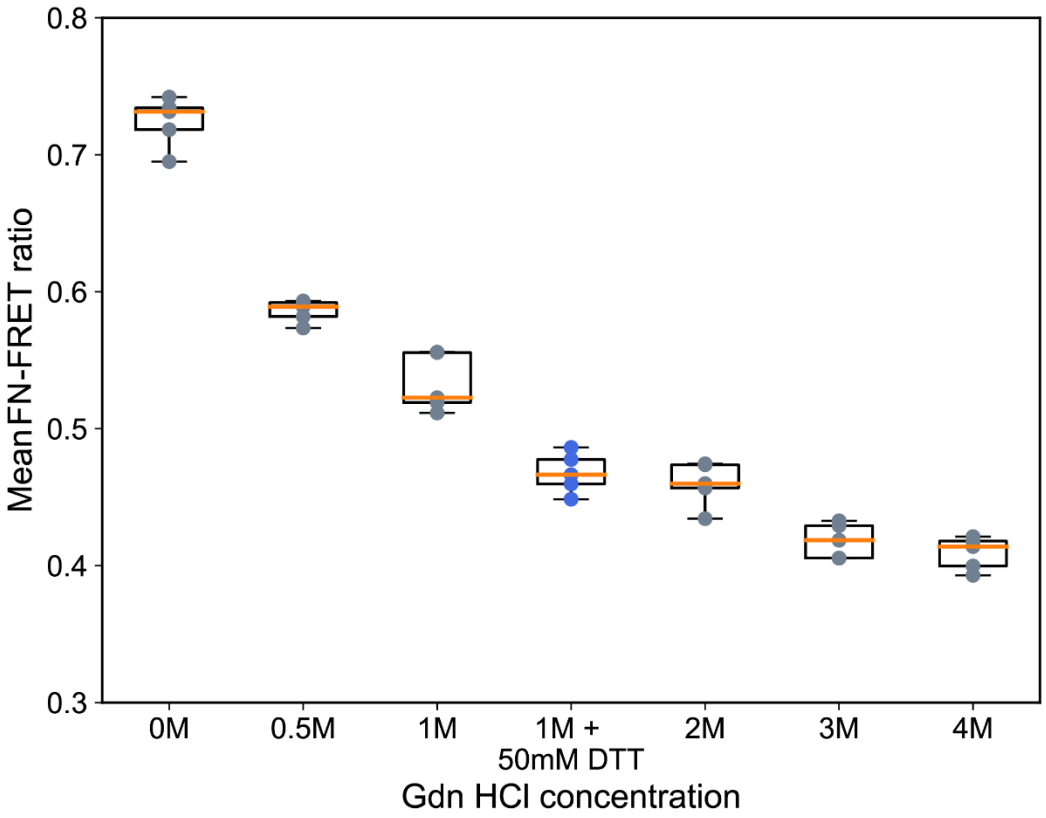

Figure 4.2.1: FN-FRET denaturation with guanidine hydrochloride in solution. Increasing concentrations of guanidine hydrochloride (GdnHCl) lead to loss of FN tertiary and then secondary structure in solution upon chemical denaturation, which is in turn reflected in progressively lower FN-FRET ratio (IA/ID), confirming the responsiveness of our FN-FRET probe to a range of FN conformations, as was described before [51,129]. Treatment of FN-FRET with 50 mM dithiothreitol (DTT) for 1 h before mixing with 1mM GdnHCl (blue circles) reduced structurally important intra-module and inter-subunit disulfide bonds of FN separating FN-homodimer into monomers, which caused further reduction in FRET ratio, as opposed to the treatment with only 1M GdnHCl, as was previously described[155].

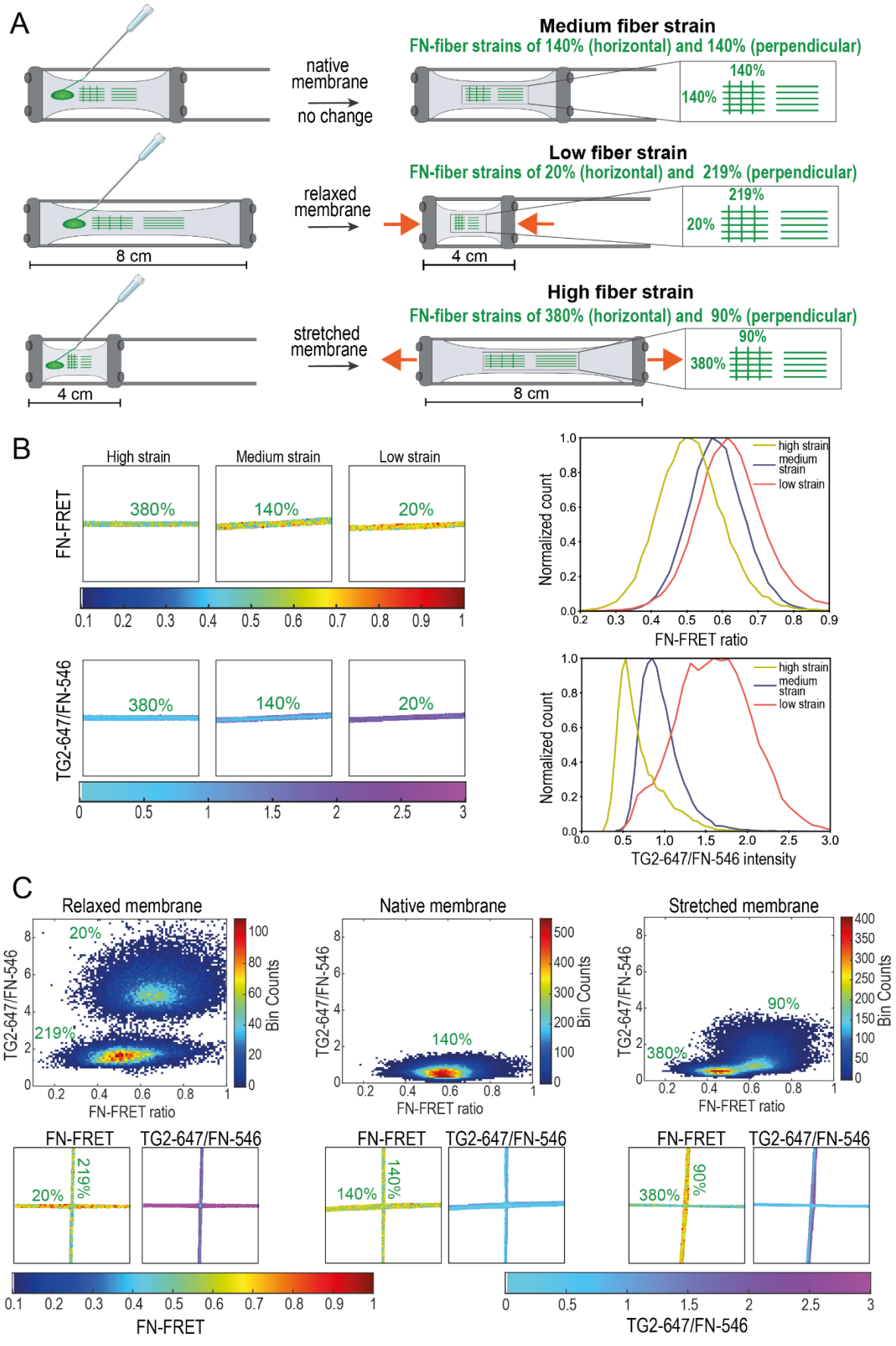

Figure 4.2.2: TG2 preferentially co-localizes with FN fibers under low strain, as revealed by the FN fiber stretch assay. A: A schematic view of the FN fiber stretch assay and the experimental

setup. FN fibers were manually pulled with a needle from a droplet of concentrated FN and deposited onto a silicone membrane mounted on the custom-made stretch device. FN fibers were pulled in two ways, either only parallel to the stretch axis, or both parallel and perpendicular as intersections. Membrane was left unchanged (native), relaxed from the pre-strained position, or stretched. Previous calibration studies converted the silicone membrane strain to the corresponding FN fiber strain[130] and are indicated on the cartoon. In this study, FN fiber strains along the stretch axis of relaxed, native, and stretched membranes are referred to as low strain (20%), medium strain (140%) and high strain (380%) respectively. TG2 labeled with an Alexa Fluorophore 647 (TG2-647) was added to the deposited FN fibers and incubated in the presence of various effectors that change its conformational state. **B:** On the left: Panels show a representative horizontal FN fiber for low, medium, and high strain with pixel-by-pixel color-coded FRET ratio and normalized TG2-647/FN-546 intensities. In the presence of 1mM GDP and 1mM EDTA, wild type human recombinant TG2 (WT hrTG2) has higher binding affinity (color-coded magenta) to the FN fiber under low strain (20%). On the right: Distributions of all FRET ratio pixels and normalized TG2-647/FN-546 from each representative fiber shown in the panels on the left were plotted as histograms. Higher FRET-ratio (low strain) in the FN fiber corresponds to the higher TG2-647/FN-546 signal. **C:** When FN fibers are deposited as intersections, after the membrane is relaxed or stretched, fibers along perpendicular and parallel axes are under different strains. TG2 preferentially binds the fibers under low strain (higher FN-FRET ratio values). All FN-FRET ratio and TG2-647/FN-546 pixels from the same intersection were plotted as binned scatterplots. When the strain of intersecting fibers was different (relaxed and stretched membranes), plotted pixels segregated into two separate groups with higher TG2-647/FN-546 values corresponding to higher FN-FRET ratios (low FN fiber strain). When the strain of the intersecting fibers was the same (native membrane) plotted pixels remained clustered together as a single group.

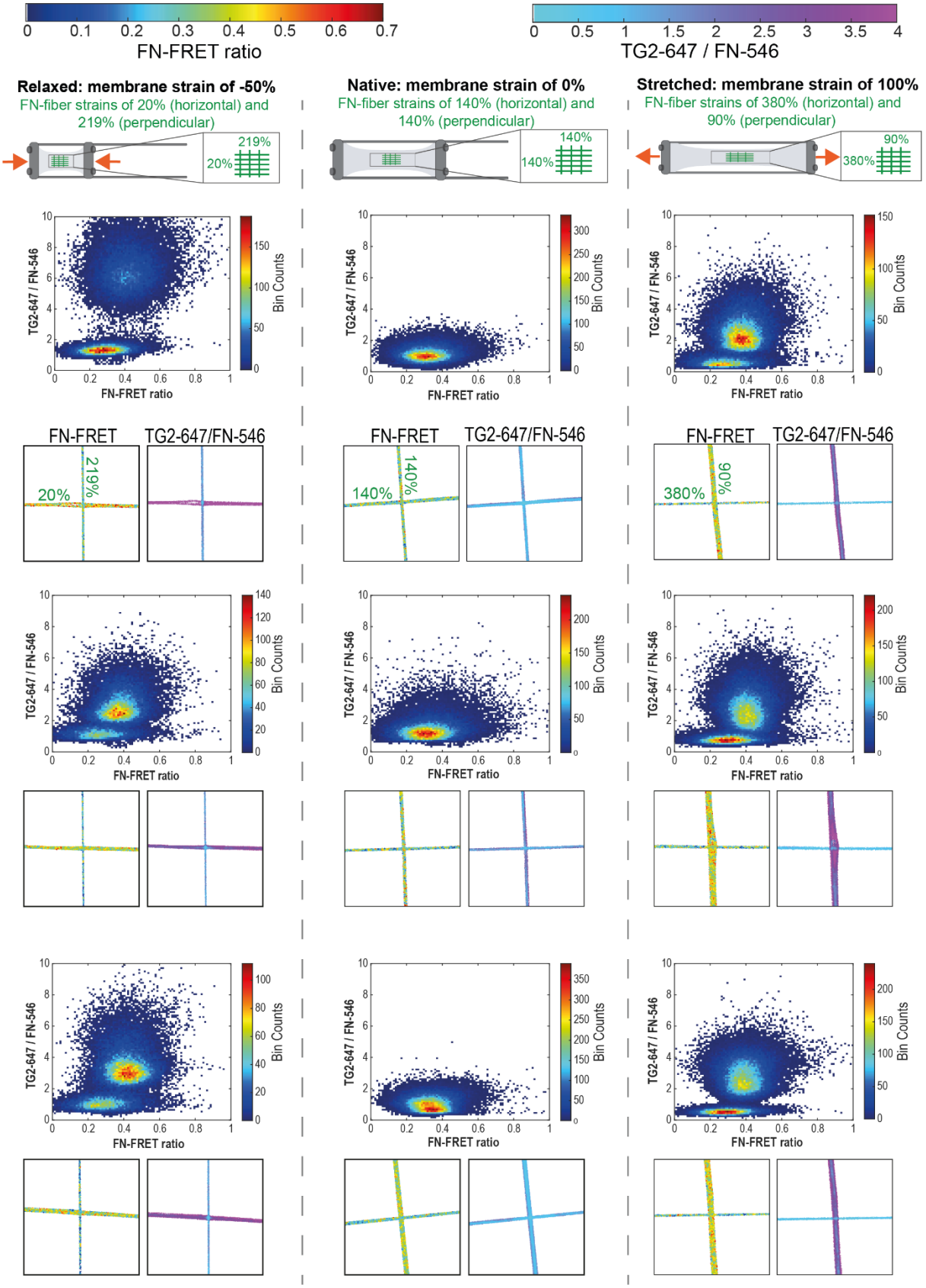

(Continued to the next page).

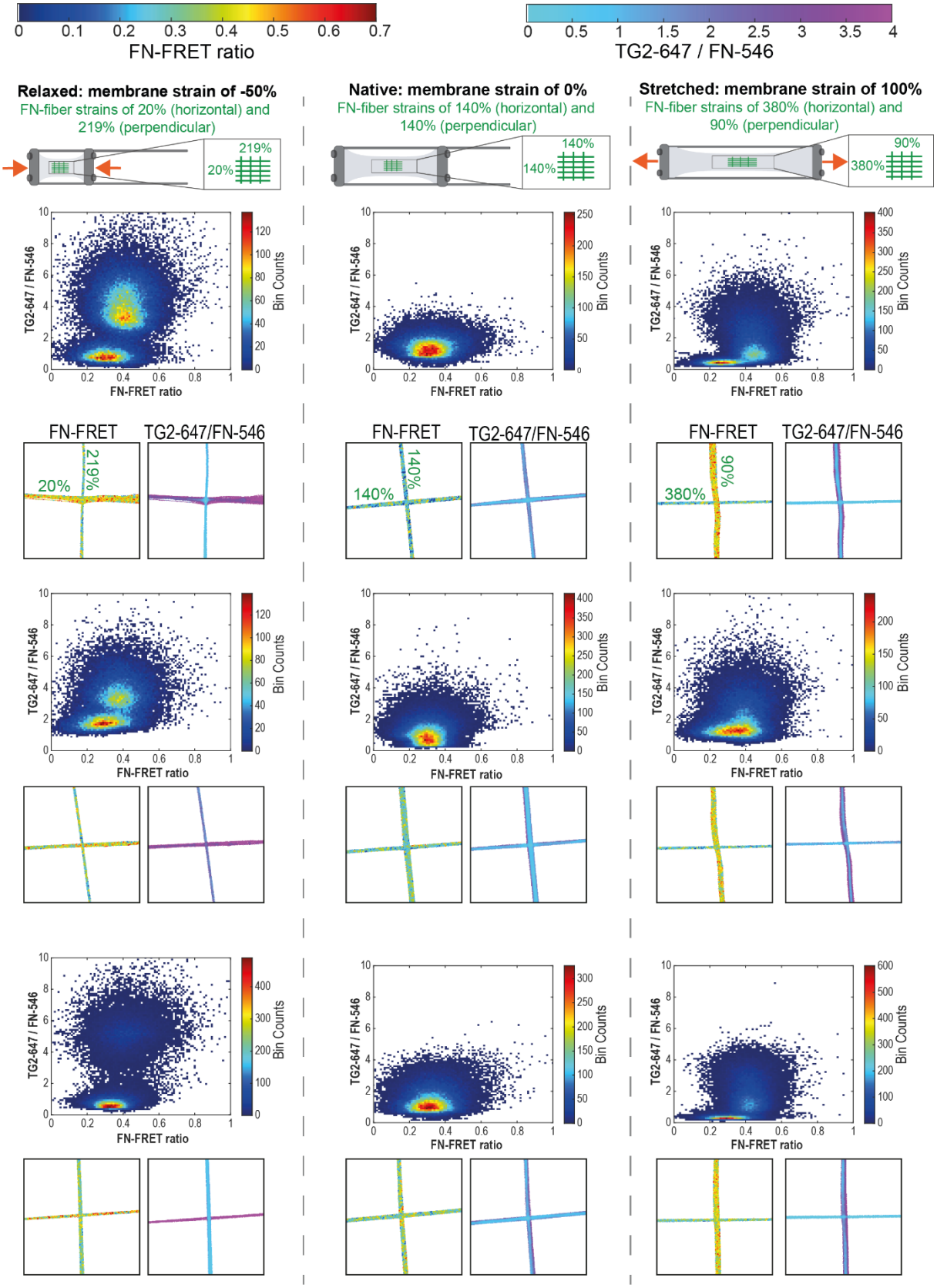

Figure 4.2.3: FN fiber stretch assay performed with WT gpTG2 in the presence of 1 mM GDP+ 1 mM EDTA on FN fibers deposited as intersections. In the presence of 1 mM GDP and 1 mM EDTA, gpTG2 preferentially binds to FN fibers when they are under low tensional state (higher FN-FRET ratio). FRET-labelled FN fibers were deposited as intersections (horizontally and

perpendicularly to the membrane stretch axis) on the silicone membrane mounted on the custom-made stretch device, which was mechanically stretched, relaxed, or left unchanged. The strains to which FN fibers were subjected due to the silicone membrane stretching or relaxation are indicated, as was reported in a previous study[130]. On the native membrane, FN fibers were pre-strained to 140% due to the forces required to pull fibers out of the droplet. FN-FRET and TG2-647/FN-546 pixels from each shown intersection were plotted as binned scatterplots. When the strain along the horizontal and perpendicular axes was different (stretched and relaxed membranes), FRET vs TG2-647/FN-546 pixels segregated into two separate groups. When the strain along the horizontal and perpendicular axes was the same (native membrane), pixels remain as a single population. This shows that TG2 binding to FN is regulated by FN tensional state with higher binding affinity to FN under low strain. 6 intersections per membrane strain are shown.

4.3 Spatial proximity between TG2's N-terminal domain and the C-terminal β-barrels is required for its mechano-regulated binding to FN.

Since an earlier study suggested that formation of the TG2-FN complex is not altered by the presence of TG2 effectors[46], we were surprised to find that the mechano-regulated binding was abolished upon addition of saturating amounts of Ca^{2+} (10 mM) (**Figure 4.3.2 B** and **Figure 4.3.3 A**). In the presence of Ca^{2+}, we no longer detected TG2's high affinity binding towards FN fibers under low strain. Instead, calcium bound TG2 (open state) showed the same, low level of binding towards fibers at all strains. A more detailed analysis revealed a dose dependent reduction of TG2 binding to FN fibers under low strain upon titration with increasing amounts of calcium (**Figure 4.3.1**).

Most of the TG2 in the ECM is thought to be reversibly inactivated due to the allosteric disulfide bond formation which locks the enzyme in the extended open state[40,85]. A similar conformation is induced by some active-site irreversible TG2 inhibitors, such as an active site-specific inhibitor Z006 (Z-DON-Val-Pro-Leu-OMe, "Z-DON") [37,41] (**Figure 2.2.1 B**). Therefore, we also investigated the binding of oxidized TG2 (oxTG2) and inhibitor Z006 bound TG2 ($TG2_{Z006}$), in comparison to $TG2_{GDP}$. (**Figure 4.3.2 E-F** and **Figure 4.3.4 A-B**). To prepare oxTG2 and $TG2_{Z006}$, WT gpTG2 was incubated for 3 h at 37ºC with 2 mM oxidized glutathione (GSSG) and 1 mM EDTA, or for 1 h at room temperature with 100 µM Z006 and 1.2 mM $CaCl_2$. As before, WT $TG2_{GDP}$ preferentially bound to FN fibers under low strain (**Figure 4.3.2 D**). In contrast, both oxTG2 and $TG2_{Z006}$ bound FN equally, regardless of the FN fiber strain (**Figure 4.3.2 E-F** and **Figure 4.3.4 A-B**) anticipated based on previous studies using soluble FN[46], we next looked for a testable structural hypothesis how TG2 binding to FN could be mechano-regulated. Cardoso *et al.* have mapped the FN binding site on TG2 to a region on the N-terminal domain[46], as indicated in Fig. 1A. Inspection of the structure suggests that the second β-barrel in the closed state is in proximity to the proposed FN binding site (**Figure 2.2.1 A**). The "beads-on-a-string" like structure of FN (**Figure 2.6.1 A**) suggests that adjacent FN modules could possibly form synergistic contacts, thereby stabilizing the TG2-FN complex on low tension FN fibers. In contrast, when TG2 is in the extended open state, the second β-barrel is out of reach and no additional contacts could be formed. To test whether β-barrels of TG2 participate in the

mechano-regulated binding to FN fibers, we have used a short TG2 variant (1-465aa, β-barrel 1 and 2 deleted) in our FN fiber stretch assay. Indeed, short TG2 showed the same behavior as calcium activated WT TG2, oxTG2 and $TG2_{Z006}$ and exhibited no mechano-regulated binding to FN fibers (**Figure 4.3.2 C** and **Figure 4.3.3 B**). This suggests that for the mechano-regulated binding, the β-barrels of TG2 need to be present and must be in spatial proximity to the N-terminal domain. Interestingly, there was no significant difference in binding between oxTG2 and $TG2_{Z006}$ to FN fibers under high strain (~380%), however $TG2_{GDP}$ binding affinity was significantly higher compared to oxTG2 and $TG2_{Z006}$ on high strain (**Figure 4.3.4 C**). Upon mechanical stretching of FN fibers, a large distribution of conformational FN states exists within each FN fiber that upon stretching gets gradually more shifted towards partially unfolded states[156]. Thus, the ensemble of specific binding sites on FN gets gradually destroyed by fiber stretching, not at one specific strain. This is due to the non-periodic bundling of FN molecules within the fibers, which interferes with the mechanical hierarchy in which FN domains would get unfolded in isolated molecules[156]. Consequently, the specific TG2-binding sites on FN are being destroyed gradually with increasing FN fiber strain, as observed previously for other binding partners[51,59,61,63,130]. Thus, FN fiber stretching results in a progressive reduction of $TG2_{GDP}$ binding. However, since the N-terminal domain and C-terminal β-barrels of $TG2_{GDP}$ are in spatial proximity, unlike in oxTG2 and $TG2_{Z006}$, $TG2_{GDP}$ can maintain additional contacts to the remaining intact binding sites on FN. Thus, this result also agrees with our hypothesis.

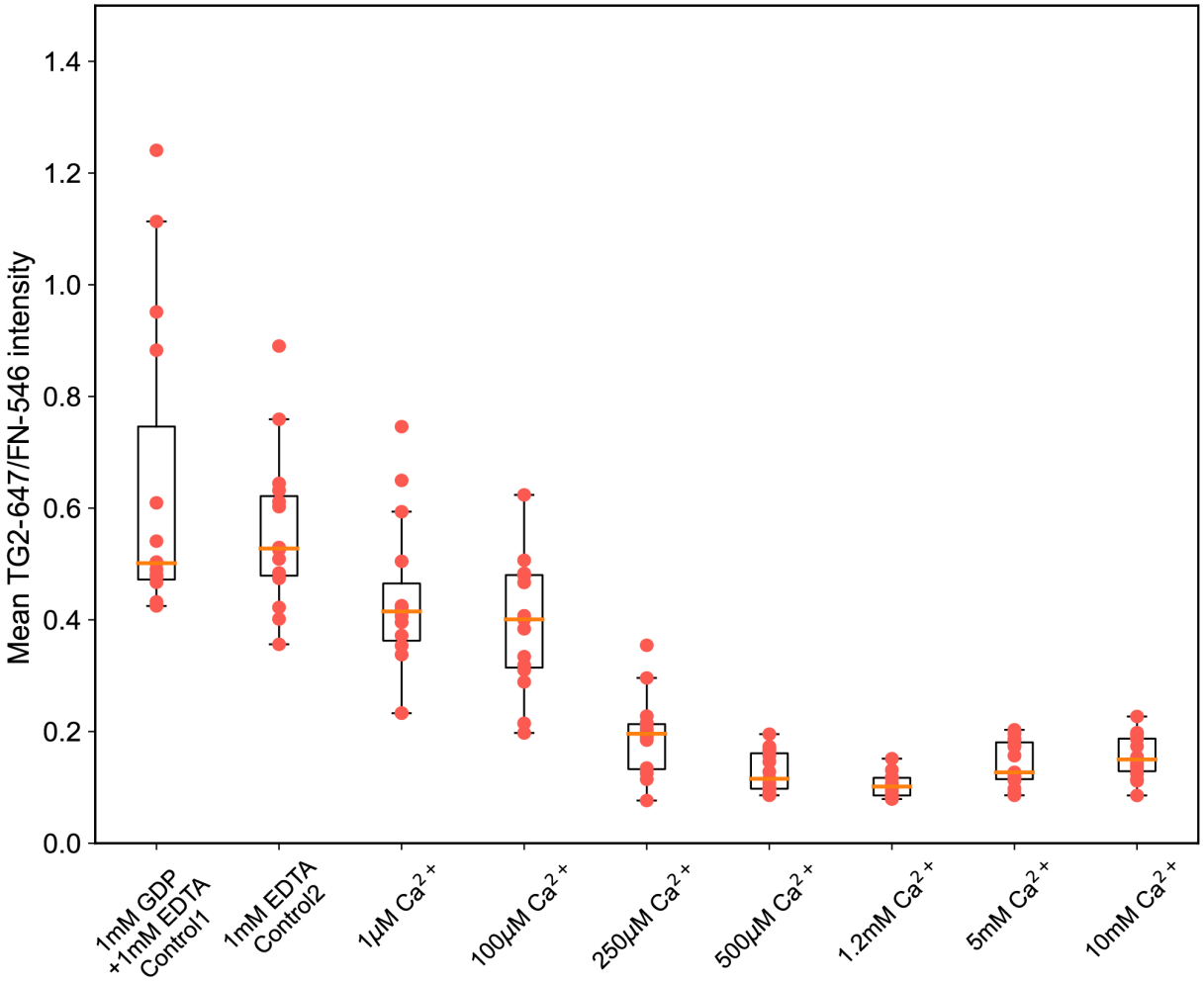

Figure 4.3.1: FN fiber stretch assay performed with WT gpTG2 in the presence of increasing Ca2+ concentrations on horizontally deposited FN fibers under low strain (20%). The mean of pixel-by-pixel normalized TG2-647/FN-488 are plotted as boxplots. WT gpTG2 binding affinity for fibrillar FN under low strain (20%) decreases in a calcium dose-dependent manner. Progressively increasing calcium concentrations reduce gpTG2 binding affinity until it reaches the baseline affinity at 500µM calcium and does not decrease anymore. TG2 binding affinity to FN is the highest in the presence of 1mM GDP (control 1) or GDP-free EDTA (control 2). 15 individual fibers were analyzed per condition.

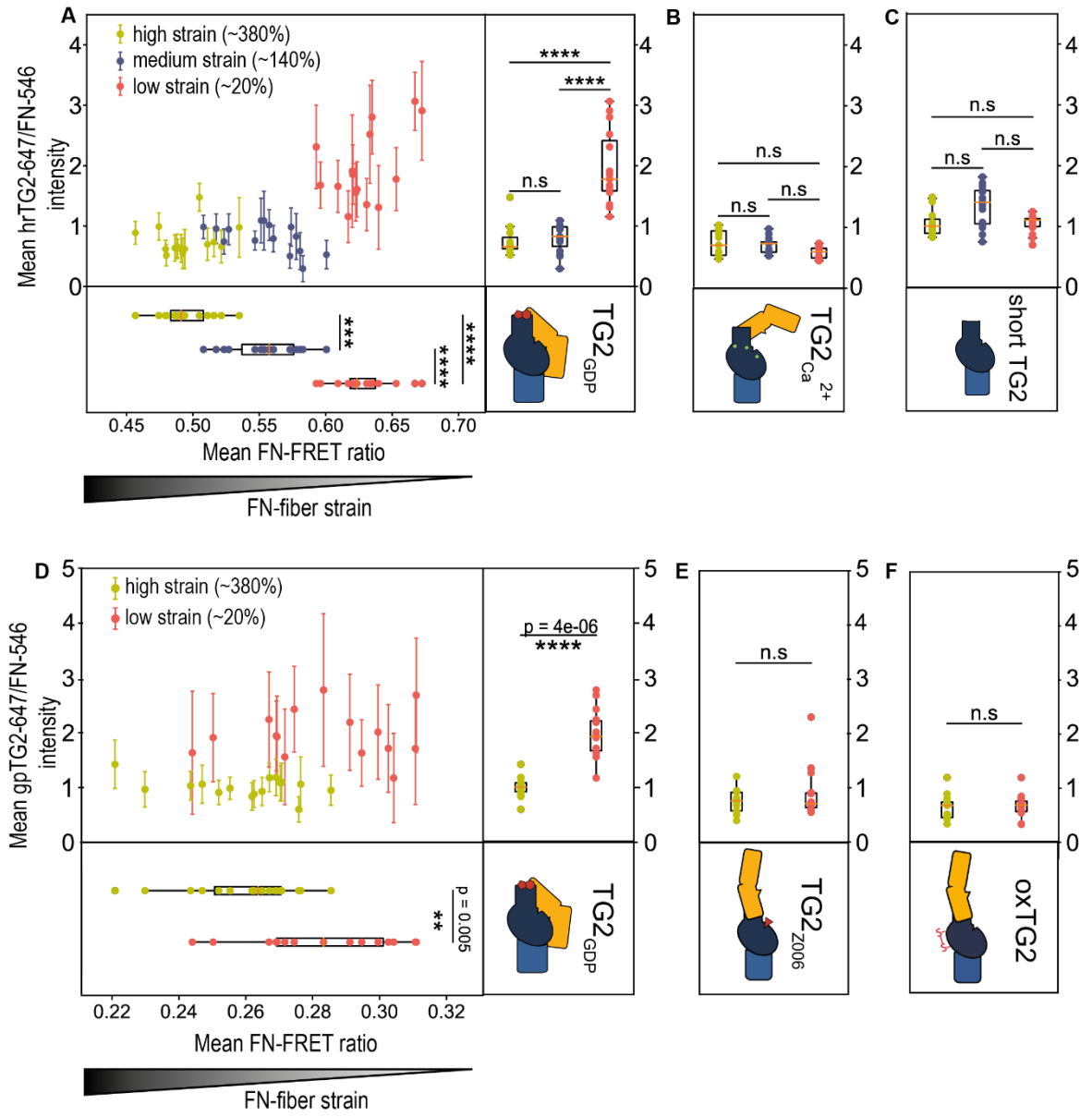

Figure 4.3.2: FN fiber stretch assay data showing the dependence of mechano-regulated TG2-FN binding on TG2's conformational states and its C-terminal β-barrels. The means of the distribution of FN-FRET ratio from all pixels of one fiber was plotted against the means of the distribution of the normalized TG2-647/FN-546 intensity. 15 fibers were analyzed per membrane strain (Full data sets: Supplementary Fig. 6 & 8). **A:** Human recombinant TG2 (hrTG2) has a higher binding affinity toward FN fibers under low strain (~20%) in the presence of 1mM GDP and 1 mM EDTA, which induce a closed TG2 conformation. **B:** hrTG2 binds FN with equal affinity in the presence of 10 mM Ca2+ which induces an open TG2 conformation regardless of FN fiber strain. **C:** Short TG2 (β-barrels 1 and 2 are deleted) binds FN with equal affinity regardless of FN fiber strain. Short TG2 was labelled separately from hrTG2 and has a different degree of labelling, therefore its fluorescent intensity should not be compared to TG2Ca2+ or $TG2_{GDP}$. **D:** Like hrTG2 in **(A)**, guinea pig liver TG2 (gpTG2), preferentially bound with higher affinity to FN fibers under low strain (~20%) in the presence of 1 mM GDP and 1 mM EDTA (closed-state TG2). When gpTG2 was incubated with the irreversible active-site inhibitor Z006 (Z-DON) **(E)** or oxidised with GSSG **(F)**, both of which induce an extended open-state TG2

conformation, TG2Z006 and oxTG2 bound FN equally, regardless of FN fiber strain. Statistical significance was computed with Wilcoxon rank-sum statistic for two samples. P-values: (*0.01≤ p <0.05; **0.001≤ p <0.01; ***10-5≤ p <0.001; ****10-6≤ p <10-5; ***** p <10-6).

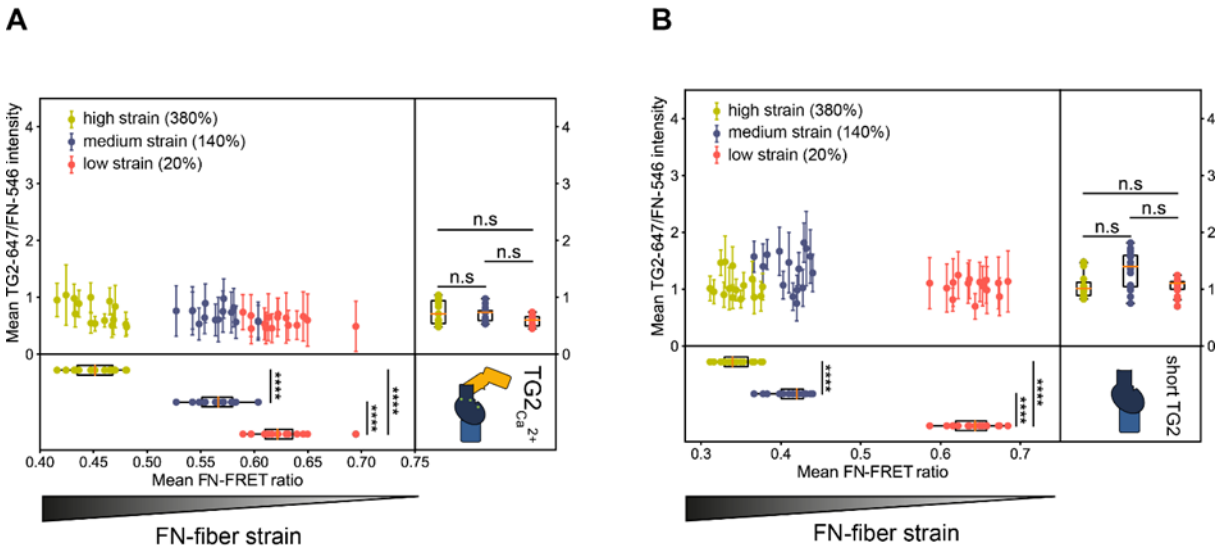

Figure 4.3.3: FN fiber stretch assay with WT hrTG2 and short hrTG2(1-465aa). The mean of the distribution of FN-FRET ratio in one fiber was plotted against the mean of the distribution of the pixel-by-pixel normalized TG2-647/FN-546 intensity. 15 fibers were analyzed per membrane strain. **(A)** WT hrTG2 incubated on FN fibers under low, high, and medium strain in the presence of 10 mM Ca^{2+} bound FN equally regardless of the FN fiber strain. Higher FN-FRET ratio is indicative of low FN fiber strain and vice versa. **(B)** short hrTG2 (β-barrels 1 and 2 deleted, 1-465aa) incubated on FN fibers under low, high, and medium strain bound FN equally regardless of the FN fiber strain. Higher FN-FRET ratio is indicative of low FN-strain and vice versa. Statistical significance was computed with Wilcoxon rank-sum statistic for two samples. P-values: (*0.01≤ p <0.05; **0.001≤ p <0.01; ***10^{-5}≤ p <0.001; ****10^{-6}≤ p <10^{-5}; ***** p <10^{-6})

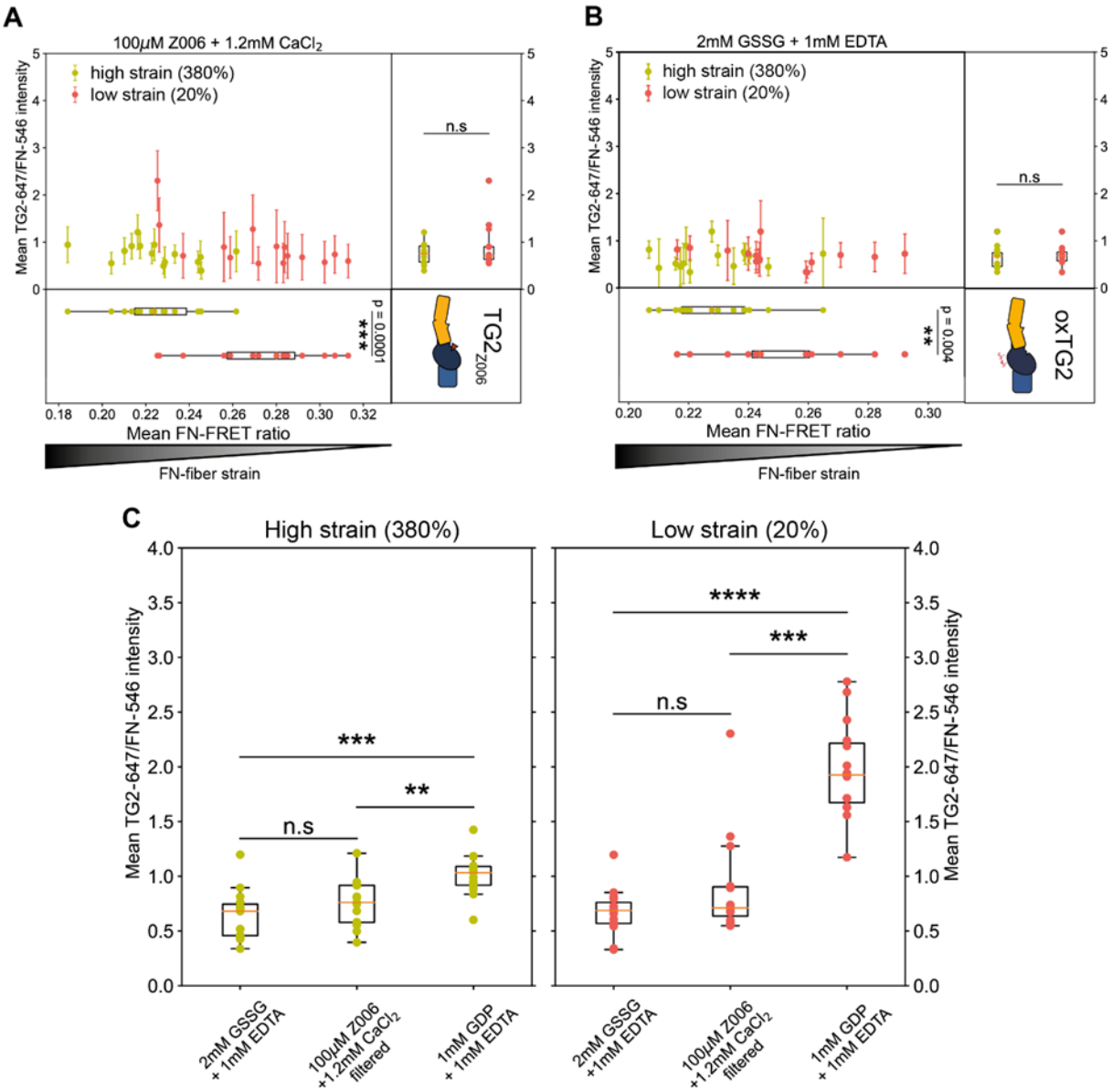

Figure 4.3.4: FN fiber stretch assay with WT gpTG2. The mean of the distribution of FN-FRET ratio in one fiber was plotted against the mean of the distribution of the pixel-by-pixel normalized TG2-647/FN-546 intensity. 15 fibers were analyzed per membrane strain. When WT gpTG2 is trapped in the extended open-state either with inhibitor Z006 **(A)** or through oxidation **(B)**, TG2 binds FN fibers under high (~380%) and low (~20%) strain equally. **C:** Means of TG2-647/FN546 intensity shown in (A) and (B) were replotted as boxplots to make comparisons between oxTG2, $TG2_{Z006}$ and $TG2_{GDP}$ when FN fibers experience the same strain. There was no significant difference in binding between oxTG2 and $TG2_{Z006}$ to FN fibers under high (~380%) and low (~20%) strain, however $TG2_{GDP}$ binding affinity was significantly higher compared to oxTG2 and $TG2_{Z006}$ on FN fibers under high and low strain. 15 individual fibers were analyzed per condition. Statistical significance was computed with Wilcoxon rank-sum statistic for two samples. P-values: (*$0.01 \leq p < 0.05$; **$0.001 \leq p < 0.01$; ***$10^{-5} \leq p < 0.001$; ****$10^{-6} \leq p < 10^{-5}$; ***** $p < 10^{-6}$)

4.4 Catalytic activity of TG2 has no effect on the loss of mechano-regulated binding to fibrillar FN.

To ensure that the loss of the mechano-regulated binding of TG2 to FN fibers in the presence of calcium was not due to TG2 crosslinking activity or TG2 self-crosslinking[157], we conducted a control experiment using an inactive Cys277Ser-TG2 mutant (**Figure 4.4.1**). TG2 is stabilized in the closed conformation by an H-bond between Cys277 (catalytic core) and Tyr516 (β-barrel 1)[90]. Cys277Ala/Ser-TG2 mutants which are less efficient in forming this H-bond, are known to assume predominantly an open conformation. We observed that in the presence of 1.2 mM calcium, the Cys277Ser-TG2 mutant bound FN fibers at both high (~380%) and low (~20%) strains equally well, indicating that it is the open conformation of TG2 that abolishes mechano-regulated binding to FN fibers, and not its crosslinking activity. Addition of 1 mM GDP increased the Cys277Ser-TG2 binding affinity to FN fibers at low strain (~20%); however, the significance of this increase was considerably less ($p = 0.004$) compared to the wild type hrTG2 ($p < 10^{-5}$). Cys277/Ala/Ser-TG2 mutants are less efficient in binding GDP and tend to assume the open conformation[90], thus explaining the reduced significance of the observed increase as well. All these results confirm that the conformational state and not the crosslinking activity of the open-state TG2 plays the central role in the loss of the mechano-regulated binding to FN fibers.

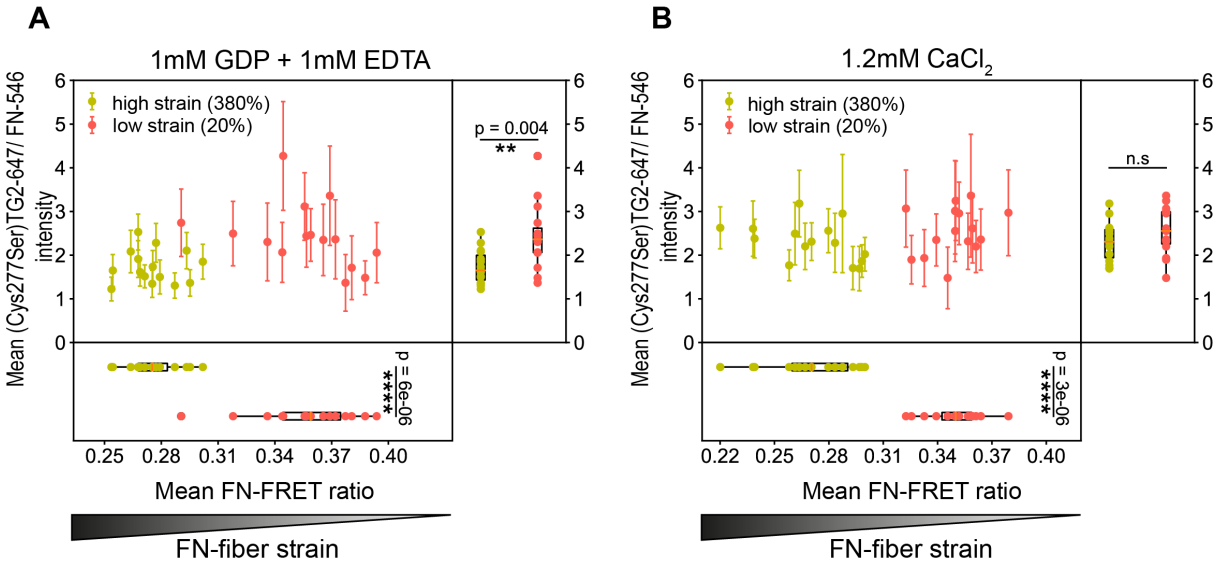

Figure 4.4.1: FN fiber stretch assay performed with hrTG2's inactive Cys277Ser mutant. A: In the presence of 1mM GDP, the Cys277Ser hrTG2 preferentially bound FN fibers under low strain, although the significance of this difference was less (p=0.004) compared to the significance of the difference in affinity we observed with the WT gpTG2 (p < 4e-06). This is consistent with the report that hrTG2's Cys277Ser mutant is unable to bind GTP/GDP efficiently[90]. **B:** In the presence of 1.2 mM Ca2+, Cys277Ser hrTG2 bound FN fibers under high (380%) and low (20%) strain equally, similarly to the result with the WT TG2 and 1.2 mM Ca2+. Since hrTG2's Cys277Ser mutant is prone to adopt an open conformation[90], this result confirms that it is the open conformational state, and not the crosslinking activity of the open-state of

TG2, which plays the role in the loss of the strain-sensitive binding to FN. 15 fibers were analyzed per membrane strain. Statistical significance was computed with Wilcoxon rank-sum statistic for two samples. P-values: (*0.01≤ p <0.05; **0.001≤ p <0.01; ***10-5≤ p <0.001; ****10-6≤ p <10-5; ***** p <10-6)

5 Providing mechanistic and structural insights into the synergistic role of TG2's C-terminal β-barrel domains in the mechano-regulated binding

The work presented has been published in Matrix Biology.

Kateryna Selcuk, Alexander Leitner, Lukas Braun, Fanny Le Blanc, Paulina Pacak, Simon Pot, Viola Vogel, **Transglutaminase 2 has higher affinity for relaxed than for stretched fibronectin fibers**, Matrix Biology, Volume 125, 2024, Pages 113-132, ISSN 0945-053X, https://doi.org/10.1016/j.matbio.2023.12.006

Author contributions: KS, LB, VV conceived the study and designed the research. Microplate protein-binding assays and data analysis were performed by KS. FLB under supervision of AL performed all crosslinking experiments and data analysis. KS visualized XL-MS data. KS, AL and VV wrote the manuscript.

5.1 Motivation.

The focus of this chapter is to gain deeper mechanistic insights into the mechano-regulated binding of TG2 to FN by investigating and demonstrating the role TG2's C-terminal β-barrels as the unrecognized synergy binding site for FN.

5.2 TG2's affinity to surface-adsorbed FN depends on its conformation and the presence of the C-terminal β-barrel domains.

While previous studies suggested that TG2 binding to surface-adsorbed FN is independent of TG2 conformational states and C-terminal domains[46], our conclusions drawn from FN fiber stretch assays supported the opposite conclusion. To understand whether our results were due to the use of the fibrillar FN in our stretch-assays, which has distinct conformational states compared to surface adsorbed FN that retains a more closed conformation[158], we repeated the studies using surface adsorbed FN. For this, 96-well microtiter plates were coated with human plasma FN or 45-kDa FN gelatin-binding domain (GBD) at concentrations ranging from 1 µg/ml to 50 µg/ml overnight at 4°C. FN was detected using a monoclonal antibody that has its epitope localized within FN's gelatin binding domain (GBD) (MAB1892, Merck), followed by staining with a secondary AF488-coupled antibody, and the fluorescence intensity was measured with a plate reader. To determine the optimal FN concentration for the plate coatings, we first plotted the adsorption isotherm for full-length dimeric FN (**Figure 5.2.1 A**). The concentration of full-length FN, at which 95% of maximal fluorescence intensity was observed, corresponded to 2.2 µg/ml, and was used for the FN coatings in all subsequent microplate assays. To determine the concentration of the GBD that would enable the coating of plates with a similar number of TG2 binding sites as with the full-length FN, we plotted the GBD adsorption isotherm, as we did for the full-length FN (**Figure 5.2.1 B**). We determined that the concentration of the GBD corresponding to 95% of the maximal fluorescence intensity of the full-length FN was 0.6 µg/ml, which we used to coat plates for subsequent experiments. To evaluate the binding of TG2 to adsorbed FN, we titrated fluorescently labelled TG2 in presence of 1 mM GDP and 1 mM EDTA, or only 1 mM EDTA, or 1.2 mM $CaCl_2$, or 1.2 mM $CaCl_2$ and 100 µM Z006, followed by incubation on full-length FN-

coated wells for 1 h at room temperature (**Figure 5.2.1 C**). Unexpected from previous reports, we found that TG2 had different binding affinities to adsorbed FN, which were in fact dependent on the conformational state of TG2 induced by a specific TG2 effector. Specifically, the binding affinities of TG2 to surface adsorbed FN were in the following order from lowest to highest: $TG2_{CaCl2}$ < $TG2_{EDTA}$ < $TG2_{GDP}$ < $TG2_{Z006}$. In contrast and in agreement with our hypothesis, the short TG2 (1-465aa, β-barrel 1 and 2 deleted) exhibited comparable binding affinities under all four conditions, irrespective of the effector (**Figure 5.2.1 D**). The maximum binding affinity was achieved at a concentration of approximately 2 µg/ml of short TG2, but non-specific binding increased continuously at concentrations above 4 µg/ml. Furthermore, we observed that the binding affinity of TG2 significantly decreased when plates were coated with the GBD, even when the same number of TG2 binding sites was present (**Figure 5.2.1 C, E**). These findings indeed suggest that TG2 has a higher binding affinity for full-length FN, likely due to additional contacts it makes with FN modules outside of the conventional GBD.

These results demonstrate that the affinity by which TG2 binds to surface-adsorbed FN is tuned by the conformation of TG2 as induced by its allosteric effectors. Moreover, our data confirm that the C-terminal domains of TG2 play a crucial role in enhancing the binding to surface-adsorbed FN, highlighting their significance in TG2 interactions with both fibrillar and surface-adsorbed FN.

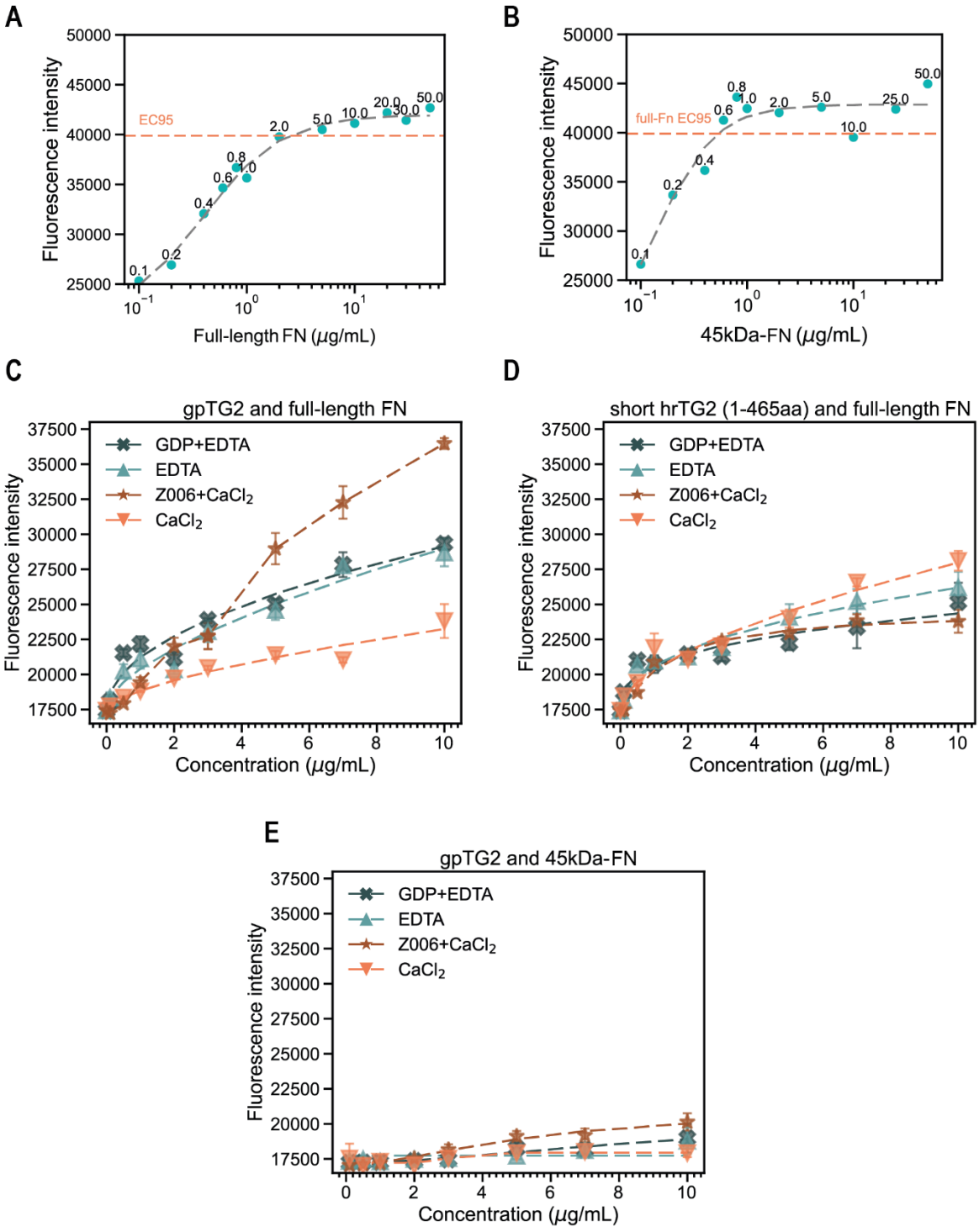

Figure 5.2.1: Microplate protein-binding assay data with TG2 binding to surface-adsorbed full-length FN, or to FN's 45 kDa gelatin binding domain (GBD) fragment.

A: 96-well microplates were coated with concentration series of full-length FN at 4°C overnight. FN was detected with a monoclonal anti-FN antibody with an epitope within the gelatin binding domain (GBD). From the fitted curve, it was determined that the maximal fluorescent intensity was reached at a concentration of 2.4 µg/ml of full-length FN 95%. B: 96-well microplates were coated with concentration series of 45 kDa-FN GBD at 4°C overnight and detected using the same anti-FN antibody as in (A). From the fitted curve, it was determined that the maximal fluorescent intensity observed for the full-length FN was reached at 0.6 µg/ml of 45 kDa-FN GBD 95%, and therefore this concentration corresponds approximately to the same number of TG2 binding sites on 45 kDa-FN GBD. C: Binding affinity of wild type guinea pig TG2 (WT gpTG2) to the surface-adsorbed FN changes depending on the presence of GDP, Ca^{2+} and Z006 TG2 effectors. D: Deletion of TG2's β-barrels 1 and 2 results in indiscriminate binding affinity of short TG2 mutant to adsorbed FN, regardless of the presence of GDP, Ca^{2+} and Z006 effectors. E: When plates were coated with 0.6 µg/ml of FN's 45 kDa-FN fragment, which corresponds to the same number of binding sites as when coated with 2.4 µg/ml full-length FN, WT gpTG2 had drastically reduced binding affinity toward 45 kDa-FN fragment. *For the coatings of microtiter plates, the 2.4 µg/ml of full-length FN and 0.6 µg/ml of 45 kDa-FN were used, which approximately correspond to the same number of binding sites for TG2, as was determined in by the titration experiments in A and B.

5.3 C-terminal β-barrels of $TG2_{GDP}$ interact with the regions outside of the canonical gelatin-binding domain (GBD) of FN in solution.

As the short form of TG2 without β-barrel domains no longer exhibited sensitivity to the FN fiber strain and bound both stretched and relaxed FN fibers equally, this implies the presence of a secondary binding site on C-terminal β-barrel domains of TG2. Yet, no information was available in the literature about the role of these domains in TG2's interaction with FN. To explore the possibility of multivalent synergy binding sites, we used crosslinking mass spectrometry[159] (XL-MS) to map contact sites between the two proteins. As one of the structural proteomics techniques, XL-MS uses chemical reagents to induce covalent bonds between spatially proximal amino acids within or between proteins. Crosslinking sites are identified after enzymatic digestion of crosslinked proteins and sequencing of the resulting connected peptide pairs by mass spectrometry. Previous similar proteomic approaches (hydrogen-deuterium exchange - HDX) using only FN's GBD in complex with $TG2_{Z006}$, did not identify any regions on the C-terminal β-barrel domains of TG2 that could interact with FN[46]. This is in agreement with our hypothesis, as the inhibitor Z006 is known to trap TG2 in the extended open conformation, which spatially separates the C-terminal domains from the N-terminal domain, making them inaccessible to FN[37]. To our knowledge, interacting regions of the $TG2_{GDP}$ (closed state) and the full-length FN have not been mapped with both approaches. Thus, we performed for the first time XL-MS analysis of $TG2_{GDP}$ in complex with full-length FN, and to better compare our findings with literature, of $TG2_{GDP}$ in complex with the GBD.

Amine-specific crosslinking of the TG2-FN complexes was performed with disuccinimidyl suberate (DSS), and to increase the coverage of structural information,

simultaneous crosslinking of acidic residues (Asp/Glu with Asp/Glu and Lys with Asp/Glu) was performed with PDH and DMTMM[160]. Crosslinked samples were further processed with trypsin or chymotrypsin digestion, SEC fractionation of the resulting peptide mixtures, followed by LC-MS/MS analysis of SEC fractions. Among the resulting FN isoforms, we were able to unequivocally identify FN isoform 1, which was used for the subsequent data analyses. Validated crosslinks were displayed on circular diagrams with the help of xVis[161] (**Figure 5.3.1**-**Figure 5.3.3**). In total, 20 unique crosslinks were identified between $TG2_{GDP}$ and FN or $TG2_{GDP}$ and GBD complexes (Supplementary Note 2 and **Figure 5.3.1**). Remarkably, the C-terminal β-barrel 2 was in close contact with $FNIII_{14-15}$ (4 unique inter-protein crosslinks), as well as with FNI_2 (3 inter-protein crosslinks). Simultaneously, $FNIII_{14-15}$ and FNI_2 were in close contact with each other, as indicated by multiple intra-protein crosslinks between those regions (magenta lines in **Figure 5.3.1**). From experiments with the TG2 and GBD and chymotrypsin as a protease, 8 additional unique inter-protein crosslinks were detected (**Figure 5.3.3**). Notably, we identified a crosslink between Lys30 (TG2) and Lys486 (GBD, numbering for full length FN). TG2 residue Lys30 is known to be one of the three residues (Lys30, Arg116, His134) that comprise the main FN-binding site on the N-terminal β-sandwich of TG2[46]. Interestingly, the crosslink involving Lys486 was not found when TG2 was in complex with the full-length FN (Supplementary Note 2 and **Figure 5.3.2**). Instead, Lys30 on TG2 was crosslinked to Lys1837 and Lys1862 on $FNIII_{14}$. This difference could arise from the variations in reactivity between these lysine residues and structural differences. These MS data clearly demonstrate that the C-terminal domains of TG2 interact with regions of FN outside of the canonical GBD when FN is in a compact quaternary conformation in solution, and when the C-terminal β-barrels are in spatial proximity to the N-terminal domain.

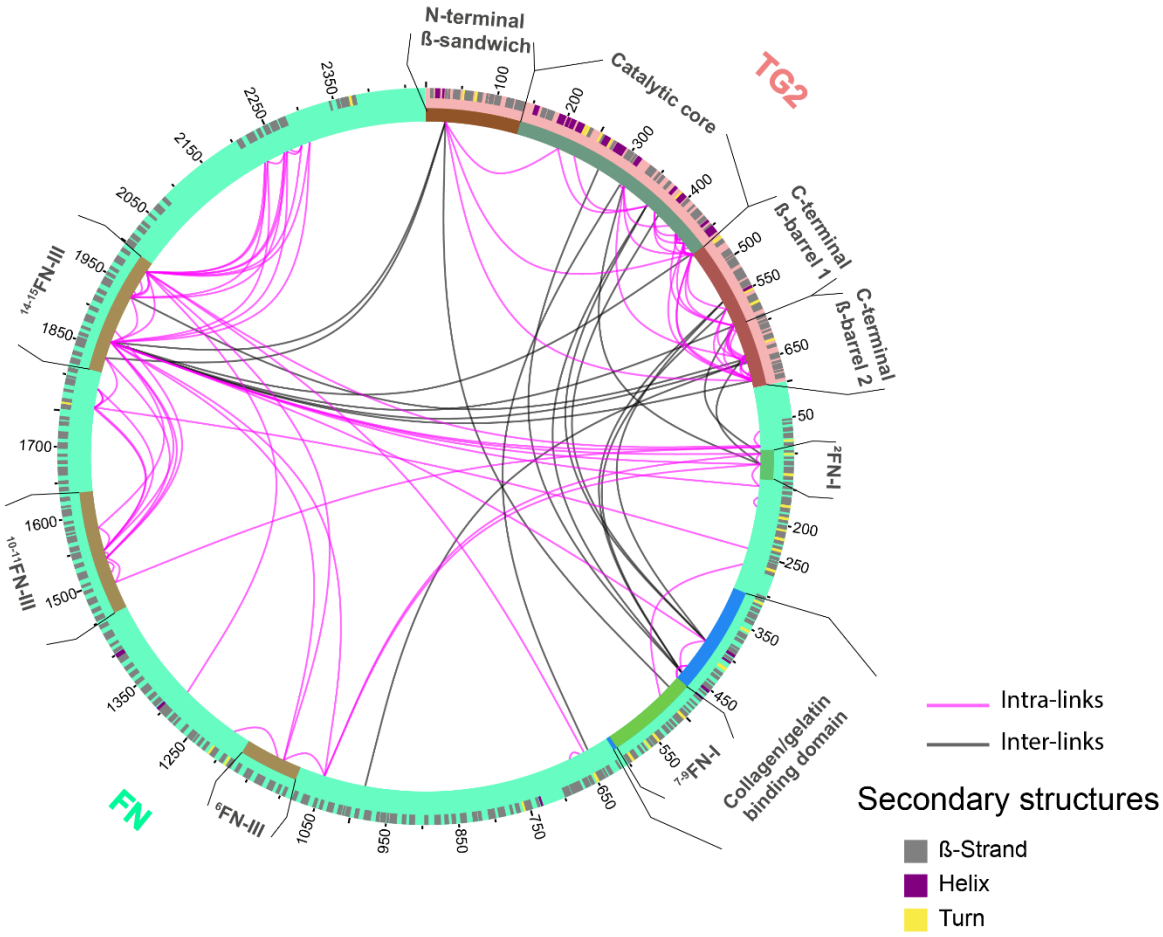

Figure 5.3.1: Crosslinks identified with the XL-MS of the $TG2_{GDP}$ and FN complex reveal that TG2's C-terminal β-barrel domains interact with regions outside of the canonical FN's GBD. Circular diagram shows simultaneously 20 unique inter-protein crosslinks identified from both TG2-FN and TG2-45 kDa-FN complexes using trypsin and chymotrypsin as proteases. To view them separately, go to **Figure 5.3.2** and **Figure 5.3.3**. Crosslinks only within TG2 or only within FN (intra-protein crosslinks) are shown in magenta, crosslinks between TG2 and FN (inter-protein crosslinks) are shown in black. C-terminal β-barrel 2 of $TG2_{GDP}$ is in close contact with FNIII14-15 (Lys1862 and Lys1936) and FNI2 (Lys100 and Lys116). Simultaneously, FNIII14-15 and FNI2 are in proximity to each other, as shown by magenta intra-protein crosslinks. TG2 residue Lys30, which is one of the three residues (Lys30, Arg116, His134) comprising the main FN-binding site on the N-terminal β-sandwich[46], was crosslinked to Lys486 (45 kDa-FN, numbering for full-length FN). In full-length FN, Lys30 was crosslinked to residues Lys1837(FNIII14) and Lys1862(FNIII14). Visualization was done with xVis Webserver[161].

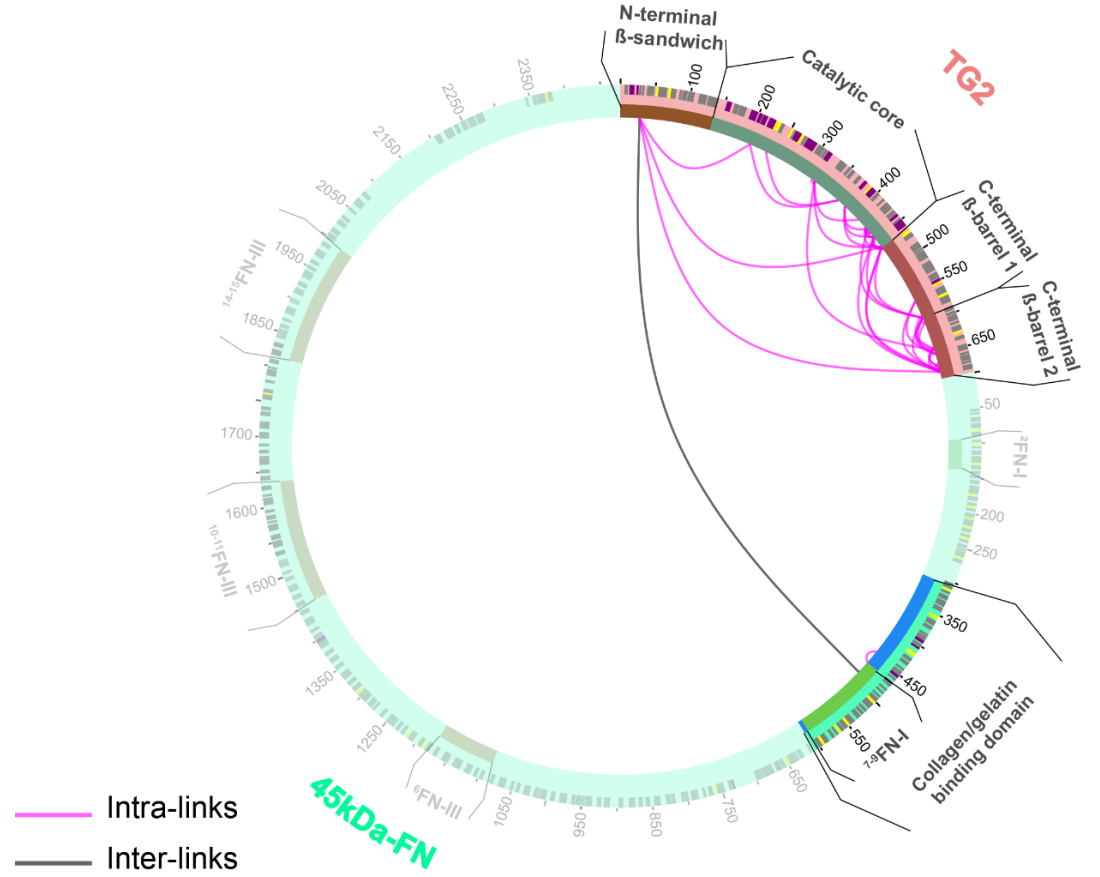
N-terminal ß-sandwich
Catalytic core
TG2
C-terminal ß-barrel 1
C-terminal ß-barrel 2
Collagen/gelatin binding domain
7-9FN-I
6FN-III
10-11FN-III
14-15FN-III
2FN-I
45kDa-FN
Intra-links
Inter-links

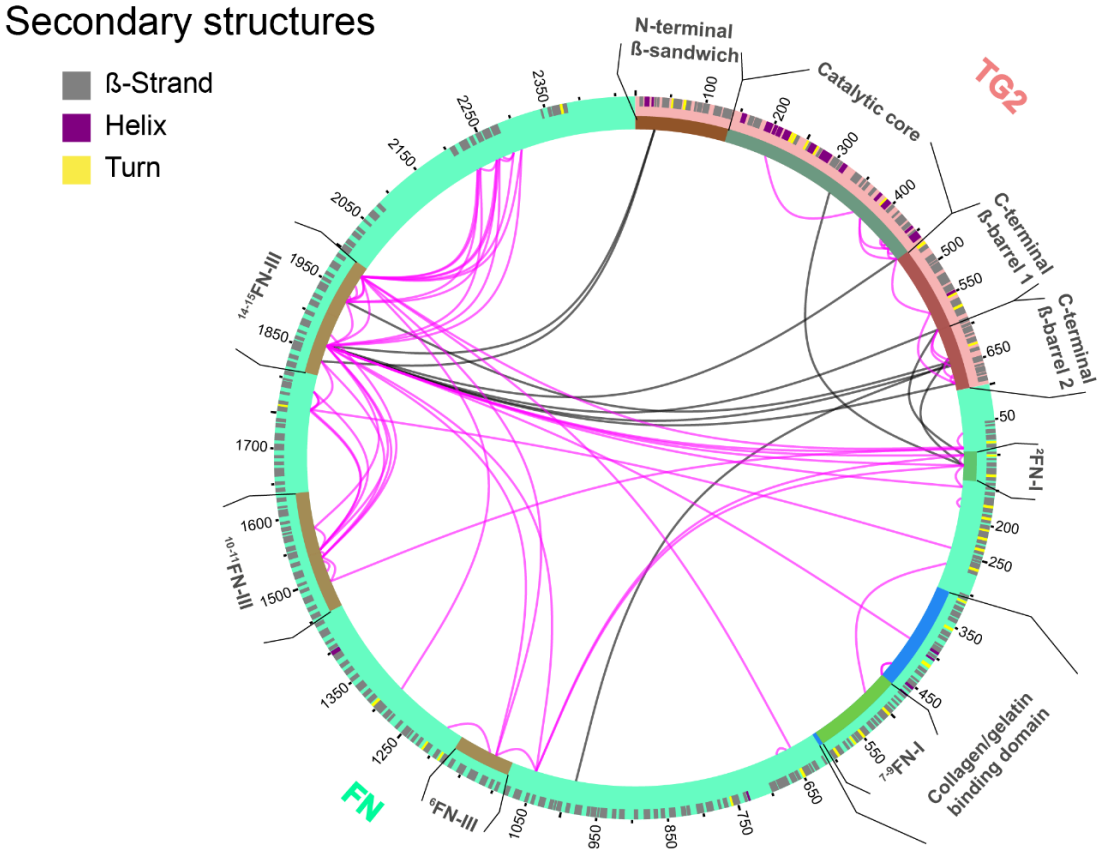
Secondary structures
ß-Strand
Helix
Turn
N-terminal ß-sandwich
Catalytic core
TG2
C-terminal ß-barrel 1
C-terminal ß-barrel 2
Collagen/gelatin binding domain
7-9FN-I
6FN-III
10-11FN-III
14-15FN-III
2FN-I
FN

Figure 5.3.2: XL-MS of TG2 and 45 kDa-FN and TG2 and FN complexes using trypsin as a protease. Circular diagrams show crosslinks identified from TG2/45 kDa-FN complex (top) and from TG2/FN complex (bottom). Inter-protein crosslinks are shown in black and intra-protein crosslinks in magenta. **Top:** The GBD is shown in solid colors and the rest of the FN is dimmed. A single inter-protein crosslink could be identified connecting FN residue Lys486 (FNI7, numbering for full-length FN) with TG2 residue Lys30 (N-terminal β-sandwich). **Bottom:** TG2 in complex with full-length FN, Lys30 (TG2) was crosslinked to residues Lys1837 and Lys1862 (FNIII14). The C-terminal β-barrel 2 interacts with FNIII14-15 (residues Lys1862 and Lys1936) and FNI2 (residues Asp110 and Lys116). Simultaneously, FNIII14-15 and FNI2 regions are in close contact with each other, as shown by the magenta intra-protein crosslinks. Crosslinks are mapped using FN monomer. Visualization was done with xVis Webserver[161].

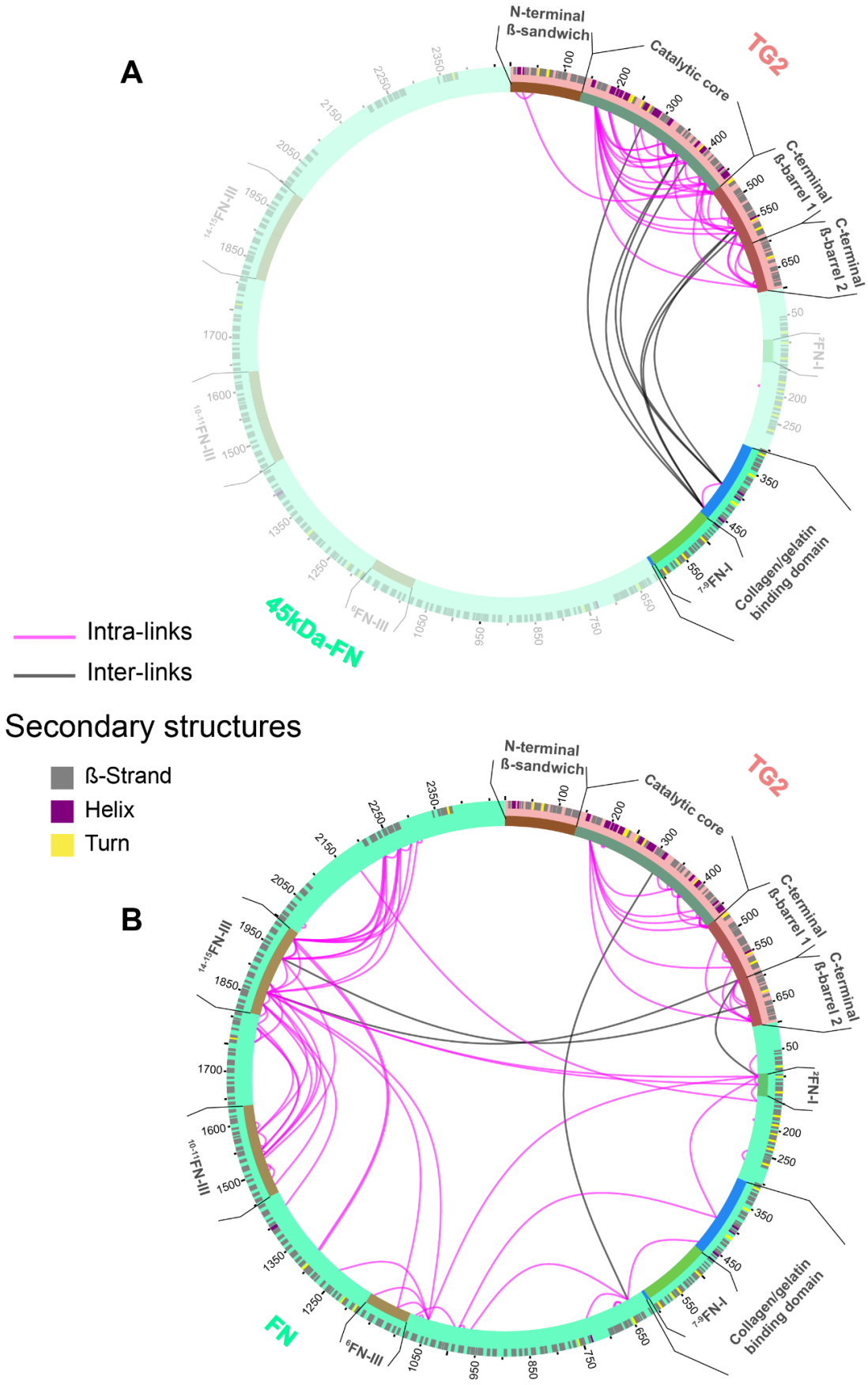

(Continued to the next page).

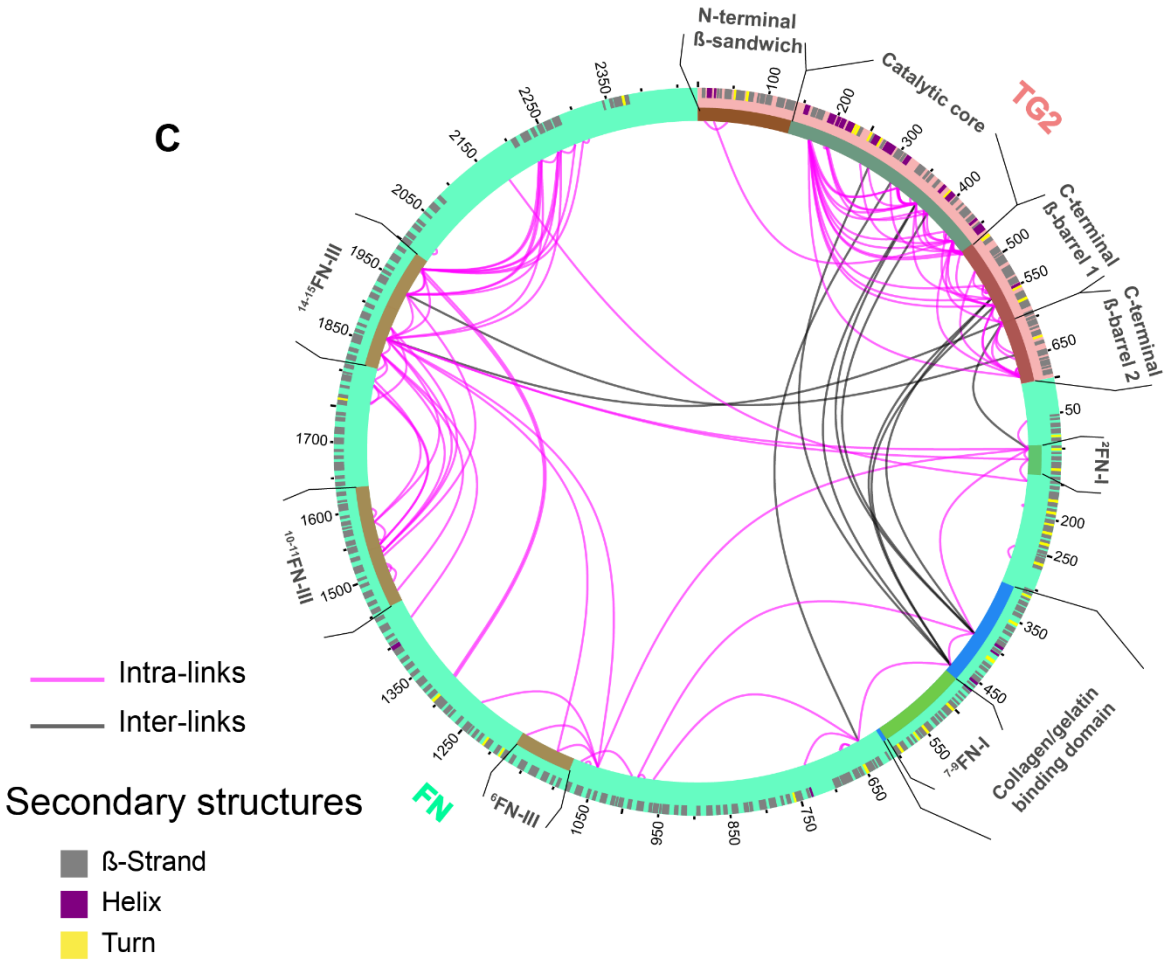

Figure 5.3.3: XL-MS of TG2 and 45 kDa-FN and TG2 and FN complexes using chymotrypsin as a protease. Circular diagrams show crosslinks identified from TG2/45 kDa-FN complex (top) and TG2/FN complex (bottom). Inter-protein crosslinks are shown in black and intra-protein crosslinks in magenta. **A:** The GBD is shown in bright colors and the rest of the FN is dimmed. Using chymotrypsin as a protease we were able to identify additionally crosslinked sites on Lys397 and Lys457 ($FNII_1$ and $FNII_2$ respectively, numbering for full-length FN). **B:** The C-terminal β-barrel 2 interacts with $FNIII_{14\text{-}15}$ (residues Lys1862 and Lys1936) and FNI_2 (residue Asp110). Simultaneously, $FNIII_{14\text{-}15}$ and FNI_2 regions are in close contact with each other, as shown by the magenta intra-links. **C:** Shows all crosslinks from A and B visualized together in one circular diagram. Crosslinks are mapped using FN monomer. Visualization was done with xVis Webserver[161].

6 TG2-FN complex: XL-MS guided integrative structural modeling and validation

The work presented has been published in Matrix Biology.

Kateryna Selcuk, Alexander Leitner, Lukas Braun, Fanny Le Blanc, Paulina Pacak, Simon Pot, Viola Vogel, **Transglutaminase 2 has higher affinity for relaxed than for stretched fibronectin fibers**, Matrix Biology, Volume 125, 2024, Pages 113-132, ISSN 0945-053X, https://doi.org/10.1016/j.matbio.2023.12.006

Author contributions: KS, VV conceived the study and designed the research. All FN fiber stretch experiments were performed by KS. Analysis of all confocal images and data visualization were performed by KS. FLB under supervision of AL performed all crosslinking experiments and data analysis. KS performed integrative structural modeling and docking with input from AL. PP performed calculation of solvent accessibility with NACCESS and contributed ideas to the discussion. KS, AL and VV wrote the manuscript.

6.1 Motivation.

The focus of this chapter is to generate predicted models of the TG2-FN complex at atomistic level by performing protein-protein docking guided by crosslinking mass spectrometry distance restraints.

6.2 Crosslink-guided structural modelling of TG2 and FN.

XL-MS not only identifies which regions of a protein complex are in close contact, but also provides valuable spatial information through physical distance restraints imposed by each crosslinker. The spatial information can be used for modelling and docking to determine the position and orientation of within a complex[162]. To determine the binding interface of the TG2-FN complex using low-resolution restraint data more accurately, we integrated the experimental crosslinks into a modelling pipeline[163,164] (**Figure 6.2.1**). We selected a few regions of FN for modelling based on criteria such as the availability of templates in PDB, coverage by crosslinks, and existing knowledge in the literature regarding binding sites. The regions that met these criteria, and were suitable for structural modelling, were $FNI_{2\text{-}3}$, $FNI_{7\text{-}9}$, $FNI_6FNII_{1\text{-}2}$ $FNI_{7\text{-}9}$ (GBD), and $FNIII_{14\text{-}15}$ (**Supplementary Note 1**). To build crosslink-guided models, we used the I-TASSER[165] and submitted experimental intra-protein crosslinks as distance restraints to structurally refine the available crystal structure templates, as was previously done[163]. To evaluate the compatibility of refined models with experimental restrains, we calculated Euclidean distances (ED) between β-carbons (CB-CB) of crosslinked residues using Xwalk[166]. We classify crosslinks into compatible and non-compatible based on the distance cut-off values[160,163]: ED for DSS < 35 Å, ED for DMTMM < 25 Å, ED for PDH < 35Å.

We identified 4 intra- and 3 inter-protein crosslinks for $FNI_{2\text{-}3}$. A high-resolution crystal structure of $FNI_{2\text{-}3}$ was available (PDB:2cg7), which we submitted as a template to I-TASSER for structural refinement with experimental crosslinks. After structural refinement, a high scoring model was selected, that satisfied all crosslinks within the distance cut-off (Supplementary Note 1). For FN's GBD, we detected 3 intra- and 8 inter-protein crosslinks. Templates covering $FNI_6FNII_{1\text{-}2}FN_7$ and $FNI_{8\text{-}9}$ domains, except for the short linker (513-516aa) between them, were

available as PDB:3mql and PDB:3ejh, respectively. However, our initial attempt to model the entire GBD with I-TASSER was not satisfactory. Thus we used ROBETTA[167] and AlphaFold[168] to determine the orientation of $FNI_6FNII_{1-2}FNI_7$ and FNI_{8-9} with respect to each other. To evaluate the quality of predicted models of GBD, we submitted them to QMEAN[169], which evaluates how the model performs in comparison to the experimental PDB structures. AlphaFold predicted that the GBD model outperformed the ROBETTA model (QMEAN Z-score=1.44 vs 1.86). This indicates better compatibility of the structural model predicted by AlphaFold than ROBETTA with the experimentally determined crosslinks. Consequently, we selected the AlphaFold predicted model of GBD for docking with HADDOCK[151].

Although we detected only one inter-protein crosslinks and no intra-protein crosslinks for the FNI_{7-9} domains, we included it in the modelling pipeline. FNI_{7-9} is well-known to be the high affinity binding region for TG2 and behaves as the whole 45-kDa GBD in mediating functions such as adhesion, spreading and migration[44]. To model FNI_{7-9}, we followed the same strategy we used for the GBD. The AlphaFold predicted model of FNI_{7-9} deviated less than one standard deviation from the experimental structures deposited in the PDB (QMEAN Z-score=0.64), whereas the ROBETTA predicted model deviated by two standard deviations (QMEAN Z-score=2.02). Therefore, we selected the AlphaFold predicted model of FNI_{7-9} for further docking steps, given its overall better performance (**Supplementary Note 1**).

We identified 11 intra- and 7 inter-protein crosslinks for $FNIII_{14-15}$ and submitted the high-resolution crystal structure of $FNIII_{14-15}$ (PDB:1fnh) along with crosslinks for structural refinement using I-TASSER. A high scoring model that satisfied 10/11 intra-protein crosslinks was selected. The non-compatible crosslink (Lys1862-Lys1936) connects two interdomain residues located on $FNIII_{14}$ and $FNIII_{15}$. As these two domains are connected by a flexible linker, it is expected that structural rearrangements might occur that favor a more closed conformation.

For TG2, we detected 46 intra-protein crosslinks, 8 of which violated the distance cut-off when we mapped them on the model. All the non-compatible crosslinks were between the interdomain residues. Specifically, 5 non-compatible crosslinks were between residues on the catalytic core and the C-terminal domain, 2 between residues on C-terminal domains, and 1 between N-terminal domain and the catalytic core (**Supplementary Note 1**). As these domains are connected by flexible linkers, non-compatible residues suggest that TG2 undergoes some structural rearrangement upon binding to FN in solution. After performing structural refinement, one notable improvement was residue Lys30, which on the available TG2 template (PDB:4pyg), did not comply with our solvent accessibility criteria **(Supplementary Note 1**). The Lys30 residue was previously shown by mutagenesis studies to be crucial for FN-binding[46]. After recalculation of the TG2 template using experimental intra-protein crosslinks, all three residues comprising the high-affinity FN-binding site (Lys30, Arg116, His134) satisfied the solvent accessibility criteria. Overall, by integrating experimental crosslinks as distance restraints, we were able to structurally refine available templates to be in better agreement with the experimental MS data.

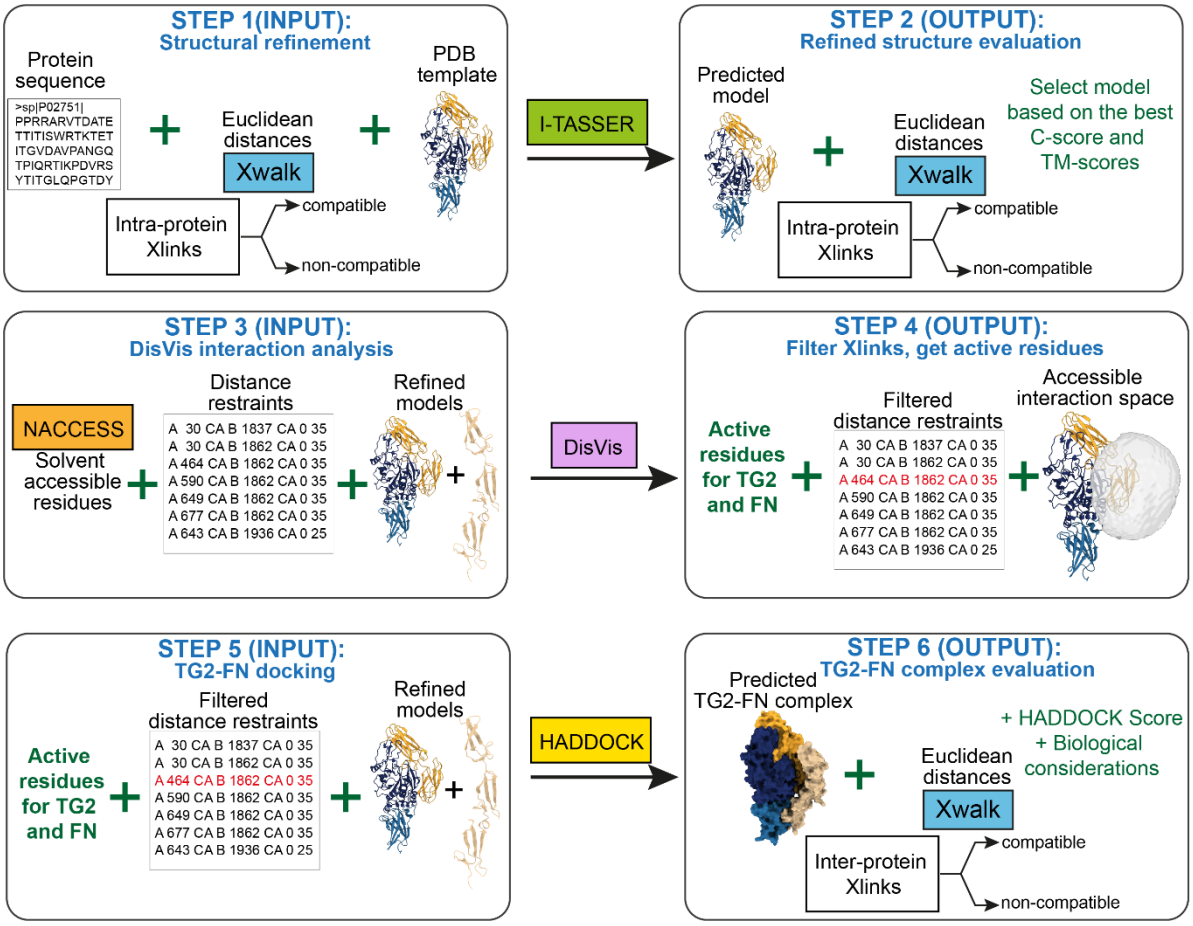

Figure 6.2.1: Schematic overview of the integrative structural modelling workflow of TG2 complexed to FN, which is presented in detail in Supplementary Note 1-3. (STEP 1- STEP2) Structure prediction and structure refinement: Structure prediction and structural refinement of available PDB templates was performed with I-TASSER[165]. At this step, PDB templates, corresponding amino acid sequences and experimental intra-protein crosslinks were submitted to I-TASSER. (STEP 1). Classification of crosslinks into "compatible" and "non-compatible" was performed with Xwalk[166] by calculation of Euclidean distances between the crosslinked residues. The best mode was selected for the next modelling steps based on the confidence score (C-score) and TM-score (STEP 2). **(STEP 3- STEP4) Analysis of accessible interaction space:** To predict active residues at the binding interfaces and to evaluate the compatibility of inter-protein crosslinks, DisVis[153] was employed. Solvent accessibility of residues on the refined models obtained from STEP 2 was calculated with NACCESS[170]. Only residues with a relative solvent accessibility of at least 40% for either the main chain or the side chain were selected. Refined models, solvent accessible residues, and inter-protein crosslinks in form of distance restraints were submitted to DisVis for analysis of accessible interaction space (STEP 3). Incompatible inter-protein crosslinks, if any, were excluded from further analysis; active residues at the predicted binding interface were obtained for the protein-protein docking step. **(STEP 5- STEP6) Protein-protein docking:** Active residues, filtered inter-protein crosslinks in form of distance restraints and refined models were submitted to HADDOCK[171] for docking. The best models of predicted protein complexes were selected based on the HADDOCK score and compatibility of experimental crosslinks with resulting models.

6.3 Crosslink-guided HADDOCK docking of TG2 with FNI_{7-9} revealed a parallel alignment of FN's type I modules with TG2's C-terminal β-barrels.

Protein complexes in solution are typically dynamic, and crosslinks can reflect an averaged ensemble of conformations. However, non-compatible crosslinks that may belong to an alternative complex conformation can negatively impact the accuracy of docking results. To address this issue, we utilized the DisVis webserver, which filters out non-compatible crosslinks and predicts key residues involved in binding at the interaction interface using experimental crosslinks[153]. Our analysis using DisVis highlighted three putative incompatible crosslinks, namely the Lys319(TG2)-Glu116(FN) crosslink between TG2 and FNI_{2-3}, the Lys550(TG2)-Lys397(FN) crosslink between TG2 and FN's GBD, and the Lys464(TG2)-Lys1862(FN) crosslink between TG2 and $FNIII_{14-15}$ (**Supplementary Note 2**). While it is important to note that these crosslinks may not necessarily be false and are likely to belong to an alternative conformation of the complex, we did not further investigate this possibility due to the insufficient number of crosslinks. Therefore, we excluded these crosslinks from further docking steps with HADDOCK to improve the accuracy of the docking results.

To identify the putative active residues at the binding interface, we filtered out the residues with less than 40% relative solvent accessibility for the backbone or side chain using NACCESS[170], and then used DisVis interaction analysis to predict active residues at the binding interface consistent with submitted experimental crosslinks (**Supplementary Note 2**). Active residues, along with confirmed crosslinks mutually compatible after selection by DisVis, were submitted for separate docking runs with HADDOCK for the TG2 and FNI_{2-3}, TG2 and FNI_{7-9}, TG2 and $FnIII_{14-15}$, TG2 and GBD complexes, respectively (**Supplementary Note 3**). After docking, we mapped crosslinks of predicted models and used Xwalk to calculate distances between crosslinked residues to identify any non-compatible crosslinks. The models of TG2-FNI_{2-3} and TG2-$FNIII_{14-15}$ complexes satisfied all crosslinks that were submitted to guide docking, and the models with the highest HADDOCK score were selected (**Figure 6.3.1**). In the case of the TG2-FN_{7-9} complex, we guided docking by a single crosslink, which was compatible on all resulting models, thus we selected the model with the highest HADDOCK score. Notably, one of the predicted models of the TG2-FN_{7-9} complex supported the parallel alignment of FNI_{8-9} with the C-terminal β-barrels of TG2, while FNI_7 was aligned with the high-affinity site on the N-terminal domain of TG2 (Lys30, Arg116, His134) (Fig 6C). This docking pose strongly supports the hypothesis of multivalent binding and suggests an underpinning structural mechanism that can indeed explain the mechano-regulated TG2 binding to fibrillar FN.

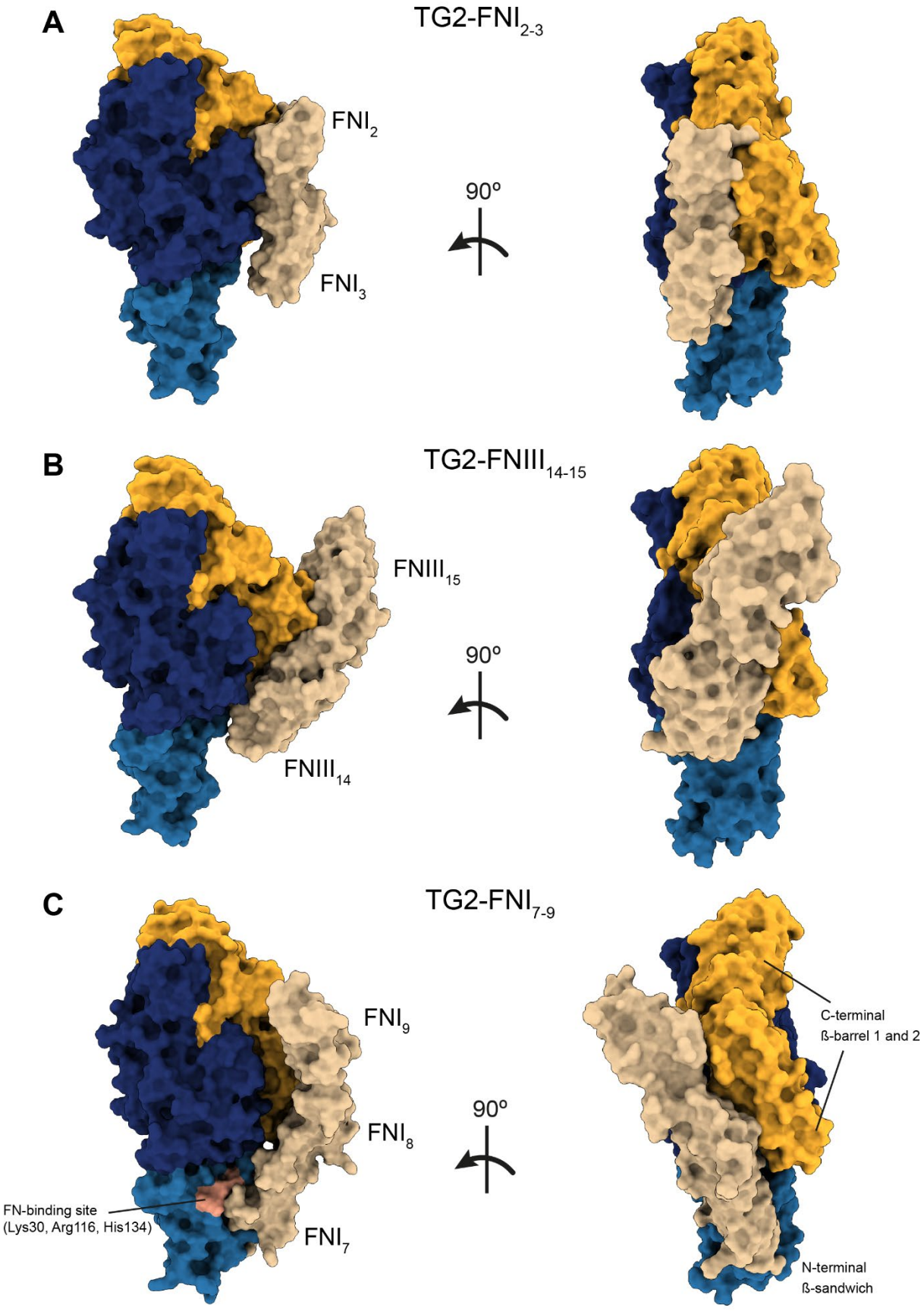

Figure 6.3.1: Protein-protein docking with HADDOCK of TG2 complexed with selected FN fragments guided with experimental crosslinks as distance restraints. Predicted models of **(A)** TG2 in complex with FNI_{2-3}. **(B)** TG2 in complex with $FNIII_{14-15}$, and **(C)** TG2 in complex with FNI_{7-}

$_{9}$. The resulting docking pose of the TG2-FNI$_{7-9}$ complex supports parallel alignment of FNI$_{8-9}$ with the C-terminal β-barrels of TG2, while FNI$_{7}$ is in contact with the canonical FN-binding site (Lys30, Arg116, His134, colored pink) on the N-terminal β-sandwich. Full data set with mapped crosslinks is available in Supplementary Note 3 and Supplementary Fig. 15-17.

6.4 Collagen-mimicking peptide R1R2 and TG2$_{GDP}$ compete for binding to FN fibers.

To better understand the results of the XL-MS experiments, where we used soluble FN in a compact conformation, in relation to the results from the FN fiber stretch assay, in which FN was in fibrillar form, we sought to validate the predicted model for the TG2-FN complex. Previous studies had mapped the TG2's as well as the collagen's binding sites on FN within its 45-kDa GBD[49,144], comprising FN's domains FNI$_{6}$FNII$_{1-2}$ FNI$_{7-9}$. Although both binding partners interact with several FN modules, FNI$_{8}$ appears to be particularly important for collagen as well as for TG2 binding[44,144]. Our predicted model of the TG2-FNI$_{7-9}$ complex suggested an overlap between TG2 and collagen-binding sites on FNI$_{8}$ within the GBD. To validate this model, we investigated whether simultaneous binding of TG2 and collagen to fibrillar FN is possible. To test this, we utilized the R1R2 collagen-mimicking peptide, which is derived from the FN-binding protein of the pathogen *Streptococcus equi*[172]. Both R1R2 and collagen share a conserved GEXGE motif which has been shown by crystallography to bind to FNI$_{8-9}$, and in accord with this R1R2 inhibits binding of FN to collagen I[144,173]. We could furthermore show previously that the R1R2 binding motif on FN is destroyed by stretching FN fibers[61].

To assess the influence of collagen binding, we added increasing concentrations of R1R2 peptide to 100 µg/ml of TG2$_{GDP}$ in 1 mM GDP, 1 mM EDTA, 1 mM $MgCl_2$ in 50 mM Tris and incubated on FN fibers under low strain for 1 h. This R1R2 titration series revealed a dose dependent reduction of TG2 binding to FN, indicating that R1R2 can indeed disrupt the specific interactions between TG2$_{GDP}$ and FN fibers under low strain (Fig. 7A). Next, we tested how TG2 would bind FN fibers in the presence of 100 µM R1R2 at all strains. Indeed, in the presence of high concentrations of R1R2, TG2 weakly, but equally bound to FN fibers at all strains (Fig. 7B). Interestingly, the addition of 100 µM R1R2 further significantly reduced TG2$_{GDP}$ binding to the FN fibers under high strain, indicating that TG2 and R1R2 are still competing for the remaining specific binding sites on FN (Supplementary Fig. 12). We previously reported that FN fibers under high strain are more prone to non-specific interactions due to the exposure of hydrophobic sites[121]. Our findings thus confirm that the binding of TG2 to the FN fibers under high strain is still specific, but weaker as the ensemble of destroyed binding epitopes increases by stretching FN fibers. Therefore, our data demonstrate for the first time that the collagen-mimicking peptide R1R2 and TG2 directly compete on fibrillar FN under low as well as high fiber strains.

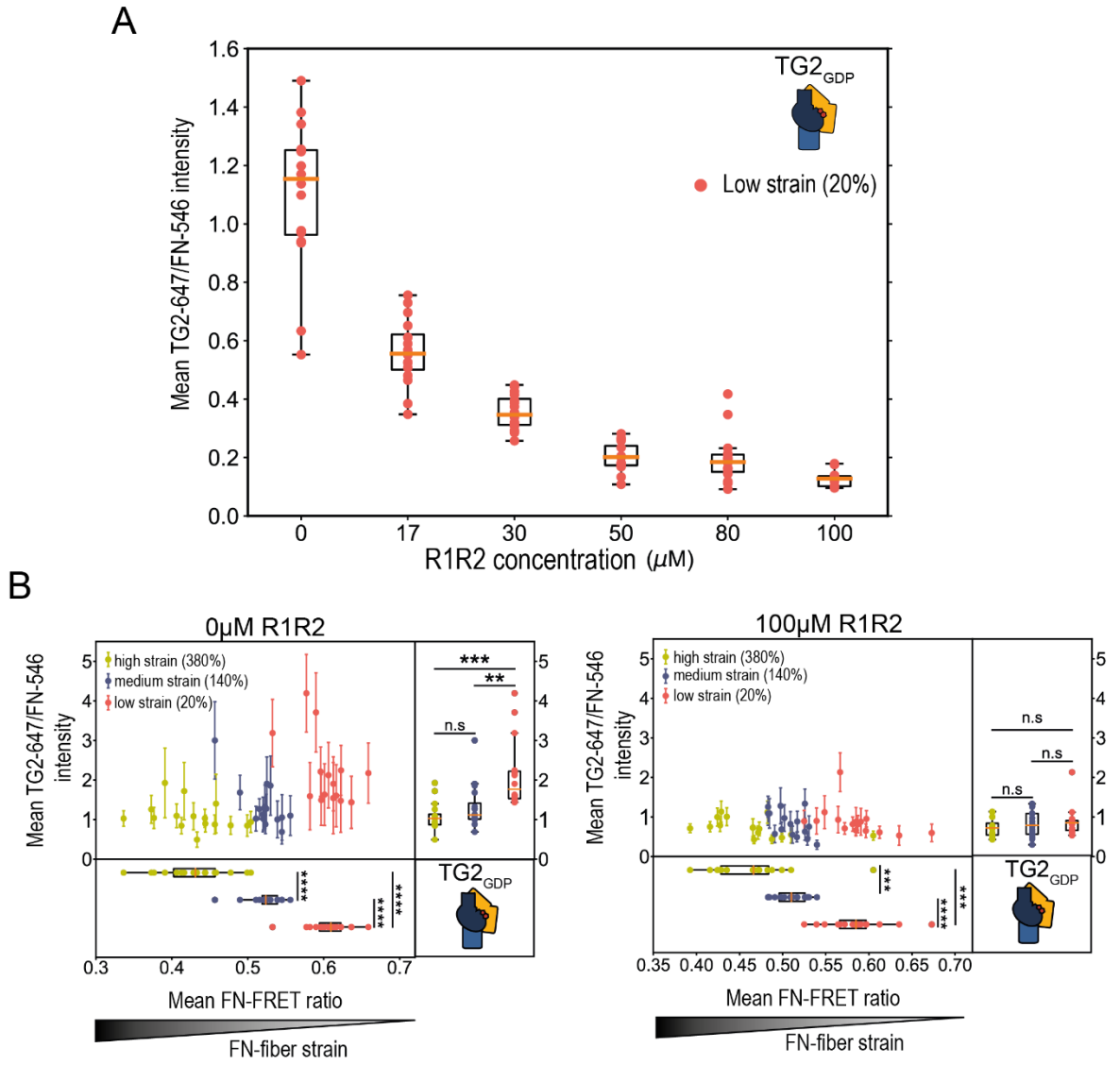

Figure 6.4.1: FN fiber stretch assay reveals a dose-dependent competition between the collagen-mimicking peptide R1R2 and WT gpTG2$_{GDP}$ for binding to FN fibers under high, as well as low strain. A: In the presence of increasingly higher concentrations of R1R2, which targets FN's GBD, TG2$_{GDP}$ binding to the FN fibers under low strain reduces in a dose-dependent manner. **B:** Saturating concentrations of R1R2 abolished mechano-regulated TG2 binding to FN, thus limiting TG2 binding to its known canonical binding site. In the presence of 100 µM R1R2, TG2 bound equally to FN fibers under high, medium, and low strain. 15 fibers were analyzed per membrane strain. Statistical significance was computed with Wilcoxon rank-sum statistic for two samples. P-values: (*0.01≤ p <0.05; **0.001≤ p <0.01; ***10-5≤ p <0.001; ****10-6≤ p <10-5; ***** p <10-6)

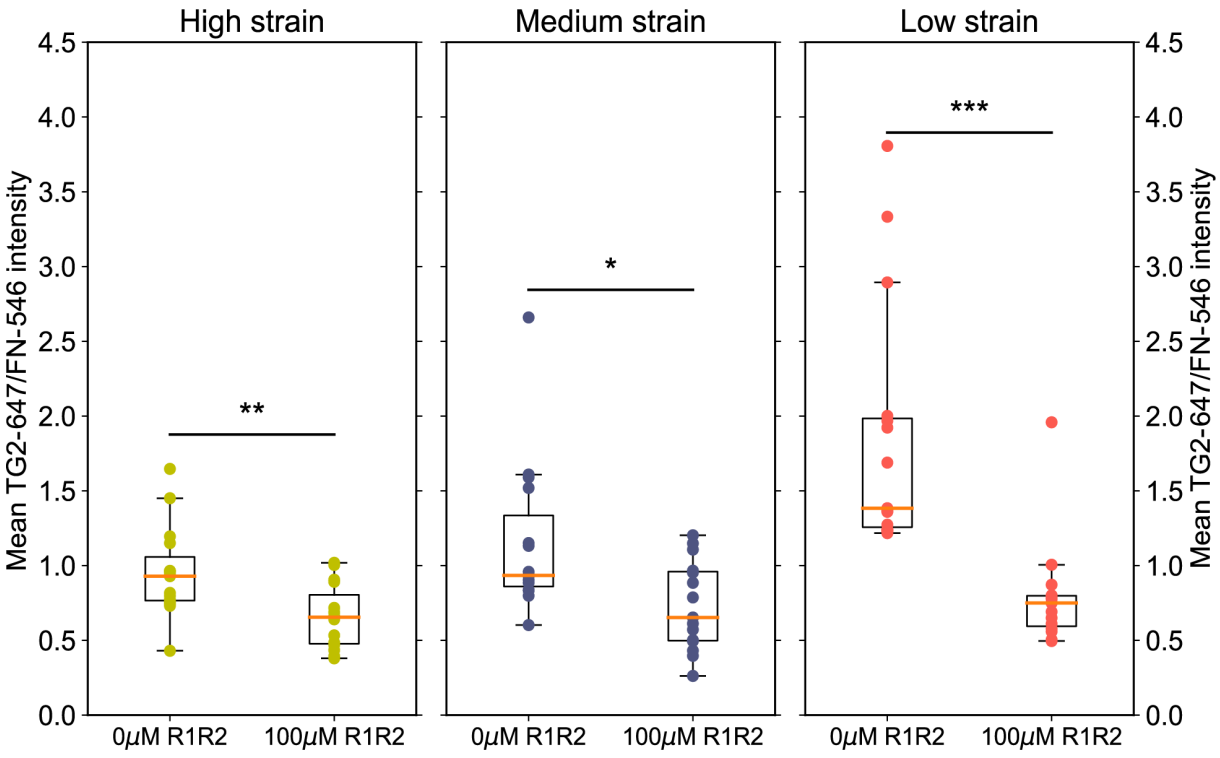

Figure 6.4.2: Competition FN fiber stretch assay between the collagen-mimicking peptide R1R2 (Streptococcus equi) and WT gpTG2 in the presence of 1mM GDP and 1mM EDTA. Means of TG2-647/FN-546 intensity shown in Fig.7C were replotted as boxplots to make comparisons between $TG2_{GDP}$ binding in the presence of 0μM R1R2 and 100 μM R1R2, when FN fibers experience the same strain. Mechanical stretching of FN fibers reduced their affinity for $TG2_{GDP}$ due to the destruction of many TG2 binding sites on FN. Addition of 100 μM R1R2 further significantly reduces $TG2_{GDP}$ binding affinity to FN fibers experiencing high (380%), medium (140%) and low (20%) strains. 15 fibers were analyzed per condition. Statistical significance was computed with Wilcoxon rank-sum statistic for two samples. P-values: (*0.01≤ p <0.05; **0.001≤ p <0.01; ***10-5≤ p <0.001; ****10-6≤ p <10-5; ***** p <10-6)

7 Significance and conclusions

7.1 Implications and outlook.

This study has addressed for the first time whether TG2's interaction with fibrillar FN might be regulated by the tensional state of FN fibers. Using an in vitro FN fiber stretch assay and a FN-FRET nanoscale strain sensor, we found that TG2 binds more strongly to relaxed FN fibers than to stretched FN fibers (**Figure 4.2.2**). This mechano-regulated binding is dependent on the spatial proximity of TG2's C-terminal β-barrels to its N-terminal domain, as demonstrated by experiments involving C-terminal β-barrel deletions, calcium, inhibition with Z-DON, and oxidation (**Figure 4.3.2**). Importantly, we also confirmed that TG2's mechano-regulated FN binding does not require its catalytic activity, but is dependent on its conformations, as shown with the Cys277Ser TG2 inactive mutant (**Figure 4.4.1**). Notably, TG2's binding affinity varies not only with fibrillar FN, but also with surface-adsorbed FN, which has a more compact conformation (**Figure 5.2.1**). Again, TG2's conformation and the presence of its C-terminal β-barrels are critical for this binding, and TG2's binding affinity to a 45-kDa FN fragment decreased drastically compared to full-length FN (**Figure 5.2.1**).

This finding is remarkable, as it contrasts with a previous study that reported TG2 binding to the GBD with the same affinity as full-length soluble FN[49]. However, the contrasting result can likely be explained by the fact that the TG2 binding between FN's GBD and full-length FN was not compared in terms of equivalent numbers of binding sites available to TG2 in that previous study. Collectively, these results indicate that the C-terminal domains of TG2 support its interaction with FN, in synergy with N-terminal domain, and that this interaction thus enhances TG2's affinity to FN beyond the known GBD interaction. This conclusion was confirmed by XL-MS, which showed that TG2's C-terminal β-barrels interact with regions of FN outside of the canonical GBD region, specifically with FNI_2 and $FNIII_{14\text{-}15}$ (**Figure 5.3.1**). Notably, an earlier study using rotary shadowing electron microscopy reported a possible TG2 binding to $FNI_{4\text{-}5}$ regions alongside the conventional GBD[145]. However, subsequent studies were not able to detect this interaction, possibly due to the use of separate FN fragments as opposed to mapping synergistic site localization[44,45,47]. Our XL-MS result is highly significant, since studies that aim to develop small molecule inhibitors of TG2-FN interaction often utilize 45-kDa FN GBD instead of the full-length FN[33,34]. While our XL-MS data did not definitively indicate whether TG2's C-terminal domains interact with $FNI_{2\text{-}3}$ and $FNIII_{14\text{-}15}$ simultaneously, such simultaneous interaction is suggested by spatial proximity of $FNI_{2\text{-}3}$ and $FNIII_{14\text{-}15}$, as is evident from numerous inter-protein crosslinks within FN connecting those two regions (**Figure 5.3.1**).

Using XL-MS and crosslink-guided structural modeling tools, we have shown that TG2 residues on both N-terminal β-sandwich and C-terminal β-barrels are predicted to interact with FN, but only when TG2 adopts a closed conformation (**Figure 6.3.1**). It is important to note that a compact conformation of soluble FN, which was present in our XL-MS experiments must be distinguished from fibrillar FN. When FN is in the soluble compact conformation, $FNI_{2\text{-}3}$ and $FNIII_{14\text{-}15}$ modules are brought in spatial proximity attracted by long-range electrostatic interactions, but are spatially separated when FN assumes a fibrillar form[52]. However, since FN molecules are not periodically arranged in FN fibers, yet are closely-packed[54,156], $FNI_{2\text{-}3}$ and $FNIII_{14\text{-}15}$ modules from neighboring molecules could happen in some locations to be at the right distance. Additionally, one of the predicted docking models of TG2 with $FNI_{7\text{-}9}$ suggested parallel alignment of the $FNI_{8\text{-}9}$ modules with the C-terminal β-barrels of TG2, while FNI_7 was

in contact with the main FN-binding site (Lys30, Arg116, His134) on TG2's N-terminal domain (**Figure 6.3.1**). Such an orientation would also allow for additional stabilizing contacts between TG2's C-terminal domains and fibrillar FN and could mediate the mechano-regulated binding between TG2 and FN-fibers. Therefore, it is possible that mechano-regulated TG2 binding to FN-fibers is mediated by synergistic interactions of C-terminal TG2 domains with FNI_{2-3}, FNI_{8-9} and/or $FNIII_{14-15}$ modules, offering multiple options for the high affinity interaction that we observed in our FN-fiber stretch assays. FN fiber stretching might thus destroy TG2's multivalent binding motif that is comprised of several FN modules, i.e., by increasing the relative distance between FNI_7, FNI_8 and FNI_9. While TG2's N-terminal residues Lys30, Arg116, His134 bind to FNI_7 with high affinity, we propose here that TG2's C-terminal domains can further enhance this interaction by simultaneously binding to FNI_8 and FNI_9, however, only when FN is in an unstretched conformation (**Figure 7.1.1**). Additional interactions of TG2's C-terminal domains with other multidomain fragments of FN, i.e., with $FNI_{2–3}$, or with $FNIII_{14–15}$, might also stabilize FN-TG2 complexes as revealed by XL-MS followed up by structural modelling (**Figure 6.3.1**). While MS averages over large populations of inter-protein interactions, structural modelling suggests that the C-terminal binding interface of TG2 with $FNI_{2–3}$ and $FnIII_{14–15}$ might partially overlap. Note furthermore, that these binding epitopes are also prone to get disrupted by FN fiber stretching as well, as stretching increases the relative distances of these tandem FN modules too and thus the multivalent binding motif with TG2.

When discussing TG2 localization outside of the cell, two distinct pools of TG2 are typically noted: TG2 located on the cell surface and TG2 located in the ECM, which appear to perform different functions and interact with different binding partners[19]. On the cell surface, where TG2 acts as an adhesion co-receptor for FN[21], it primarily associates with integrins and the heparan sulfate proteoglycan syndecan-4, forming ternary and/or quaternary adhesive complexes with FN[19,20,174]. Recent advances in understanding of TG2-syndecan-4 interactions, as mediated by its heparan sulfate chains, suggest that this interaction stabilizes TG2 in a closed conformation, thanks to a composite binding site consisting of two clusters that form a single high affinity heparin-binding site when brought in proximity in a closed conformation[97,98]. This is highly relevant to our findings, suggesting that Syndecan-4 could stabilize TG2 in the closed conformation, when in heterocomplex with FN, despite high (millimolar) Ca^{2+}concentrations. These quaternary complexes of FN, TG2, Syndecan-4 and β1-integrins are veritable signaling hubs and can elicit more robust downstream RhoA-ROCK activation and profibrotic signaling effects, amongst others[174,175]. Formation of a heterocomplex between FN-TG2 and β1-integrins, contributes to cell survival and has been implicated in several pathologies. For instance, TG2 enhances ovarian cancer cell anchoring to fibronectin, promoting metastasis[110]. In breast cancer, cooperation between TG2, integrins, and fibronectin enhances cell attachment, invasion and survival[28]. In the ECM of multiple sclerosis lesions, TG2 enhances adhesion and migration of astrocytes on fibronectin in the ECM, which contributes to glial scarring[115,116]. Noteworthy, TG2 also promotes FN-fiber deposition in multiple sclerosis lesions[117,118] and in glioblastoma[111]. Independent studies utilized the irreversible inhibitor KCC009[100], which targets TG2 enzymatic activity, to block TG2-mediated adhesion and migration of astrocytes on FN in multiple sclerosis[115,116], as well as the deposition of FN matrix in glioblastoma both *in vitro* and *in vivo*[111], and in multiple sclerosis lesions by astrocytes[117].

Our new synergistic binding model can also explain some other unresolved observations in the literature. Although the precise mechanism of KCC009 interference with TG2-FN interactions remains unclear, this small molecule inhibitor irreversibly binds to the active site Cys277 of TG2, inactivating TG2 and trapping it in an open extended conformation[94], similar to Z-DON inhibitor used in our study. The ability of KCC009 to disrupt TG2-mediated adhesion to FN cannot be solely attributed to the blocking of TG2 enzymatic activity, since TG2-FN adhesive interactions are independent of TG2 crosslinking activity[45]. It was furthermore discussed that TG2's ability to cooperate with integrins to enhance deposition of FN-fibers does not require enzymatic TG2 crosslinking[24] and that the "anti-adhesive" effect of KCC009 cannot be explained by direct blocking of the binding interface of TG2 and FN, as KCC009 does not bind directly at the TG2-FN binding interface[100]. However, our findings might suggest a mechano-regulated mechanism as KCC009 traps TG2 in the open conformation, similarly to Z-DON, disrupting TG2's multivalent FN binding site and thereby reducing the affinity of TG2 for FN.

In the ECM, TG2 predominantly co-localizes with the FN matrix, although to a lesser extent, TG2 may also associate with other non-FN interaction partners, such as collagen VI[107]. Unlike on the cell surface, TG2 in the ECM is likely to adopt an open, effector-free conformation due to oxidation and the formation of a Cys370-Cys371 disulfide bridge[40].

TG2 might furthermore multimerize in extracellular space. SAXS measurements by Singh *et al.* demonstrated that constitutively open TG2 mutants form homodimers in solution[89]. The fit of TG2 in the extended conformation into the envelope suggests that the two monomers dimerize in an overlapping head-to-tail configuration. Another independent study found that homodimer formation in wild type TG2 is increased at higher temperatures[176]. The authors also used SAXS to measure the multimerization state of TG2 and similar to Singh *et al.,* found that the fitting into the SAXS envelope resulted in a head-to-tail homodimer configuration. It can be speculated that a fraction of TG2 in this dimeric state could be immobilized on FN-matrix fibrils in the ECM and be stored there in inactive state until the requirement for TG2 crosslinking arises to stabilize the matrix in case of injury. As we previously discovered that FN fibers are highly stretched under homeostasis in most healthy organs[177], this suggests a plausible stabilizing mechanism for storing inactivated oxidized TG2 dimers bound with lower affinity to stretched than to relaxed FN-matrix fibers. As FN fibers get mechanically cleaved at sites of injury, or proteolytically cleaved at sites of inflammation, the structurally relaxed FN will compete effectively for TG2 binding. We thus propose here that this tension dependent switch might allow TG2 storage in ECM of healthy organs, and for fast recruitment of TG2 to damaged FN fibers in case of injury. Supporting this idea, it has been shown that TG2 bound to FN-matrix can be reduced by the enzymatic activity of Thioredoxin and recruited in this way for the crosslinking activity of matrix proteins[85]. Also, the FN bound closed state TG2 can readily form quaternary cell surface complexes with Syndecan-4 and β1-integrins with profibrotic signaling effects supportive of wound healing and tissue stabilization[174,175,178]. Future research should investigate whether the TG2 homodimer can bind fibrillar FN and if such binding can be regulated by FN-fiber strain.

Bringing our findings that TG2 binding is modulated by FN fiber tension together with the existing literature, we propose a novel model of mechano-regulated TG2-FN interactions and how this might tune TG2's catalytic activity (**Figure 7.1.1**). TG2 is inactive when TG2's N-

terminal and C-terminal domains are in spatial proximity due to GDP/GTP binding and/or when TG2 interacts with syndecan-4[98]. We propose here that TG2 and FN can form additional interactions due to the C-terminal β-barrels making synergistic contacts with $FNI_{8–9}$, while TG2's N-terminal domain interacts with FNI7 (**Figure 7.1.1 A**) and/or $FNI_{2–3}$ and $FNIII_{14–15}$. Upon FN fiber stretching, the multivalent binding motif is disrupted by, for example, increasing distances between FNI_7, FNI_8 and FNI_9 modules, therefore reduced affinity interactions can be formed (**Figure 7.1.1 B**). When TG'2 C-terminal domains move away due to calcium binding (**Figure 7.1.1 C**) or oxidation (**Figure 7.1.1 D**), it forms reduced affinity interaction with FN, since C-terminal domains are out of reach. Finally, we propose that oxidized TG2 could form high affinity interactions with adjacent FN fibers due to dimeric TG2 association thus perhaps serving as physical crosslinker as well (**Figure 7.1.1 E**). In this case, spatial proximity between C-terminal and N-terminal domains could be achieved locally within such homodimer. More research is required to establish the physiological role of this homodimer and its binding mode to fibrillar FN.

Therefore, our results indicate that, like for Syndecan-4, the FN-binding epitope on TG2 is composite and conformational. Interestingly, studies have identified anti-TG2 autoantibodies that induce a shift in a pool of effector-free TG2, either toward the "closed" or "open" conformation, depending on the epitope on TG2 to which they bind[41,92]. Although the exact reasons are not known, this could be a common regulatory mechanism shared by many TG2 binding partners to exert an effect on TG2 conformation and thereby, its function. Our findings shed light on the role of the TG2-FN complex in cell-ECM interactions in various physiological processes.

In an *in vitro* microtissue culture assay, we recently observed that cellular decision-making occurs when FN fiber tension switches from highly stretched in the microtissue growth region that is rich in myofibroblasts, to relaxed fiber tension in the collagen rich maturing core region that is rich in fibroblasts. A well-tuned tenascin-C, TG2, and matrix metalloprotease driven matrix remodeling activity was crucial to mediate the myofibroblast-fibroblast transition, as well as for tissue repair in this in vitro model[179]. We also recently demonstrated that tumor tracks are bordered by an endothelial-like basement membrane and are enriched in low-tension FN fibers, which correlates with high tenascin-C content[180]. It can be speculated that in this transition zone the mechanosensitive TG2 storage and release mechanisms and mechanosensory regulation of cellular behavior are to be of great significance. As such, our findings that the interaction of TG2 with FN is tuned by its fiber tension is highly significant.

Our observation that the collagen-mimicking peptide R1R2 and TG2 directly compete for the same binding site on fibrillar FN suggests that the composition of the ECM affects the interaction of its components, and that an elevated collagen content will decrease TG2-FN binding in the ECM. This is interesting, since a high collagen-low fibronectin ratio was identified as a potential driver behind the observed reversion of scar tissue myofibroblasts into fibroblasts in 2 and 3D cell culture[179,181]. Through the assembly of a dense collagenous matrix, myofibroblasts were suggested to create an ECM niche that favors their own downregulation, setting the stage for tissue homeostasis and regenerative remodeling. FN-binding driven shifts in "closed" or "open" conformation TG2 availability, TG2 modulated storage and release of TGFβ1 in the ECM[182,183], and TG2-driven cell-ECM interactions are possible underlying mechanisms for this observation.

The ECM is a very complex environment that consists of a multitude of structural, supportive, and soluble factors, representing biophysical and biochemical stimuli that present a plethora of simultaneous triggers and regulators of cell behavior. Also, assembly, crosslinking, degradation and remodeling of the ECM are complex processes with critical effects on its various physical traits, including plasticity, viscoelasticity, solid tissue stress, tissue stiffness and microarchitecture, that guide normal and aberrant (neoplastic and fibrotic) tissue development[184]. This notion is underlined by the wide variety of strategies attempted to inhibit tumor stroma and scar fibrosis, including epigenetic modulators, and inhibitors of ECM crosslinking, mechanotransduction and integrin-mediated TGFb activation[185]. The FN fiber stretch assay used in the experiments presented here must therefore be viewed as a reductionist method, where the effects of modulating single elements can be evaluated at a time.

Beyond its well described function, our data suggest that TG2 can serve as a FN fiber strain sensor, thereby modulating cell-ECM interactions depending on the tensional state of ECM fibers, including cell adhesion, spreading and migration, as well as cell phenotype modulation. And reciprocally, FN-fibers could serve as a reversible ECM storage space for TG2. These properties of the TG2-FN interaction would thereby modulate tissue responses in homeostasis, tissue growth and repair, as well as under pathological conditions, including fibrosis and cancer.

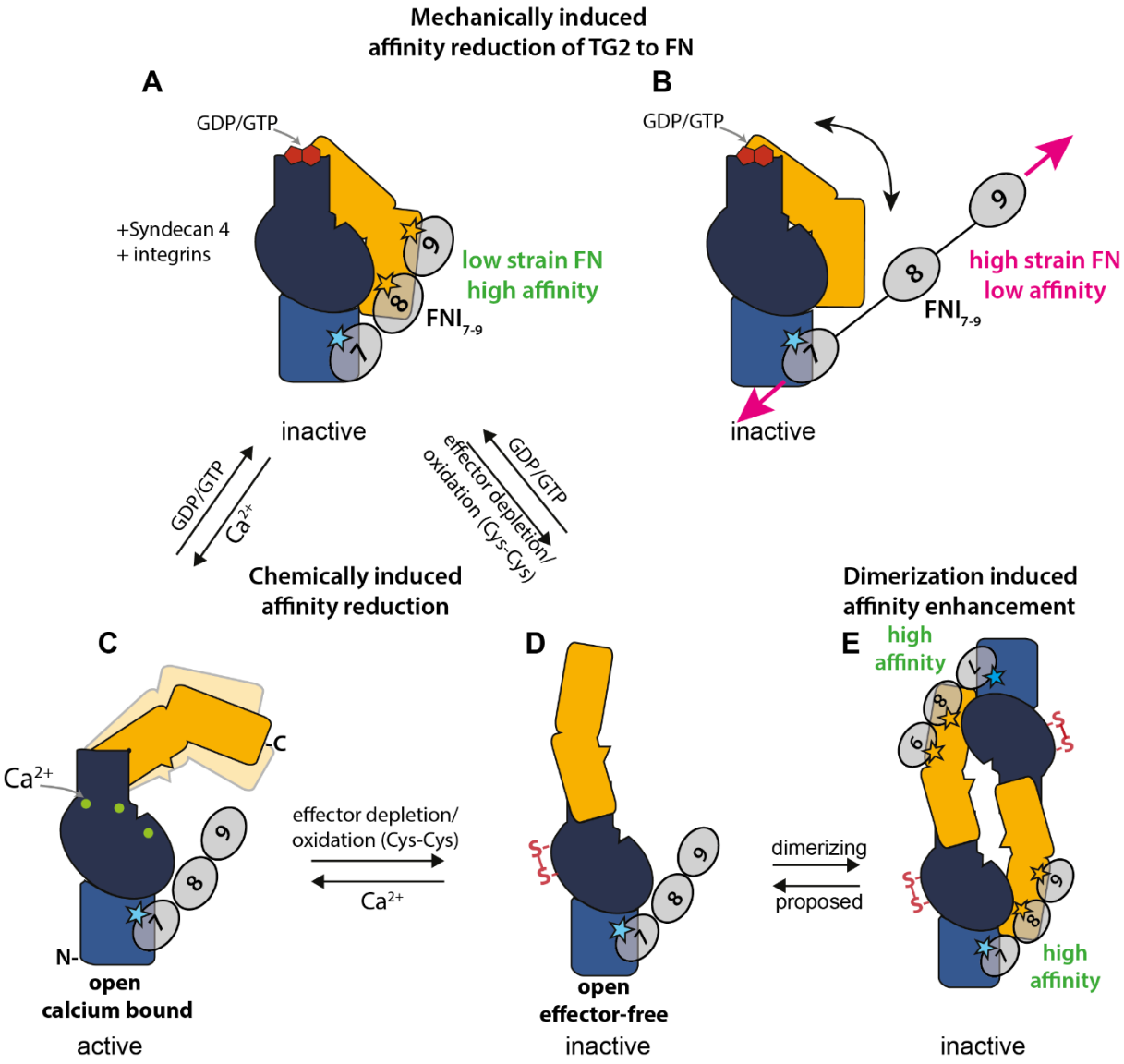

Figure 7.1.1: Sketch illustrating the proposed model of TG2's mechano-regulated binding to FN fibers.A, C, D: TG2 interacts differently with FN fibers depending on the conformational state of TG2 and **(B)** tensional state of FN fibers. **(A): TG2 in its compact and inactive conformation.** When TG2's N-terminal β-sandwich is in spatial proximity to its C-terminal β-barrel 2, FNI_7 to the N-terminal domain of TG2 (light blue), while the tandem domains $FNI_{8–9}$ bind to TG2's C-terminal domains (yellow), enhancing synergistically the interaction. **(B) Mechanically induced affinity reduction.** When mechanical forces acting on FN fibers stretch the FN modules apart, the multivalent TG2-FN interactions are destroyed and TG2 can bind FN only via its canonical binding site. **(C): Chemically induced affinity reduction by calcium binding.** Calcium binding causes C-terminal β-barrels to move away from the N-terminal domain, and TG2 assumes distinct open states that are catalytically active. In this case, TG2's C-terminal β-barrels are out of reach and FN can bind only to TG2's N-terminal β-sandwich domain, forming a lower affinity interaction. **(D) Chemically induced affinity reduction by formation of a disulfide bond redox-sensitive cysteines (Cys230, Cys370, Cys371).** Oxidation of TG2 in the ECM inhibits its catalytic activity. Although oxidized TG2 adopts the open conformation (effector-free), it could still form a high affinity synergy interaction with FN through dimeric TG2 association. **(E) Dimerization**

induced affinity enhancement. Spatial proximity between N-terminal and C-terminal domains could be achieved locally, in which case the domains would be provided by two different TG2 molecules of a TG2 homodimer. Parallel alignment of $FNI_{7–9}$ modules with TG2's C-terminal β-barrel domains was predicted by crosslink-guided docking.

7.2 Study limitations and future directions.

The FN fiber stretch assay employed in this study has proven to be a powerful tool, allowing us to gain mechanistic insights into the novel mechano-regulated interactions between TG2 and FN under controlled conditions. This approach offers several distinct advantages, including the ability to easily correlate ligand binding with the mechanical strain of FN fibers due to their homogeneous diameter and non-interwoven nature. However, it is important to acknowledge the limitations of this cell-free method and consider potential avenues for future research.

One crucial area for future exploration involves investigating TG2 interactions with cell-derived FN matrices. These matrices, assembled by fibroblasts in cell culture, can be generated by introducing exogenous plasma FN. To better mimic the physiological extracellular matrix (ECM), the addition of L-ascorbic acid can stimulate collagen production, while growth factors like TGF-β can replicate wound healing conditions. Fibroblasts can assemble ECM matrices rich in FN and collagen within just a few days[186]. The incorporation of FRET-based mechanical strain sensors into these cell-derived scaffolds would enable the monitoring of the mechanical strain experienced by FN within the matrix. Furthermore, this system could be extended to investigate exogenously added TG2 interactions with various ECM components, such as collagen I, collagen IV, heparin, and FN itself.

Another challenge encountered in this study pertains to the use of XL-MS to analyze the TG2-FN complex. The multidomain structure of FN dimers and the existence of multiple isoforms due to alternative splicing complicated the identification of peptides and crosslinked residues. Currently, UniProt lists 17 isoforms of FN generated by alternative splicing, with variations in the variable (V) region and the inclusion or exclusion of the two extra domains (**Figure 2.6.1 A**). Although isoform 1 (Uniprot: P02751-1) was confidently identified, the presence of other FN isoforms could not be entirely ruled out, introducing potential ambiguity in attributing crosslinks. While utilizing recombinantly produced FN could resolve this issue, it would come at the cost of lacking post-translational modifications present in naturally isolated FN.

Additionally, for integrative structural modeling purposes, it was necessary to assume that FN behaved as a monomer, even though plasma FN exists as a dimer in solution. This assumption was made due to the difficulty in distinguishing crosslinks formed within a single FN monomer from those formed between two monomers of a dimer.

While this study has contributed to our understanding of the TG2-FN binding interface, the structural base of TG2 interactions with β-integrins or Syndecan 4 remains disputed. Future investigations might consider more advanced techniques to explore the binding interface of the TG2-FN-β-integrin ternary complex and even the TG2-FN-β-integrin-Syndecan 4 quaternary adhesive complexes. Knowledge of the binding interfaces of these ternary and

quaternary adhesive complexes holds significant potential for gaining mechanistic and structural insights into the pathological mechanisms they may drive in disease progression, for example, in promoting cell survival in transformed cells. This knowledge could also pave the way for the development of novel therapeutic approaches aimed at blocking these interactions in pathological conditions.

However, it is crucial to recognize that mapping the binding interfaces of such large, flexible protein assemblies presents a formidable challenge, particularly when polysaccharides are involved. XL-MS possesses several advantages for elucidating the binding interfaces of heterogeneous protein complexes and large protein assemblies. Firstly, it does not require the formation of well-ordered crystals, a common challenge in crystallography. XL-MS can be performed in solution, allowing for the study of proteins in their native states and biologically relevant conformations. Secondly, it can capture transient or weak interactions within a protein complex, providing insights into dynamic processes that other techniques might miss. Lastly, XL-MS is well-suited for examining structural heterogeneity and dynamics, which can be particularly challenging for crystallography. This technique's ability to capture transient interactions and accommodate the flexibility of large assemblies makes it a valuable tool for studying the conformational variability and dynamic interactions that underlie complex biological processes.

In conclusion, while this study has made significant strides in elucidating the mechanistic details of TG2-FN interactions, future research offers the potential to deepen our understanding of protein interactions in complex biological systems and their relevance to various pathological conditions.

8 Supplementary Information

Table S1: FN-FRET and TG2-AF647 image acquisition parameters

Phase	Channel	Laser excitation (nm)	Detection range (nm)	Description
1	1	488	566-578	FRET excited acceptor
	2	-	514-526	Donor FN488
2	3	543	566-578	Direct acceptor excitation FN546
	4	-	514-526	Bleed through
3	5	633	645-745	TG2-AF647

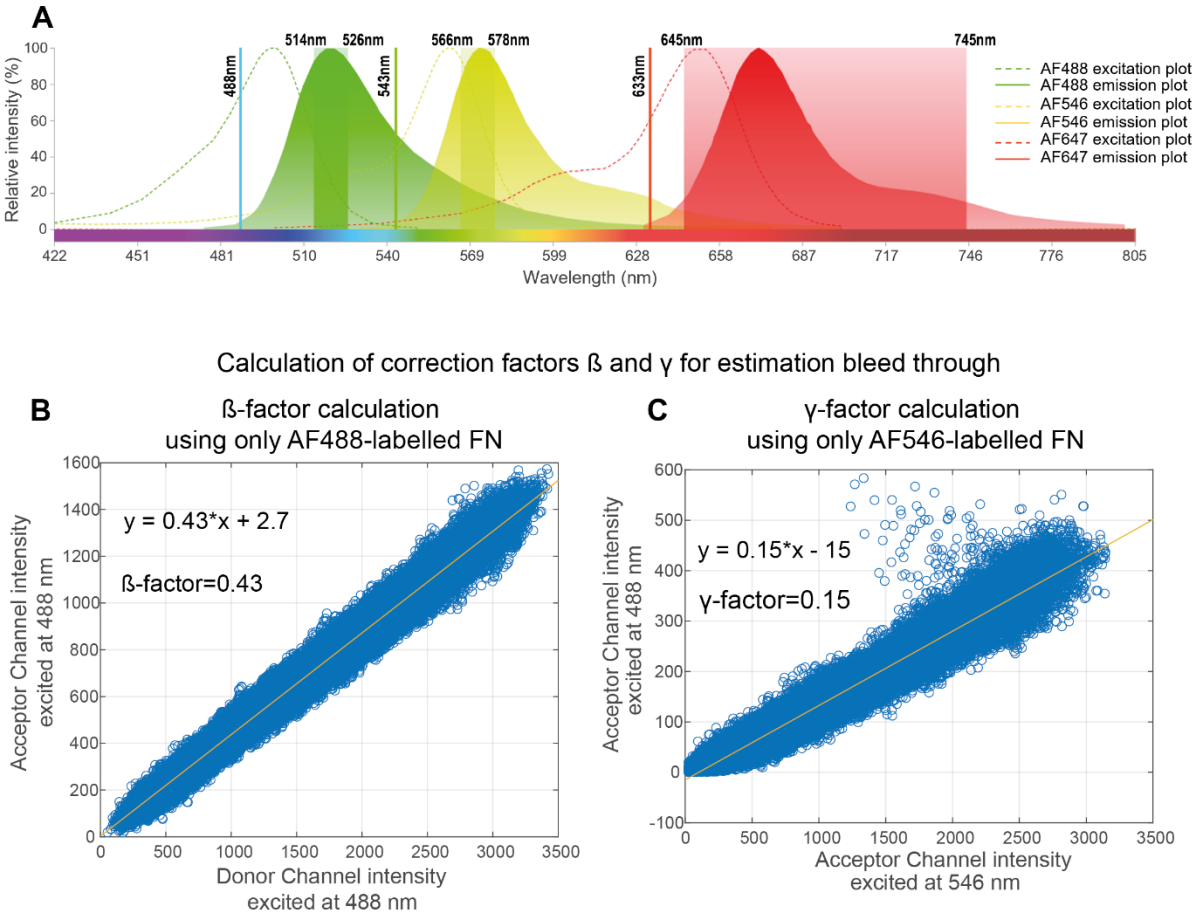

Figure 7.2.1: FN-FRET and TG2-647 image acquisition and correction parameters. Table S1 summarizes image acquisition parameters, which were used for all FN-FRET and TG2-647 confocal imaging experiments. Image acquisition was performed with Olympus FV-1000 in 3 sequential steps with 5 channels as was previously described[63]. (A) Plots depicting excitation and emission spectra for the AF488 (donor), AF546 (acceptor) and 647 (TG2) fluorophores are shown. Excitation wavelengths and detection windows of each channel in table S1 are marked as well. Donor, acceptor, and FRET intensities were measured with 12nm bandwidths over acceptor and donor emission peaks. TG2-647 excitation and detection were always performed in a separate channel (channel 5), to avoid unwanted crosstalk from the donor FN488 and acceptor FN546 signals upon excitation with 488nm and 543nm lasers. The plot shows an overlap between the AF-488 and AF-546 spectra, which upon excitation with 488nm laser would result in the leak of AF-488 into the "FRET excited acceptor" channel 1 and, therefore,

requires correction. (B and C) As was experimentally shown in the past, upon excitation with 488nm laser, there is a bleed through of both AF-488 (donor) and AF-546 (acceptor) signals into the FRET-excited acceptor channel (channel 1)[63]. Since this will influence the FRET ratios (I_A/I_D), the correction of the FRET signal is required. An example for calculation of β-factor and γ-factors for the correction of the FRET signal is provided in (B) and (C) respectively, and was performed as was described in detail previously[63,187]. β-factor and γ-factors for correction were always re-calculated for each experiment whenever the laser intensities or detection voltages were adjusted for the image acquisition.

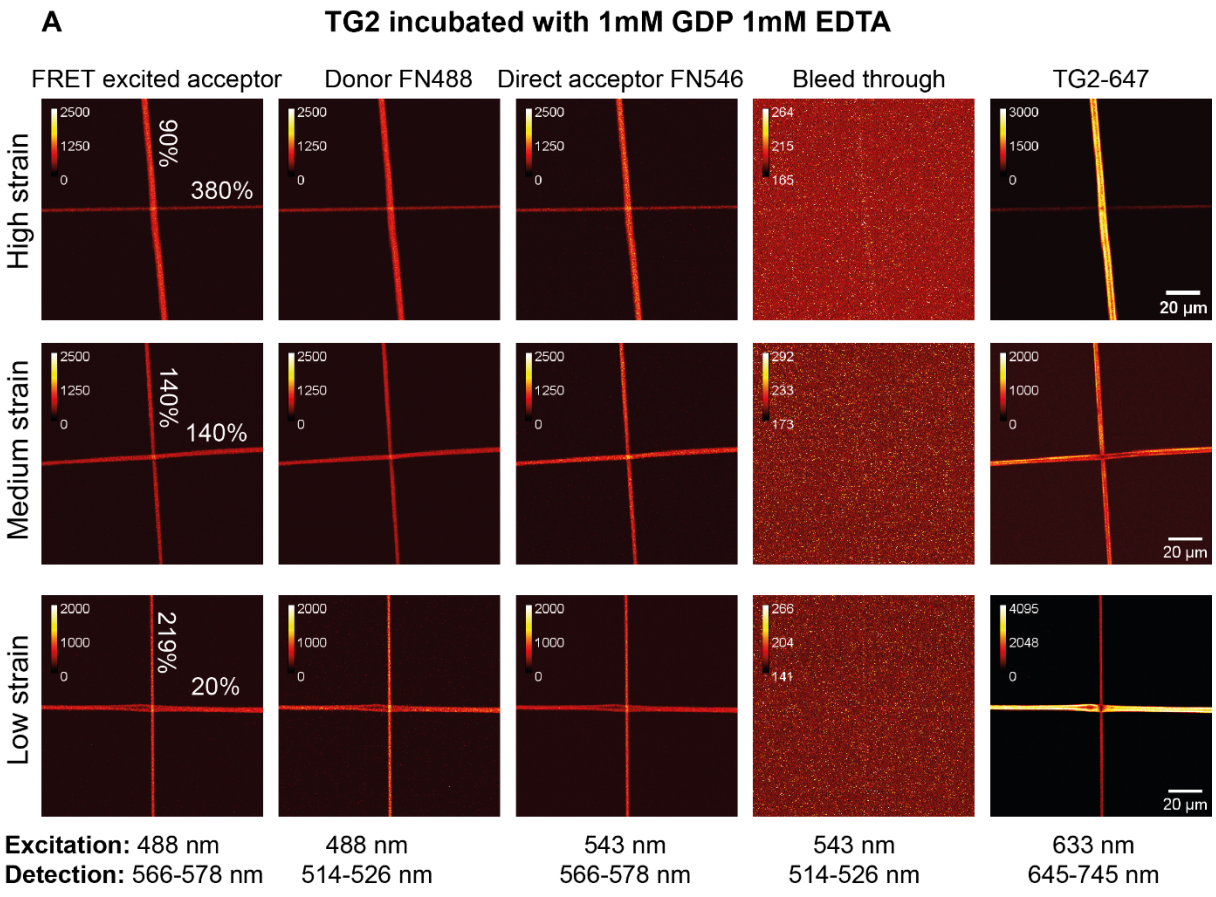

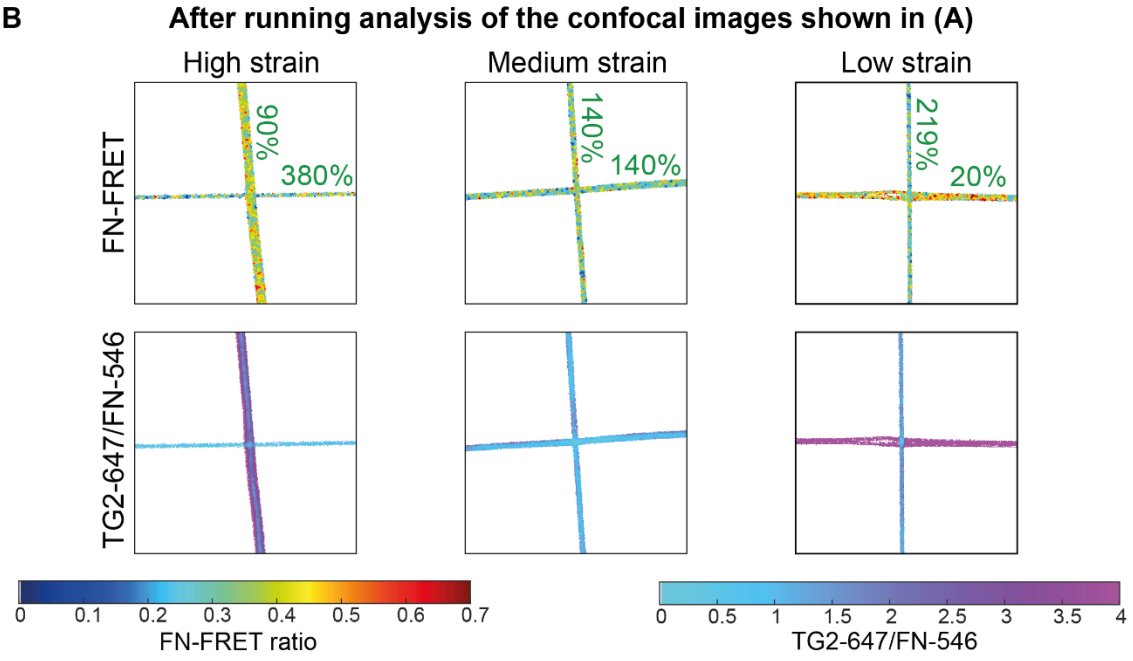

Figure 7.2.2: TG2-647 binding to FN-FRET fibers deposited orthogonally to each other in the presence of 1mM GDP and 1mM EDTA, imaging, and image analysis illustration. **(A)** Confocal images of a representative intersection for each membrane strain (low strain (relaxed membrane), medium strain (native membrane), high strain (stretched membrane)) are shown. Images were acquired as described in Supplementary figure 1. FN fiber strains induced by the silicone membrane strain are indicated, as was previously reported[130]. **(B)** Confocal images

shown in (A) were analyzed with the custom written Matlab script, which allows pixel-by-pixel correlation of normalized TG2 binding to the FN tensional state assessed by pixel-to-pixel FN-FRET ratio measurements[63]. As FRET ratio reduces with the increasing distance between donors and acceptors, lower FN-FRET ratios correspond to a higher FN tensional state, and higher FN-FRET ratios correspond to lower FN-FRET tensional states. Pixels of FN-intersections were color coded based on their corresponding FN-FRET ratio values. FN fibers under a specific strain, display a distinct range of heterogeneous FN-conformations as was previously observed in the ECM fibers assembled by fibroblasts[51,122,156]. TG2 fluorescence intensities were normalized pixel-by-pixel to the directly excited FN-546 (TG2-647/FN-546), and these pixels were also color coded based on the TG2-647/FN-546 value. TG2 preferentially binds FN fibers under low strain. Multiple intersections for each membrane strain were probed and analyzed in the same manner (Supplementary figure 4).

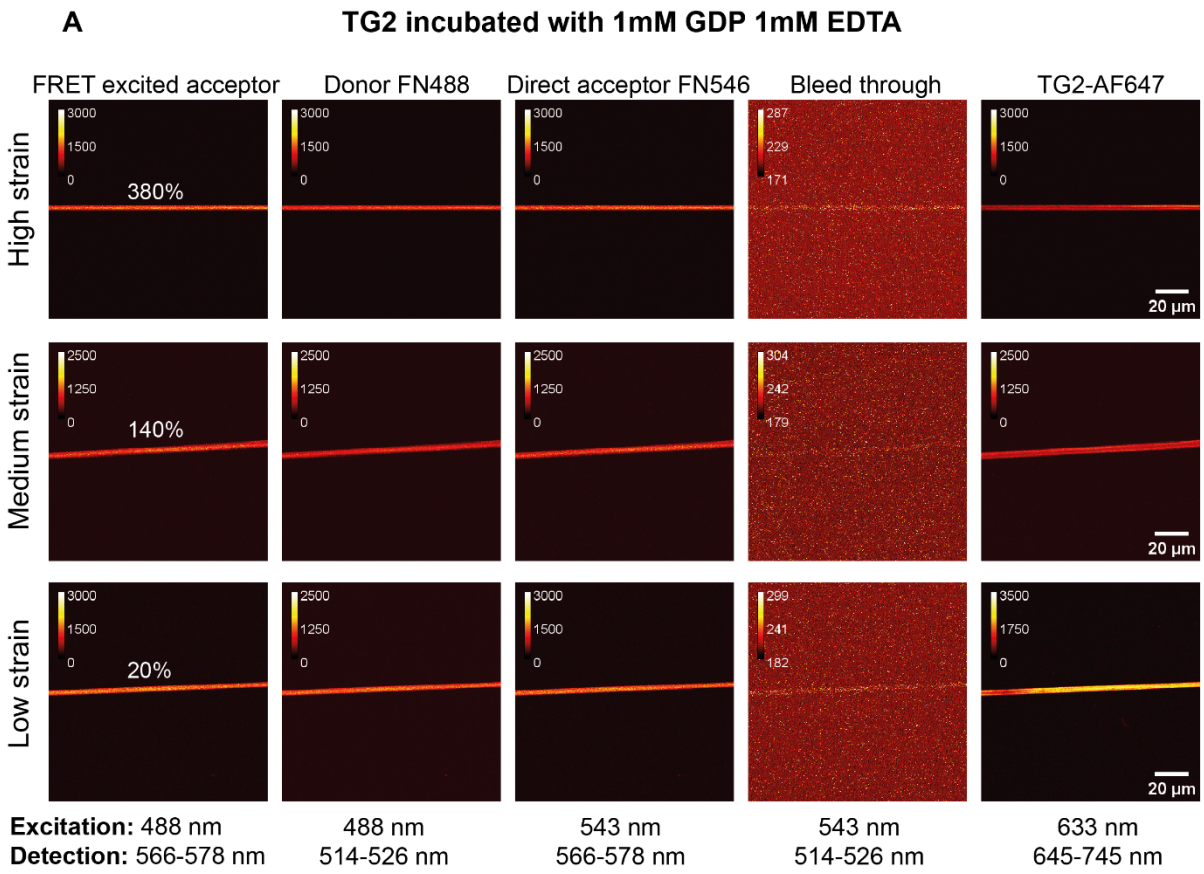

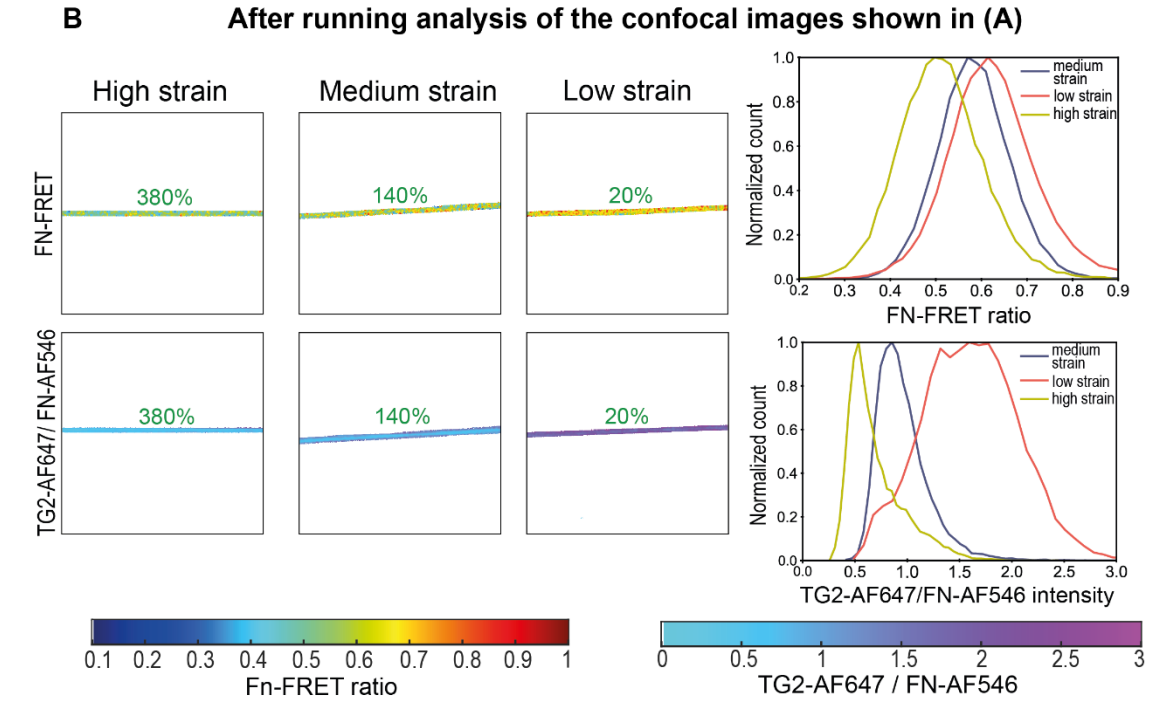

Figure 7.2.3: TG2-647 binding to FN-FRET fibers unidirectionally deposited in the presence of 1 mM GDP and 1 mM EDTA, imaging, and image analysis illustration. (A) Confocal images of a representative FN fiber for each membrane strain (low strain (relaxed membrane), medium strain (native membrane), high strain (stretched membrane)) are shown. Images were acquired as described in Supplementary figure 1. FN fiber strains induced by the silicone membrane

strain are indicated, as was previously reported[130]. **(B)** Confocal images shown in (A) were analyzed with the custom written Matlab script, which allows pixel-by-pixel correlation of normalized TG2 binding to the FN tensional state expressed by FN-FRET ratio[63]. The lower FN-FRET ratio corresponds to the higher FN tensional state, and higher FN-FRET ratio corresponds to the lower FN-FRET tensional state. Pixels of FN-intersections were color coded based on their corresponding FN-FRET ratio values. As can be seen, FN fibers under each tensional strain, display a distinct range of heterogeneous FN-conformations as was previously observed in the ECM fibers assembled by fibroblasts[51,122]. FN fibers which were subjected to low membrane strain are characterized by a range of pixels corresponding to the higher FN-FRET ratios, as expected[130]. TG2 fluorescence intensity was normalized pixel-by-pixel to the directly excited FN-546 (TG2-647/FN-546), and these pixels were color coded based on the TG2-647/FN-546 value. Distributions of all FN-FRET and TG2-647/FN-546 pixels of a representative fiber were plotted as normalized histograms. TG2 preferentially binds FN under low strain. To increase the statistical significance, typically 15 horizontal fibers were analyzed in this manner per membrane strain in all subsequent experiments.

8.1 Supplementary Note 1: Structure prediction and structure refinement.

Structural modelling and refinement of 3D crystal structure templates of individual fibronectin fragments and TG2 using intra-protein crosslinks.

To ensure accuracy in structural modelling of FN fragments, we exclusively used the UniProt P02751-1 FINC_HUMAN (isoform 1) sequence. This decision was based on the results of our XL-MS experiments, which unequivocally identified the presence of FN isoform 1. Additionally, our modelling approach considered the detected crosslinks between TG2 and FN, as well as the knowledge of FN domains in UniProt and the availability of PDB template structures. As a result, we selected the following FN fragments for modelling:

FN fragment/domains	FN aa sequence in UniProt P02751-1	PDB structure available?	Number of detected inter-protein crosslinks with TG2
FNI_{2-3}	94-183	PDB: 2cg6; 2cg7; 2rkz; 3cal; 3zrz; 4pz5	3
FNI_6-$FNII_1$-$FNII_2$-FNI_{7-9}(GBD)	306-604	Partially. PDB:3mql; PDB:3ejh	8
FNI_{7-9}	467-604	Partially. PDB:3ejh, 3gxe	1
$FNIII_{14-15}$	1816-1995	PDB:1fnh; 3r8q	7

To model and refine protein structures we followed the previously published protocols[163,164]. Briefly, we selected I-TASSER[165,188] server (iterative threading assembly refinement) for structural prediction and refinement of available templates, because this server allows to integrate experimental distance restraints from XL-MS into structure prediction and structure refinement. Intra-protein crosslinks were classified as compatible or non-compatible by measuring the Euclidean distance (ED) between the β-carbons of crosslinked residues using Xwalk[166].The filtering of non-compatible crosslinks was based on specific Euclidean distance cutoff, above which the crosslink was defined as non-compatible[160,163]: ED for DSS < 35 Å, ED for DMTMM < 25 Å, ED for PDH < 35Å. If there were both compatible and non-compatible crosslinks, we attempted structural refinements of available PDB templates using all, only compatible or only non-compatible crosslinks, to calculate, if possible, a structure of an alternative conformation to which non-compatible crosslinks could belong. To assess the quality of predicted structures, experimental crosslinks were mapped, and CB-CB distances were measured again. We then selected the best model for further modelling steps.

FNI_{2-3} structure refinement and evaluation.

Submitted amino acid sequence (UniProt P02751-1 94-183aa):

EETCFDKYTGNTYRVGDTYERPKDSMIWDCTCIGAGRGRISCTIANRCHEGGQSYKIG
DTWRRPHETGGYMLECVCLGNGKGEWTCKPIA

Several templates of the FNI_{2-3} region were available in the PDB. We selected PDB:2cg7 as a template because of its high resolution. We detected in total four unique crosslinks within FNI_{2-3}, all of which were compatible with the PDB:2cg7 template. We submitted all these crosslinks, along with the PDB:2cg7 template to I-TASSER for further structural refinement. For the two DMTMM crosslinks, we set the distance restraint at 25 Å, while for the other two DSS crosslinks, we set a distance restraint at 35 Å. The best model was selected based on the confidence score (C-score=0.74) and estimated TM-score=0.81+/-0.09, which indicated high degree of structural similarity and correct topology, as evidenced by TM-score>0.5. Importantly, this model satisfied all of the detected crosslinks.

Table 8.1-1: Crosslinked residues within FNI2-3:

AbsPos1	AbsPos2	Link	Crosslinker	CB-CB Euclidean distances (Å) Xwalk
166	180	GLU-LYS	DMTMM	6.3
116	149	LYS-LYS	DSS	16.4
100	116	LYS-LYS	DSS	10.4
95	100	GLU-LYS	DMTMM	16.6

Crosslinks within FNI$_{2-3}$ shown as Euclidean distances mapped onto the predicted model (compatible crosslinks - cyan):

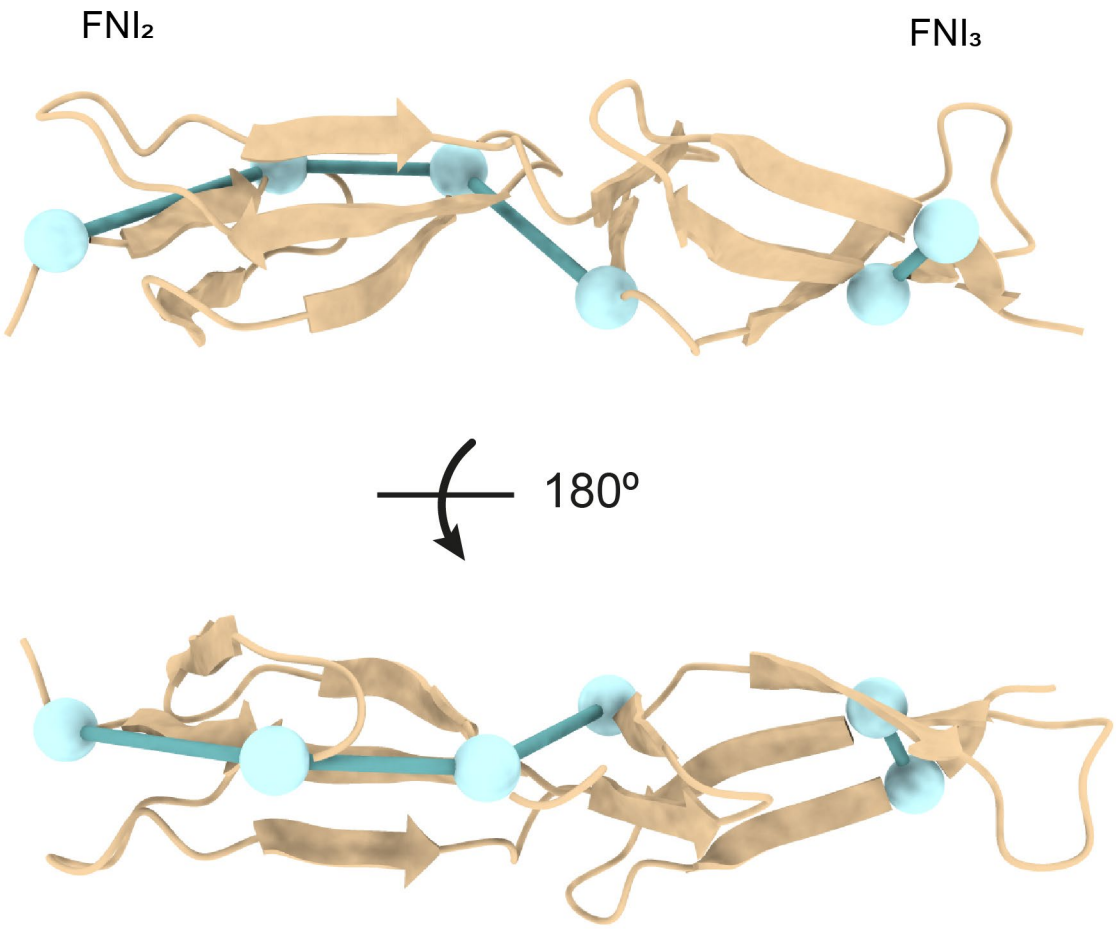

GBD (FNI_6-$FNII_1$-$FNII_2$-$FNI_{7\text{-}9}$) structure modelling and evaluation.

Submitted amino acid sequence (UniProt P02751-1 306-604aa):

GHCVTDSGVVYSVGMQWLKTQGNKQMLCTCLGNGVSCQETAVTQTYGGNSNGEPCVLP
FTYNGRTFYSCTTEGRQDGHLWCSTTSNYEQDQKYSFCTDHTVLVQTRGGNSNGALCHFPFLY
NNHNYTDCTSEGRRDNMKWCGTTQNYDADQKFGFCPMAAHEEICTTNEGVMYRIGDQWDKQHD
MGHMMRCTCVGNGRGEWTCIAYSQLRDQCIVDDITYNVNDTFHKRHEEGHMLNCTCFGQGRGR
WKCDPVDQCQDSETGTFYQIGDSWEKYVHGVRYQCYCYGRGIGEWHCQPLQT

Currently, two PDB crystal structures (PDB:3mql and PDB:3ejh) cover regions 306-513aa ($FNI_6FNII_{1\text{-}2}FNI_7$) and 516-606aa ($FNI_{8\text{-}9}$), respectively, providing coverage for the entire GBD, except for the short 513-516aa linker that connects FNI_7 to FNI_8. As a result, the orientation of $FNI_6FNII_{1\text{-}2}FNI_7$ and $FNI_{8\text{-}9}$ regions relative to one another is not known. Initially, we attempted to model the entire GBD using I-TASSER to understand the orientation of $FNI_6FNII_{1\text{-}2}FNI_7$ and $FNI_{8\text{-}9}$ regions relative to one another, but the results were not satisfactory. Therefore, we utilized ROBETTA[167] and AlphaFold to model the GBD. To assess the quality of the predicted structures, we utilized QMEAN[169] tool, which compares the degree of "nativeness" of the predicted model with experimental PDB structures. The predicted models from ROBETTA were more than one standard deviation away (QMEAN=1.86 and 1<|Z-score|<2), whereas AlphaFold predicted structure demonstrated better scores (QMEAN =1.44 and |Z-score|<1). To further evaluate the quality of structures, we measured CB-CB distances with Xwalk on the predicted models and compared them to the distances between the same residues on the experimental crystal structure PDB:3mql. Interestingly, the AlphaFold predicted structure had a shorter distance between Lys457-Lys397 (35.2 Å) compared to the distance between same residues on the crystal structure (36.5 Å), indicating that the predicted model better satisfied the crosslink. However, since this crosslink is located in a flexible region, structural rearrangements can be expected. Based on the above findings, the AlphaFold predicted model was selected for further modelling steps.

Table 8.1-2: Crosslinked residues within GBD (FNI_6-$FNII_{1\text{-}2}FNI_{7\text{-}9}$):

AbsPos1	AbsPos2	Link	Crosslinker	CB-CB Euclidean distances (Å) Xwalk
467	444	GLU-LYS	DMTMM	10.3
457	397	LYS-LYS	DSS	35.2
468	444	GLU-LYS	DMTMM	15.2

Crosslinks within GBD shown as Euclidean distances mapped onto the predicted model (compatible crosslinks - cyan):

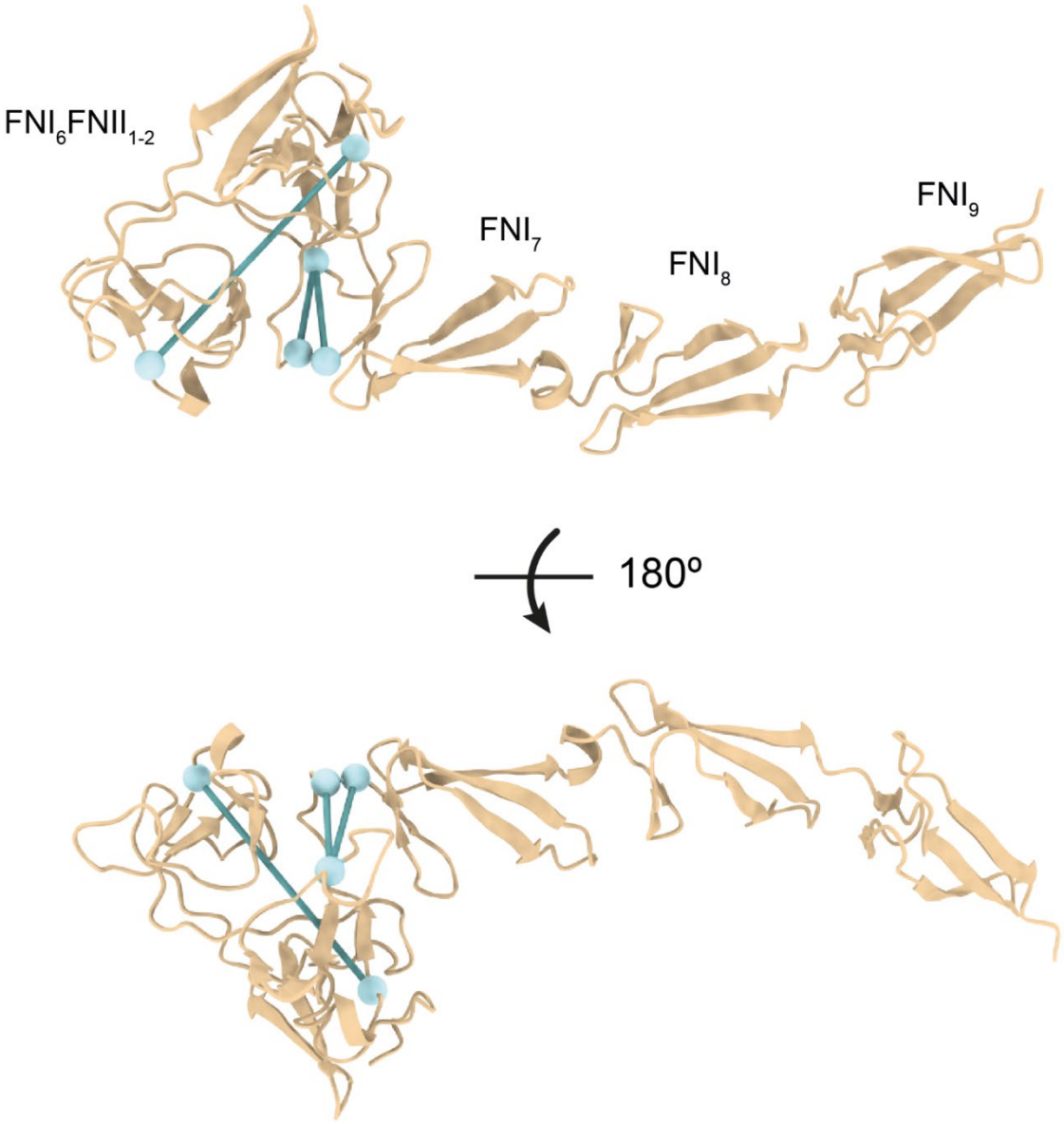

FNI_{7-9} structure modelling and evaluation.

Submitted amino acid sequence (UniProt: P02751-1 467-604aa):

EEICTTNEGVMYRIGDQWDKQHDMGHMMRCTCVGNGRGEWTCIAYSQLRDQCIVDDIT
YNVNDTFHKRHEEGHMLNCTCFGQGRGRWKCDPVDQCQDSETGTFYQIGDSWEKYVHGVRYQC
YCYGRGIGEWHCQPLQT

No crosslinks could be detected within the FNI_{7-9} region, which can be explained by two factors. Firstly, this region has low number of lysine residues, which are necessary for DSS reagents to crosslink on primary amines. As a result, generating DSS crosslinked peptides becomes more challenging in this case. Secondly, protein interaction interfaces can often be protected from crosslinking due to protein-protein contacts. Thus, crosslinks usually form around the contact sites rather than directly at the contact site itself. It is well-known that FNI_{7-9} is the primary high-affinity interaction site for TG2. Consistent with this, only one crosslinked residue was found on the N-terminal domain of TG2, where the main interaction site for FN is located. To model the FNI_{7-9} region, it was necessary to establish the orientation of FNI_7 and of FNI_{8-9} regions with respect to each other. Our initial attempts to model the entire FNI_{7-9} region with I-TASSER were not successful, so we utilized ROBETTA and AlphaFold for modelling of this region. Since no crosslinks were available to assess the quality of the predicted model, we utilized QMEAN to select the best model. The highest scoring model predicted by AlphaFold had a score that compared well with experimental PDB structures within one standard deviation (QMEAN=0.64 and $|Z\text{-score}|<1$). In contrast, ROBETTA predicted models had a worse score (QMEAN=2.02 and $1<|Z\text{-score}|<2$), placing the predicted model more than one standard deviation away from experimental PDB structures of similar qualities. Therefore, AlphaFold predicted model was selected for further modelling steps.

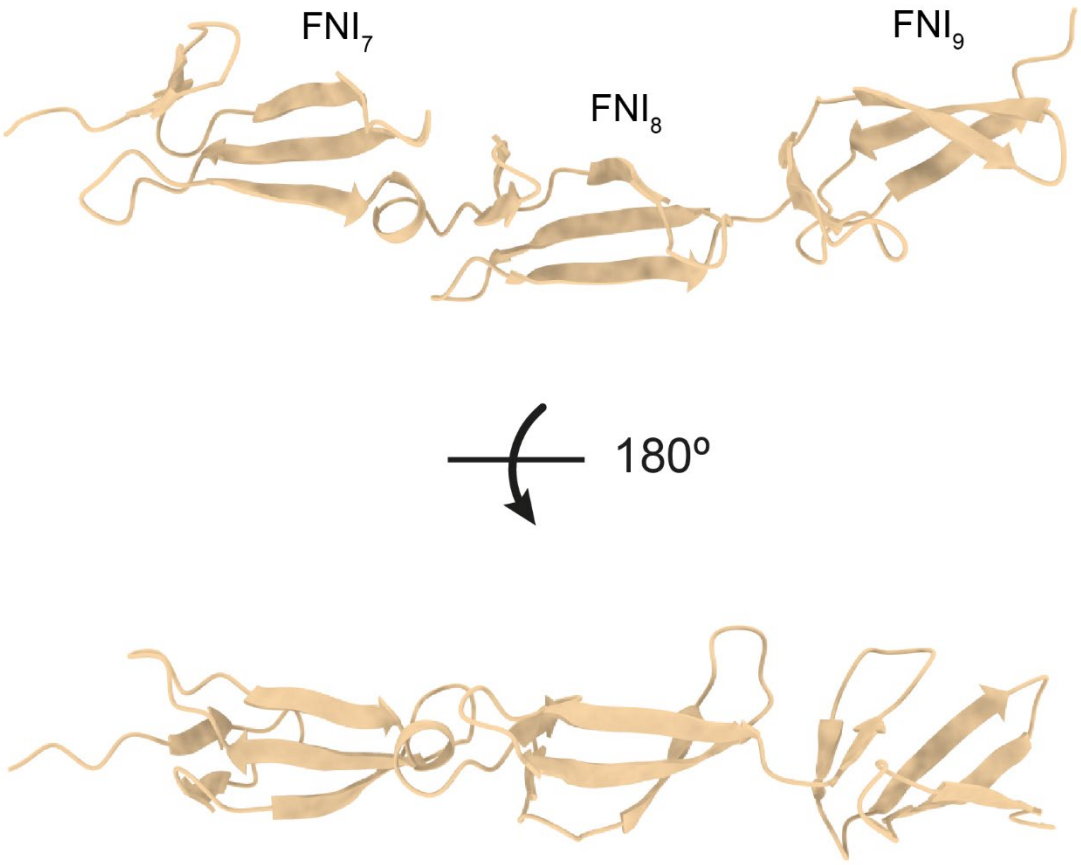
FNI7
FNI8
FNI9
180°

FNIII$_{14\text{-}15}$ structure refinement and evaluation.

Submitted amino acid sequence (UniProt: P02751-1 1816-1995aa):

PPRRARVTDATETTITISWRTKTETITGFQVDAVPANGQTPIQRTIKPDVRSYTITGL
QPGTDYKIYLYTLNDNARSSPVVIDASTAIDAPSNLRFLATTPNSLLVSWQPPRARITGYIIK
YEKPGSPPREVVPRPRPGVTEATITGLEPGTEYTIYVIALKNNQKSEPLIGRKKTDELP

We selected PDB:1fnh to use as a suitable template for modelling of FNIII$_{14\text{-}15}$ region because it covered the entire region we aimed to model. We were able to identify 11 crosslinks within FNIII$_{14\text{-}15}$ region, of which only one (Lys1936-Lys1862) did not comply with the selected distance cutoff. on the PDB:1fnh template. We performed structural refinement of the PDB:1fnh template using I-TASSER in three steps: using all crosslinks (compatible and non-compatible), only compatible crosslinks, or only one non-compatible crosslink. We set the distance restraint at 35 Å for the 7 DSS crosslinks and 25 Å for the 4 DMTMM crosslinks. Recalculation of structures did not produce any distinct models with alternative conformation. The models refined using all crosslinks or only compatible crosslinks had identical C-scores and TM-scores (C-score=0.80; TM-score=0.82+/-0.08). The model derived by structural refinement of the template using one non-compatible crosslink had a slightly lower C-score=0.79. However, all structures satisfied 10/11 crosslinks, indicating the similarity of the protein in solution to the model. One non-compatible crosslink connects residues one both the FNIII$_{14}$ and FNIII$_{15}$ domains, which are connected by a flexible linker and can move with respect to one another. This suggests that in an ensemble of conformations, some of the molecules were present in a more compact conformation. Therefore, we selected model refined with all crosslinks.

Table 8.1-3: Crosslinked residues within FNIII$_{14\text{-}15}$:

AbsPos1	AbsPos2	Link	Crosslinker	CB-CB Euclidean distances (Å) Xwalk
1981	1983	LYS-GLU	DMTMM	7.8
1946	1939	GLU-LYS	DMTMM	8.7
1964	1939	GLU-LYS	DMTMM	7.5
1981	1862	LYS-LYS	DSS	34.8
1936	1981	LYS-LYS	DSS	11.0
1981	1939	LYS-LYS	DSS	22.2
1936	1862	LYS-LYS	DSS	43.7
1936	1939	LYS-LYS	DSS	11.9
1936	1983	LYS-GLU	DMTMM	13.1

1862	1880	LYS-LYS	DSS	23.0
1862	1837	LYS-LYS	DSS	13.2

Crosslinks within $FNIII_{14-15}$ *shown as Euclidean distances mapped onto the predicted model (compatible crosslinks – cyan; non-compatible crosslinks - magenta):*

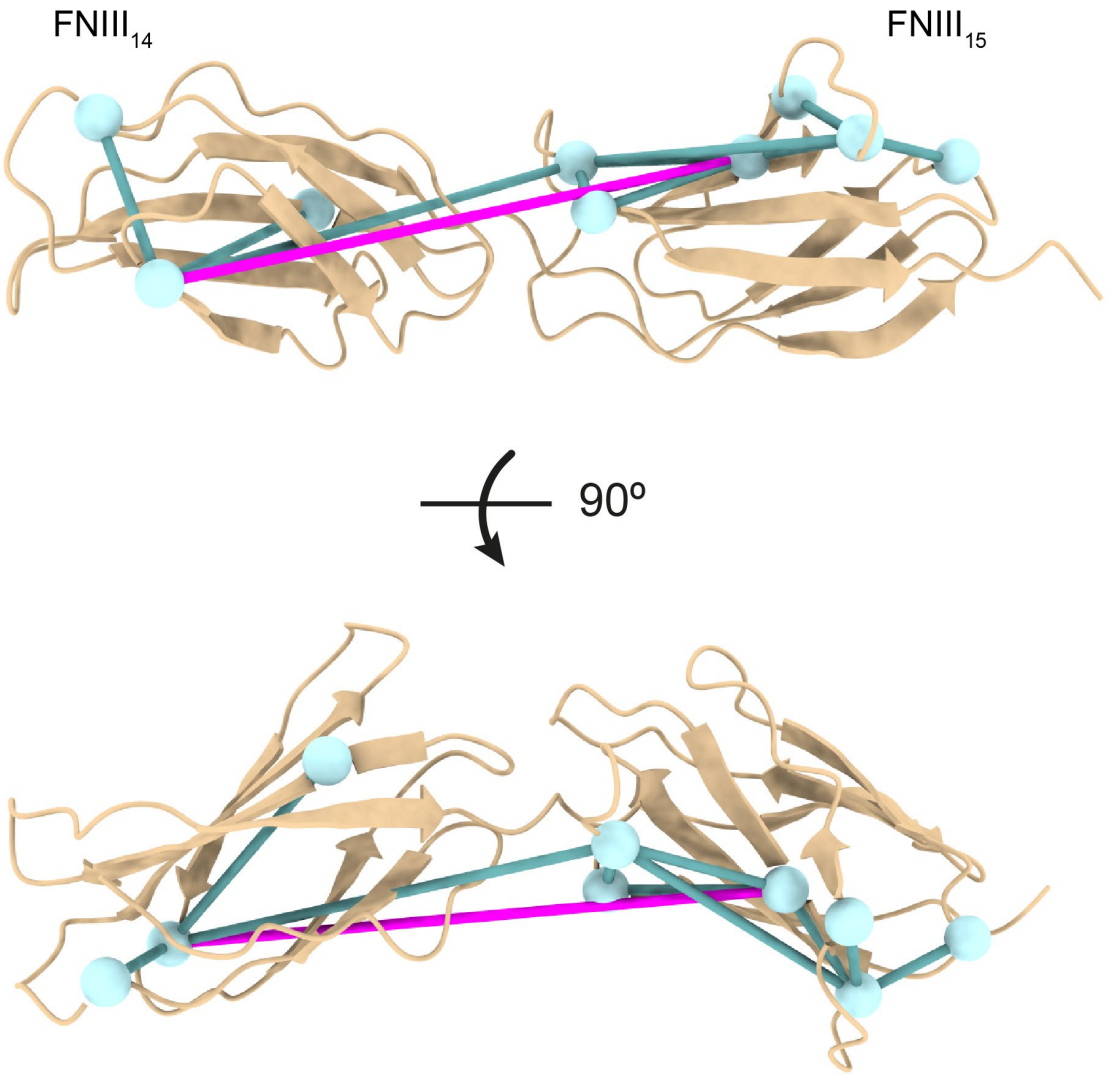

TG2 structure refinement and evaluation.

Submitted amino acid sequence (UniProt P21980):

MAEELVLERCDLELETNGRDHHTADLCREKLVVRRGQPFWLTLHFEGRNYEASVDSLTFSVVT
GPAPSQEAGTKARFPLRDAVEEGDWTATVVDQQDCTLSLQLTTPANAPIGLYRLSLEASTGYQ
GSSFVLGHFILLFNAWCPADAVYLDSEEERQEYVLTQQGFIYQGSAKFIKNIPWNFGQFEDGI
LDICLILLDVNPKFLKNAGRDCSRRSSPVYVGRVVSGMVNCNDDQGVLLGRWDNNYGDGVSPM
SWIGSVDILRRWKNHGCQRVKYGQCWVFAAVACTVLRCLGIPTRVVTNYNSAHDQNSNLLIEY
FRNEFGEIQGDKSEMIWNFHCWVESWMTRPDLQPGYEGWQALDPTPQEKSEGTYCCGPVPVRA
IKEGDLSTKYDAPFVFAEVNADVVDWIQQDDGSVHKSINRSLIVGLKISTKSVGRDEREDITH
TYKYPEGSSEEREAFTRANHLNKLAEKEETGMAMRIRVGQSMNMGSDFDVFAHITNNTAEEYV
CRLLLCARTVSYNGILGPECGTKYLLNLNLEPFSEKSVPLCILYEKYRDCLTESNLIKVRALL
VEPVINSYLLAERDLYLENPEIKIRILGEPKQKRKLVAEVSLQNPLPVALEGCTFTVEGAGLT
EEQKTVEIPDPVEAGEEVKVRMDLLPLHMGLHKLVVNFESDKLKAVKGFRNVIIGPA

High resolution crystal structures of TG2 in the closed conformation bound to GTP (guanosine triphosphate) and GDP (guanosine diphosphate) are available. For this study, we selected PDB:4pyg due to its better quality. We were able to detect in total 46 unique crosslinks within TG2. On the PDB:4pyg templated structure 8 out of 46 crosslinks violated the distance cutoff. To refine the template structure, we submitted all detected crosslinks as distance restraints of 35 Å for DSS and PDH or 25 Å for DMTMM crosslinks to I-TASSER. Additionally, we submitted only non-compatible crosslinks to see if an alternative conformation of the structure can be obtained. We evaluated the resulting models by measuring the distances between crosslinked residues with Xwalk. No alternative structures could be obtained and all resulting models violated 8 crosslinks out of 46. However, the model refined with only non-compatible crosslinks had a higher confidence score and TM-score (C-score=1.75 and TM-score0.96+/-0.05), compared to the model refined with all crosslinks (C-score=1.46 and TM-score=0.92+/-0.06). Notably, the relative solvent accessibility of that Lys30 on PDB:4pyg did not conform to our solvent accessibility criteria of at least 40% for the backbone or the side chain. However, the relative solvent accessibility of Lys30 side chain increased considerably after refinement using non-compatible crosslinks (48.6% on refined model vs 24.7% on PDB:4pyg). Therefore, we selected the model structurally refined with noncompatible crosslinks for further docking steps.

Crosslinks within TG2 *shown as Euclidean distances mapped onto the predicted model (compatible crosslinks – cyan; non-compatible crosslinks - magenta):*

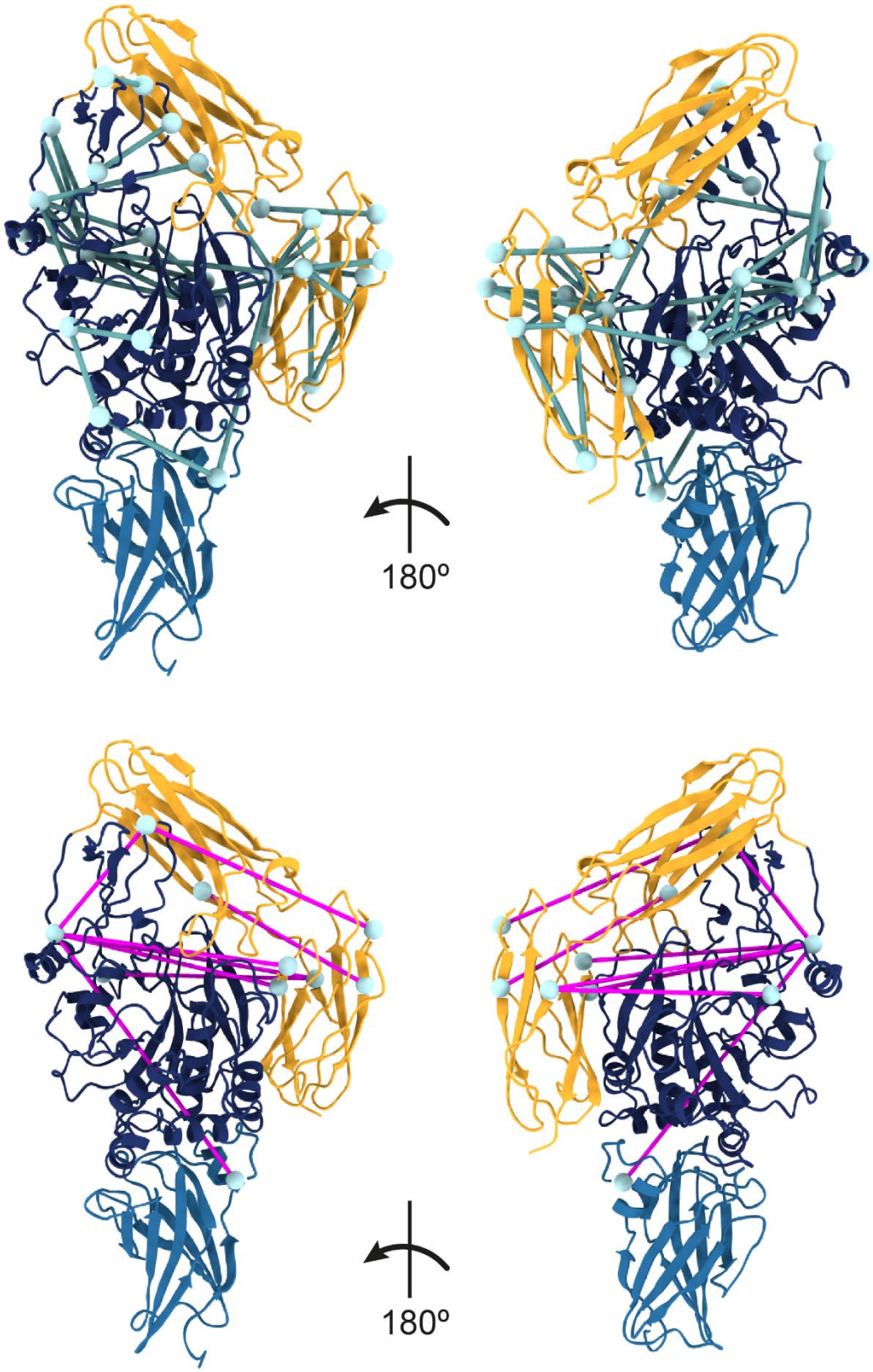

Table 8.1-4: Crosslinked residues within TG2.

AbsPos1	AbsPos2	Link	Crosslinker	CB-CB Euclidean distances (Å) Xwalk
444	380	LYS-LYS	DSS	6.3
380	464	LYS-LYS	DSS	15.5
649	590	LYS-LYS	DSS	10.2
663	677	LYS-LYS	DSS	11.8
444	464	LYS-LYS	DSS	12.5
562	677	LYS-LYS	DSS	22.4
672	677	LYS-LYS	DSS	16.0
562	464	LYS-LYS	DSS	26.0
444	429	LYS-LYS	DSS	20.8
677	30	LYS-LYS	DSS	34.4
205	30	LYS-LYS	DSS	28.8
464	674	LYS-LYS	DSS	40.3
444	677	LYS-LYS	DSS	30.5
444	425	LYS-LYS	DSS	11.7
425	464	LYS-LYS	DSS	21.3
590	429	LYS-LYS	DSS	22.6
444	590	LYS-LYS	DSS	39.1
444	468	LYS-LYS	DSS	20.5
464	30	LYS-LYS	DSS	53.3
590	464	LYS-LYS	DSS	48.1
590	598	LYS-LYS	DSS	22.9
464	677	LYS-LYS	DSS	38.6
590	677	LYS-LYS	DSS	11.7
429	380	LYS-LYS	DSS	21.1
649	598	LYS-LYS	DSS	25.1
649	562	LYS-LYS	DSS	36.3
444	435	LYS-GLU	DMTMM	22.4
444	454	LYS-GLU	DMTMM	11.7
640	590	ASP-LYS	DMTMM	20.7

366	205	GLU-LYS	DMTMM	12.9
425	437	LYS-GLU	DMTMM	10.6
669	677	GLU-LYS	DMTMM	10.1
640	677	ASP-LYS	DMTMM	23.0
437	429	GLU-LYS	DMTMM	6.7
447	468	GLU-LYS	DMTMM	15.6
671	677	ASP-LYS	DMTMM	17.6
464	319	LYS-GLU	DMTMM	46.1
425	434	LYS-ASP	DMTMM	17.2
444	467	LYS-GLU	DMTMM	21.0
637	669	GLU-GLU	PDH	10.3
640	669	ASP-GLU	PDH	15.2
643	585	GLU-GLU	PDH	21.5
232	366	ASP-GLU	PDH	10.9
409	319	ASP-GLU	PDH	9.8
643	319	GLU-GLU	PDH	46.1
314	322	GLU-GLU	PDH	15.8

8.2 Supplementary Note 2: Analysis of accessible interaction space.

Validation of inter-protein crosslinks and prediction of interaction interfaces with DisVis

To evaluate the compatibility of inter-protein crosslinks and to predict active residues at the binding interface, we employed the following workflow. We utilized DisVis, a tool that allows to incorporate experimental crosslinks in form of distance restraints to identify active residues involved in the interaction, simultaneously it can help to filter out incompatible inter-protein crosslinks[153,189]. To aid the identification process, we combined DisVis with the NACCESS[170] tool, which calculates the relative solvent accessibility of each residue. For DisVis interaction analysis, we submitted residues with a relative solvent accessibility of at least 40% for either the main chain or the side chain. As putative active residues, we considered residues with more than 0.5 interaction on average for complexes consistent with the maximum number of restraints. The identified putative active residues were then utilized in the subsequent steps for docking with HADDOCK.

Solvent accessible residues with at least 40% relative solvent accessibility for either the main chain or the side chain calculated with NACCESS, which were submitted to DisVis interaction analysis:

Fixed chain (TG2): 1 2 3 6 7 8 9 10 11 13 15 16 19 20 22 24 25 27 28 29 30 38 40 42 46 47 48 49 51 52 53 54 56 65 66 67 69 70 72 76 78 80 81 82 84 85 86 87 92 93 94 95 96 97 105 107 109 114 116 122 124 125 126 127 128 129 130 131 132 134 142 144 145 151 152 153 154 157 172 173 175 177 187 191 195 201 202 204 205 206 207 209 213 231 232 233 238 242 243 244 246 247 248 249 263 265 266 267 268 269 270 273 306 308 309 310 312 320 322 324 326 327 329 343 345 346 348 349 350 352 361 362 364 365 366 367 368 369 377 385 387 391 407 408 409 410 411 412 413 419 420 421 425 432 433 435 436 438 441 446 447 448 450 451 453 454 457 458 461 462 464 465 466 467 468 469 470 472 474 475 476 480 481 482 484 487 488 490 498 499 500 501 502 504 506 519 520 522 523 526 528 529 530 531 533 535 536 537 538 539 541 543 545 547 549 550 552 553 555 570 571 572 573 579 580 588 590 592 593 594 595 596 600 601 602 610 612 614 615 618 619 631 632 634 635 637 639 640 641 643 644 645 646 649 651 653 655 657 659 660 661 671 674 677 679 680 681 683 685 686 687

Scanning chain (FNI_{2-3}): 94 95 96 98 100 101 102 103 104 105 107 108 109 110 111 112 113 115 116 117 118 119 126 127 128 129 130 132 134 135 136 138 139 142 144 145 146 147 149 150 151 153 155 157 159 160 161 162 163 164 170 172 173 174 176 177 178 179 180 181 182 183

Scanning chain (GBD): 308 309 311 312 313 315 317 318 319 323 324 325 326 327 328 329 330 336 337 338 339 340 341 342 343 344 346 347 349 350 351 352 353 354 356 358 359 360 361 362 367 368 369 376 377 378 379 380 381 382 383 393 394 395 396 397 402 403 404 405 406 407 409 411 413 414 416 417 422 423 427 428 429 430 432 433 436 437 438 439 440 441 442 450 451 453 454 455 456 465 466 471 473 474 475 479 480 481 482 483 485 486 487 489 490 491 493 495 501 502 503 505 507 508 509 513 514 515 516 519 521 522 523 524 526 527 528 529 530 532 534 535 536 537 538 542 546 548 549 550 552 554 555 556 557 562 564 565

566 567 568 569 571 572 573 574 575 577 579 581 582 583 584 588 590 592 593 594 596 597 598 600 601 602 603 604

Scanning chain (FNI_{7-9}): 465 466 471 473 474 475 479 480 481 482 483 485 486 487 489 490 491 493 495 501 502 503 505 507 508 509 513 514 515 516 519 521 522 523 524 526 527 528 529 530 532 534 535 536 537 538 542 546 548 549 550 552 554 555 556 557 562 564 565 566 567 568 569 571 572 573 574 575 577 579 581 582 583 584 588 590 592 593 594 596 597 598 600 601 602 603 604

Scanning chain ($FNIII_{14-15}$): 1816 1818 1819 1820 1821 1823 1824 1825 1826 1828 1835 1838 1839 1840 1841 1842 1851 1852 1853 1854 1855 1856 1857 1858 1859 1860 1862 1863 1864 1866 1867 1869 1871 1872 1878 1880 1887 1888 1889 1890 1891 1893 1894 1896 1898 1907 1908 1909 1911 1912 1913 1914 1915 1917 1924 1925 1926 1927 1929 1930 1931 1940 1941 1942 1943 1944 1945 1947 1949 1950 1952 1953 1954 1955 1956 1957 1959 1961 1962 1964 1965 1966 1978 1979 1980 1981 1983 1984 1986 1987 1988 1990 1992 1993 1994 1995

DisVis analysis of TG2 and FNI_{2-3}

We identified three unique crosslinks between TG2 and FNI_{2-3}, all of which we subjected to DisVis analysis. For the two DMTMM crosslinks, we set the upper distance limit to 25 Å and 35 Å for the DSS crosslink. However, DisVis analysis failed to identify complexes that were consistent with all three restraints, and highlighted restraint 1 GLU319(TG2)-LYS116(FN) as a false positive candidate with the highest Z-score. In addition, the GLU319(TG2)-LYS116(FN) restraint violated complexes consistent with two restraints 95.92% of the time, while the other two restraints violated the same complexes 4.08% and 0% of the time. After excluding GLU319(TG2)-LYS116(FN) restraint and re-running DisVis analysis, we were able to identify 1346192 complexes consistent with 2 restraints. Given the evidence of GLU319(TG2)-LYS116(FN) incompatibility, we decided to exclude it from further docking steps with HADDOCK.

Table 8.2-1: Crosslinked residues between TG2 and FNI_{2-3}.

AbsPos FN	AbsPos TG2	Link	Crosslinker
116	319	LYS-GLU	DMTMM
116	637	LYS-GLU	DMTMM
100	590	LYS-LYS	DSS

Table 8.2-2: Accessible complexes consistent with at least N restraints.

# of consistent restraints	# of accessible complexes consistent with at least N restraints	Fraction of accessible complexes consistent with at least N restraints
0	36202322	1
1	7018163	0.193859
2	1403420	0.038766
3	0	0

Table 8.2-3: Z-score for each restraint

# of consistent restraints	Average violated fraction	Standard deviation	Z-score	Restraint
1	0.861	0.098	1.329	A319(CA)-B116(CA)
2	0.394	0.353	-0.245	A637(CA)-B116(CA)
3	0.145	0.145	-1.084	A590(CA)-B100(CA)

Active residues output from DisVis interaction analysis with at least 0.5 interactions on average in the complexes satisfying the maximum number of distance restraints:

Fixed chain (TG2): 639, 640, 641, 637, 643, 619, 646, 618, 651, 649, 653, 645, 644, 247, 602, 246, 615, 635, 634, 614, 594, 601, 671, 248, 267, 595, 266

Scanning chain (FNI_{2-3}): 103, 117, 100, 101, 102, 116, 104, 118, 145, 130, 105, 98, 115, 129, 144, 119, 146, 94, 132, 96, 128, 95, 107, 134, 112

DisVis analysis of TG2 and GBD (FNI_6-$FNII_1$-$FNII_2$-FNI_{7-9})

We were able to identify a total of 8 unique crosslinks between TG2 and GBD, all of which we submitted to analysis with DisVis. Since all crosslinks were on lysines, we set the upper distance limit at 35 Å. Complexes consistent with all 8 restraints could not be found, and as evident by the highest Z-score, DisVis analysis indicated that restraint 5 (LYS550(TG2)-LYS397(FN)) was the most likely false positive. Restraint 8 (LYS30(TG)-LYS486(FN)) had the second highest Z-score, indicating that it too might also be a false positive. However, residue LYS30(TG2) is well-known to be part of the main FN-binding site on TG2 N-terminal domain[46]. The high Z-score for restraint 8 may be due to the asymmetric distribution of detected restraints, where all but one restraint are clustered on the two FN residues (4 on LYS457 and 3 on LYS397), creating a heavy bias. Additionally, restraint 5 violated complexes consistent with the maximum number of restraints 100% and 99.68% of the time for the complexes consistent with 6 restraints, whereas restraint 8 violated those complexes 0% and 94.5% respectively. After excluding the LYS550(TG2)-LYS397(FN) restraint and re-running the DisVis analysis using same parameters, accessible complexes consistent with 7 submitted restraints could be found. Therefore, we excluded restraint LYS550(TG2)-LYS397(FN) from further docking steps with HADDOCK.

Table 8.2-4: Crosslinked residues between TG2 and GBD.

AbsPos FN	AbsPos TG2	Link	Crosslinker
486	30	LYS-LYS	DSS
457	562	LYS-LYS	DSS
457	273	LYS-LYS	DSS
457	364	LYS-LYS	DSS
397	364	LYS-LYS	DSS
397	387	LYS-LYS	DSS
397	550	LYS-LYS	DSS
457	550	LYS-LYS	DSS

Table 8.2-5: Accessible complexes consistent with at least N restraints.

# of consistent restraints	# of accessible complexes consistent with at least N restraints	Fraction of accessible complexes consistent with at least N restraints
0	63210314	1
1	16953225	0.268203

2	6825639	0.107983
3	1453687	0.022998
4	370523	0.005862
5	44879	0.00071
6	4847	0.000077
7	12	0
8	0	0

Table 8.2-6: Z-score for each restraint.

# of consistent restraints	Average violated fraction	Standard deviation	Z-score	Restraint
1	0.288	0.336	-0.944	A273(CA)-B457(CA)
2	0.44	0.297	-0.184	A364(CA)-B397(CA)
3	0.321	0.331	-0.78	A364(CA)-B457(CA)
4	0.527	0.323	0.255	A387(CA)-B397(CA)
5	0.823	0.123	1.737	A550(CA)-B397(CA)
6	0.321	0.286	-0.78	A550(CA)-B457(CA)
7	0.321	0.317	-0.777	A562(CA)-B457(CA)
8	0.771	0.317	1.474	A30(CA)-B486(CA)

Active residues output from DisVis interaction analysis with at least 0.5 interactions on average in the complexes satisfying the maximum number of distance restraints:

Fixed chain (TG2): 233, 232, 231, 238, 368, 367, 242, 361, 364, 204, 369, 201, 205, 326, 362, 270, 269, 268, 273, 244, 365, 366, 202, 519, 243, 329, 520, 327, 246, 522, 247, 206, 324, 267, 30

Scanning chain (GBD): 442, 441, 440, 439, 482, 481, 438, 436, 483, 428, 429, 427, 437, 479, 368, 480, 369, 485, 367, 430, 453, 495, 515, 514

DisVis analysis of TG2 and FNI_{7-9}

We detected one unique crosslink between TG2 and FNI_{7-9}, which we submitted to DisVis for interaction analysis. The upper distance limit was set to 35 Å. We then used the active residues obtained for both the fixed and scanning chains for further docking steps with HADDOCK. Notably, DisVis analysis revealed that Glu29 formed at least 0.5 interactions on average in the

complexes that satisfied the maximum number of restraints, rather than Lys30, which was crosslinked and is known to be part of the binding interface with FN.

Table 8.2-7: Crosslinked residues between TG2 and FNI_{7-9}.

AbsPos FN	AbsPos TG2	Link	Crosslinker
486	30	LYS-LYS	DSS

Active residues output from DisVis interaction analysis with at least 0.5 interactions on average in the complexes satisfying the maximum number of distance restraints:

Fixed chain (TG2): 687, 1, 8, 9, 686, 96, 2, 600, 97, 268, 601, 29, 47, 46, 266, 15

Scanning chain (FNI_{7-9}): 474, 475, 473, 465, 466, 489, 502, 503, 490, 491, 471, 501, 487, 479, 482, 481, 485, 486, 480, 483, 549, 522, 528, 548, 505, 515, 529, 521, 527, 526

DisVis analysis of TG2 and $FNIII_{14-15}$

We identified a total of 7 unique crosslinks between TG2 and $FNIII_{14-15}$, all of which we submitted to DisVis for analysis. For the six DSS crosslinks we set the upper distance limit to 35 Å, and for one DMTMM crosslink, we set the upper limit to 25 Å. However, DisVis analysis was unable to identify complexes consistent with all seven restraints. The analysis revealed that restraint 3 (LYS464(TG2)-LYS1862(FN)) had the highest Z-score and was highlighted by DisVis as the candidate for a false positive. This was further supported by the fact that restraint 3 had a 100% and 99.74% violation fractions for the complexes consistent with 6 and 5 restraints respectively. After excluding restraint 3 and re-running the DisVis analysis, we were able to identify 10599 complexes consistent with 6 restraints. As a result, we excluded the LYS464(TG2)-LYS1862(FN) restraint from further docking steps with HADDOCK.

Table 8.2-8: Crosslinked residues between TG2 and $FNIII_{14-15}$.

AbsPos FN	AbsPos TG2	Link	Crosslinker
1936	643	LYS-GLU	DMTMM
1862	677	LYS-LYS	DSS
1862	30	LYS-LYS	DSS
1862	464	LYS-LYS	DSS
1862	590	LYS-LYS	DSS
1862	649	LYS-LYS	DSS
1837	30	LYS-LYS	DSS

Table 8.2-9: Accessible complexes consistent with at least N restraints.

# of consistent restraints	# of accessible complexes consistent with at least N restraints	Fraction of accessible complexes consistent with at least N restraints
0	45457055	1
1	17186935	0.378092
2	7517654	0.165379
3	3729043	0.082034
4	889924	0.019577
5	344514	0.007579
6	10599	0.000233
7	0	0

Table 8.2-10: Z-score for each restraint.

# of consistent restraints	Average violated fraction	Standard deviation	Z-score	Restraint
1	0.4	0.305	-0.183	A30(CA)-B1837(CA)
2	0.381	0.313	-0.253	A30(CA)-B1862(CA)
3	0.933	0.094	1.81	A464(CA)-B1862(CA)
4	0.211	0.275	-0.89	A590(CA)-B1862(CA)
5	0.224	0.272	-0.839	A649(CA)-B1862(CA)
6	0.224	0.286	-0.84	A677(CA)-B1862(CA)
7	0.768	0.345	1.194	A643(CA)-B1936(CA)

Active residues output from DisVis interaction analysis with at least 0.5 interactions on average in the complexes satisfying the maximum number of distance restraints:

Fixed chain (TG2): 639, 640, 637, 653, 602, 641, 634, 619, 601, 635, 655, 600, 643, 266, 631, 651, 618, 632, 267, 615, 247, 644, 646, 263, 268, 246, 645, 657, 614

Scanning chain ($FNIII_{14-15}$): 1864, 1866, 1867, 1824, 1869, 1862, 1823, 1826, 1835, 1871, 1863, 1908, 1872, 1828, 1983, 1986, 1825, 1907, 1984, 1987, 1838, 1821, 1860, 1819, 1842, 1859, 1988, 1909

8.3 Supplementary Note 3: Protein-protein docking.

Crosslink-driven HADDOCK protein-protein docking of TG2 with FN fragments

For all docking runs the maximum number of models considered for clustering was limited to 200.

TG2 and FNI_{2-3}

To dock TG2 and FNI_{2-3} we submitted the two crosslinks as unambiguous distance restraints, which DisVis interaction analysis identified as true positives as well as the active residues that DisVis predicted to be involved in the interaction. The linker between the FNI_2 and FNI_3 domains (Thr136-Arg140) was defined as a flexible segment. HADDOCK clustered 140 structures in 14 clusters, which represented 70.0% of the water-refined models HADDOCK generated. The distance restraints were mapped onto the best 4 predicted models from the top 10 clusters each (a total of 40 models), and the ED was measured. We found that all predicted models satisfied the distance restraints used for guiding of docking. Based on the HADDOCK scores, we selected the cluster4_1 model, which had the highest score of -210.3+/-11.3.

Submitted distance restraints:

```
assi (segid A and resid 637 and name CA) (segid B and resid 116 and name CA) 25 25 0
assi (segid A and resid 590 and name CA) (segid B and resid 100 and name CA) 35 35 0
```

TG2 and GBD (FNI_6-$FNII_1$-$FNII_2$-FNI_{7-9})

For docking of TG2 and GBD, we submitted to HADDOCK seven crosslinks as unambiguous distance restraints, which DisVis interaction analysis confirmed to be true positive. Interestingly, DisVis interaction analysis instead of a well-known from the literature residue Lys30, identified a nearby residue Glu29 as an active residue at the binding interface. To the list of the active residues on TG2, we added Lys30, His134, Arg116, which were identified by the mutagenesis studies as the high affinity binding site for FN on TG2[46]. HADDOCK clustered 181 structures in 8 clusters, which represented 90.5% of the water-refined models HADDOCK generated. We mapped crosslinks used for guiding of the docking onto best 4 predicted models in each cluster, which resulted in a total of 32 models. Among those 32 models, only 9 models satisfied the distance cutoff for all 7 crosslinks. Out of those 9 models, 3 models belonged to the top-scoring cluster1 with the highest HADDOCK score of -196.6 +/- 18.6. Therefore, we selected the cluster1_1 model.

Submitted distance restraints:

```
assi (segid A and resid 273 and name CA) (segid B and resid 457 and name CA) 35 35 0
assi (segid A and resid 364 and name CA) (segid B and resid 397 and name CA) 35 35 0
assi (segid A and resid 364 and name CA) (segid B and resid 457 and name CA) 35 35 0
assi (segid A and resid 387 and name CA) (segid B and resid 397 and name CA) 35 35 0
assi (segid A and resid 550 and name CA) (segid B and resid 457 and name CA) 35 35 0
assi (segid A and resid 562 and name CA) (segid B and resid 457 and name CA) 35 35 0
assi (segid A and resid  30 and name CA) (segid B and resid 486 and name CA) 35 35 0
```

TG2 and FNI_{7-9}

To dock TG2 and FNI_{7-9}, we submitted a single Lys30(TG2)-Lys486(FN) crosslink as an unambiguous distance restraint. As with the docking of TG2 and GBD, we added residues Lys30, His134, Arg116 to the list of active residues directly involved in the interaction. We also defined linkers between the three FN domains (Ala510-Asp515; Pro557-Gln560) as flexible regions. HADDOCK clustered 147 structures in 11 clusters, which represents 73.5% of the water-refined models HADDOCK generated. Since all predicted models satisfied the crosslink, we carefully examined the best structure in each cluster and found that the second highest scoring model (cluster9_1) supported the parallel alignment of TG2 C-terminal β-barrels with FNI_{8-9} domains, while FNI_7 was in contact with the high affinity binding site (Lys30, Arg116, His134) on the N-terminal β-sandwich of TG2. Moreover, the standard deviations of the second and first scoring models was also overlapping (top scoring: -200.5 +/- 6.4 and second: -184.1 +/- 19.0).

Submitted distance restraints:

```
assi (segid A and resid 30 and name CA) (segid B and resid 486 and name CA) 35 35 0
```

TG2 and $FNIII_{14-15}$

To dock TG2 and $FNIII_{14-15}$ we submitted six crosslinks as unambiguous distance restraints, which DisVis identified as true positives, alongside the active residues at the putative binding interface. The linker connecting the $FNIII_{14}$ and $FNIII_{15}$ domains (Ser1900-Asp1904) was defined as a flexible segment. HADDOCK clustered 193 structures in 7 clusters, which represents 96.5 % of the water-refined models HADDOCK generated. We mapped crosslinks on the best 4 structures in each cluster (28 models) and found that all models satisfied all 6 crosslinks within the distance cutoff. Therefore, we selected the model with the highest HADDOCK score, which was the cluster1_2 predicted model.

Submitted distance restraints:

```
assi (segid A and resid 30  and name CA) (segid B and resid 1837 and name CA) 35 35 0
assi (segid A and resid 30  and name CA) (segid B and resid 1862 and name CA) 35 35 0
assi (segid A and resid 590 and name CA) (segid B and resid 1862 and name CA) 35 35 0
assi (segid A and resid 649 and name CA) (segid B and resid 1862 and name CA) 35 35 0
assi (segid A and resid 677 and name CA) (segid B and resid 1862 and name CA) 35 35 0
assi (segid A and resid 643 and name CA) (segid B and resid 1936 and name CA) 25 25 0
```

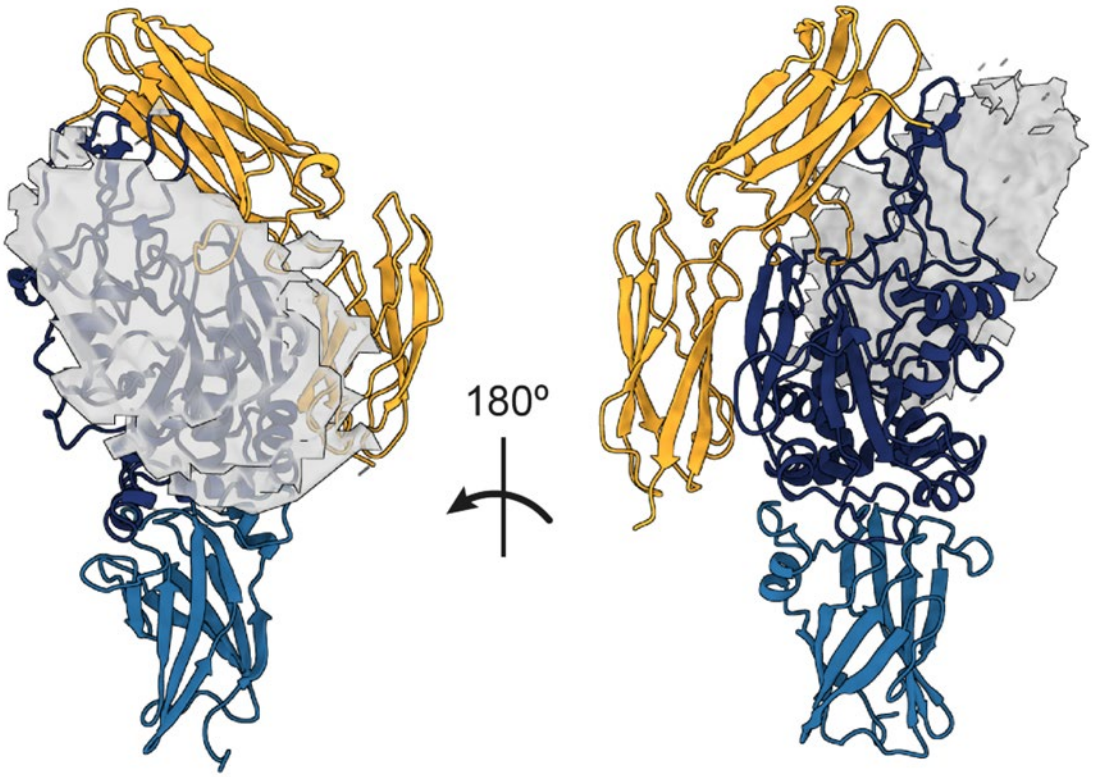

Figure 8.3.1: DisVis analysis of the accessible interaction space between TG2 and GBD. Grey density represents the center of mass of the GBD for complexes consistent 6 restraints. The number of restraints was adjusted for visualization purposes to show interaction interfaces. DisVis analysis was performed using 7 distance restraints.

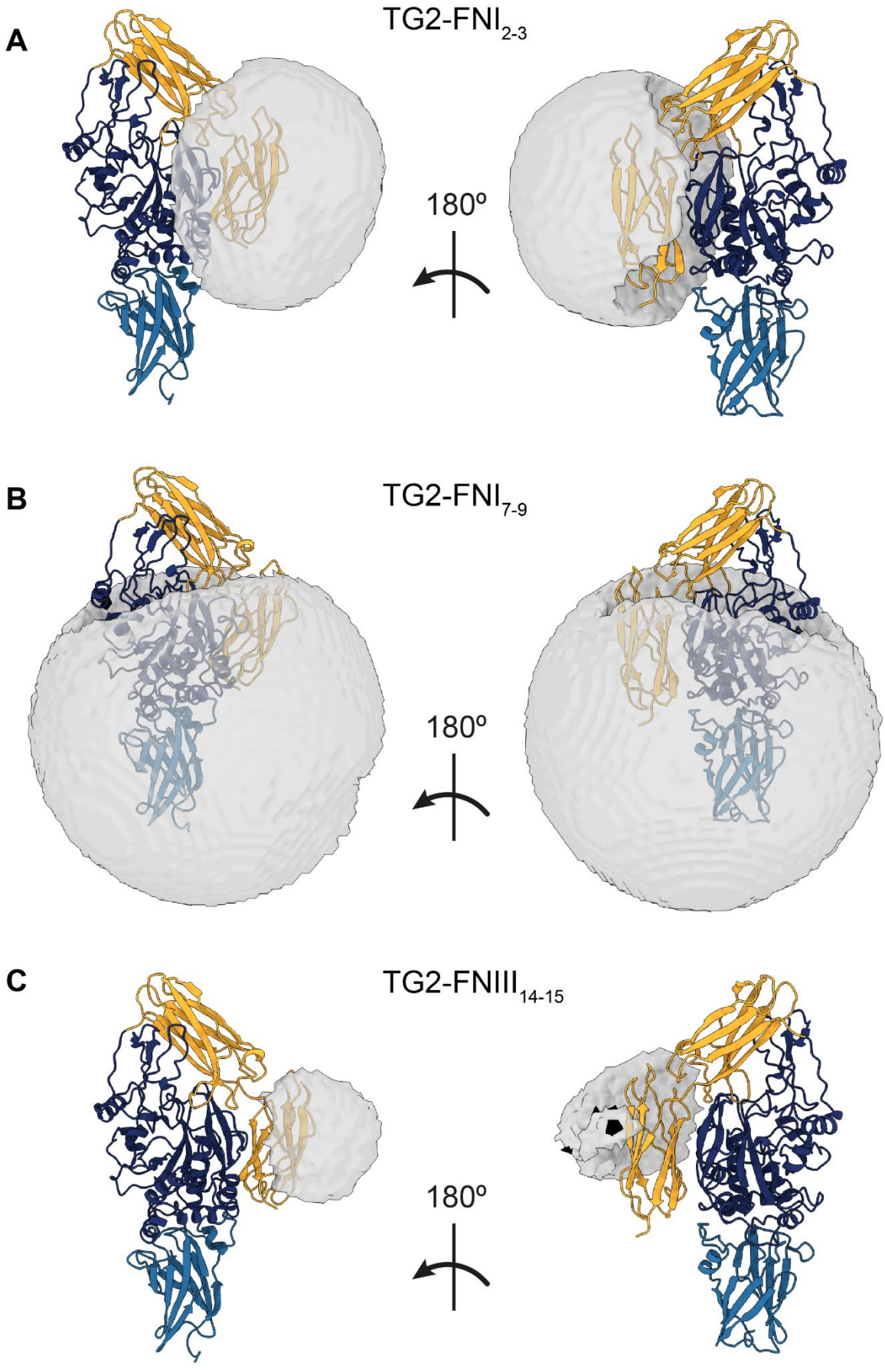
A
TG2-FNI2-3
180º
B
TG2-FNI7-9
180º
C
TG2-FNIII14-15
180º

Figure 8.3.2: DisVis analysis of the accessible interaction space between TG2 and FN fragments. **(A)** Center of mass of FNI_{2-3} shown in a density map representation for complexes consistent with 2 restraints. **(B)** Center of mass of FNI_{7-9} shown in a density map representation for complexes consistent with 1 restraint. **(C)** Center of mass of $FNIII_{14-15}$ shown in a density map representation for complexes consistent with 6 restraints. The number of restraints was adjusted for visualization purposes to show interaction interfaces.

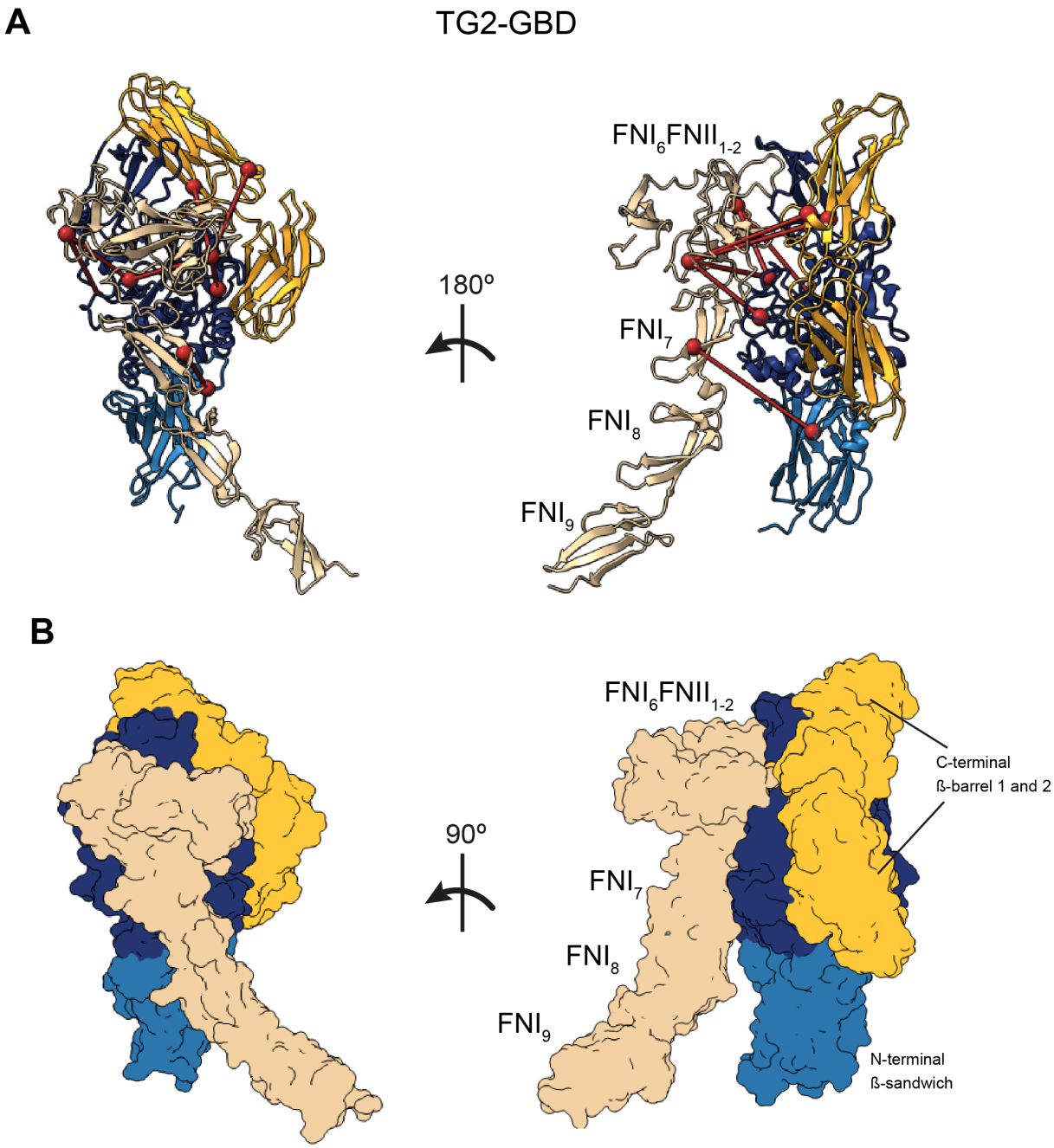

Figure 8.3.3: Predicted model of TG2 and GBD complex obtained using crosslink-guided docking with HADDOCK. (A) Ribbon visualization of the TG2 and GBD complex. The seven experimental crosslinks used for guiding of the docking are visualized together with α-carbons. **(B)** Surface visualization of the TG2 and GBD complex.

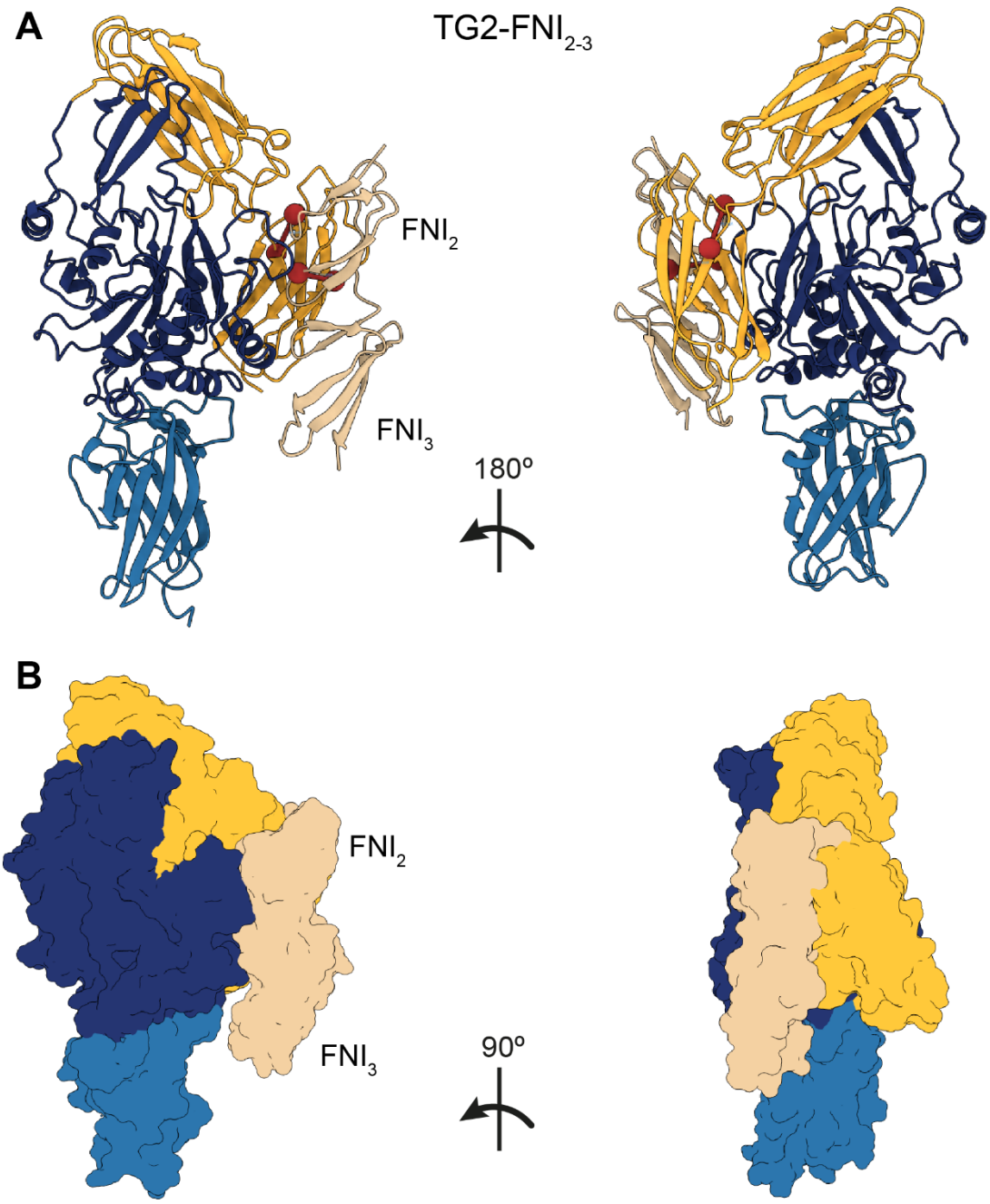

Figure 8.3.4: Predicted model of TG2 and FNI2-3 complex obtained using crosslink-guided docking with HADDOCK. (A) Ribbon visualization of the TG2 and FNI_{2-3} complex. The two experimental crosslinks (637(TG2)-116(FN), 590(TG2)- 100(FN)), used for guiding of the docking are visualized together with α-carbons. **(B)** Surface visualization of the TG2 and FNI_{2-3} complex.

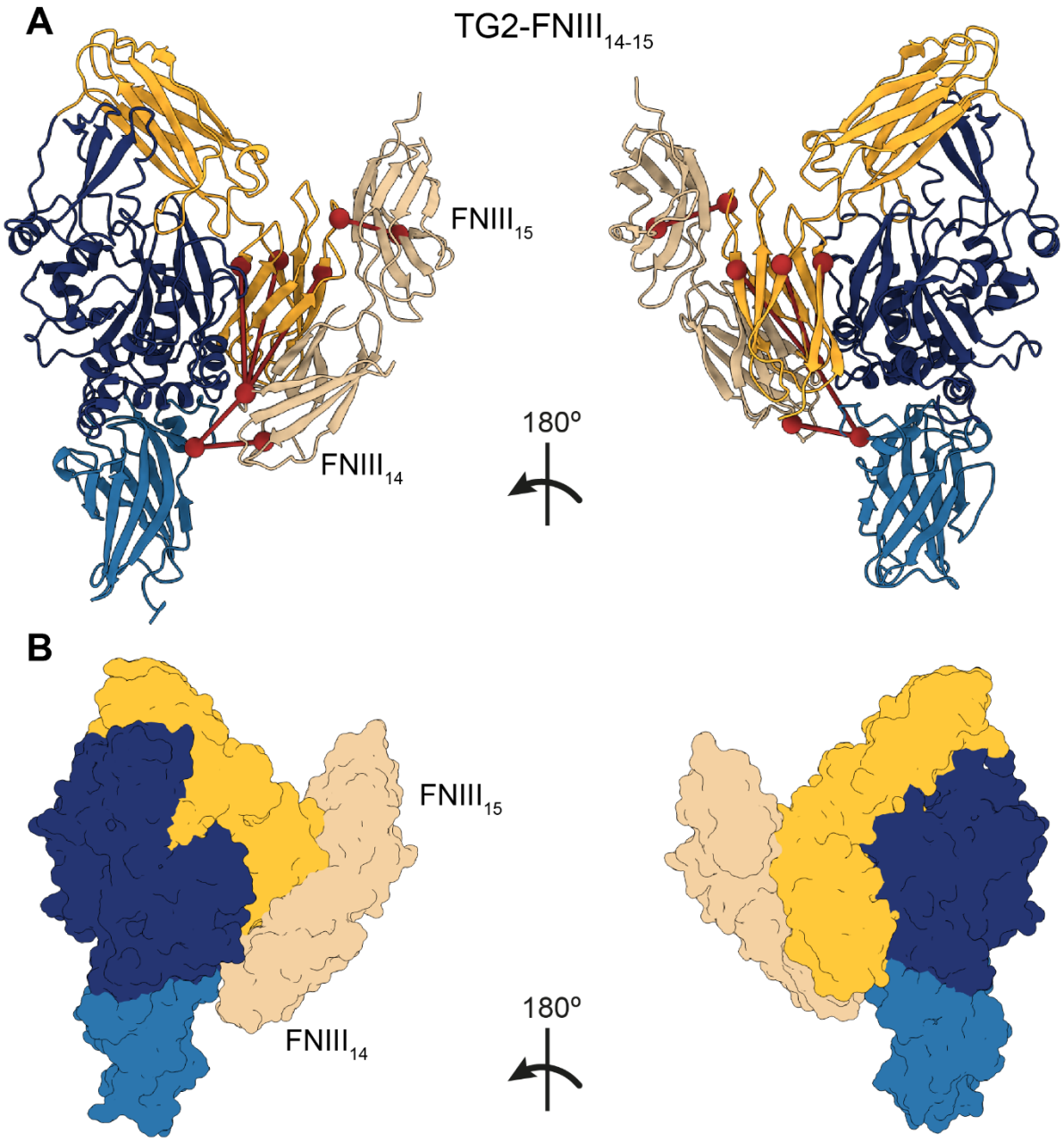

Figure 8.3.5: Predicted model of TG2 in complex with FNIII14-15 as obtained using crosslink-guided docking with HADDOCK. (A) Ribbon visualization of the TG2 and $FNIII_{14-15}$ complex. The six experimental crosslinks used for guiding of the docking are visualized together with α-carbons. **(B)** Surface visualization of the TG2 and $FNIII_{14-15}$ complex.

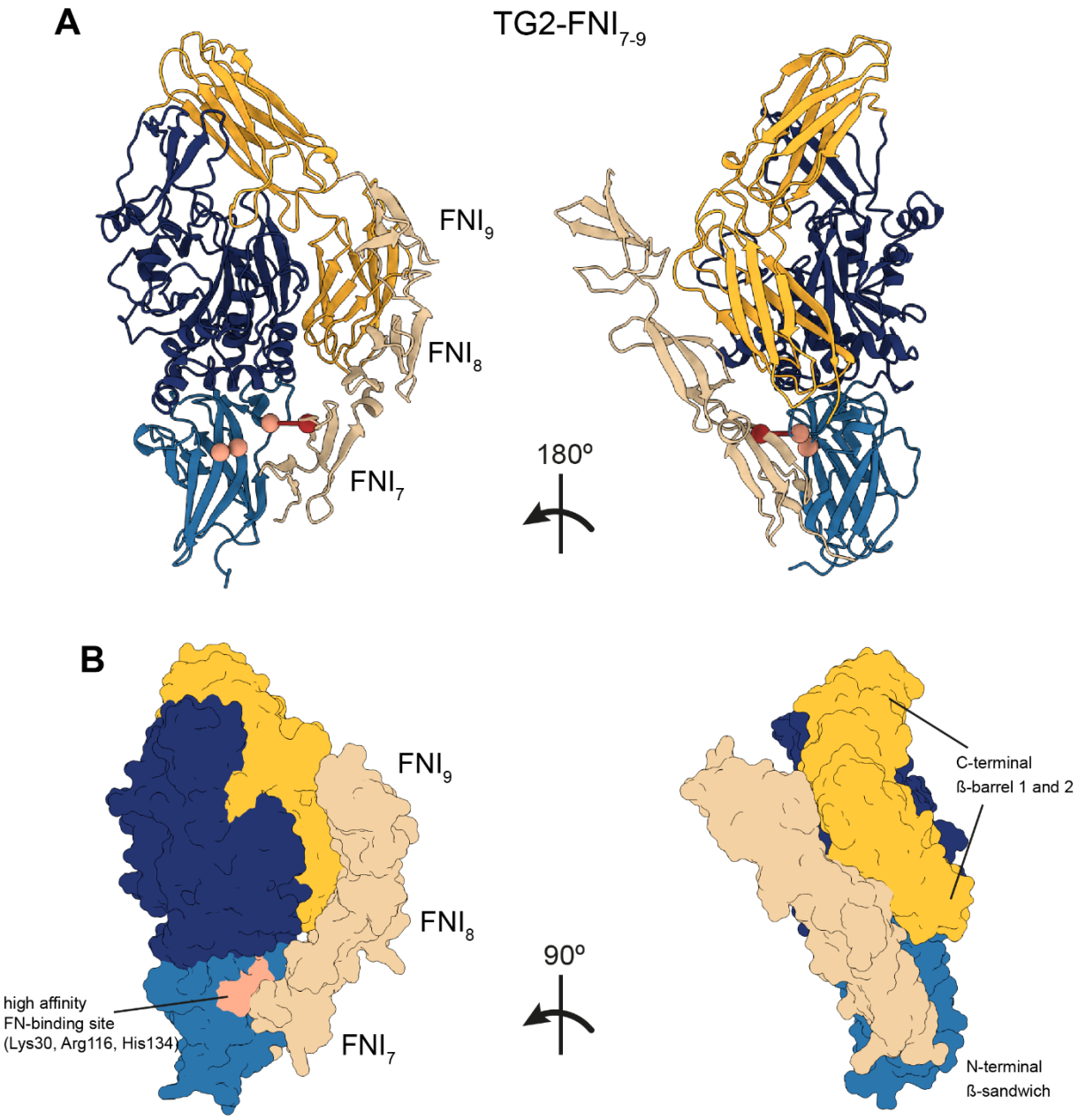

Figure 8.3.6: Predicted model of TG2 and FNI7-9 complex obtained using crosslink-guided docking with HADDOCK. (A) Ribbon visualization of the TG2 and FNI_{7-9} complex. The single experimental crosslink (30(TG2)-486(FN)) used for guiding of the docking is visualized together with the α-carbons. Three residues known to comprise a high affinity binding site on TG2 (Lys30, Arg116, His134) are shown as pink spheres. **(B)** Surface visualization of the TG2 and FNI_{7-9} complex. The high affinity FN-binding site on the N-terminal β-sandwich of TG2 (Lys30, Arg116, His134) is colored in pink. FNI_{8-9} domains of FN align parallel to C-terminal β-barrel domains of TG2, while FNI_7 is in contact with the high affinity binding site on the N-terminal β-sandwich.

9 Materials and methods

9.1 Reagents

Reagents were purchased from Sigma Aldrich, if not mentioned otherwise. Guinea pig liver transglutaminase (gpTG2), Zedira, T006; human tissue transglutaminase (hrTG2, recombinantly produced in *E.coli*), Zedira, T002; short human tissue transglutaminase, aa 1-465 (short hrTG2, barrel 1and 2 deletion mutant, recombinantly produced in *E.coli*), Zedira (T167); inactive human tissue transglutaminase (Cys277Ser mutant, recombinantly produced in *E.coli*), Zedira (T018); Z-DON-Val-Pro-Leu-OMe, Zedira, (Z006); R1R2 peptide[172,190] (amino acid sequence: GLNGENQKEPEQGERGEAGPPLSGLSGNNQGRPSLPGLNGENQKEPEQGERGEAGPP) was manufactured by GenScript ; Alexa Fluor 647 NHS Ester (A20006), ThermoFisher; Alexa Fluor 488 NHS Ester (A20000), ThermoFisher; Alexa Fluor 546 C5 Maleimide (A10258), ThermoFisher; fibronectin proteolytic fragment from human plasma collagen/gelatin-binding domain (GBD), 45kDa, F0162, Sigma Aldrich; anti-fibronectin antibody, gelatin binding domain, close IST-10, from mouse 1 mg/ml (MAB1892), Sigma Aldrich; secondary pAB (ab150107) DK anti-mouse (to MS IgG) (2mg/ml), Abcam; guanosine 5'-diphosphate disodium salt (GDP), G7127 Sigma Aldrich; silicone sheeting, .010'' NRV G/G 40D 12''x12'', SMI specialty manufacturing, inc.; Slide-A-Lyser Dialysis Casette, 20,000MWCO, 66005 ThermoScientific; centrifugal filter units Amicon Ultra – 0.5ml, 30K UFC503096 Merck Millipore; disposable PD-10 desalting columns, GE17-0851-01 Merck Millipore; Amicon Ultra 0.5 ml Ultracel 30k Centrifugal filter units, Merk, Millipore; L-Glutathione oxidised (GSSG), G4376-5G, Lot#SLCJ0220, MW: 612.63g/mol.

9.2 FN isolation from human blood plasma

Fibronectin (FN) was isolated from human plasma according to a previously described protocol[51]. Briefly, 2 mM phenylmethylsulphonyl fluoride (PMSF) and 10 mM ethylenediaminetetraacetic acid (EDTA) were added to human plasma (Zürcher Blutspendedienst SRK) and centrifuged at 15,000 g for 40 min. Next, plasma was passed through a size-exclusion column (PD-10 Desalting columns, GE Healthcare) and loaded onto a gelatin-sepharose 4B column (VWR Schweiz). After washing with phosphate buffered saline (PBS+10mM EDTA), NaCl (1 M in PBS) and arginine (0.2 M in PBS), FN was eluted with 1.5 M arginine in PBS. For FRET labelling of FN with donors and acceptors, the gelatin-sepharose 4B column was washed with 1M NaCl, 1M urea, and was eluted from the column with 6 M urea. FN purity was checked by SDS-PAGE and western blotting (data not shown). The purified FN was aliquoted and stored in 1.5 M arginine in PBS at -80°C.

9.3 Fluorescence labelling of FN and transglutaminases

FN and TG2 were labelled with ALEXA fluorophores (AF) on primary amines with AF488-NHS-ester (for FN fiber stretch assay with calcium titration) and AF674-NHS-ester respectively, to obtain FN-488 and TG2-674 according to the manufacturer's instructions (ThermoFisher). Briefly, the buffer was exchanged to carbonate-bicarbonate labelling buffer (0.2 M $NaHCO_3$ – Na_2CO3, pH 8.5) using Slide-A-Lyser dialysis cassettes. Next, FN was incubated with 40-fold

molar excess of AF488-NHS-ester, and transglutaminases with 45-fold molar excess of AF647-NHS-ester for 1 h at RT on rotator. Free dye was removed by buffer exchange with 50 mM Tris, pH 7.4, using Slide-A-Lyser dialysis cassettes. The protein purity, concentration and degree of labelling were assessed by spectrophotometric measurements of absorbances at 280 nm, 488 nm, and 647 nm. Proteins were aliquoted, snap frozen in liquid nitrogen and stored at -20°C.

9.4 FN labelling with donors and acceptors for FRET

FN was labelled for FRET as previously described[51,129]. Briefly, FN-dimer was doubly labelled on primary amines with AF488 (donor), and with AF546 (acceptor) on the four free cryptic cysteines in modules $FNIII_7$ and $FNIII_{15}$. Briefly, FN was denatured in 6 M Urea by addition of equal volume of 8 M guanidine hydrochloride and incubated for 1 h at RT with 20-fold molar excess of AF546-maleimide. Free dye was removed with buffer exchange to carbonate-bicarbonate buffer (0.2 M $NaHCO_3$ – Na_2CO3, pH 8.5) using size-exclusion chromatography (PD-10 Desalting columns, GE Healthcare). Next, FN in carbonate-bicarbonate buffer was immediately incubated on rotator with a 40-fold molar excess of AF488-NHS-ester for 1 h at room temperature. Afterwards, free dye was removed by buffer exchange to PBS, pH 7.4 using PD-10 Desalting columns. The protein purity, concentration and degree of labelling were assessed by spectrophotometric measurements of absorbances at 280 nm, 488 nm, and 546 nm. FN-FRET was aliquoted, snap-frozen in liquid nitrogen and stored at -80°C. To construct FN-FRET denaturation curve in order to assess the correlation of the FRET signal to the loss of FN tertiary and quaternary structure in solution, FN-FRET was chemically denatured with increasing concentrations of guanidine hydrochloride as was previously described[51,129]. Briefly, the coverslips were blocked with 4% bovine serum albumin (BSA) for 1 h at RT, then washed with PBS. FN-FRET was mixed with an equal volume of guanidine hydrochloride in PBS to a final concentration of 0 M, 0.5 M, 1 M, 2 M, 3 M, and 4 M and incubated for 1 h at RT. To separate FN dimer to monomers, disulfide bonds between two FN monomers were reduced with 50 mM DTT for 1 h at RT, before incubating FN-FRET with 1 M guanidine hydrochloride. A droplet from each solution was added onto the prepared coverslip and imaged using Olympus FV1000 confocal microscope as described below.

9.5 FN fiber stretch assay

FN fiber stretch assay was performed as was previously described[59,63]. FN fibers were manually pulled from a droplet of 0.4 mg/ml FN solution (to avoid inter-molecular FRET, not more than 10% FN-FRET probes were added) with the needle tip and deposited on the silicone sheet mounted on the custom-made uniaxial stretch device. For the single fiber studies, 15 fibers were deposited parallel to the stretch axis. To create intersecting fibers, 10 fibers were deposited both parallel and perpendicular to the stretch axis (Fig. 2A). Next, FN fibers were washed with PBS, and silicone sheets were stretched, relaxed, or left unchanged (native), subjecting the silicone membranes to strains of 100%, -50% or 0% respectively. Previous calibration studies converted the silicone membrane strains to the respective FN fiber strains of 380% (stretched membrane: high FN fiber strain), 20% (relaxed membrane: low FN fiber strain) and 140% (native membrane: medium FN fiber strain) parallel to the stretch axis and

90% (stretched membrane), 219% (relaxed membrane) and 140% (native membrane) perpendicular to the stretch axis[130]. Though the native membrane is not subjected to any strain, FN fibers are typically pre-strained to ~140% due to the forces required to pull them out of the droplet[130]. Next, FN fibers were blocked with 4% BSA for 30 min at RT, then washed with PBS. Transglutaminases were induced into a specific conformation by 30 min pre-incubation with corresponding allosteric effectors, immediately added to FN fibers at a concentration of 10 µg/ml TG2-647 in 50mM Tris, and incubated for 1h at RT. TG2 solutions were added to FN fibers and incubated on fibers for 1 h at RT. This was followed by 3 times washes for 5 min each with 50 mM Tris and fixation with 4% PFA in PBS for 15 min at RT. FN fibers were imaged immediately using Olympus FV1000 confocal microscope.

9.6 Induction of conformational changes of TG2 in the presence of its allosteric effectors

To induce the closed conformation (TG_{GDP}), 10 µg/ml TG2-647 was pre-incubated for 30 min at RT in 1 mM GDP, 1 mM EDTA in 50 mM Tris. To induce catalytically active open conformation, TG2 was pre-incubated for 20 min at RT in 1.2 mM $CaCl_2$ in 50 mM Tris. To induce catalytically inactive extended conformation (effector-free on Fig. 2A), TG2 was pre-incubated with 100 µM "Z-DON" Z006 (Zedira) in 5 mM $CaCl_2$ in 50 mM Tris for 30 min at RT. To get rid of free Z006, the solution was passed through centrifugal filter units (Ultracel 30k, Merk, Millipore), according to manufacturer's instructions, and TG2 bound to Z006 "Z-DON" ($TG2_{Z006}$) was resuspended in 50 mM Tris or 1.2 mM $CaCl_2$ in 50 mM Tris. To oxidise TG2 (oxTG2), guinea pig liver TG2 (gpTG2) was incubated in 2 mM GSSG and 1 mM EDTA in 50 mM Tris for 3 h at 37ºC. oxTG2 was passed through centrifugal filter units and resuspended in 50 mM Tris.

9.7 A dose-response competition assay with the R1R2 peptide

A dose-response competition study with R1R2 peptide and a constant concentration of $TG2_{GDP}$ (10 µg/ml gpTG2) was performed using only horizontally pulled FN-FRET fibers (parallel to the stretch axis) on relaxed membranes (low FN fiber strain). After blocking FN fibers with BSA, 10 µg/ml $TG2_{GDP}$ labelled with AF647 was added to the fibers together with R1R2 peptide at one of the concentrations: 0 µM, 17 µM, 30 µM, 50 µM, 80 µM and 100 µM. $TG2_{GDP}$ and R1R2 were diluted in 1 mM GDP, 1mM EDTA, 1mM $MgCl_2$ in 50 mM Tris. Solutions were incubated on FN fibers for 1 h at RT, FN fibers were washed 3 times for 5 min with 50 mM Tris and fixed with 4% PFA in PBS for 15 min at RT.

9.8 Calcium dose-response experiment

For calcium dose-response experiments, FN labelled only with AF488 was used and guinea pig liver (gpTG2) was labelled with AF-647. Like R1R2 competition studies, only horizontally pulled FN-AF488 fibers (parallel to the stretch axis) on relaxed membranes (low FN fiber strain) were used for this experiment. 10 µg/ml gpTG2 was pre-incubated for 20 min at RT with 1 µM, 100 µM, 250 µM, 500 µM, 1.2 mM, 5 mM, and 10 mM $CaCl_2$ in 50 mM Tris.

10 µg/ml gpTG2 pre-incubated in 1 mM GDP, 1 mM EDTA in 50 mM Tris and 10 µg/ml gpTG2 pre-incubated in 1 mM EDTA in 50 mM Tris were used as controls. gpTG2 solutions were incubated on the fibers for 1 h at room temperature, followed by 3 times for 5 min washes and fixation with 4% PFA in PBS. z-stacks of 3 focal planes with steps of 1micron were obtained with Nikon Visitron Spinning disk confocal, 60x water immersion objective, using 488 and 640 lasers and confGFP and confCy5 emission filter cubes. Images were analyzed with custom-written Python script. Briefly, Gaussian filter (sigma=1) was applied to both FN and TG2 channels, FN channel was thresholded using Otsu algorithm and binary mask created, the mask was applied to both the FN and TG2 channel, replacing all background pixels with NaN, which were excluded from analysis. Then, TG2 signal was normalized pixel-by-pixel to the FN signal (TG2-647/FN-488), and the mean normalized TG2 intensity was calculated over the maximum intensity projection of the normalized TG2 signal.

9.9 FRET confocal microscopy of FN fibers with bound TG2-647

Z-stacks parameters were set so that the acquisition of stacks of three images always started from the top surface of an FN fiber, moving inside the fiber interior (toward silicone membrane), first by 1 and then by 2 µm. Z-stack images were acquired with Olympus FV1000 confocal microscope with 0.9NA 40X water immersion objective, according to a procedure described in detail previously[63]. Briefly, image acquisition was performed in three sequential steps with five channels using excitation and detection windows as depicted in **Figure 7.2.1**. Donor, acceptor, and FRET intensities were measured with 12 nm bandwidths over acceptor and donor emission peaks. TG2-647 excitation and detection were always performed in a separate channel (channel 5), to avoid unwanted crosstalk from the donor AF488 and acceptor AF546 signals upon excitation with 488 nm and 543 nm lasers. FRET-signal correction due to the bleed-through of both donor and acceptor signals into the FRET-excited acceptor channel was performed as was described in detail previously[63,187], and an example of the calculation of β- and γ-correction factors is shown in **Figure 7.2.1**. Acquisition parameters (laser intensity and PMT voltage) were set to maximize the detected signal, while minimizing bleaching and background signal, and were kept constant throughout the experiment.

9.10 Ratiometric FRET image analysis and a correlation of TG2-647 binding with FN-FRET ratios

Ratiometric FRET signal calculation and a correlation of TG2-647 signal to the FN-FRET ratios was performed pixel-by-pixel using custom written Matlab script, which was validated and described in detail before[63]. Briefly, images from different channels were aligned using "imregister" Matlab function, thresholded, mean background signal subtracted, and a mask generated. To remove the pixels at the edges of fibers, where light scattering can create false FRET values, edges of the mask were eroded, then a local 3x3 averaging filter and a one-deviation Gaussian averaging filter were applied. FRET ratios were calculated by dividing pixel-by-pixel the corrected intensity from the acceptor emission due to FRET (channel 1 in **Figure 7.2.1**) by the donor emission (channel 2 in **Figure 7.2.1**). Since the intensity of TG2 signal is dependent on the amount of FN to which it binds, we normalized the TG2-647 signal (channel

5 in **Figure 7.2.1**) by dividing it pixel-by-pixel by the directly excited acceptor AF546 (channel 3 in **Figure 7.2.1**): TG2-647/FN-546. Examples of raw confocal images and corresponding color-coded pixel-by-pixel result after the image processing are shown in **Figure 7.2.2** (intersecting fibers) and **Figure 7.2.3** (horizontal fibers). To plot the mean, maximum intensity projections (MIP) of obtained three-dimensional arrays were taken and the mean intensity of FN-FRET ratio and mean intensity of TG2-647 signal were calculated from MIP and plotted as mean scatterplots. To relate each pixel FN-FRET value with its corresponding TG2 pixel intensity, they were plotted versus each other as two-dimensional density plots (**Figure 4.3.2**).

9.11 Statistical analysis for FN fiber stretch assays

Since not all data had a normal distribution, statistical significance between groups was assessed by the nonparametric two-sided Wilcoxon rank sum statistic for two samples, which does not imply data distribution normality, as was performed previously in a similar study[63]. Statistical significance was assessed for *$0.01 \leq p < 0.05$; **$0.001 \leq p < 0.01$; ***$10^{-5} \leq p < 0.001$; **** $10^{-6} \leq p < 10^{-5}$; ***** $p < 10^{-6}$

9.12 Microplate FN-TG2 binding assay

To determine the concentrations of full-length FN and with 45kDa-FN at which microtiter plates would be coated with approximately a similar number of binding sites for TG2, titration experiments were carried out. For this, 96-well black flat non-transparent bottom microtiter plates were coated with 0.1, 0.2, 0.4, 0.6, 0.8, 1, 2, 5, 10, 20, 30 and 50 µg/ml full-length FN or 45 kDa-FN GBD in PBS at 4°C overnight. Wells were washed with PBS 3 times for 5 min and blocked for 30 min with 4% BSA in PBS, followed by another wash. Full-length FN and 45 kDa-FN GBD were detected with monoclonal mouse anti-FN antibody with epitope within GBD (MAB1892, Sigma), clone IST-10 (1:1000 in 2% BSA in PBS) for 1 h at RT, followed by incubation with anti-mouse pAB ab150107 AF647 (1:1000 in 2% BSA in PBS) for another 1 h at RT, and finally fixation with 4% PFA for 10 min. After each antibody incubation wells were washed with PBS 3 times for 5 min. Fluorescence intensity was measured with Tecan Spark plate reader. Obtained data were fit using a four-parameter logistic (4PL) curve. Next, the concentration of the full-length FN at which 95% of maximum intensity was reached were calculated from the curve as 2.4 µg/ml. Then, the concentration of 45 kDa-FN GBD, which corresponded to the 95% of full-length FN intensity was calculated from the curve as 0.6 µg/ml. In all subsequent experiments, microtiter plates were coated with 2.4 µg/ml of full-length FN and 0.6 µg/ml of 45 kDa-FN GBD.

For experiments with wild type gpTG2 and short hrTG2, 96-well black flat non-transparent bottom microtiter plates were coated with either 2.4 µg/ml full-length FN or 0.6 µg/ml 45 kDa-FN at 4°C overnight. After incubation, wells were washed 3 times for 5 min with 50 mM Tris and blocked for 30 min with 4% BSA in 50 mM Tris at RT. TG2-647 solutions of 0.1, 0.5, 1, 2, 3, 5, 7, 10 µg/ml were prepared in either 1mM GDP, 1 mM EDTA in 50 mM Tris, or 1 mM EDTA in 50 mM Tris, or 1.2 mM $CaCl_2$ in 50 mM Tris, or 1.2 mM $CaCl_2$, 100 µM Z006 in 50 mM Tris and pre-incubated for 20 min at RT. Transglutaminase dilutions were added to the FN-coated wells and incubated at RT for 1 h. Wells were washed 3 times for 5 min with 50 mM

Tris and fixed with 4% PFA for 10 min. Fluorescence intensity was measured with Tecan Spark plate reader. Obtained data were fit using a four-parameter logistic (4PL) curve and plotted.

9.13 Chemical crosslinking

TG2 was incubated either with either full-length FN, or the 45-kDa FN fragment in 1 mM GDP, 1 mM EDTA in PBS for 1 hr at room temperature. Crosslinking experiments were performed with 50 µg total protein at concentrations of approximately 0.7 mg/ml for samples containing full-length fibronectin and at approximately 0.25 mg/ml for samples containing the 45-kDa FN (GBD). All steps were performed on a ThermoMixer (Eppendorf) at 750 rpm.

Lysine crosslinking with a 1:1 mixture of non-deuterated and deuterated disuccinimidyl suberate (DSS-d_0/d_{12}, Creative Molecules) was initiated by adding the crosslinking reagent from a freshly prepared 25 mM stock solution in dimethyl formamide to a final concentration of 1 mM[191]. The reaction was allowed to proceed for 60 min at room temperature (23 °C) before adding ammonium bicarbonate to a final concentration of 50 mM and incubating further for 30 min.

Crosslinking of carboxyl groups and of amine groups with carboxyl groups was performed using non-deuterated and deuterated pimelic dihydrazide (PDH-d_0, ABCR, and PDH-d_{10}, Sigma-Aldrich) and the coupling reagent 4-(4,6-dimethoxy-1,3,5-triazin-2-yl)-4-methylmorpholinium (DMTMM) chloride (Sigma-Aldrich). Stock solutions were prepared in phosphate-buffered saline at concentrations of 140 mM (PDH, 1:1 mixture of d_0 and d_{10}) and 520 mM (DMTMM). Two different reaction conditions were used for combined PDH/DMTMM crosslinking: 44 mM PDH and 88 mM DMTMM or 22 mM PDH and 11 mM DMTMM, respectively[192]. Samples were incubated for 60 min at room temperature and the reaction was stopped by passing the sample solutions through a Zeba spin desalting column (ThermoFisher Scientific) according to the manufacturer's instructions. Quenched samples solutions were subsequently evaporated to dryness in a vacuum centrifuge.

9.14 Sample processing and mass spectrometric analysis

Dried samples were dissolved in 50 µL of 8 M urea solution. Cysteine thiols were reduced by addition of tris(2-carboxyethyl)phosphine to a final concentration of 2.5 mM and incubation for 30 min at 37 °C, and free thiol groups were alkylated with iodoacetamide (final concentration of 5 mM, incubation for 30 min at room temperature, protected from light) prior to enzymatic digestion.

Proteolysis with endoproteinase Lys-C and trypsin was performed as follows: The reduced and alkylated samples were diluted to 5.5 M urea with 150 mM ammonium bicarbonate solution and Lys-C (Wako) was added at an enzyme-to-substrate ratio of 1:100. After incubation at 37 °C for 2 h, the solutions were further diluted to 1 M urea with 50 mM ammonium bicarbonate, and trypsin (Promega) was added at an enzyme-to-substrate ratio of 1:50. Trypsin digestion was then allowed to proceed overnight.

Proteolysis with chymotrypsin (Roche) was performed by diluting the solutions to 1 M urea with 50 mM ammonium bicarbonate and adding the protease at an enzyme-to-substrate ratio of 1:50. Samples were incubated for 2 h at 25 °C.

Enzymatic digestion reactions were stopped by adding 100% formic acid to a final concentration of 2% (v/v) and samples were purified by solid-phase extraction using 50 mg SepPak tC18 cartridges (Waters). Purified samples were fractionated by peptide size exclusion chromatography (SEC) on an Äkta micro FPLC system equipped with a Superdex 30 Increase column (300 × 3.2 mm, GE/Cytiva). The separation was carried out with a mobile phase consisting of water/acetonitrile/trifluoroacetic acid (30/70/0.1, v/v/v) at a flow rate of 50 µL/min. For each sample, three or four 100 µL fractions from the high mass region were individually collected and evaporated to dryness.

Liquid chromatography-tandem mass spectrometry was performed on an Easy nLC-1200 HPLC system coupled to an Orbitrap Fusion Lumos mass spectrometer equipped with a Nanoflex electrospray ionization source (all ThermoFisher Scientific). Approximately one µg or less for each SEC fraction was injected and the peptides were separated on an Acclaim PepMap RSLC column (150 mm × 75 µm, 2 µm particle size, ThermoFisher Scientific) at a flow rate of 300 nl/min. The mobile phase gradient was set to 11% B to 40% B in 60 min, with mobile phase A = water/acetonitrile/formic acid (98/2/0.15, v/v/v) and B = acetonitrile/water/formic acid (80/20/0.15, v/v/v). The mass spectrometer was operated in the data-dependent, "top speed" acquisition mode with a cycle time of 3 s. Precursor ion spectra were acquired in the orbitrap analyzer at a resolution setting of 120000. Precursors with a charge state between +3 and +7 were selected for collision-induced fragmentation in the linear ion trap with a normalized collision energy of 35%. For most experiments, fragment ions were detected in the orbitrap analyzer at a resolution setting of 30000. For some samples, one of the two replicate injections was performed with MS/MS detection in the linear ion trap to achieve higher sensitivity. In that case, fragmentation conditions remained unchanged, and the linear ion trap was operated with a "rapid" scan rate.

9.15 Identification of crosslinked peptides

Preliminary experiments found unequivocal evidence for UniProt proteoforms P02751-1 and -9, with isoform 1 having the most proteotypic peptides. This isoform was therefore included in the sequence database and all numbering refers to it. In addition, the database consisted of the sequence of transglutaminase and the sequence of three contaminants identified from E. coli: CH60, SLYD, and ARNA. Target/decoy searches were performed using a decoy database containing the reversed sequences of all database entries.

MS/MS spectra were searched against these databases using xQuest, version 2.1.5 (available from https://gitlab.ethz.ch/leitner_lab)[193]. The crosslinking specificities were set as follows: For DSS, K and the protein N terminus; for PDH, D and E; for DMTMM, K with D and K with E. For Lys-C/trypsin digestion, protease specificity was set to cleavage after K and R unless followed by P, with a maximum of two missed cleavages per peptide allowed (excluding the crosslinking site, if applicable). For chymotrypsin, cleavage was considered after F, L, M, W, and Y, with a maximum number of missed cleavages set to four. Carbamidomethylation of C was treated as a fixed modification, and oxidation of M as a variable modification during the search. The mass error was set to ±15 ppm for orbitrap detection and to 0.2 Da and 0.3 Da for the detection of "common" and "xlink" fragment ion types for detection in the linear ion trap, respectively. All identifications were further filtered for a %TIC value ≥0.1 and a main xQuest

score of ≥20 for fragment ion detection in the ion trap and ≥25 for fragment ion detection in the orbitrap analyzer, respectively. MS/MS spectra of the remaining candidates were evaluated and rejected if they did not contain at least four bond cleavages in total per peptide or at least three consecutive bond cleavages per peptide.

9.16 Integrative structural modeling and docking

A detailed description of the entire modeling process, which allows for replication of the results is provided in Supplementary Notes 1-3, overview of the modeling workflow is provided in Supplementary Fig.13. Briefly, I-TASSER[165] was used for structural refinement of available PDB templates of TG2, and FN fragments using experimental crosslinks within those regions as distance restraints (Supplementary Note 1). ROBETTA[167] and AlphaFold[168] were used for modeling of FN_{7-9} and 45-kDa FN (GBD), followed by evaluation of resulting structures using QMEAN[169]. Intra-protein crosslinks were used both as distance restraints for structural refinement and for evaluation of resulting models based on their compatibility/non-compatibility with the imposed distance cutoff. To assign compatibility/non-compatibility criteria, Euclidean distances between β-carbons (CB-CB) of the crosslinked residues were calculated using Xwalk[166]. Euclidean distance cut-offs we set as follows: for DSS < 35 Å, ED for DMTMM < 25 Å, ED for PDH < 35Å, and crosslinks above the set cut-off value were considered as incompatible. Inter-protein crosslinks were validated and active residues predicted using DisVis[153] (Supplementary Note 2). To predict active residues involved in the interaction, we submitted to DisVis server residues with relative solvent accessibility of at least 40% for either the main chain or the side chain. The relative solvent accessibility was calculated using NACCESS[170]. Inter-protein crosslinks that were predicted by DisVis to be incompatible were excluded from further docking steps. Docking was performed with HADDOCK[151]. Detailed description of each docking run, and all used distance restraints are provided in Supplementary Note 3. Experimental inter-protein crosslinks were mapped onto predicted models and Euclidean distances calculated using Xwalk. Obtained structures were visualized with ChimeraX[194].

9.17 Data availability statement

The mass spectrometry proteomics data have been deposited to the ProteomeXchange Consortium[195] via the PRIDE[196] partner repository with the dataset identifier PXD043976. Integrative modelling structures have been deposited to PDB-Dev[197] with accession codes PDBDEV_00000216, PDBDEV_00000218, PDBDEV_00000219 and PDBDEV_00000220.

10 Appendices

10.1 Protocols

This appendix provides ready-to-print protocols. Protocols include detailed practical tips and important information regarding bioconjugation of proteins with fluorescent dyes and performing FN-fiber stretch assays.

10.1.1 Fluorescent bioconjugation of proteins (TG2 or FN) with amine-reactive dyes

Aim: Fluorescently label proteins (TG2 or FN) on primary amines with amine-reactive dyes which can be further used in the FN-fiber stretch assay.

Materials:

- Slide-A-Lyzer Dialysis Cassettes MWCO 20,000 (Thermo Scientific).

Note: *Molecular Weight Cutoff (MWCO) of 20,000 is optimal for purification of both TG2 and FN. You may need to select a different MWCO depending on the MW of your protein of choice.*

- **Labelling buffer** - carbonate-bicarbonate buffer: 0.1M $NaHCO_3$:Na_2CO_3, pH 8.5

Note: *pH of 8.5 is important for conjugation reaction of succinimidyl esters of the dye with primary amines of the proteins. Avoid using Tris-buffer as it will compete in reaction with primary amines and will significantly decrease the efficiency of the labelling.*

- 1X PBS, pH 7.4
- Amine reactive dyes (succinimidyl ester or NHS-ester) with the fluorophore of choice
- Protein of interest to be fluorescently labelled (resuspended)

Procedure:

1. Hydrate dialysis device.
   - ☐ **Slide-A-Lyzer:** Slip cassette into appropriate buoy and hydrate in labelling buffer for at least 2min.

2. Add sample.
   - ☐ **Slide-A-Lyzer:** Use syringe with the needle. Fill the syringe with protein, insert the tip of the needle through one of the four syringe ports located at each corner of the cassette.

Note: *Take care not to touch membrane! Don't go with the syringe tip too deep inside. When the syringe tip is just visible, is usually enough.*

- ☐ Inject protein slowly. Then withdraw air by pulling up on the syringe piston until both membranes stick closely together and no air remains in the cassette.

3. Dialysis to exchange arginine solution to the labelling buffer.
   - ☐ Leave the dialysis device in large enough amount of labelling buffer so that it floats freely (typically 400-500 times the volume of the sample to be dialyzed, so for 1ml sample size use ~ 400-500ml of dialysis buffer)
   - ☐ Add magnetic stirrer and leave at 4C on the plate stirrer (don't create a strong vortex!)
   - ☐ Exchange buffer, preferably 3 times: first after 2-4 h, second time after 6-8 h, and finally after 10-14 h (Note that times are approximate, can be adjusted or extended, see explanation below).

4. Labelling.
   - ☐ After buffer exchange is complete, transfer all the protein (now in labelling buffer) from the dialysis device to the eppi-tube:
   - ☐ **Slide-A-Lyzer:** Fill the syringe with a volume of air equal to the sample size. Insert the needle tip into one of the four the needle ports located at the corners of the cassette. Inject air slowly and carefully to separate the membranes. Turn the unit so the needle is at the bottom and collect all the solution by pulling on the syringe piston.

Note: *Take care not to touch the membrane with the needle! Once you insert the needle, don't twist it! Don't insert the needle too deep!*

   - ☐ Measure the absorbance of protein in solution with spectrophotometer at 280nm (A_{280}) with Nanodrop and calculate its concentration as described in step 6.
   - ☐ Calculate the amount of the molar excess of the dye in relation to the protein. (Typically, with amine-reactive dyes I used ~40 Molar excess of the dye).
   - ☐ Add the required amount of the dye directly to the tube with the protein in the labelling buffer, wrap tube in aluminium foil and put on rotator (in 50ml falcon) at lowest speed (do not shake!) for 1 h at room temperature.

5. Removing free dye residues.
   - ☐ Repeat steps 1-3, but this time use PBS as the dialysis buffer.
   - ☐ Collect the labelled protein.
   - ☐ To calculate the concentration and the degree of labelling (DOL) of the recovered protein, measure the absorbance with Nanodrop at 280nm (A_{280}) and the respective excitation wavelength of the fluorophore used for labelling. See step 6 on how to calculate DOL.
   - ☐ If desired, labelled FN can be aliquoted, frozen in liquid nitrogen and stored at -80C.

6. Calculating protein concentration from absorbance using Beer-Lambert equation.

- **Calculate protein concentration (M):**

$$Protein\ concentration\ (M) = \frac{A280-(Amax \times CF)}{\varepsilon(p)}$$

,where

ε(p): *protein molar extinction coefficient ($M^{-1}\ cm^{-1}$)*

A_{max} : *Absorbance of a dye solution measured at a max wavelength (λmax) for the dye molecule*

CF: *correction factor for absorbance at 280 nm by the dye*

- ***Calculate the degree of labelling (DOL) – moles of dye per mole of protein:***

$$DOL = \frac{Amax\ of\ labelled\ protein}{\varepsilon(d) \times protein\ concentration\ (M)}$$

,where

ε(d): *molar extinction coefficient of the dye*

- Extinction coefficient (ε(d)) and correction factor (CF) of the dye are typically provided by the manufacturer of the dye (can be found on their web-page)
- Protein molar extinction coefficient (ε(p)) is dependent on the protein tryptophan (W), tyrosine (Y) and cysteine (C) amino acid composition, described with the equation

$$\varepsilon(d) = (nW \times 5500) + (nY \times 1490) + (nC \times 125)$$

,where

n: *the number of each amino acid residue in the protein*

- Protein molar extinction coefficient (ε(p)) can be calculated from amino acid sequence of the protein using a web-tool: https://web.expasy.org/protparam/

General information:

Note 1: *You may conjugate amine-reactive reagents with virtually any protein or peptide. TFP, SDP, and succinimidyl esters are preferred for the conjugation to proteins because they form a very stable amide bond between the dye or hapten and the protein. Amine-reactive reagents react with non-protonated aliphatic amine groups, including the amine terminus of proteins and the ε-amino group of lysines. The ε-amino group has a pK_a of around 10.5; to maintain this amine group in the non-protonated form, the conjugation must take place in a buffer with slightly basic pH. It is important to avoid buffers that contain primary amines, such as Tris, as these will compete for conjugation with the amine-reactive compound. After the amide-bond reaction formation between protein and the dye has been completed, there will be a lot of free dye residues in the solution, which has to be purified. Purification can be*

achieved by performing the dialysis procedure with Slizde-A-Lyzer Cassettes (as described in this protocol), or size-exclusion chromatography (e.g. PD-10 columns) or another suitable purification procedure of your choice.

Note 2: *Dialysis is the movement of molecules by diffusion from high concentration to low concentration through a semi-permeable membrane. Only those molecules that are small enough to fit through the membrane pores are able move through the membrane and reach equilibrium with the entire volume of solution in the system. Once equilibrium is reached, there is no further net movement of the substance because molecules will be moving through the pores into and out of the dialysis unit at the same rate. To remove additional unwanted substance, it is necessary to replace the dialysis buffer so that a new concentration gradient can be established. Once the buffer is changed, movement of particles from high (inside the membrane) to low (outside the membrane) concentration will resume until equilibrium is once again reached. With each change of dialysis buffer, substances inside the membrane are further purified by a factor equal to the volume difference of the two compartments. For example, if one is dialyzing 1 ml of sample against 200 ml of dialysis buffer, the concentration of the dialyzable substance at equilibrium will be diluted 200 less than at the start. Each new exchange against 200 ml of new dialysis buffer will dilute the sample 200 times more. For example, for three exchanges of 200 ml, the sample will be diluted 200 x 200 x 200 or 8,000,000 times, assuming complete equilibrium was reached each time before the dialysis buffer was changed.*

Note 3: *Labelling reactions are influenced by the molar ratio of the reactants, contaminants, and the activity of labelling reagent. In general, a high level of labelling is desirable in fluorescence-based assays because it allows high sensitivity. However, over-labelling can cause quenching because of fluorescent emissions from one dye molecule being absorbed by neighboring dye molecules. when labelling any molecule with a fluorescent dye, test different dye: protein molar ratios (molar excess) in the conjugation reaction to determine which conditions allow for optimal labelling levels and result in signal-to-noise ratios compatible with the intended assays. (Molar excess of the dye required for addition to the protein can change depending on how fresh the dye is. Amine-reactive dyes become less reactive with time and require higher molar excess, up to 50-60. From my experience, fresh dyes are very reactive and require smaller molar excess, around 10-20. Molar excess should be determined by trial).*

10.1.2 Fibronectin-fiber stretch assay

FN-fiber stretch assay with TG2 was adapted from procedures that were previously described[59,63].

Materials:

- PBS and/or another buffer of choice, e.g., Tris
- 1% BSA in PBS
- 4% BSA in PBS
- FN labeled with donor (AF488) and acceptor (AF546) pairs in PBS
- Unlabeled FN in PBS
- 4% PFA

- Uniaxial stretch device, clamp for microscopy imaging
- Silicone sheeting, .010'' NRV G/G 40D 12''x12'', SMI specialty manufacturing, inc.

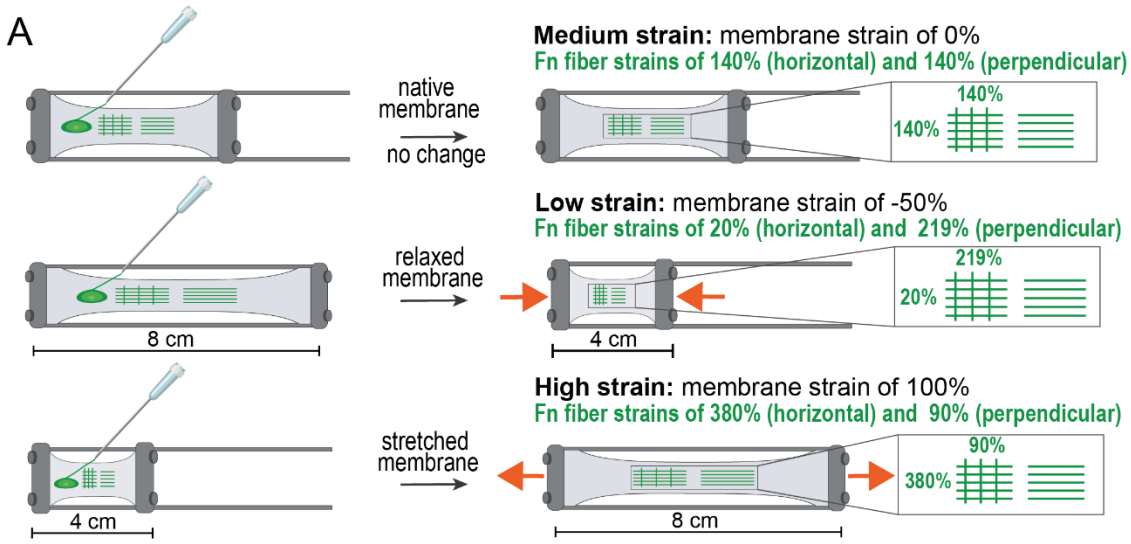

Figure 10.1.1: A schematic view of the FN fiber-stretch assay and the experimental setup. FN fibers were manually pulled with a needle from a droplet of concentrated FN and deposited onto a silicone membrane mounted on the custom-made stretch device. FN-fibers were pulled in two ways, either parallel to the stretch axis, or both parallel and perpendicular as intersections. Membrane was left unchanged – native, relaxed from the pre-strained position or stretched. The approximate FN-fiber strain corresponding to the silicone membrane strain was determined by previous calibration studies and are indicated on the cartoon. In this study, FN-fiber strains along the stretch axis of relaxed, native, and stretched membranes are referred to as low strain (20%), medium strain (140%) and high strain (380%) respectively. TG2-AF647 was added to the deposited fibers and incubated in the presence of various effectors that change its conformational state.

Table 10.1-1: FN fiber pulling, and uniaxial stretch device set up – short summary.

Step	Native membrane	Stretched membrane	Relaxed membrane
STEP 1: Stretch device with the mounted silicone membrane starting point (distance measured between the two inner edges of a stretching device)	Start at ~4cm	Start at 4cm (pre-relaxed)	Pre-strained at 8cm
STEP 2: Pull fibers with the needle tip from a 2-4 µl droplet of 0.4mg/ml ~5% Fn-FRET (to avoid inter-molecular FRET, not more than 10% FN-FRET must be used[51]). Choice of			

<table>
<tr><td colspan="4">direction for fiber pulling can be parallel to the stretch axis or as intersections parallel and perpendicular to the stretch axis</td></tr>
<tr><td colspan="4">STEP3: Let FN-fibers dry for ~10 min, wash with PBS 2X, then leave 1% BSA in PBS on the fibers</td></tr>
<tr><td>STEP4:
Membrane stretching and final Fn-fiber strain after membrane stretching[130]</td><td>Stretch device remains at ~4cm (no change) = 0% membrane strain
Horizontal: ~140% Fn-fiber strain; 0% membrane strain
Perpendicular: ~140% Fn-fiber strain</td><td>Stretch membrane to 8cm = 100% membrane strain

Horizontal: ~380% Fn-fiber strain;
Perpendicular: ~90% Fn-fiber strain</td><td>Relax membrane to 4cm = 50% membrane strain

Horizontal: ~20% Fn-fiber strain;
Perpendicular: ~219% Fn fiber strain</td></tr>
<tr><td colspan="4">STEP5: Block for 20 min with 4% BSA in Tris at RT, pH 7.4</td></tr>
<tr><td colspan="4">STEP6: Wash with PBS (or another buffer of choice) 2x</td></tr>
<tr><td colspan="4">STEP7: Add the FN binding partner in 1% BSA in PBS (or another buffer of choice), incubate for 1hr at RT</td></tr>
<tr><td colspan="4">STEP8: Wash 3x for 5 min with 1%BSA PBS, pH 7.4</td></tr>
<tr><td colspan="4">STEP9: Fix with 4% PFA in PBS for 15 min at RT</td></tr>
<tr><td colspan="4">STEP10: Wash 3x for 5 min with PBS, pH 7.4</td></tr>
<tr><td colspan="4">STEP11: Image on the same day with Olympus FV1000 confocal microscope</td></tr>
</table>

Detailed steps:

☐ Always thaw FN-FRET (labeled with AF488/AF546 donor/acceptor pairs[51]) on ice. Prepare 0.4 mg/ml 5%-10% FN-FRET solution (must not be more than 10% FN-FRET to avoid intermolecular FRET[51]). Store on ice in dark.

Tip #1: *Centrifuge thawed FRET-labelled FN at ~5000 rpm for 10 min to remove aggregates which accumulate after thawing! Carefully transfer FN-FRET to another tube without disturbing the pellet. Otherwise, aggregates intercalate into the fibers and make the image analysis afterwards difficult.*

☐ Cut out silicone sheeting according to a "bone shaped" stencil and mount it on the uniaxial stretch device.

☐ Clean silicone sheets with 70% ethanol for ~5 min, rinse with diH_2O, blow dry with the air stream.

☐ Pull fibers with the needle tip from a 2-4 µl droplet of 0.4mg/ml ~5% FN-FRET. When needed, additional 2µl droplet was added as the previous dried out. Choice direction for fiber pulling - parallel to the stretch axis as intersections parallel and perpendicular to the stretch axis (see Fig. 1 for reference). Pull 12-15 fibers.

☐ Let FN-fibers dry for ~10 min, wash with PBS 2X, then leave in 1% BSA in PBS. Keep fibers in the dark, whenever possible during incubation steps.

Tip #2: *to prevent the buffer form leaking off the membrane, draw the edges of the membrane with the hydrophobic pen. It helps a bit to retain the buffer on the fibers.*

- ☐ Silicone sheets were left either native (~4cm), stretched (from ~4 cm to ~8 cm) or relaxed (from ~8 cm to ~4 cm.) (see Fig. 1 for reference).
- ☐ Block for 20 min with 4% BSA in PBS at RT, pH 7.4 PBSs-buffer wash 1x.
- ☐ Wash with PBS (or another buffer of choice) 2x
- ☐ Add the FN binding partner in 1% BSA in PBS (or another buffer of choice), incubate for 1hr at RT

Tip #3: *Centrifuge fluorescently labeled TG2 solutions at ~5000rpm for 8-10 min to remove aggregates which accumulate after thawing!! Otherwise, aggregates can create high background and problems during the imaging step.*

- ☐ Wash 3x for 5 min with 1%BSA PBS, pH 7.4
- ☐ Fix with 4% PFA in PBS for 15 min at RT
- ☐ Wash 3x for 5 min with PBS, pH 7.4
- ☐ Image on the same day with Olympus FV1000 confocal microscope

10.2 ImageJ macro for quick batch conversion of images saved in a proprietary format to TIFF format

The ImageJ macro presented in this section allows to quickly convert a batch of images proprietary format into TIFF format, which can be further used as an input for further image processing and analysis steps. After opening an image, this ImageJ macro splits the image into "_TG2" and "_FN" channels and saves each one separately as a TIFF file in the folder of choice. Therefore, this ImageJ macro was developed and only works for cases when image acquisition was performed in two separate channels.

ImageJ macro performs the following steps:

1. Asks the user to select a folder with images to be processed.
2. Asks the user to select a folder to save the output images in TIFF format.
3. Ignores the ".oif.file" folder. This is specific for Olympus proprietary format. In case of processing images in format other than Olympus proprietary format ".oif", comment out these lines.
4. Splits channels and stitches "_TG2" or "_FN" to the respective channel.
5. Saves each image in TIFF format in the folder selected by the user.

```
/*November 2020
 * Kateryna Selcuk kateryna.selcuk@hest.ethz.ch
 * This ImajeJ Macro is written to open Olympus images (.oif format), skipping the .oif.file folder,
 * which Olympus system saves for every oif. image
 * Macro splits the Fn and TG2 channel, renames every image by stitching "_Fn" or "_TG2" to the end respectively.
 * Macro loops over all images in the folder which user selects. Images are saved as TIFF format.
 */
//START HERE

//batch processing
//will ask the user to select a folder with images for processing
input_path = getDirectory("Choose a folder with images you want to process");
//will return a list of the names of all files in the selected folder
fileList = getFileList(input_path);

//will ask the user to select a folder in which the TIFF images should be saved
input_path_save=getDirectory("Choose a directory to save TIFF images");

//loops over all images in the given directory
for (f=0; f<fileList.length; f++){
    //closes all open images before the next loop starts
    run("Close All");

     /*Olympus along with .oif image (which should be opened), generates a folder (.oif.file) for each .oif image.
     When the batch processing script tries to open .oif.file the macro crashes. The block of code below
     is necessary to only open .oif format file skipping the .oif.file folder, which is a odd-numbered element in the fileList */

    // open only oif. image formated file
    if (f%2==0) {
    open(input_path + fileList[f]);
    // if f is odd-numbered, macro will skip to the top of the loop without completing the rest of the loop
    } else continue;

    //print statement displays file that is being processed
    print("The loop number is: "+f+" The image path is: "+ input_path + fileList[f]);

    //Get image title and store it in "title" variable
    title = getTitle();
    //print statement displays the image title that is being processed
    print("The loop number is: " +f+  " The image title is: "+ title);
    //splits the aqcuired image name into two strings using '.' delimiter
    new_title=split(title, '.');

    //Splitting channels; stiching name of the channel ('_Fn' or '_TG2') to the end of the image name
    run("Split Channels");
    selectWindow("C1-"+title);
    rename(new_title[0]+"_Fn");
    Fn_channel_title=getTitle();
    //saves Fn channel image-stack as TIFF
    saveAs("Tiff", input_path_save+Fn_channel_title);

    selectWindow("C2-"+title);
    rename(new_title[0]+"_TG2");
    TG2_channel_title=getTitle();
    //saves TG2 channel image-stack as TIFF
    saveAs("Tiff", input_path_save+TG2_channel_title);
}

//THE END!
```

10.3 Condensed script which computes TG2-AF647 intensity and normalizes it pixel-by-pixel to FN-AF488 intensity

We present here a description of the image analysis script which was developed to compute TG2 intensity (TG2 was labeled with AF647) and normalize it pixel-by-pixel to FN-fiber intensity (FN was labelled with AF488), when TG2 was bound to FN-fibers. Normalized TG2-AF647FN-AF488 intensity can thus be used to evaluate TG2 binding affinity to FN-fibers under various conditions or presence of some allosteric TG2 effectors. The script was developed using a web-based interactive computer platform Jupyter Notebook and is presented here in a Notebook format. The code is presented in blocks as it was originally

written in Jupyter Notebook cells, and for clarity the output of each cell is included as well. Detailed comments are provided for each relevant block of code to explain the purpose of each step. Therefore, the code or parts of the code can be copied and pasted into Jupyter Notebook as required.

Although the code was originally developed for correlating the intensity of TG2 bound to FN-fibers in the FN-fiber stretch assay, it can be applied to compute intensity of any other ligand bound to manually pulled FN-fibers as well as the native FN fibrillar matrix assembled by fibroblasts. This code can be applied if the ligand and FN are labelled/stained with one distinct fluorophore each. The code was used to compute the results presented in (**Figure 4.3.1**).

The code performs the following steps:

1) Takes two images as an input. The images from FN and TG2 channel must be provided in TIFF format. Images must be renamed with a string ending with "_Fn" or "_TG2" for the FN and TG2 channels respectively. (Run ImageJ macro presented in section C.1 to separate the channels, assign proper names, and save images in TIFF format).
2) Applies Gaussian filter to both images for smoothing.
3) Applies automatic thresholding Otsu algorithm to the Fn channel (can be changed to a fixed threshold value).
4) Generates a binary mask.
5) Applies the mask to both FN channel and TG2 channel.
6) Normalizes pixel-by-pixel TG2 signal to FN signal by dividing elements in the resulting TG2 3Darray by the corresponding elements in the FN 3Darray.
7) Takes maximum intensity projection (MIP) of the normalized TG2-3D array.
8) Calculates the mean intensity, standard deviation of the normalized TG2 MIP.
9) Saves results in a .csv file.

==========START OF THE CODE==========

```
from tkinter import filedialog
import numpy as np
import pandas as pd
import matplotlib.pyplot as plt
import os, re, glob
import skimage.io as io
#load filters module of scikit-image to apply filtering functions
import skimage.filters
import skimage.morphology

#Propmt the user to select a directory with images
img_dir = filedialog.askdirectory(title="Select the directory with tiffs to
process")

#Search for Fn channel and TG2 channel images separately.
#Store the path to all Fn channel and TG2 channel images in the selected
#directory in two separate lists
channel_Fn = np.sort(glob.glob(os.path.join(img_dir,'*_Fn.tif')))
channel_TG2 = np.sort(glob.glob(os.path.join(img_dir,'*_TG2.tif')))
```

```
#Create a dataframe in which results will be stored
results = pd.DataFrame(columns=['file_name','mean_intensity', 'std','mean_i
ntensity_TG2_MIP','std_TG2_MIP'])

for ind in range(len(channel_Fn)):

    # load the images of each channel
    image_Fn = skimage.io.imread(channel_Fn[ind])
    image_TG2 = skimage.io.imread(channel_TG2[ind])

    #Apply gaussian filter for smoothing, sigma=1. Warning: typically the g
aussian filter used above rescales the image between 0 and 1.
    #To preserve the original range of the image, specify preserve_range=Tr
ue.
    image_Fn_gauss = skimage.filters.gaussian(image_Fn, sigma=1,multichanne
l=False,preserve_range=True)

    #Similarly, do the same for TG2 channel
    image_TG2_gauss = skimage.filters.gaussian(image_TG2, sigma=1,multichan
nel=False,preserve_range=True)

    #Determine the threshold. Apply Otsu thresholding algorithm to Fn chann
el to the third slice,
    #because the signal intensity there is the weakest
    threshold = skimage.filters.threshold_otsu(image_Fn_gauss[:,:,2])

    #Create a binary mask from the thresholded Fn channel
    mask = image_Fn_gauss > threshold

    #Apply the mask to the TG2 channel, replacing all background pixels wit
h NaN
    masked_image_TG2 = np.where(mask,image_TG2_gauss,np.NaN)

    #Apply the mask to the Fn channel, replacing all background pixels with
NaN
    masked_image_Fn = np.where(mask,image_Fn_gauss,np.NaN)

    #Normalize TG2 signal to Fn signal pixel-by-pixel after the mask was ap
plied
    normalized_TG2 = masked_image_TG2 / masked_image_Fn

    #Take the maximum intensity  projection of the TG2 normalized stack
    normalized_TG2_MIP = np.amax(normalized_TG2,axis=2)

    #Recover the filename and add it to the dataframe. Split along "\\"!!!
    filename = channel_TG2[ind].split('\\')[-1]

    #Calculate the mean normalized TG2 intensity before taking MIP.
    mean_intensity = np.nanmean(normalized_TG2)

    #Calculate the standard deviation of the normalized TG2 before taking M
IP.
```

```
    std = np.nanstd(normalized_TG2)

    #Calculate the mean of the MIP.
    mean_intensity_MIP = np.nanmean(normalized_TG2_MIP)

    #Calculate the standard deviation of the MIP.
    std_MIP = np.nanstd(normalized_TG2_MIP)

    #Append all calculated statistics to the results dataframe. Keep ignore
_index=True, otherwise appending doesn't work!
    results = results.append({'file_name': filename, 'mean_intensity': mean
_intensity,'std': std,'mean_intensity_TG2_MIP': mean_intensity_MIP,'std_TG2
_MIP': std_MIP},ignore_index=True)

    #Flatten the multidimensional array into 1D array in a row-major order
#   pooled_TG2_MIP=normalized_TG2_MIP.flatten(order='C')
    #save flattened array as csv.
#   np.savetxt(filename, pooled_TG2_MIP)

#Save results. This will prompt the user to select a directory to save the
results.
name_to_save=img_dir.split('/')[-1]+"_results.csv"
results.to_csv(os.path.join(filedialog.askdirectory(title="Select a directo
ry to save the results"),name_to_save),index = False, header=True)
results
```

==========END OF THE CODE==========

References

1. Humphrey, J. D., Dufresne, E. R. & Schwartz, M. A. Mechanotransduction and extracellular matrix homeostasis. *Nat. Rev. Mol. Cell Biol.* **15**, 802–812 (2014).
2. Janmey, P. A., Fletcher, D. A. & Reinhart-King, C. A. Stiffness sensing by cells. *Physiol. Rev.* **100**, 695–724 (2020).
3. Chaudhuri, O., Cooper-White, J., Janmey, P. A., Mooney, D. J. & Shenoy, V. B. Effects of extracellular matrix viscoelasticity on cellular behaviour. *Nature* **584**, 535–546 (2020).
4. Valet, M., Siggia, E. D. & Brivanlou, A. H. Mechanical regulation of early vertebrate embryogenesis. *Nat. Rev. Mol. Cell Biol.* **23**, 169–184 (2022).
5. Panciera, T., Citron, A., Di Biagio, D., Battilana, G., Gandin, A., Giulitti, S., Forcato, M., Bicciato, S., Panzetta, V., Fusco, S., Azzolin, L., Totaro, A., Dei Tos, A. P., Fassan, M., Vindigni, V., Bassetto, F., Rosato, A., Brusatin, G., Cordenonsi, M. & Piccolo, S. Reprogramming normal cells into tumour precursors requires ECM stiffness and oncogene-mediated changes of cell mechanical properties. *Nat. Mater.* **19**, 797–806 (2020).
6. Mario C. Benn, Willi Weber, Enrico Klotzsch, V. V. and S. A. P. Tissue transglutaminase in fibrosis — more than an extracellular matrix cross-linker. *Curr. Opin. Biomed. Eng.* **10**, 156–164 (2019).
7. Eckert, R. L. Transglutaminase 2 takes center stage as a cancer cell survival factor and therapy target. *Mol. Carcinog.* **58**, 837–853 (2019).
8. Eckert, R. L., Fisher, M. L., Grun, D., Adhikary, G., Xu, W. & Kerr, C. Transglutaminase is a tumor cell and cancer stem cell survival factor. *Mol. Carcinog.* **54**, 947–958 (2015).
9. Nurminskaya, M. V. & Belkin, A. M. Cellular Functions of Tissue Transglutaminase. in *International Review of Cell and Molecular Biology* vol. 294 1–97 (Elsevier Inc., 2012).
10. Telci, D. & Griffin, M. Tissue transglutaminase (TG2) - A wound response enzyme. *Front. Biosci.* **11**, 867–882 (2006).
11. Verderio, E. A. M., Johnson, T. & Griffin, M. Tissue transglutaminase in normal and abnormal wound healing: Review article. *Amino Acids* **26**, 387–404 (2004).
12. Upchurch, H. F., Conway, E., Patterson, M. K. & Maxwell, M. D. Localization of Cellular Transglutaminase on the Extracellular Matrix After Wounding: Characteristics of the

Matrix Bound Enzyme. *J. Cell. Physiol.* **149**, 375–382 (1991).

13. Agnihotri, N. & Mehta, K. Transglutaminase-2: evolution from pedestrian protein to a promising therapeutic target. *Amino Acids* **49**, 425–439 (2017).
14. Verderio, E. A. M., Telci, D., Okoye, A., Melino, G. & Griffin, M. A Novel RGD-independent Cell Adhesion Pathway Mediated by Fibronectin-bound Tissue Transglutaminase Rescues Cells from Anoikis. *J. Biol. Chem.* **278**, 42604–42614 (2003).
15. Eckert, R. L., Kaartinen, M. T., Nurminskaya, M., Belkin, A. M., Colak, G., Johnson, G. V. W. & Mehta, K. Transglutaminase regulation of cell function. *Physiol. Rev.* **94**, 383–417 (2014).
16. Siegel, M., Strnad, P., Watts, R. E., Choi, K., Jabri, B., Omary, M. B. & Khosla, C. Extracellular transglutaminase 2 is catalytically inactive, but is transiently activated upon tissue injury. *PLoS One* **3**, 1–11 (2008).
17. Plugis, N. M., Palanski, B. A., Weng, C. H., Albertelli, M. & Khosla, C. Thioredoxin-1 selectively activates transglutaminase 2 in the extracellular matrix of the small intestine: Implications for celiac disease. *J. Biol. Chem.* **292**, 2000–2008 (2017).
18. Gundemir, S., Colak, G., Tucholski, J. & Johnson, G. V. W. Transglutaminase 2: A molecular Swiss army knife. *Biochim. Biophys. Acta - Mol. Cell Res.* **1823**, 406–419 (2012).
19. Belkin, A. M. Extracellular TG2: Emerging functions and regulation. *FEBS J.* **278**, 4704–4716 (2011).
20. Telci, D., Wang, Z., Li, X., Verderio, E. A. M., Humphries, M. J., Baccarini, M., Basaga, H. & Griffin, M. Fibronectin-tissue transglutaminase matrix rescues RGD-impaired cell adhesion through syndecan-4 and β1 integrin co-signaling. *J. Biol. Chem.* **283**, 20937–20947 (2008).
21. Akimov, S. S., Krylov, D., Fleischman, L. F. & Belkin, A. M. Tissue transglutaminase is an integrin-binding adhesion coreceptor for fibronectin. *J. Cell Biol.* **148**, 825–38 (2000).
22. Wang, Z., Collighan, R. J., Gross, S. R., Danen, E. H. J., Orend, G., Telci, D. & Griffin, M. RGD-independent cell adhesion via a tissue transglutaminase-fibronectin matrix promotes fibronectin fibril deposition and requires syndecan-4/2 and α5β1 integrin co-signaling. *J. Biol. Chem.* **285**, 40212–40229 (2010).
23. Wang, Z., Telci, D. & Griffin, M. Importance of syndecan-4 and syndecan -2 in osteoblast cell adhesion and survival mediated by a tissue transglutaminase-fibronectin complex.

Exp. Cell Res. **317**, 367–381 (2011).

24. Akimov, S. S. & Belkin, A. M. Cell-surface transglutaminase promotes fibronectin assembly via interaction with the gelatin-binding domain of fibronectin: a role in TGFβ-dependent matrix deposition. *J. Cell Sci.* **114**, 2989–3000 (2001).
25. Yang, L., Friedland, S., Corson, N. & Xu, L. GPR56 inhibits melanoma growth by internalizing and degrading its ligand TG2. *Cancer Res.* **74**, 1022–1031 (2014).
26. Yakubov, B., Chelladurai, B., Schmitt, J., Emerson, R., Turchi, J. J. & Matei, D. Extracellular tissue transglutaminase activates noncanonical NF-κB signaling and promotes metastasis in ovarian cancer. *Neoplasia (United States)* **15**, 609–619 (2013).
27. Fisher, M. L., Keillor, J. W., Xu, W., Eckert, R. L. & Kerr, C. Transglutaminase is required for epidermal squamous cell carcinoma stem cell survival. *Mol. Cancer Res.* **13**, 1083–1094 (2015).
28. Mangala, L. S., Fok, J. Y., Zorrilla-Calancha, I. R., Verma, A. & Mehta, K. Tissue transglutaminase expression promotes cell attachment, invasion and survival in breast cancer cells. *Oncogene* **26**, 2459–2470 (2007).
29. Chen, S. H., Lin, C. Y., Lee, L. T., Chang, G. D., Lee, P. P., Hung, C. C., Kao, W. Te, Tsai, P. H., Schally, A. V., Hwang, J. J. & Lee, M. T. Up-regulation of fibronectin and tissue transglutaminase promotes cell invasion involving increased association with integrin and MMP expression in A431 cells. *Anticancer Res.* **30**, 4177–4186 (2010).
30. Bagatur, Y., Ilter Akulke, A. Z., Bihorac, A., Erdem, M. & Telci, D. Tissue transglutaminase expression is necessary for adhesion, metastatic potential and cancer stemness of renal cell carcinoma. *Cell Adhes. Migr.* **12**, 138–151 (2018).
31. Sima, L. E., Matei, D. & Condello, S. The Outside-In Journey of Tissue Transglutaminase in Cancer. *Cells* **11**, 1–24 (2022).
32. Shinde, A., Paez, J. S., Libring, S., Hopkins, K., Solorio, L. & Wendt, M. K. Transglutaminase-2 facilitates extracellular vesicle-mediated establishment of the metastatic niche. *Oncogenesis* **9**, 1–12 (2020).
33. Yakubov, B., Chen, L., Belkin, A. M., Zhang, S., Chelladurai, B., Zhang, Z. Y. & Matei, D. Small molecule inhibitors target the tissue transglutaminase and fibronectin interaction. *PLoS One* **9**, 1–10 (2014).
34. Sima, L. E., Yakubov, B., Zhang, S., Condello, S., Grigorescu, A. A., Nwani, N. G., Chen, L., Schiltz, G. E., Arvanitis, C., Zhang, Z. Y. & Matei, D. Small molecules target the interaction

between tissue transglutaminase and fibronectin. *Mol. Cancer Ther.* **18**, 1057–1068 (2019).

35. May Khanna, Bhadrani Chelladurai, Aruna Gavini, Liwei Li, Minghai Shao, David Courtney, John J. Turchi, D. M. and S. M. Targeting ovarian tumor cell adhesion mediated by tissue transglutaminase. *Mol. Cancer Ther.* **10**, 626–636 (2011).
36. Keillor, J. W., Apperley, K. Y. P. & Akbar, A. Inhibitors of tissue transglutaminase. *Trends Pharmacol. Sci.* **36**, 32–40 (2015).
37. Pinkas, D. M., Strop, P., Brunger, A. T. & Khosla, C. Transglutaminase 2 undergoes a large conformational change upon activation. *PLoS Biol.* **5**, 2788–2796 (2007).
38. Liu, S., Cerione, R. A. & Clardy, J. Structural basis for the guanine nucleotide-binding activity of tissue transglutaminase and its regulation of transamidation activity. *Proc. Natl. Acad. Sci. U. S. A.* **99**, 2743–2747 (2002).
39. Király, R., Demény, M. Á. & Fésüs, L. Protein transamidation by transglutaminase 2 in cells: A disputed Ca 2+-dependent action of a multifunctional protein. *FEBS J.* **278**, 4717–4739 (2011).
40. Stamnaes, J., Pinkas, D. M., Fleckenstein, B., Khosla, C. & Sollid, L. M. Redox regulation of transglutaminase 2 activity. *J. Biol. Chem.* **285**, 25402–25409 (2010).
41. Iversena, R., Myslingb, S., Hnidaa, K., Jørgensenb, T. J. D. & Sollida, L. M. Activity-regulating structural changes and autoantibody epitopes in transglutaminase 2 assessed by hydrogen/deuterium exchange. *Proc. Natl. Acad. Sci. U. S. A.* **111**, 17146–17151 (2014).
42. Mariani, P., Carsughi, F., Spinozzi, F., Romanzetti, S., Meier, G., Casadio, R. & Bergamini, C. M. Ligand-Induced Conformational Changes in Tissue Transglutaminase: Monte Carlo Analysis of Small-Angle Scattering Data. *Biophys. J.* **78**, 3240–3251 (2000).
43. Staffler, R., Pasternack, R., Hils, M., Kaiser, W. & Möller, F. M. Nucleotide binding kinetics and conformational change analysis of tissue transglutaminase with switchSENSE. *Anal. Biochem.* **605**, 1–7 (2020).
44. Soluri, M. F., Boccafoschi, F., Cotella, D., Moro, L., Forestieri, G., Autiero, I., Cavallo, L., Oliva, R., Griffin, M., Wang, Z., Santoro, C. & Sblattero, D. Mapping the minimum domain of the fibronectin binding site on transglutaminase 2 (TG2) and its importance in mediating signaling, adhesion, and migration in TG2-expressing cells. *FASEB J.* **33**, 2327–2342 (2019).

45. Turner, P. M. & Lorand, L. Complexation of Fibronectin with Tissue Transglutaminase*. *Annu. Rev. Physiol* **28**, 688–691 (1989).

46. Cardoso, I., Østerlund, E. C., Stamnaes, J., Iversen, R., Andersen, J. T., Jørgensen, T. J. D. & Sollid, L. M. Dissecting the interaction between transglutaminase 2 and fibronectin. *Amino Acids* **49**, 489–500 (2017).

47. Jeong, J. M., Murthy, S. N. P., Radek, J. T. & Lorand, L. The fibronectin-binding domain of transglutaminase. *J. Biol. Chem.* **270**, 5654–5658 (1995).

48. Hang, J., Zemskov, E. A., Lorand, L. & Belkin, A. M. Identification of a novel recognition sequence for fibronectin within the NH2-terminal β-sandwich domain of tissue transglutaminase. *J. Biol. Chem.* **280**, 23675–23683 (2005).

49. Radek, J. T., Jeong, J.-M., Prasanna Murthy, S. N., Inghamt, K. C. & Lorand, L. Affinity of human erythrocyte transglutaminase for a 42-kDa gelatin-binding fragment of human plasma fibronectin. *Proc. Natl. Acad. Sci. USA* **90**, 3152–3156 (1993).

50. Abu-Lail, N. I., Ohashi, T., Clark, R. L., Erickson, H. P. & Zauscher, S. Understanding the elasticity of fibronectin fibrils: Unfolding strengths of FN-III and GFP domains measured by single molecule force spectroscopy. *Matrix Biol.* **25**, 175–184 (2006).

51. Smith, M. L., Gourdon, D., Little, W. C., Kubow, K. E., Eguiluz, R. A., Luna-morris, S. & Vogel, V. Force-Induced Unfolding of Fibronectin in the Extracellular Matrix of Living Cells. *PLoS Biol.* **5**, 2243–2254 (2007).

52. Maurer, L. M., Ma, W. & Mosher, D. F. Dynamic structure of plasma fibronectin. *Crit. Rev. Biochem. Mol. Biol.* **51**, 213–227 (2016).

53. Schwarzbauer, J. E. & DeSimone, D. W. Fibronectins, their fibrillogenesis, and in vivo functions. *Cold Spring Harb. Perspect. Biol.* **3**, 1–19 (2011).

54. Früh, S. M., Schoen, I., Ries, J. & Vogel, V. Molecular architecture of native fibronectin fibrils. *Nat. Commun.* **6**, 1–10 (2015).

55. Vogel, V. Unraveling the Mechanobiology of Extracellular Matrix. *Annu. Rev. Physiol.* **80**, 353–387 (2018).

56. Ingham, K. C., Brew, S. A., Huff, S. & Litvinovich, S. V. Cryptic self-association sites in type III modules of fibronectin. *J. Biol. Chem.* **272**, 1718–1724 (1997).

57. Zhong, C., Chrzanowska-Wodnicka, M., Brown, J., Shaub, A., Belkin, A. M. & Burridge, K. Rho-mediated contractility exposes a cryptic site in fibronectin and induces fibronectin matrix assembly. *J. Cell Biol.* **141**, 539–551 (1998).

58. Hocking, D. C., Sottile, J. & McKeown-Longo, P. J. Fibronectin's 111-1 Module Contains a Conformation-dependent Binding Site for the Amino-terminal Region of Fibronectin. *J. Biol. Chem.* **269**, 19183–19191 (1994).

59. Little, W. C., Smith, M. L., Ebneter, U. & Vogel, V. Assay to mechanically tune and optically probe fibrillar fibronectin conformations from fully relaxed to breakage. *Matrix Biol.* **27**, 451–461 (2008).

60. Chabria, M., Hertig, S., Smith, M. L. & Vogel, V. Stretching fibronectin fibres disrupts binding of bacterial adhesins by physically destroying an epitope. *Nat. Commun.* **1**, 1–9 (2010).

61. Kubow, K. E., Vukmirovic, R., Zhe, L., Klotzsch, E., Smith, M. L., Gourdon, D., Luna, S. & Vogel, V. Mechanical forces regulate the interactions of fibronectin and collagen i in extracellular matrix. *Nat. Commun.* **6**, 1–11 (2015).

62. Wang, Y., Yan, J. & Goult, B. T. Force-Dependent Binding Constants. *Biochemistry* **58**, 4696−4709 (2019).

63. Ortiz Franyuti, D., Mitsi, M. & Vogel, V. Mechanical Stretching of Fibronectin Fibers Upregulates Binding of Interleukin-7. *Nano Lett.* **18**, 15–25 (2018).

64. Katt, W. P., Antonyak, M. A. & Cerione, R. A. The diamond anniversary of tissue transglutaminase: a protein of many talents. *Drug Discov. Today* **23**, 575–591 (2018).

65. Nirmal K. Sarkar, Donald D. Clarke, H. W. An enzymically catalyzed incorporation of amines into proteins. *Biochim. Biophys. Acta* **25**, 451–452 (1957).

66. Savoca, M. P., Tonoli, E., Atobatele, A. G. & Verderio, E. A. M. Biocatalysis by transglutaminases: A review of biotechnological applications. *Micromachines* **9**, 9–11 (2018).

67. Szondy, Z., Korponay-Szabó, I., Király, R., Sarang, Z. & Tsay, G. J. Transglutaminase 2 in human diseases. *Biomed.* **7**, 1–13 (2017).

68. Hideaki Nakaoka, Dianne M. Perez, Kwang Jin Baek, Tanya Das, Ahsan Husain, Kunio Misono, Mie-Jae Im, and R. M. G. Gh: a GTP-Binding Protein with Transglutaminase Activity and Receptor Signaling Function. *Science (80-.).* **264**, 1593–1596 (1994).

69. Mishra, S. & Murphy, L. J. Tissue transglutaminase has intrinsic kinase activity: identification of transglutaminase 2 as an insulin-like growth factor-binding protein-3 kinase. *J. Biol. Chem.* **279**, 23863–23868 (2004).

70. Hasegawa, G., Suwa, M., Ichikawa, Y., Ohtsuka, T., Kumagai, S., Kikuchi, M., Sato, Y. &

Saito, Y. *A novel function of tissue-type transglutaminase: protein disulphide isomerase*. *Biochem. J* vol. 373 (2003).

71. Di Sabatino, A., Vanoli, A., Giuffrida, P., Luinetti, O., Solcia, E. & Corazza, G. R. The function of tissue transglutaminase in celiac disease. *Autoimmunity Reviews* vol. 11 746–753 at https://doi.org/10.1016/j.autrev.2012.01.007 (2012).
72. Rauhavirta, T., Hietikko, M., Salmi, T. & Lindfors, K. Transglutaminase 2 and Transglutaminase 2 Autoantibodies in Celiac Disease: a Review. *Clinical Reviews in Allergy and Immunology* vol. 57 23–38 at https://doi.org/10.1007/s12016-016-8557-4 (2019).
73. Dudek, S. M. & Johnson, G. V. W. Transglutaminase facilitates the formation of polymers of the/3-amyloid peptide. *Brain Res.* **651**, 129–133 (1994).
74. Miller, M. L. & Johnson, G. V. W. Transglutaminase Cross-Linking of the τ Protein. *J. Neurochem.* **65**, 1760–1770 (1995).
75. Jeitner, T. M., Pinto, J. T., Krasnikov, B. F., Horswill, M. & Cooper, A. J. L. Transglutaminases and neurodegeneration. *J. Neurochem.* **109**, 160–166 (2009).
76. Verma, A., Guha, S., Wang, H., Fok, J. Y., Koul, D., Abbruzzese, J. & Mehta, K. Tissue transglutaminase regulates focal adhesion kinase/AKT activation by modulating PTEN expression in pancreatic cancer cells. *Clin. Cancer Res.* **14**, 1997–2005 (2008).
77. Condello, S., Cao, L. & Matei, D. Tissue transglutaminase regulates β-catenin signaling through a c-Src-dependent mechanism. *FASEB J.* **27**, 3100–3112 (2013).
78. Eckert, R. L., Fisher, M. L., Grun, D., Adhikary, G., Xu, W. & Kerr, C. Transglutaminase is a tumor cell and cancer stem cell survival factor. *Mol. Carcinog.* (2015) doi:10.1002/mc.22375.
79. William P. Katt, Marc A. Antonyak, R. A. C. Opening up about Tissue Transglutaminase: When Conformation Matters More than Enzymatic Activity. *Med One* **3**, 1–23 (2018).
80. Caron, N. S., Munsie, L. N., Keillor, J. W. & Truant, R. Using FLIM-FRET to Measure Conformational Changes of Transglutaminase Type 2 in Live Cells. *PLoS One* **7**, (2012).
81. Achyuthans, K. E. & Greenberg, C. S. Identification of a Guanosine Triphosphate-binding Site on Guinea Pig Liver Transglutaminase. *J. Biol. Chem.* **262**, 1901–1906 (1987).
82. Lai, T. S., Slaughter, T. F., Peoples, K. A., Hettasch, J. M. & Greenberg, C. S. Regulation of human tissue transglutaminase function by magnesium- nucleotide complexes. Identification of distinct binding sites for Mg-GTP and Mg-ATP. *J. Biol. Chem.* **273**, 1776–

1781 (1998).

83. Di Venere, A., Rossi, A., De Matteis, F., Rosato, N., Finazzi Agrò, A. & Mei, G. Opposite Effects of Ca 2 and GTP Binding on Tissue Transglutaminase Tertiary Structure. *J. Biol. Chem.* **275**, 3915–3921 (2000).

84. Király, R., Cssz, É., Kurtán, T., Antus, S., Szigeti, K., Simon-Vecsei, Z., Korponay-Szabó, I. R., Keresztessy, Z. & Fésüs, L. Functional significance of five noncanonical Ca2+-binding sites of human transglutaminase 2 characterized by site-directed mutagenesis. *FEBS J.* **276**, 7083–7096 (2009).

85. Jin, X., Stamnaes, J., Klöck, C., DiRaimondo, T. R., Sollid, L. M. & Khosla, C. Activation of extracellular transglutaminase 2 by thioredoxin. *J. Biol. Chem.* **286**, 37866–37873 (2011).

86. Ahvazi, B., Boeshans, K. M. & Rastinejad, F. The emerging structural understanding of transglutaminase 3. *J. Struct. Biol.* **147**, 200–207 (2004).

87. Jang, T. H., Lee, D. S., Choi, K., Jeong, E. M., Kim, I. G., Kim, Y. W., Chun, J. N., Jeon, J. H. & Park, H. H. Crystal structure of transglutaminase 2 with GTP complex and amino acid sequence evidence of evolution of GTP binding site. *PLoS One* **9**, 1–8 (2014).

88. Zhang, J., Antonyak, M. A., Singh, G. & Cerione, R. A. A novel mechanism for the up-regulation of EGF-receptor levels in glioblastomas. *Cell Rep.* **3**, 2008 (2013).

89. Singh, G., Zhang, J., Ma, Y., Cerione, R. A. & Antonyak, M. A. The different conformational states of tissue transglutaminase have opposing affects on cell viability. *J. Biol. Chem.* **291**, 9119–9132 (2016).

90. Begg, G. E., Carrington, L., Stokes, P. H., Matthews, J. M., Wouters, M. A., Husain, A., Lorand, L., Iismaa, S. E. & Graham, R. M. Mechanism of allosteric regulation of transglutaminase 2 by GTP. *Proc. Natl. Acad. Sci. U. S. A.* **103**, 19683–19688 (2006).

91. Simon-Vecseia, Z., , Róbert Királya, b, Péter Bagossia, Boglárka Tótha, Ingrid Dahlbomc, Sergio Cajad, É. C., Katri Lindforsd, Daniele Sblatteroe, É. N., , Markku Mäkid, László Fésüsa, b, and Ilma R. Korponay-Szabóf, g, 1 & A. A single conformational transglutaminase 2 epitope contributed by three domains is critical for celiac antibody binding and effects. **109**, 431–436 (2012).

92. Hnida, K., Stamnaes, J., Du Pré, M. F., Mysling, S., Jørgensen, T. J. D., Sollid, L. M. & Iversen, R. Epitope-dependent functional effects of celiac disease autoantibodies on transglutaminase 2. *J. Biol. Chem.* **291**, 25542–25552 (2016).

93. Klöck, C., DiRaimondo, T. R. & Khosla, C. Role of transglutaminase 2 in celiac disease pathogenesis. *Semin. Immunopathol.* **34**, 513–522 (2012).

94. Iversen, R., Di Niro, R., Stamnaes, J., Lundin, K. E. A., Wilson, P. C. & Sollid, L. M. Transglutaminase 2–Specific Autoantibodies in Celiac Disease Target Clustered, N-Terminal Epitopes Not Displayed on the Surface of Cells. *J. Immunol.* **190**, 5981–5991 (2013).

95. Furini, G. & Verderio, E. A. M. Spotlight on the Transglutaminase 2-Heparan Sulfate Interaction. *Med. Sci.* **7**, 5 (2019).

96. Wang, Z., Collighan, R. J., Pytel, K., Rathbone, D. L., Li, X. & Griffin, M. Characterization of heparin-binding site of tissue transglutaminase: Its importance in cell surface targeting, matrix deposition, and cell signaling. *J. Biol. Chem.* **287**, 13063–13083 (2012).

97. Lortat-Jacob, H., Burhan, I., Scarpellini, A., Thomas, A., Imberty, A., Vivès, R. R., Johnson, T., Gutierrez, A. & Verderio, E. A. M. Transglutaminase-2 interaction with heparin: Identification of a heparin binding site that regulates cell adhesion to fibronectin-transglutaminase-2 matrix. *J. Biol. Chem.* **287**, 18005–18017 (2012).

98. Müller, C. D., Ruiz-Gómez, G., Cazzonelli, S., Möller, S., Wodtke, R., Löser, R., Freyse, J., Dürig, J.-N., Rademann, J., Hempel, U., Pisabarro, M. T. & Vogel, S. Sulfated glycosaminoglycans inhibit transglutaminase 2 by stabilizing its closed conformation. *Sci. Rep.* **12**, 1–16 (2022).

99. Song, M., Hwang, H., Im, C. Y. & Kim, S.-Y. Recent Progress in the Development of Transglutaminase 2 (TGase2) Inhibitors. *J. Med. Chem.* **60**, 554–567 (2017).

100. Choi, K., Siegel, M., Piper, J. L., Yuan, L., Cho, E., Strnad, P., Omary, B., Rich, K. M. & Khosla, C. Chemistry and Biology of Dihydroisoxazole Derivatives: Selective Inhibitors of Human Transglutaminase 2. *Chem. Biol.* **12**, 469–475 (2005).

101. Lindemann, I., Böttcher, J., Oertel, K., Weber, J., Hils, M., Pasternack, R., Linne, U., Heine, A. & Klebe, G. Inhibitors of transglutaminase 2: A therapeutic option in celiac disease. in *XXth International Symposium on Medical Chemistry. Drugs of the Future. 33.* (2014).

102. Zemskov, E. A., Mikhailenko, I., Hsia, R. C., Zaritskaya, L. & Belkin, A. M. Unconventional secretion of tissue transglutaminase involves phospholipid-dependent delivery into recycling endosomes. *PLoS One* **6**, (2011).

103. Aeschlimann, D. & Thomazy, V. Protein crosslinking in assembly and remodelling of

extracellular matrices: The role of transglutaminases. *Connect. Tissue Res.* **41**, 1–27 (2000).

104. Akimov, S. S. & Belkin, A. M. Cell surface tissue transglutaminase is involved in adhesion and migration of monocytic cells on fibronectin. *Blood* **98**, 1567–1576 (2001).
105. Evgeny A. Zemskov, Anna Janiak, Jun Hang, A. W. and A. M. B. The role of tissue transglutaminase in cell-matrix interactions Evgeny. *Front. Biosci.* **11**, 1057–1076 (2006).
106. Janiak, A., Zemskov, E. A. & Belkin, A. M. Cell surface transglutaminase promotes RhoA activation via integrin clustering and suppression of the Src-p190RhoGAP signaling pathway. *Mol. Biol. Cell* **17**, 1606–1619 (2006).
107. Cardoso, I., Stamnaes, J., Andersen, J. T., Melino, G., Iversen, R. & Sollid, L. M. Transglutaminase 2 interactions with extracellular matrix proteins as probed with celiac disease autoantibodies. *FEBS J.* **282**, 2063–2075 (2015).
108. Stamnaes, J., Cardoso, I., Iversen, R. & Sollid, L. M. Transglutaminase 2 strongly binds to an extracellular matrix component other than fibronectin via its second C-terminal beta-barrel domain. *FEBS J.* **283**, 3994–4010 (2016).
109. Shao, M., Cao, L., Shen, C., Satpathy, M., Chelladurai, B., Bigsby, R. M., Nakshatri, H. & Matei, D. Epithelial-to-mesenchymal transition and ovarian tumor progression induced by tissue transglutaminase. *Cancer Res.* **69**, 9192–9201 (2009).
110. Satpathy, M., Cao, L., Pincheira, R., Emerson, R., Bigsby, R., Nakshatri, H. & Matei, D. Enhanced peritoneal ovarian tumor dissemination by tissue transglutaminase. *Cancer Res.* **67**, 7194–7202 (2007).
111. Yuan, L., Siegel, M., Choi, K., Khosla, C., Miller, C. R., Jackson, E. N., Piwnica-Worms, D. & Rich, K. M. Transglutaminase 2 inhibitor, KCC009, disrupts fibronectin assembly in the extracellular matrix and sensitizes orthotopic glioblastomas to chemotherapy. *Oncogene* **26**, 2563–2573 (2007).
112. Jee, Y. H., Mangala, L. S., Fok, J. Y., Lin, Y. G., Merritt, W. M., Spannuth, W. A., Nick, A. M., Fiterman, D. J., Vivas-Mejia, P. E., Deavers, M. T., Coleman, R. L., Lopez-Berestein, G., Mehta, K. & Sood, A. K. Clinical and biological significance of tissue transglutaminase in ovarian carcinoma. *Cancer Res.* **68**, 5849–5858 (2008).
113. Verma, A., Wang, H., Manavathi, B., Fok, J. Y., Mann, A. P., Kumar, R. & Mehta, K. Increased expression of tissue transglutaminase in pancreatic ductal adenocarcinoma

and its implications in drug resistance and metastasis. *Cancer Res.* **66**, 10525–10533 (2006).

114. Jeong, J. H., Cho, B. C., Shim, H. S., Kim, H. R., Lim, S. M., Kim, S. K., Chung, K. Y., Bakhtiar Ul Islam, S. M., Song, J. J., Kim, S. Y. & Kim, J. H. Transglutaminase 2 expression predicts progression free survival in non-small cell lung cancer patients treated with epidermal growth factor receptor tyrosine kinase inhibitor. *J. Korean Med. Sci.* **28**, 1005–1014 (2013).
115. Van Strien, M. E., Drukarch, B., Bol, J. G., Van Der Valk, P., Van Horssen, J., Gerritsen, W. H., Breve, J. J. & Van Dam, A. M. Appearance of tissue transglutaminase in astrocytes in multiple sclerosis lesions: A role in cell adhesion and migration? *Brain Pathol.* **21**, 44–54 (2011).
116. van Strien, M. E., Brevé, J. J. P., Fratantoni, S., Schreurs, M. W. J., Bol, J. G. J. M., Jongenelen, C. A. M., Drukarch, B. & van Dam, A. M. Astrocyte-derived tissue Transglutaminase interacts with fibronectin: A role in astrocyte adhesion and migration? *PLoS One* **6**, 1–12 (2011).
117. Espitia Pinzón, N., Brevé, J. J. P., Bol, J. G. J. M., Drukarch, B., Baron, W. & van Dam, A. M. Tissue transglutaminase in astrocytes is enhanced by inflammatory mediators and is involved in the formation of fibronectin fibril-like structures. *J. Neuroinflammation* **14**, 1–13 (2017).
118. Espitia Pinzon, N., Sanz-Morello, B., Brevé, J. J. P., Bol, J. G. J. M., Drukarch, B., Bauer, J., Baron, W. & Van Dam, A. M. Astrocyte-derived tissue Transglutaminase affects fibronectin deposition, but not aggregation, during cuprizone-induced demyelination. *Sci. Rep.* **7**, 1–13 (2017).
119. Patten, J. & Wang, K. Fibronectin in development and wound healing. *Adv. Drug Deliv. Rev.* **170**, 1–16 (2021).
120. Dalton, C. J. & Lemmon, C. A. Fibronectin: Molecular structure, fibrillar structure and mechanochemical signaling. *Cells* **10**, 1–20 (2021).
121. Little, W. C., Schwartlander, R., Smith, M. L., Gourdon, D. & Vogel, V. Stretched extracellular matrix proteins turn fouling and are functionally rescued by the chaperones albumin and casein. *Nano Lett.* **9**, 4158–4167 (2009).
122. Baneyx, G., Baugh, L. & Vogel, V. Fibronectin extension and unfolding within cell matrix fibrils controlled by cytoskeletal tension. *PNAS* **99**, 5139–5143 (2002).

123. Bultmann, H., Santas, A. J. & Peters, D. M. P. Fibronectin Fibrillogenesis Involves the Heparin II Binding Domain of Fibronectin*. *J. Biol. Chem.* **273**, 2601–2609 (1998).

124. Schwarzbauer, J. E. Identification of the Fibronectin Sequences Required for Assembly of a Fibrillar Matrix. *J. Cell Biol.* **113**, 1463–1473 (1991).

125. Hocking, D. C., Smith, R. K. & Mckeown-Longo, P. J. A Novel Role for the Integrin-binding III-10 Module in Fibronectin Matrix Assembly. *J. Cell Biol.* **133**, 431–444 (1996).

126. Mitsi, M., Handschin, S., Gerber, I., Schwartländer, R., Klotzsch, E., Wepf, R. & Vogel, V. The ultrastructure of fibronectin fibers pulled from a protein monolayer at the air-liquid interface and the mechanism of the sheet-to-fiber transition. *Biomaterials* **36**, 66–79 (2015).

127. Briknarová, K., Åkerman, M. E., Hoyt, D. W., Ruoslahti, E. & Ely, K. R. Anastellin, an FN3 fragment with fibronectin polymerization activity, resembles amyloid fibril precursors. *J. Mol. Biol.* **332**, 205–215 (2003).

128. Stine, J. M., Ahl, G. J. H., Schlenker, C., Rusnac, D. V. & Briknarová, K. The Interaction between the Third Type III Domain from Fibronectin and Anastellin Involves β-Strand Exchange. *Biochemistry* **56**, 4667–4675 (2017).

129. Baneyx, G., Baugh, L. & Vogel, V. Coexisting conformations of fibronectin in cell culture imaged using fluorescence resonance energy transfer. *PNAS* **98**, 14464–14468 (2001).

130. Enrico Klotzsch, Michael L. Smith, Kristopher E. Kubow, Simon Muntwyler, William C. Little, Felix Beyeler, Delphine Gourdona, Bradley J. Nelsonb, and V. V. Fibronectin forms the most extensible biological fibers displaying switchable force-exposed cryptic binding sites. *Proc. Natl. Acad. Sci.* **106**, 18267–18272 (2009).

131. Zollinger, A. J. & Smith, M. L. Fibronectin, the extracellular glue. *Matrix Biol.* **60**–**61**, 27–37 (2017).

132. Vogel, V. & Sheetz, M. Local force and geometry sensing regulate cell functions. *Nat. Rev. Mol. Cell Biol.* **7**, 265–275 (2006).

133. Sun, Z., Guo, S. S. & Fässler, R. Integrin-mediated mechanotransduction. *J. Cell Biol.* **215**, 445–456 (2016).

134. Ross, T. D., Coon, B. G., Yun, S., Baeyens, N., Tanaka, K., Ouyang, M. & Schwartz, M. A. Integrins in mechanotransduction. *Curr. Opin. Cell Biol.* **25**, 613–618 (2013).

135. Schoen, I., Pruitt, B. L. & Vogel, V. The Yin-Yang of Rigidity Sensing: How Forces and Mechanical Properties Regulate the Cellular Response to Materials. *Annu. Rev. Mater.*

Res. **43**, 589–618 (2013).

136. Wang, H., Dembo, M. & Wang, Y.-L. Substrate flexibility regulates growth and apoptosis of normal but not transformed cells. *Am J Physiol Cell Physiol* **279**, 1345–1350 (2000).
137. Huelsz-Prince, G., Belkin, A. M., Vanbavel, E. & Bakker, E. N. T. P. Activation of extracellular transglutaminase 2 by mechanical force in the arterial wall. *J. Vasc. Res.* **50**, 383–395 (2013).
138. Hytönen, V. P. & Vogel, V. How force might activate talin's vinculin binding sites: SMD reveals a structural mechanism. *PLoS Comput. Biol.* **4**, (2008).
139. Colin P. Johnson, Hsin-Yao Tang, Christine Carag, David W. Speicher, D. E. D. Forced unfolding of proteins within cells. *Science (80-.).* **317**, 663–665 (2007).
140. Sawada, Y., Tamada, M., Dubin-Thaler, B. J., Cherniavskaya, O., Sakai, R., Tanaka, S. & Sheetz, M. P. Force Sensing by Mechanical Extension of the Src Family Kinase Substrate p130Cas. *Cell* **127**, 1015–1026 (2006).
141. Adhikari, A. S., Chai, J. & Dunn, A. R. Mechanical load induces a 100-fold increase in the rate of collagen proteolysis by MMP-1. *J. Am. Chem. Soc.* **133**, 1686–1689 (2011).
142. Vogel, V. Mechanotransduction involving multimodular proteins: Converting force into biochemical signals. *Annu. Rev. Biophys. Biomol. Struct.* **35**, 459–488 (2006).
143. Hertig, S., Chabria, M. & Vogel, V. Engineering mechanosensitive multivalent receptor-ligand interactions: Why the nanolinker regions of bacterial adhesins matter. *Nano Lett.* **12**, 5162–5168 (2012).
144. Le, M., Erat, C., Slatter, D. A., Lowe, E. D., Millard, C. J., Farndale, R. W., Campbell, I. D. & Vakonakis, I. Identification and structural analysis of type I collagen sites in complex with fibronectin fragments. *PNAS March* **17**, 4195–4200 (2009).
145. LeMosys, E. K., Erickson, H. P., Beyer, W. F., Radek, J. T., Jeong, J.-M., Murthy, S. N. P. & Lorand, L. Visualization of Purified Fibronectin-Transglutaminase Complexes*. **267**, 7880–7885 (1992).
146. Stryer, Lubert; Haugland, R. P. Energy transfer. Spectroscopic ruler. *PNAS* **58**, 719–726 (1967).
147. Clegg, R. M. Chapter 1 Förster resonance energy transfer—FRET what is it, why do it, and how it's done. *Lab. Tech. Biochem. Mol. Biol.* **33**, 1–57 (2009).
148. Sun, Y., Wallrabe, H., Seo, S. A. & Periasamy, A. FRET microscopy in 2010: The legacy of Theodor Förster on the 100th anniversary of his birth. *Chemphyschem* **12**, 462 (2011).

149. Jones, Garth A., D. S. B. Resonance Energy Transfer: From Fundamental Theory to Recent Applications. *Front. Phys.* **7**, (2019).

150. Khrenova, M., Topol, I., Collins, J. & Nemukhin, A. Estimating Orientation Factors in the FRET Theory of Fluorescent Proteins: The TagRFP-KFP Pair and Beyond. *Biophys. J.* **108**, 126–132 (2015).

151. Van Zundert, G. C. P., Rodrigues, J. P. G. L. M., Trellet, M., Schmitz, C., Kastritis, P. L., Karaca, E., Melquiond, A. S. J., Van Dijk, M., De Vries, S. J. & Bonvin, A. M. J. J. The HADDOCK2.2 Web Server: User-Friendly Integrative Modeling of Biomolecular Complexes. *J. Mol. Biol.* **428**, 720–725 (2016).

152. Karaca, E., Melquiond, A. S. J., De Vries, S. J., Kastritis, P. L. & Bonvin, A. M. J. J. Building macromolecular assemblies by information-driven docking: Introducing the haddock multibody docking server. *Mol. Cell. Proteomics* **9**, 1784–1794 (2010).

153. Van Zundert, G. C. P. & Bonvin, A. M. J. J. DisVis: Quantifying and visualizing accessible interaction space of distance-restrained biomolecular complexes. *Bioinformatics* **31**, 3222–3224 (2015).

154. Erickson, H. P. Reversible unfolding of fibronectin type III and immunoglobulin domains provides the structural basis for stretch and elasticity of titin and fibronectin. *Proc. Natl. Acad. Sci.* **91**, 10114–10118 (1994).

155. Baugh, L. & Vogel, V. Structural changes of fibronectin adsorbed to model surfaces probed by fluorescence resonance energy transfer. *J. Biomed. Mater. Res. - Part A* **69**, 525–534 (2004).

156. Peleg, O., Savin, T., Kolmakov, G. V., Salib, I. G., Balazs, A. C., Kröger, M. & Vogel, V. Fibers with integrated mechanochemical switches: Minimalistic design principles derived from fibronectin. *Biophys. J.* **103**, 1909–1918 (2012).

157. Stamnaes, J., Iversen, R., Fleur Du Pré, M., Chen, X. & Sollid, L. M. Enhanced B-cell receptor recognition of the autoantigen transglutaminase 2 by efficient catalytic self-multimerization. *PLoS One* **10**, 1–19 (2015).

158. Klotzsch, E., Schoen, I., Ries, J., Renn, A., Sandoghdar, V. & Vogel, V. Conformational distribution of surface-adsorbed fibronectin molecules explored by single molecule localization microscopy. *Biomater. Sci.* **2**, 883–892 (2014).

159. Piersimoni, L., Kastritis, P. L., Arlt, C. & Sinz, A. Cross-Linking Mass Spectrometry for Investigating Protein Conformations and Protein-Protein Interactions-A Method for All

Seasons. *Chem. Rev.* **122**, 7500–7531 (2022).

160. Leitner, A., Joachimiak, L. A., Unverdorben, P., Walzthoeni, T., Frydman, J., Förster, F. & Aebersold, R. Chemical cross-linking/mass spectrometry targeting acidic residues in proteins and protein complexes. *Proc. Natl. Acad. Sci. U. S. A.* **111**, 9455–9460 (2014).
161. Grimm, M., Zimniak, T., Kahraman, A. & Herzog, F. XVis: A web server for the schematic visualization and interpretation of crosslink-derived spatial restraints. *Nucleic Acids Res.* **43**, W362–W369 (2015).
162. Graziadei, A. & Rappsilber, J. Leveraging crosslinking mass spectrometry in structural and cell biology. *Structure* **30**, 37–54 (2022).
163. Orbán-Németh, Z., Beveridge, R., Hollenstein, D. M., Rampler, E., Stranzl, T., Hudecz, O., Doblmann, J., Schlögelhofer, P. & Mechtler, K. Structural prediction of protein models using distance restraints derived from cross-linking mass spectrometry data. *Nat. Protoc.* **13**, 478–494 (2018).
164. Rampler, E., Stranzl, T., Orban-Nemeth, Z., Hollenstein, D. M., Hudecz, O., Schloegelhofer, P. & Mechtler, K. Comprehensive Cross-Linking Mass Spectrometry Reveals Parallel Orientation and Flexible Conformations of Plant HOP2-MND1. *J. Proteome Res.* **14**, 5048–5062 (2015).
165. Yang, J. & Zhang, Y. Protein Structure and Function Prediction Using I-TASSER. *Curr. Protoc. Bioinforma.* **52**, 5.8.1-5.8.15 (2015).
166. Kahraman, A., Malmström, L. & Aebersold, R. Xwalk: Computing and visualizing distances in cross-linking experiments. *Bioinformatics* **27**, 2163–2164 (2011).
167. Kim, D. E., Chivian, D. & Baker, D. Protein structure prediction and analysis using the Robetta server. *Nucleic Acids Res.* **32**, W526–W531 (2004).
168. Mirdita, M., Schütze, K., Moriwaki, Y., Heo, L., Ovchinnikov, S. & Steinegger, M. ColabFold: making protein folding accessible to all. *Nat. Methods* **19**, 679–682 (2022).
169. Benkert, P., Biasini, M. & Schwede, T. Toward the estimation of the absolute quality of individual protein structure models. *Bioinformatics* **27**, 343–350 (2011).
170. S.Hubbard, J. T. NACCESS, Computer Program. *Department of Biochemistry and Molecular Biology, University College London* at (1993).
171. De Vries, S. J., Van Dijk, M. & Bonvin, A. M. J. J. The HADDOCK web server for data-driven biomolecular docking. *Nat. Protoc.* **5**, 883–897 (2010).
172. Lindmark, H. & Guss, B. SFS, a novel fibronectin-binding protein from Streptococcus

equi, inhibits the binding between fibronectin and collagen. *Infect. Immun.* **67**, 2383–2388 (1999).

173. Ma, W., Ma, H., Fogerty, F. J. & Mosher, D. F. Bivalent ligation of the collagen-binding modules of fibronectin by SFS, a non-anchored bacterial protein of streptococcus equi. *J. Biol. Chem.* **290**, 4866–4876 (2015).
174. Janiak, A., Zemskov, E. A. & Belkin, A. M. Cell surface transglutaminase promotes RhoA activation via integrin clustering and suppression of the Src-p190RhoGAP signaling pathway. *Mol. Biol. Cell* **17**, 1606–1619 (2006).
175. Pocaterra, A., Romani, P. & Dupont, S. YAP/TAZ functions and their regulation at a glance. *J. Cell Sci.* **133**, (2020).
176. Kim, N., Lee, W. K., Lee, S. H., Jin, K. S., Kim, K. H., Lee, Y., Song, M. & Kim, S. Y. Inter-molecular crosslinking activity is engendered by the dimeric form of transglutaminase 2. *Amino Acids* **49**, 461–471 (2017).
177. Fonta, C. M., Arnoldini, S., Jaramillo, D., Moscaroli, A., Oxenius, A., Behe, M. & Vogel, V. Fibronectin fibers are highly tensed in healthy organs in contrast to tumors and virus-infected lymph nodes. *Matrix Biol. Plus* **8**, 1–15 (2020).
178. Dupont, S., Morsut, L., Aragona, M., Enzo, E., Giulitti, S., Cordenonsi, M., Zanconato, F., Le Digabel, J., Forcato, M., Bicciato, S., Elvassore, N. & Piccolo, S. Role of YAP/TAZ in mechanotransduction. *Nature* **474**, 179–184 (2011).
179. Benn, M. C., Pot, S. A., Moeller, J., Yamashita, T., Fonta, C. M., Orend, G., Kollmannsberger, P. & Vogel, V. How the mechanobiology orchestrates the iterative and reciprocal ECM-cell cross-talk that drives microtissue growth. *Sci. Adv.* **9**, 1–19 (2023).
180. Fonta, C. M., Loustau, T., Li, C., Surendran, S. P., Hansen, U., Murdamoothoo, D., Benn, M. C., Velazquez-Quesada, I., Carapito, R., Orend, G. & Vogel, V. Infiltrating CD8+ T cells and M2 macrophages are retained in tumor matrix tracks enriched in low tension fibronectin fibers. *Matrix Biol.* **116**, 1–27 (2023).
181. Pot, S. A., Lin, Z., Shiu, J., Benn, M. C. & Vogel, V. Growth factors and mechano-regulated reciprocal crosstalk with extracellular matrix tune the keratocyte–fibroblast/myofibroblast transition. *Sci. Reports 2023 131* **13**, 1–19 (2023).
182. Klingberg, F., Chow, M. L., Koehler, A., Boo, S., Buscemi, L., Quinn, T. M., Costell, M., Alman, B. A., Genot, E. & Hinz, B. Prestress in the extracellular matrix sensitizes latent

TGF-β1 for activation. *J. Cell Biol.* **207**, 283–297 (2014).

183. Klingberg, F., Chau, G., Walraven, M., Boo, S., Koehler, A., Chow, M. L., Olsen, A. L., Im, M., Lodyga, M., Wells, R. G., White, E. S. & Hinz, B. The fibronectin ED-A domain enhances recruitment of latent TGF-β-binding protein-1 to the fibroblast matrix. (2018) doi:10.1242/jcs.201293.
184. Nia, H. T., Munn, L. L. & Jain, R. K. Physical traits of cancer. *Science (80-.).* **370**, (2020).
185. Tschumperlin, D. J. & Lagares, D. Mechano-therapeutics: Targeting Mechanical Signaling in Fibrosis and Tumor Stroma. *Pharmacol. Ther.* **212**, 107575 (2020).
186. Kubow, K. E., Klotzsch, E., Smith, M. L., Gourdon, D., Little, W. C. & Vogel, V. Crosslinking of cell-derived 3D scaffolds up-regulates the stretching and unfolding of new extracellular matrix assembled by reseeded cells. *Integr. Biol.* **1**, 635–648 (2009).
187. Van Rheenen, J., Langeslag, M. & Jalink, K. Correcting Confocal Acquisition to Optimize Imaging of Fluorescence Resonance Energy Transfer by Sensitized Emission. *Biophys. J.* **86**, 2517–2529 (2004).
188. Yang, J. & Zhang, Y. I-TASSER server: New development for protein structure and function predictions. *Nucleic Acids Res.* **43**, W174–W181 (2015).
189. van Zundert, G. C. P., Trellet, M., Schaarschmidt, J., Kurkcuoglu, Z., David, M., Verlato, M., Rosato, A. & Bonvin, A. M. J. J. The DisVis and PowerFit Web Servers: Explorative and Integrative Modeling of Biomolecular Complexes. *J. Mol. Biol.* **429**, 399–407 (2017).
190. Sottile, J., Shi, F., Rublyevska, I., Chiang, H. Y., Lust, J. & Chandler, J. Fibronectin-dependent collagen I deposition modulates the cell response to fibronectin. *Am. J. Physiol. - Cell Physiol.* **293**, 1934–1946 (2007).
191. Leitner, A., Walzthoeni, T. & Aebersold, R. Lysine-specific chemical cross-linking of protein complexes and identification of cross-linking sites using LC-MS/MS and the xQuest/xProphet software pipeline. *Nat. Protoc.* **9**, 120–137 (2014).
192. Mohammadi, A., Tschanz, A. & Leitner, A. Expanding the Cross-Link Coverage of a Carboxyl-Group Specific Chemical Cross-Linking Strategy for Structural Proteomics Applications. *Anal. Chem.* **93**, 1944–1950 (2021).
193. Walzthoeni, T., Claassen, M., Leitner, A., Herzog, F., Bohn, S., Förster, F., Beck, M. & Aebersold, R. False discovery rate estimation for cross-linked peptides identified by mass spectrometry. *Nat. Methods* **9**, 901–903 (2012).
194. Pettersen, E. F., Goddard, T. D., Huang, C. C., Meng, E. C., Couch, G. S., Croll, T. I., Morris,

J. H. & Ferrin, T. E. UCSF ChimeraX: Structure visualization for researchers, educators, and developers. *Protein Sci.* **30**, 70–82 (2021).

195. Deutsch, E. W., Bandeira, N., Perez-Riverol, Y., Sharma, V., Carver, J. J., Mendoza, L., Kundu, D. J., Wang, S., Bandla, C., Kamatchinathan, S., Hewapathirana, S., Pullman, B. S., Wertz, J., Sun, Z., Kawano, S., Okuda, S., Watanabe, Y., Maclean, B., Maccoss, M. J., Zhu, Y., Ishihama, Y. & Vizcaíno, J. A. The ProteomeXchange consortium at 10 years: 2023 update. *Nucleic Acids Res.* **51**, D1539–D1548 (2023).
196. Perez-Riverol, Y., Bai, J., Bandla, C., García-Seisdedos, D., Hewapathirana, S., Kamatchinathan, S., Kundu, D. J., Prakash, A., Frericks-Zipper, A., Eisenacher, M., Walzer, M., Wang, S., Brazma, A. & Vizcaíno, J. A. The PRIDE database resources in 2022: A hub for mass spectrometry-based proteomics evidences. *Nucleic Acids Res.* **50**, D543–D552 (2022).
197. Vallat, B., Webb, B., Fayazi, M., Voinea, S., Tangmunarunkit, H., Ganesan, S. J., Lawson, C. L., Westbrook, J. D., Kesselman, C., Sali, A. & Berman, H. M. New system for archiving integrative structures. *Acta Crystallogr. Sect. D Struct. Biol.* **77**, 1486–1496 (2021).

Acknowledgements

As concluding remarks, I would like to acknowledge the contributions and support of the people along my path as a doctoral researcher.

First and foremost, I extend my heartfelt thanks to my doctoral supervisor, Prof. Dr. Viola Vogel, for graciously allowing me to conduct my doctoral research within her research group. In her lab, I had the freedom to explore unexpected scientific questions and to challenge conventional thinking. This experience taught me the invaluable lesson that in scientific research, it's impossible to fully "plan science". The importance of pursuing unexpected and intriguing questions became clear to me, and I am deeply grateful for the excitement and rewards that came with it.

I also wish to express my gratitude to my second thesis advisor and thesis co-examiner, Dr. Alexander Leitner. Our collaboration on cross-linking mass spectrometry enriched this project with valuable insights into structural proteomics and integrative structural modeling. His guidance and recommendations during manuscript writing and publication were immensely helpful. I am especially thankful for his support in the realm of integrative structural modeling guided by XL-MS data and for his general encouragement of my venturing out into the structural modeling world, without which I would not have been able to have accomplished it. I further extend my thanks to Fanny Le Blanc for her work on XL-MS of the TG2-FN protein complex and for acquiring the data that served as the foundation for the modeling.

Next, I would like to express my gratitude to Prof. Dr. Elisabetta Verderio Edwards for dedicating her time to be a part of my doctoral committee and for reading and providing valuable comments on my dissertation.

I express my gratitude to Prof. Simon Pot, Velux Stiftung Foundation and ETH Zurich who funded this project. I am thankful to Prof. Simon Pot for bringing me into the transglutaminase 2 topic, as well as for contributing ideas and insights. I am grateful to Dr. Lukas Braun for our brief but significant collaboration at the beginning of this project. He introduced me to the world of structural biology and different “TG2 conformations”, which remained a key focus throughout my PhD. I am also extremely thankful to Dr. Paulina Pacak for her insightful discussions, expertise in structural biology, and assistance with structural modeling. Our friendship, mutual support, and creative coffee breaks were a highlight of my time in the lab. Additionally, I would like to thank Dr. Mario Benn for introducing me to the business of “fiber-pulling and stretching”, and for his consistent moral support and encouragement throughout my PhD. I am thankful to Dr. Enrico Klotzsch for sharing his expertise in FRET and practical tricks for fiber-pulling experiments that allowed me to perform experiments for the revised manuscript.

I am grateful to Dr. Johanna Mehl for being my officemate even though just briefly and for introducing me to the Life Science Zurich Young Scientist Network. I extend a special thanks to the Life Science Zurich Young Scientist Network, which I was fortunate enough to join and where I have made many new acquaintances. Organizing various career networking events between academia and the biotech/pharma industry has been an extremely valuable experience for me. I am particularly grateful to Michael Schmitz, Fabienne Tschanz, Verena

Waller, and Sarah Klinnert, with whom I served on the Board of LSZYSN from April 2021 to April 2022. The teamwork I shared with you on the Board has been enormous fun and provided me with an invaluable learning experience. Observing how each of you solved problems or navigated sensitive circumstances, which were quite frequent, has been an insightful journey of skill acquisition for me.

I would like to thank my officemate Dr. Charlotte Fonta for support, useful discussions, and your kind moral support during the first half of 2022, when I was having a very difficult time. I am grateful to Dr. Elise Aeby for her friendship and kind support during that time as well. I have greatly enjoyed our mountain bike rides and appreciate you sharing your knowledge of the bikes with me, an inexperienced rider and organizing “Bike to work” competitions. Thanks to Elise, I finally made it to the ETH Makerspace and completed a few DIY projects of my own in laser cutting. It was amazingly fun, and I wish I had started with it earlier so that I could have done much more at Makerspace.

A special thank you goes to our Administrative Assistant Norma De Giuseppe, for her exceptional organizational skills and sensitivity. She made our work much easier and faster on numerous occasions.

I thank all my colleagues of the Vogel lab, current and former, with whom I crossed paths and shared memorable moments. I express my gratitude to Ronja Rappold and Arnaud Melville for their optimism and positivity, Konstantin Wolf for conversational lunches, fun "Exploding Kittens" evenings, and awesome beach volleyball games. I am grateful to Tamara Zünd, Tassilo von Trotha, Fabrizio Pennacchio, Michele Crestani, Dilara Perver, and Sebastian Lickert for your friendship and exchanges that enriched my experience. To former lab members Andrea Fernandes, Jenna Graham, and Olivera Evrova, I am grateful to have you all in my network and to maintain connections with each of you. I am grateful to Dr. Daniela Ortiz-Franyuti, who standardized the Matlab script for FN-FRET image analysis during her PhD, which has been a go-to tool throughout my PhD.

I am incredibly grateful to my family and friends for supporting me on my PhD journey in every possible way. I am enormously grateful to my acquaintances and colleagues, who in the first months of the Russian invasion of Ukraine reached out to me directly and extended their words of support and compassion. Finally, I extend my most humbled admiration to the men and women at the frontlines defending Ukraine. I am humbled by your limitless courage, your readiness for self-sacrifice, and unwavering love of freedom.